UNIVERSITÉ DE NANTES

FACULTÉ DES SCIENCES ET DES TECHNIQUES

———

ÉCOLE DOCTORALE 3MPL
MATIÈRE, MOLÉCULES, MATÉRIAUX EN PAYS DE LA LOIRE

Année 2013

Modélisation du graphène avec les techniques *ab initio*
–
Ab initio modelling of graphene

———

THÈSE DE DOCTORAT
Discipline : Physique
Spécialité : Science des Matériaux

Présentée
et soutenue publiquement par

Philipp WAGNER

Le 19 avril 2013, devant le jury ci-dessous

Président	Olivier CHAUVET, Professeur, Université de Nantes, IMN, France
Rapporteurs	Jean-Christophe CHARLIER, Professeur, Université catholique de Louvain, Belgique Milo SHAFFER, Professeur, Imperial College London, Royaume-Uni
Examinateurs	Patrick BRIDDON, Senior Lecturer, Newcastle University, Royaume-Uni Christopher EWELS, CR1 (HDR), CNRS, IMN Nantes, France Bernard HUMBERT, Professeur, Université de Nantes, IMN, France
Membres invités	Jean-Luc DUVAIL, Professeur, Université de Nantes, IMN, France Serge LEFRANT, Professeur émérite, Université de Nantes, IMN, France

Directeur de thèse : Dr. Christopher Ewels

Co-Directeur de thèse : Prof. Bernard Humbert

Résumé de la thèse en français

Modélisation du graphène avec les techniques *ab initio*

Philipp Wagner

Avril 2013

Table des matières

1 Introduction

La nanotechnologie est présente aujourd'hui dans de nombreuses situations de la vie moderne. Nous utilisons des téléphones mobiles et des ordinateurs (portables) tous les jours et nous avons pris l'habitude de manipuler des jeux vidéo 3D avec des graphismes réalistes et de communiquer par courrier électronique ou vidéo en utilisant Internet. Tout cela est aujourd'hui possible parce que les études intensives au 20ème siècle du semi-conducteur silicium ont permis une maîtrise de fabrication des circuits (intégrés) électroniques à base de silicium, composés de transistors, résistances, condensateurs ou de diodes, électroniquement connectés entre eux. Ordinateurs, téléphones portables («smartphones»), tablettes tactiles, téléviseurs, voitures, avions, Si-photovoltaïques, appareils photographiques numériques, différentes sortes de détecteurs ou systèmes médicaux utilisent tous une électronique fondée sur le silicium. L'intensité et l'influence croissante des utilisations des appareils électroniques dans notre vie moderne ont créé au cours des 30 dernières années un énorme marché pour le matériau silicium avec l'émergence d'une forte industrie du silicium totalisant en 2012, un chiffre d'affaires d'environ 300 milliards de dollars américains.

L'histoire des puces informatiques modernes a commencé en 1958 avec Jack S. Kilby [1] et l'invention du «circuit intégré» dans un laboratoire de Texas Instruments, aux Etats-Unis. Il a fallu attendre 1971 pour qu'Intel fabrique les premières puces informatiques commercialement disponibles à base silicium, en utilisant une technologie «PMOS» et des transistors avec 10 μm de longueur de grille (2300 transistors sur une seule puce). Les puces de silicium commercialisées sont produites (en masse) à base de silicium «wafers», des disques de diamètres jusqu'à 450 mm («18 pouces») de silicium cristallin, très pur et presque sans défaut et des épaisseurs jusqu'à 925 μm [2, 3]. Sur les wafers, de nombreux circuits intégrés sont fabriqués en parallèle et les wafers sont découpés ensuite [4]. Aujourd'hui, les puces puissantes peuvent contenir plusieurs milliards de transistors. En 2012, la plupart des circuits intégrés avancés ont été produits en utilisant une technologie «CMOS» à 22

nm de longueur de grille, et des feuilles de route pour les puces avec des longueurs de grille à moins de 10 nm observées [5, 6]. Alors qu'avec près de 5 nm, les limites physiques des puces à base de silicium sont atteintes, se développent dans le même temps de nouveaux matériaux tels que des Si-nanofils, des nanotubes de carbone et le graphène. Ces matériaux sont des candidats prometteurs pour de futurs circuits intégrés [6]. Pour les Si-nanofils, certaines techniques de fabrication connues peuvent être adaptées, pour favoriser des structures adoptant des architectures de puces d'aujourd'hui. Un gain réel de performance pour les nouvelles puces d'ordinateur serait attendue lors de l'intégration de matériaux carbonés tels que les nanotubes de carbone ou le graphène.

La technologie du 21ème siècle sera très probablement dominée par les nouveaux nanomatériaux carbonés, tels que les fullerènes, les nanotubes de carbone (NTC) et le graphène [7], conduisant à de nouveaux circuits électriques de haute performance, à des matériaux composites plus fonctionnels, plus riches en terme de champs d'applications, plus «intelligents», et de nouveaux bio-systèmes électroniques, pour ne citer que quelques grandes possibilités rêvées [8]. En plus de l'application purement électronique, les nanomatériaux de carbone sont également envisagés pour l'exploitation de leurs autres propriétés soit de conduction thermique soit mécaniques dans la conception de nouveaux matériaux composites. Citons les composites polymère-NTC [9, 10] et les matériaux composites polymères-graphène [11, 12]. Leurs possibilités d'applications multiples sont un avantage majeur par rapport à d'autres matériaux.

Pour atteindre ces diverses applications, d'importants investissements par les plus grandes entreprises technologiques ont été réalisés dans le domaine de la recherche en nanotechnologie, effectivement en plus de développer des nouveaux nanomatériaux à base de carbone, de nouveaux procédés de production rentables sont à établir. Au vu du marché de 300 milliards de dollars (2012) pour l'électronique fondée sur le silicium et de sa continuelle progression, la perspective d'avenir est très alléchante pour le graphène (et les matériaux carbonés apparentés pertinents)

[7]. En outre, rappelons que l'élément carbone est très répandu sur notre terre et donc que son prix est bien plus indépendant des problèmes politico-géographiques, que pour d'autres éléments comme les terres rares utilisées par exemple dans les semiconducteurs de type III-V, tels que l'indium, le gallium ou l'arsenic.

Au niveau de connaissance actuel, l'industrie est contrainte à s'intéresser encore à la compréhension fondamentale de la physique et de la chimie sous-jacente à ces matériaux [7]. Particulièrement ces derniers temps, le graphène est devenu un sujet d'étude fondamentale populaire dans les universités et les laboratoires de recherche dans le monde entier, tandis que la recherche parallèle des nanotubes de carbone et des fullerènes est en cours.

Les deux nanomatériaux de carbone actuellement privilégiés sont : (i) les Nano-Tubes de Carbones (NTC), découverts en 1991 [13] et (ii) le graphène suspendu étudié pour la première fois en 2004 [14] tandis que des recherches sur les formes fullerènes se poursuivent. Notons que le matériel expérimental graphène n'est donc disponible que depuis seulement neuf ans et que pourtant il a déjà des applications pratiques et qu'il a valu le prix Nobel de physique en 2010 à Andre Geim et Konstantin Novoselov [15] de l'Université de Manchester, conférant le statut de «matériau miracle» au graphène. Geim et Novoselov ont été honorés pour leurs travaux sur le graphène, qui démontraient expérimentalement le grand potentiel de ses propriétés électroniques, thermiques, optiques et mécaniques de ce matériau bi-dimensionnel. Les propriétés de ce matériau devraient conduire en théorie à des performances nettement supérieures à celles des matériaux en usage aujourd'hui comme le graphite, le silicium ou encore le cuivre, comme il rappele le Tableau 1.

	Graphène	Graphite	Silicium	Cuivre
Dimensions	2D (épaisseur ≈ 3,3 Å)	3D (solide)	3D (solide)	3D (solide)
Densité ρ à la TA (g cm^{-3})	$\sim$ 2,25	2,27	2,33	8,95
Point de fusion (K)	-	3925 **	1683	1358
Module de Young E (TPa)	1,06	0,35 - 1,06 *	0,13 - 0,18	0,11 - 0,13
Coefficient de Poisson ν	0,0 / 0,2 *	0,0 / 0,2 *	0,2 - 0,3	$\sim$ 0,34
Conductivité thermique K (W m^{-1} K^{-1})	$\sim$ 5000	25 - 1000 *	$\sim$ 150	$\sim$ 400
Mobilité d'électrons μ (cm^2 V^{-1} s^{-1})	5000 - > 200.000	3 - 15.000 *	$\leq$ 1400	$\sim$ 20.000
Résistivité à la TA (Ω m)	$\sim 1 \cdot 10^{-8}$	$3 \cdot 10^{-6}$ - $3 \cdot 10^{-3}$ *	$\sim 6{,}4 \cdot 10^{2}$	$\sim 1{,}7 \cdot 10^{-8}$
Bande interdite (eV)	- (semi-métal)	- (semi-métal)	1,12 (semi-conducteur)	- (métal)

* : Notez que le graphène et le graphite sont fortement anisotropes, par exemple perpendiculaire et parallèle au plan(s) de base.

** : Sublimation directe.

Tableau 1 – Résumé des propriétés de base du graphène, du graphite, du silicium cristallin et du cuivre cristallisé. (La plupart des valeurs du graphite, du silicium et du cuivre peuvent être trouvées dans la littérature classique [16–21]. Les paramètres concernant le graphène proviennent quant à elles des références [8, 12, 22–27] ainsi que du chapitre 3 de cette thèse.)

Le graphène - le nanomatériau du 21ème siècle ?

Le nanomatériau graphène correspond à un simple feuillet en deux dimensions constitué uniquement d'atomes de carbone caractérisé par une épaisseur correspondant à celle d'un atome de carbone. L'arrangement des atomes dans ce feuillet à deux dimensions (2D) suit un motif hexagonal, en treillis de nid d'abeilles. En enroulant cette structure, des structures de nanotubes de carbone (1D) et de fullerènes (0D) sont générées, alors que l'empilement des feuillets 2D conduit à la structure du graphite (3D). Par conséquent, la structure du graphène peut être considérée comme la structure «mère» de tous les matériaux de carbone graphitiques [22]. La distinction entre matériaux 2D et 3D, se fait à environ une dizaine de couches de graphène empilées [22, 28, 29]. Par la suite dans cette thèse, ces matériaux seront nommés (simple-couche) graphène, bi-couche de graphène, tri-couche de graphène etc.

Les propriétés électroniques du graphène sont donc exceptionnelles. Depuis plusieurs décennies, le matériau a fait l'objet d'études théoriques [30–32], souvent sous l'appelation «graphite 2D». Une seule couche de graphène sans défauts et parfaite est un semi-métal (ou «semi-conducteur avec une bande interdite de zero») ne faisant pas apparaître d'écart d'énergie dans la structure de bande. En effet autour du niveau de Fermi au point K, les bandes de valence et de conduction se croisent linéairement, formant ce qu'on appelle un «cône de Dirac». Tandis que les électrons sont normalement décrits par l'équation de Schrödinger, cette linéarité des bandes signifie que les électrons dans cette région ne peuvent être décrits que par l'équation relativiste de Dirac. Ils constituent donc des quasi-particules relativistes, appellées fermions de Dirac sans masse [22]. En d'autres termes près du niveau de Fermi (au point K), les électrons se déplacent comme des particules sans masse avec une vitesse de $v_F \approx 10^6$ m/s (vitesse Fermi) dans le réseau du graphène. Ces propriétés du graphène ont été confirmées expérimentalement près de 60 ans après leur prédiction théorique en 2004 par Novoselov *et al.* [14]. Des mobilités de porteurs extrêmement élevées ont été mesurées. Mobilités electroniques de valeurs μ plus de 200.000 $cm^2\ V^{-1}\ s^{-1}$ ont été mesurées pour une feuille de graphène suspendue

[33], avec un comportement s'approchant d'un transport balistique [34]. En outre, un comportement d'effet Hall quantique a été induit par l'application externe d'un champ magnétique [35].

Cette propriété associée à un grande module de Young dans le plan de 1,06 TPa et à une conductivité thermique extrêmement élevée d'environ 5000 W m^{-1} K^{-1} prédestinait le graphène pour la prochaine génération de circuits électroniques et de dispositifs. Même les faibles densités de défauts dans le plan du graphène n'influençent pas fortement les fermions de Dirac en raison du paradox de Klein [36] et ne dégradent pas de façon significative les propriétés électroniques.

Pour les applications électroniques avec des caractéristiques «on-off», tels que des transistors à effet de champ, des puces informatiques, une bande interdite modérée est normalement nécessaire. Pour ce faire, les propriétés intrinsèques de graphène doivent être modifiées ou redessinées. L'introduction d'une bande interdite dans la structure de bande du feuillet 2D est possible en découpant le graphène en rubans fins, appelés nano-rubans de graphène. En effet, cette nano-structure crée un confinement quantique le long du ruban en réduisant les dimensions pour aller vers un objet 1D. L'ouverture de bande va dépendre des propriétés de bordure et de la largeur du ruban ; une ouverture significative de bande interdite est prévue pour des rubans fins de largeur inférieure à 20 Å [37, 38].

Différentes voies pour produire des nanorubans de graphène ont été proposées et réalisées ces dernières années, y compris d'ouvrir sur la longueur, « dézipper », des nanotubes de carbone [39], de découper avec un faisceau d'électrons un feuillet de graphène [40] ou d'auto-assembler moléculairement des précurseurs organiques, procédé «bottom-up» [41]. La largeur du ruban joue un rôle crucial sur la propriété obtenue, à ce jour, seuls des nano-rubans de graphène, en structure «armchair» (fauteuil) avec une précision atomique de largeur proche de 7,3 Å ont été reproduits avec succès, donnant une bande interdite d'environ 2,3 eV, sur une surface Au(111) [42]. La croissance de GNRs étant très complexe, il est alors important de

maîtriser et éventuellement modifier les propriétés électroniques pour une largeur de ruban définie.

Avant cette thèse, peu de calculs sur les propriétés de bord de nanorubans de graphène et de feuillets de graphène en général étaient présents dans la littérature. Les bords de graphène sont chimiquement plus réactifs que les faces basales du réseau hexagonal plat 2D, en raison de la présence soit de liaisons pendantes soit d'hétéroatomes, et d'offrir ainsi un moyen accessible et bien contrôlable pour changer les propriétés électroniques des nanorubans de graphène.

La théorie de la fonctionnelle de la densité

Le théorème de Hohenberg-Kohn [43] donne la base fondamentale de la théorie de la fonctionnelle de la densité :

L'état fondamental d'un système défini peut être complètement décrit à l'aide de la densité de charge $n(r)$, ce qui correspond à la description d'une fonction d'onde de l'état fondamentale non dégénérée et non polarisée $\Psi(r)$.

Pour vraiment utiliser la densité de charge pour décrire un état fondamental d'un système, Kohn et Sham ont reformulé le problème dans ce qu'on appelle les équations de Kohn-Sham [44]. En utilisant des unités atomiques les trois équations suivantes auto-cohérentes ont été donnés par Kohn et Sham (avec les unités atomiques $m_e = e = \hbar = 4\pi\epsilon_0 \equiv 1$) :

$$\underbrace{\left[-\frac{1}{2}\nabla^2 + \int \frac{n(\vec{r'})}{|\vec{r} - \vec{r'}|} d\vec{r} + V_{ext}(\vec{r}) + V_{XC}(\vec{r})\right]}_{\hat{H}_{KS_\lambda}} \Psi_\lambda(\vec{r}) = E_\lambda \Psi_\lambda(\vec{r}) \tag{1}$$

$$n(\vec{r}) = \sum_\lambda^N |\Psi_\lambda(\vec{r})|^2 \tag{2}$$

$$V_{XC}(\vec{r}) = \frac{\delta E_{XC}\left[n(\vec{r})\right]}{\delta n(\vec{r})} \tag{3}$$

La densité de charge de l'état fondamental peut être représenté comme la somme des orbitales électroniques (2), sans interaction considérée entre N électrons. Les Kohn-Sham orbitales Ψ_λ sont les états de l'équation de Schrödinger indépendante du temps (1) pour chaque électron. En ce qui concerne le nouveau Kohn-Sham hamiltonien $\hat{H}_{KS_\lambda}$ il y a encore une autre approximation nécessaire pour décrire le potentiel de corrélation d'échange $V_{XC}(\vec{r})$. $E_{XC}\left[n(\vec{r})\right]$ est appelée l'énergie de corrélation d'échange (3), utilisé pour décrire le potentiel de corrélation d'échange.

En utilisant (1), (2) et (3) l'énergie totale du système peut être efficacement réduite de manière itérative pour trouver l'état fondamental, commencé avec une première distribution de densité de charge estimée. Ensuite, le principe variationnel va être appliqué pour trouver la densité de charge $n(\vec{r})$, sachant que la densité de charge correcte représente l'état fondamental avec le minimum d'énergie du système.

L'approximation de la densité locale a été utilisée comme approximation pour décrire le potentiel de corrélation d'échange $V_{XC}(\vec{r})$ dans cette thèse. Le principe variationnel a été appliqué dans ce qu'on appelle le «cycle auto-cohérent» pour trouver itérativement l'énergie minimale du système, et donc la densité de charge de l'état fondamental, telle que transposée dans le code *AIMPRO* utilisé dans cette étude.

Le code *AIMPRO*

L'abréviation AIMPRO signifie «**A**b **I**nitio **M**odelling **Pro**gram» et est codé en langage de programmation Fortran. Une méthode *ab initio* est fondée sur uniquement une base théorique, à l'exception des espèces atomiques prédéfinies. Dans le cas de *AIMPRO*, la théorie fonctionnelle de la densité (DFT) constitue la base de calculs des propriétés structurales, électroniques ou vibrationnelles.
Une bonne vue d'ensemble des évolutions en cours et de l'état de l'art du code *AIMPRO* est accessible dans les références suivantes [45–47]. Le code AIMPRO a déjà été utilisé avec succès sur de nombreux matériaux différents (à base de carbone, de silicium, les zéolithes, etc.) dans environ une dizaine de laboratoires et d'universités différentes dans cinq pays européens.

Objectifs de la thèse

L'objectif principal de cette thèse est d'étudier systématiquement le comportement des propriétés de bord de nanofeuillets de graphène, et des nanorubans de graphène en particulier, pour différents types classique de bord possible («armchair», «zigzag», «chiral» et «Klein» [48, 49], y compris plusieurs configurations de bords reconstruits), combiné avec divers groupes de terminaison de bord réalistes. En y ajoutant la possibilité de terminer ces différents bords par différents groupes chimiques réalistes, j'ai modélisé ces propriétés à l'aide du code *AIMPRO* utilisant les calculs fondés sur la théorie de la fonctionnelle de densité dans l'approximation de la densité locale. En outre, les propriétés mécaniques de different nanofeuillets, nanotubes et polymères organiques ont été étudiés, à l'aide d'un nouveau concept de volume développé dans cette thèse.

2 Structures de graphène et matériaux dérivés

Formes allotropiques du carbone

Historiquement, le carbone est l'un des rares éléments que l'humanité connait depuis l'Antiquité. Par exemple, les Égyptiens et les Sumériens, il y a 5000-6000 ans [50], l'utilisent pour obtenir le bronze. Sa première principale utilisation fut le chauffage sous forme de charbon de bois. Plus tard d'autres applications du charbon, en médecine ou encore dans les procédés de purification de l'eau, ont été reportées. Le mot anglais, «carbon», dérive peut-être de l'expression française, «charbon», ou du mot latin «carbo» désignant le charbon et le charbon de bois. L'élément carbone (**C**) a le numéro atomique 6 et se trouve dans le groupe 14 du tableau périodique. Il possède la configuration électronique $[1s^2 2s^2 2p^2]$. Par conséquent, l'atome de carbone isolé possède deux électrons de cœur $1s$ et quatre électrons de valence (deux décrits par les spin-orbitales $2s$ et deux par $2p$). L'atome de carbone peut former de fortes liaisons simples, doubles et triples avec d'autres atomes de carbone ou d'autres éléments. En raison de cette variabilité des liaisons chimiques adoptables par l'élément carbone, il existe plusieurs formes allotropiques pour la formule brute, C, telles que le diamant, le graphite / le graphène, le carbone amorphe, la phase graphyne, les formes schwarzites et les fullerènes / les nanotubes.

L'atome de carbone peut évidement se lier à un grand nombre d'autres atomes. Aujourd'hui, on connait plus de dix millions de différents composés à base de carbone, définissant ainsi un domaine propre de la chimie, la chimie organique. Le carbone est présent aussi dans toutes les formes de vie découvertes à ce jour ; par exemple, environ 18 % de la masse corporelle totale de l'homme est constituée de carbone [51]. Comme un élément clé dans l'univers, le carbone semble pour l'instant être la base chimique nécessaire à toute vie connue.

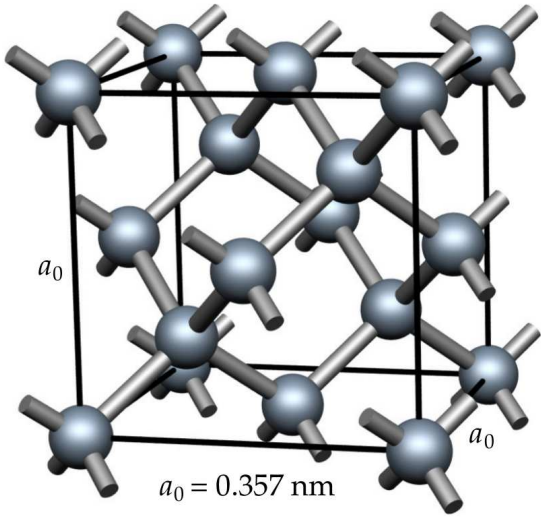

FIGURE 1 – Schéma de la cellule d'unité conventionnelle cubique fcc de diamant, avec a_0 paramètre de maille cubique. Les boules grise sont des atomes de carbone, tandis que les lignes grises symbolisent les liaisons. (Image de [52])

Diamant

Dans la structure diamant, un atome de carbone a quatre premiers voisins carbone, placés dans une coordination régulière tétraédrique. Une description simplifiée entre ces quatre atomes voisins de carbone et un atome central sur la base d'orbitales hybrides sp^3 conduit à quatre liaisons fortes, avec un électron de valence apporté par chaque atome de carbone, quatre liaisons σ. Agencé de cette manière, le matériau dans son volume, possède «la structure diamant», structure cubique à faces centrées (fcc), avec deux atomes aux positions $((0,0,0);(\frac{1}{4},\frac{1}{4},\frac{1}{4}))$. Dans la Figure 1 une cellule unitaire classique de la structure de diamant est représentée avec le paramètre de maille cubique a_0=3,57 Å =0,357 nm à 300 K [20, 21, 53]. La distance C-C y est de $d_{C-C} = \frac{\sqrt{3}}{4}a_0 \approx$ 1,54 Å [17, 52] et chaque direction C-C possède avec sa voisine un angle C-C-C de 109,5°.

Le diamant est un semi-conducteur avec une large bande interdite indirecte de 5,45 à 5,47 eV à 300 K [20, 21]. Les diamants très purs sont donc très transparents dans le visible et peuvent parfois être utilisés comme isolants électroniques. Le diamant est également connu pour son extrême dureté, par rapport à de nombreux autres

matériaux. Même si le module de Young n'est pas isotrope les valeurs sont remarquablement élevé d'environ 1,05 à TPa dans le plan (100) et jusqu'à 1,22 TPa dans le plan (111) [54–56]. La conductivité thermique du diamant est très élevée à température ambiante (293,15 K) jusqu'à 2200 W m^{-1} K^{-1} [57], plusieurs fois plus élevée que pour les métaux (cuivre $\approx$ 400 W m^{-1} K^{-1} [57]). Certaines formes du diamant peuvent être chauffées jusqu'à environ 2000 K dans une atmosphère inerte en restant stables [58].

Toutes ces propriétés font du diamant un matériau très intéressant pour diverses applications. Depuis plusieurs décennies, les propriétés mécaniques et thermiques du diamant ont été utilisées dans des lames de sciage pour la coupe de la pierre, du métal et de céramique, dans des lames d'outils chirurgicaux ou dans des dissipateurs de chaleur pour des fenêtres. Par dopage du diamant, il est possible de modifier les propriétés électroniques, en diminuant par exemple la largeur de bande interdite. Ainsi, un grand potentiel de cette nouvelle structure a été prédit dans les années 1990 pour des dispositifs à base de semi-conducteurs, cependant cela reste difficile à réaliser, notamment pour obtenir des dopants de type p avec un niveau peu profond [59]. Actuellement, les nano-diamants et les «dots» quantiques de diamant constituent des voies prometteuses [60]. Mais jusqu'à ce jour, la grande percée industrielle attendue du diamant dans l'industrie du semi-conducteur n'a pas pu être réalisée, tandis que d'autres formes allotropiques du carbone telles que la forme graphène deviennent compétitives.

Graphite

Le graphite est une autre forme allotropique du carbone, où tous les atomes sont cette fois liés en coordination trigonale (hybridation sp^2). Ainsi cet assemblage des atomes donne un réseau d'atomes de carbone disposés sur un plan : le feuillet de graphène. Dans chaque feuillet, un atome de carbone possède trois plus proches voisins disposés en une structure hexagonale (aussi appelé «nid d'abeille» en réseau, voir la Figure 2). Les atomes dans le plan sont fortement liés par des liaisons covalentes σ, et des liaisons π, permettant une délocalisation importante d'une partie

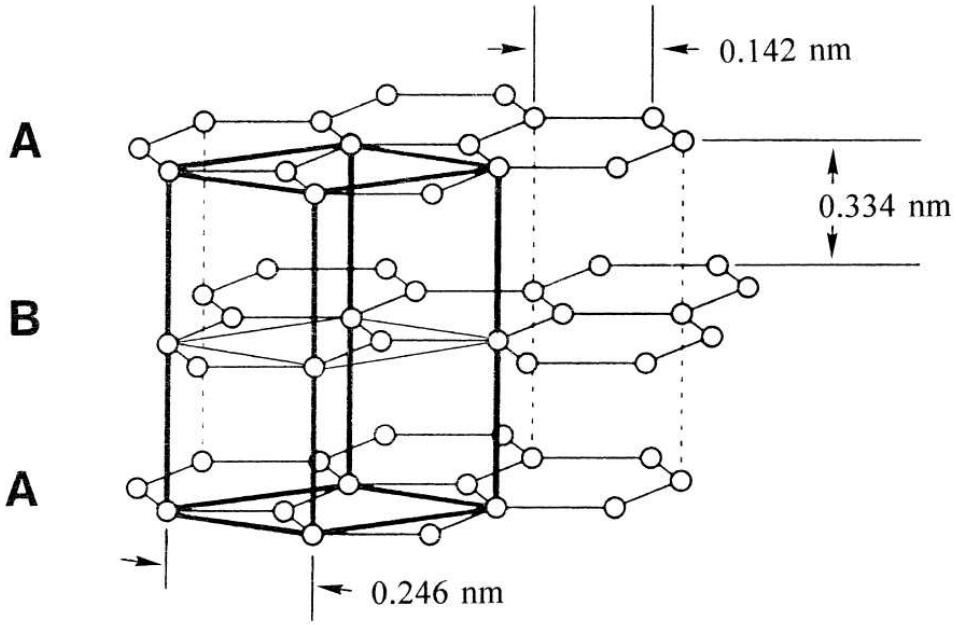

FIGURE 2 – Schéma de la structure cristallographique du graphite avec la maille conventionnelle et le modèle d'empilement «AB stacking». Les cercles symbolisent les atomes de carbone, tandis que les lignes noires représentent les liaisons. (Image de [19])

des électrons (électron libre $2p$) apportant un caractère métallique fort. Les feuillets interagissent entre eux faiblement via des interactions de Van der Waals et des interactions faibles induites par chevauchement des orbitales p_z des plans voisins [18]. Dans la configuration la plus stable, les feuillets sont empilés dans une structure A-B-A-B suivant l'axe orthogonal aux plans (voir Figure 2). Cet empilement est appelé «AB stacking» ou empilement de «Bernal». J. D. Bernal a découvert cette structure par analyse de la diffraction des rayons X obtenue sur un échantillon de graphite en 1924 [61]. La longueur de la liaison C-C dans le plan de base est d_{C-C} = 1,42 Å, et l'espacement entre plans a été mesurée à environ 3,35 Å [19, 62]. La maille cristallographique conventionnelle montrée en Figure 2 de la structure du graphite en «AB stacking» contient 4 atomes.

Le graphite est un semi-métal avec un chevauchement de bande presque nul (0.03 eV suivant les travaux de Chung [18]). Les bandes les plus proches du niveau de

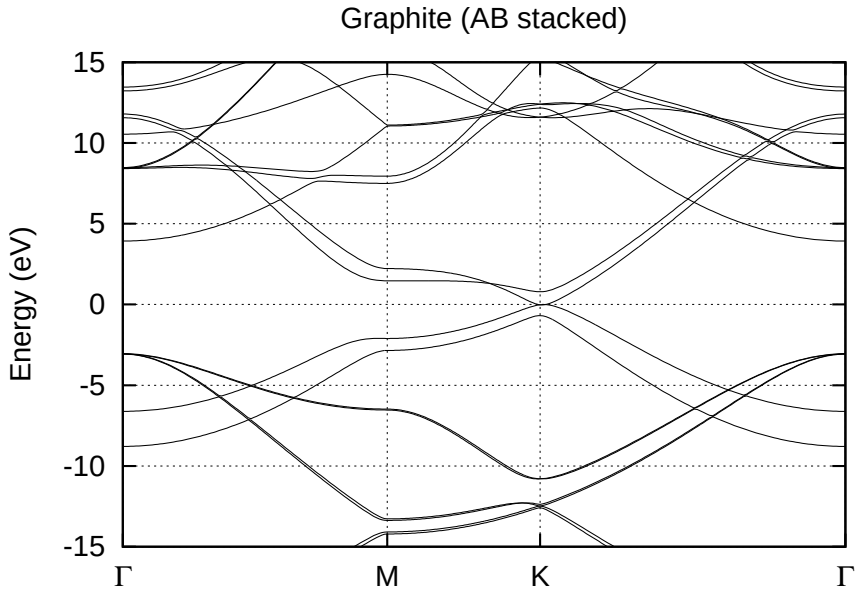

FIGURE 3 – Diagramme de bande autour du niveau de Fermi pour l'empilement AB du graphite dans l'espace réciproque le long $\Gamma - M - K - \Gamma$ utilisant LDA-DFT calculs. (Voir Figure 10 (b) pour la première zone de Brillouin dans le plan)

Fermi proviennent des π- et π^*-liaisons, alors que les liaisons σ- et σ^*- dans le plan de base sont largement séparées comme dans la structure diamant. La Figure 3 montre le diagramme de bande du graphite, calculé en utilisant le code *AIMPRO* (LDA-DFT). On vérifie ainsi le bon accord entre cette structure calculée avec les résultats publiés dans la littérature (Tight-Binding [63], LDA-DFT [29, 64]). Le continuum d'états autour du niveau de Fermi explique l'apparence noire du graphite perçue par l'œil humain.

En raison du caractère métallique du système de liaisons π, la conductivité électrique dans le plan est très bonne (pareille pour la conductivité thermique à cause d'un libre parcours moyen des phonons très grande), tandis que perpendiculairement au plan de base, les conductivités sont beaucoup plus faibles [18]. Cette remarque souligne le comportement fortement anisotrope du graphite.

L'occurrence naturelle du minéral graphite est plus grande que celle du diamant ; ainsi, le graphite est le moins cher des deux minéraux. Il est utilisé par exemple

dans la sidérurgie, comme anodes dans les batteries, comme constituants de freins ou en tant que lubrifiant. Les poudres de graphite sont utilisées comme lubrifiants secs. Les mines de crayons de papier constituent une autre application populaire du composé graphite où il est mélangé avec une argile pour donner le dépôt noir du trait de crayon. Aujourd'hui des formes synthétiques du graphite sont produites en grande quantité pour disposer d'un matériel de haute pureté, ouvrant sur d'autres utilisations par exemple dans les recteurs de fusion en tant que modérateurs de neutrons, ou dans l'industrie pétrolière.

Composés d'intercalation du graphite

La structure en feuillet du graphite offre également de grandes possibilités de combinaisons avec d'autres espèces à intercaler. En effet, des atomes, des ions ou des molécules de petite taille peuvent être insérés entre les feuillets du graphite, provoquant une augmentation de la distance inter-feuillet. L'intercalation permet de changer les propriétés électroniques, chimiques, thermiques et magnétiques du graphite [32]. L'intercalation bien connue du potassium en stade 1 (C_8K, avec des atomes K entre chaque couche de graphite) donne un supraconducteur à basse température (<1 K) [65]. L'intercalation de molécules, comme par exemple Br_2 a été étudiée [66, 67]. Tout particulièrement, les caractères donneur-accepteur des espèces intercalées et les effets induits de transferts de charge du système π attirent beaucoup d'attention.

Fullerènes

Après des décennies de recherche sur le carbone et ses structures tridimensionnelles, en 1985 la découverte de C_{60} (également connu sous le nom «Buckminsterfullerène», «Buckyball» ou «fullerènes») est observée [68, 69], suite à la vaporisation du graphite à l'aide d'un puissant laser Nd :YAG. En effet, l'analyse des petites grappes de carbone produites, par spectrométrie de masse montre alors la présence d'une espèce dominante formée exactement de 60 atomes de carbone. L'interpréta-

(a) (b)

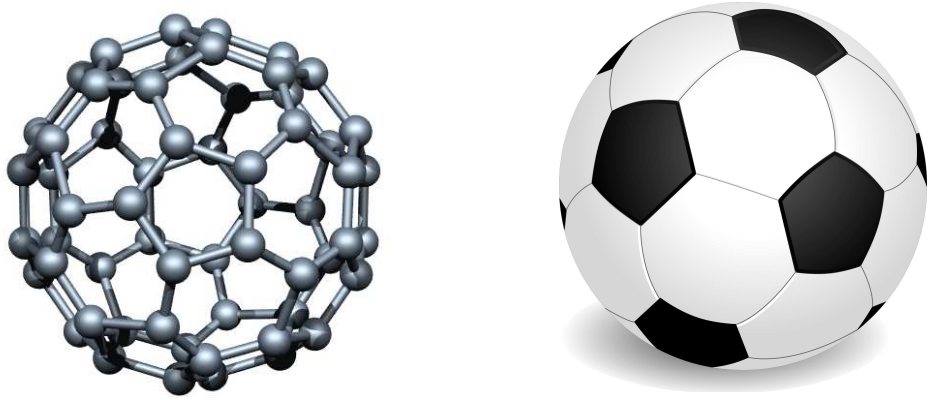

FIGURE 4 – (a) C_{60} Buckminsterfullerene et (b) un ballon de football avec la même symétrie. (Images de (a) : [70], (b) : [71])

tion de ce résultat proposait une nouvelle structure très stable et de haute symétrie, sphérique, montrée en Figure 4 (a), qui rappelle aussi la structure des anciens ballons de football en cuir (Figure 4 (b)). La structure C_{60} contient 20 hexagones et 12 pentagones d'atomes de carbone et est caractérisée par deux longueurs C-C, l'un de d_{C-C}= 1,39 Å entre deux hexagones et l'autre de d_{C-C} = 1,43 Å pour les «bords» des pentagones [69].

Dés 1985, d'autres types de fullerènes ont pu être produites (C_{20},..,C_{70}, C_{76}, C_{82},...) et avec d'autres méthodes, par exemple à l'aide d'un arc électrique pour évaporer le matériau graphite [72]. Récemment le mécanisme fondamental de croissance de ces structures a été expliqué [73]. Suite au développement de nouveaux procédés à grandes échelles, il est aujourd'hui possible de produire de grandes quantités de fullerènes. En revanche, un débouché commercial ne s'est pas clairement dégagé, même si l'utilisation des fullerènes pour des cellules solaires organiques, ou des médicaments ou encore comme agents de contraste d'imagerie IRM sont envisagés [7]. Scientifiquement la découverte des fullerènes a ouvert la voie aux concepts de nouvelles formes à base de carbone de dimensions 0, 1 et 2 et de matériaux dérivés (par exemple les nanotubes de carbone et les fullerènes de bore B_{80} [74]).

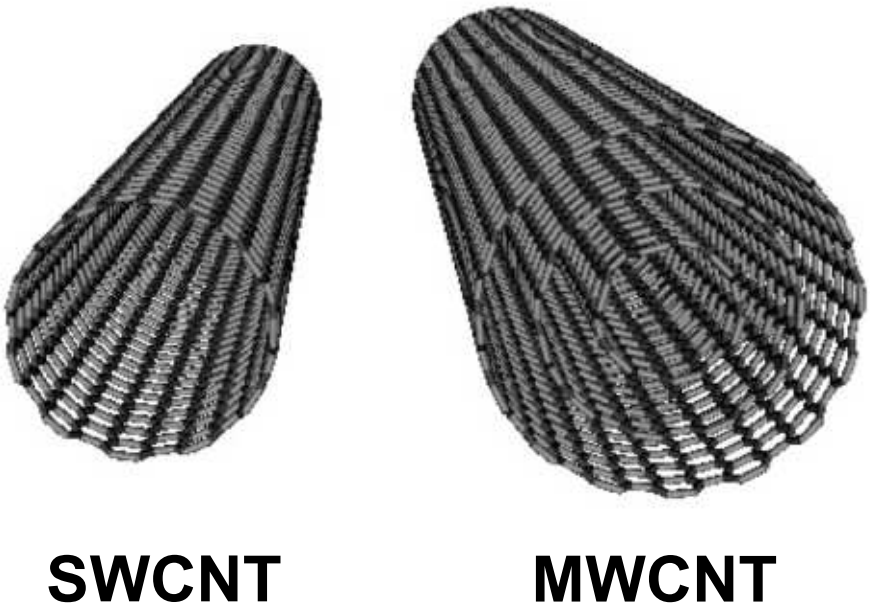

FIGURE 5 – Deux types de nanotubes de carbone, SWCNT et MWCNT. (Image de [78])

Les nanotubes de carbone

En 1991, Iijima [13] reporte l'observation de micro-tubules cylindriques de carbone, sur une base de structure graphite, aujourd'hui connu sous le nom de nanotubes de carbone (NTC). Les images en microscopie TEM d'échantillons produits par des procédés «arc-évaporation» révèlent des structures longues avec des surfaces courbes de carbone similaires à celle des fullerènes [72]. Les nanotubes de carbone sont construits sur un réseau hexagonal de carbone comme celui du graphite, mais enroulés en cylindre. Les premièrs nanotubes isolés avait été trouvés avec des parois contenant plusieurs couches de carbone, appelés nanotubes de carbone multi-parois («multi-wall carbon nanotubes» : MWCNTs). En 1993, d'autres nanotubes de carbone isolés avec une seule paroi («single-wall carbon nanotubes» : SWCNT) ont été trouvés [75]. Ces deux types de nanotubes de carbone sont présentés dans la Figure 5. Les extrémités de tous ces nanotubes (SWCNT et MWCNT) adoptent des structures de type fullerène. Le diamètre des tubes varie pour les SWCNTs d'environ 3 à 20 Å [76, 77] et pour les MWCNTs de 20 à 250 Å [77].

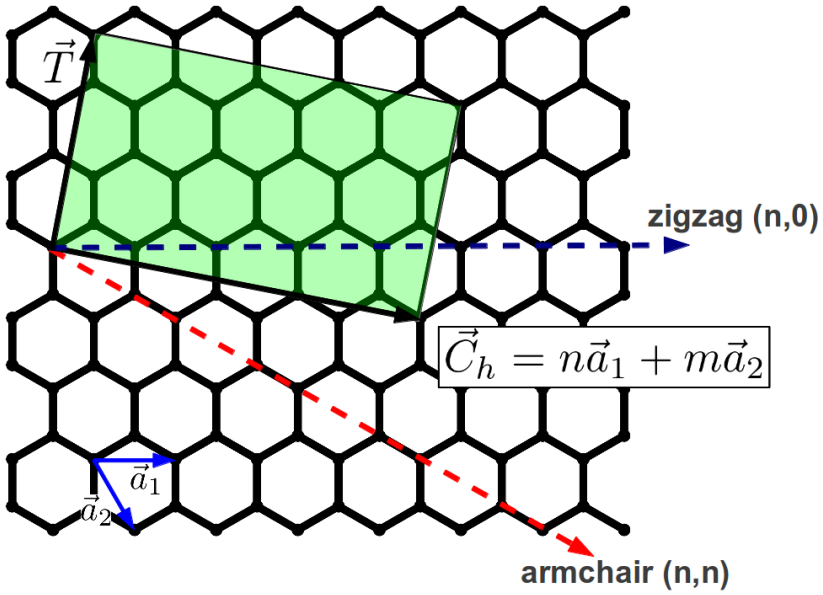

FIGURE 6 – Définition de la chiralité des nanotubes (n,m), sur la base d'une feuille de graphène enroulée sur elle-même en reliant les deux extrémités du vecteur $\vec{C}_h$. Le vecteur $\vec{T}$ est orienté le long de l'axe du tube, dont le module représente la plus petite maille répétition.

Les caractéristiques de la structure d'un NTC s'expliquent à partir du plan du feuillet de graphène [79], comme il est montré en Figure 6. Les vecteurs $\vec{a}_1$ et $\vec{a}_2$ définissent une cellule unitaire de base hexagonale du plan contenant 2 atomes (voir aussi la Figure 2). Ensuite, sur la base du vecteur $\vec{C}_h = n\vec{a}_1 + m\vec{a}_2$, obtenu comme la somme de n fois le vecteur $\vec{a}_1$ et m fois le vecteur $\vec{a}_2$, avec $n, m = 0, 1, 2, ...$, on définit l'enroulement du feuillet en connectant les deux extrémités de ce vecteur $\vec{C}_h$, formant ainsi un tube. La circonférence du tube est ainsi : $L = |\vec{C}_h| = a\sqrt{n^2 + m^2 + nm}$ et le diamètre $d = L/\pi$. Les deux paramètres (n,m) définissent exactement la symétrie du tube, et donc sa chiralité. Dans le cas de $n = m$, le vecteur $\vec{C}_h$ donne la direction armchair du plan de base ; dans ce cas, les NTC sont appelés «armchair». Pour $m = 0 \neq n$, le vecteur $\vec{C}_h$ est suivant la direction zigzag, et dans ce cas, les nanotubes sont appelés «zigzag». Le vecteur de translation, $\vec{T}$, définit la largeur d'une maille unitaire le long de l'axe du tube [79]. Ce récapitulatif théorique montre les nombreuses possibilités d'avoir un NTC et donne une explication aux difficultés de définir la chiralité d'un NTC à partir des seules images TEM.

Les NTC ont suscité beaucoup d'intérêt depuis leur découverte, en raison de leurs extraordinaires propriétés électroniques, thermiques et mécaniques. En effet, en courbant le plan de base du graphite pour obtenir un tube, la dimension du matériau décroit de 2 à 1. Les propriétés quantiques vont être différentes entre ces deux structures notamment à cause des conditions aux limites nettement différentes. Par exemple, les relations de dispersion «chiralité» spécifiques sont décrites seulement suivant l'axe NTC. Ainsi les NTC sont soit métalliques, si $n-m$ est un multiple de 3, soit semi-métalliques ou semi-conducteurs [80]. Grosso modo, un tiers des chiralités possibles donne des tubes métalliques et deux tiers des NTC semi-conducteurs ou semi-métalliques.
Egalement un rôle important joue le comportement de transport électronique des NTC. Alors que la résistance d'un matériau normal augmente avec la longueur à cause des phénomènes de diffusion, la résistance des nanotubes de carbone reste constante avec la longueur ; en effet les électrons y peuvent possèder un régime de transport balistique. Ce comportement, ouvre de grandes possibilités d'application dans des dispositifs, puisqu'ils peuvent conduire des courants importants sans perte et sans production de chaleur [79].

Du coté propriétés mécaniques, les NTC possèdent un module de Young «dans-le-plan» similaire au graphite avec une grande rigidité le long de l'axe du tube d'environ $\sim$ 1 TPa [81–85]. Les propriétés mécaniques ne montrent pas de dépendance forte à la chiralité et sont surtout une conséquence de la dimension de ce matériau, comme pour les propriétés électroniques, le long du tube. Les NTC sont élastiques perpendiculairement à l'axe du tube, et peuvent être déformés facilement. Ces comportements mécaniques des nanotubes de carbone sont très intéressantes pour l'ingénierie des matériaux composites ou hybrides. Si on y ajoute la possibilité de produire des NTC à grande échelle aujourd'hui, leur champ d'utilisation industrielle s'élargit avec de nouvelles voies [86]. Les NTC sont déjà utilisés dans la conception de structures légères en carbone (sous forme de faisceaux ou de tapis NTC), dans les piles [87], mais sont aussi des candidats dans le domaine médical en vectorisation de médicaments [88], ou aussi comme matériau de base de capteurs

de gaz [89] et surtout comme élément à fort potentiel dans le domaine des circuits électroniques [79].

De nombreuses autres formes que celles présentés ci-dessus, correspondant toujours à la simple formule C existent, comme des nano-cones de carbone, ou peuvent être imaginées et sont continuellement découvertes.

Le graphène - Propriétés fondamentales

Le matériau graphène correspond à une monocouche d'atomes de carbone sp^2, disposés dans un réseau hexagonal bi-dimensionnel correspondant à un seul feuillet isolé de la structure graphite. Principalement fondée sur une étude théorique de Mermin et Wagner [90] de 1966, il a semblé longtemps impossible d'obtenir un matériau constitué d'une seule couche d'atomes. Cette étude, fondée sur le modèle isotrope de Heisenberg prouvait «rigoureusement» l'absence de propriétés ferro- et anti-ferromagnétiques dans des systèmes à 1 ou 2 dimensions et suggérait que des cristaux purs 1D ou 2D ne pouvaient exister. Même si des résultats de 1962, bien documentés, obtenus pour des lamelles ultra-minces de graphite mentionnaient la possibilité de présence de feuilles isolées de graphène monocouches de Boehm *et al.* [91], le point de vue de Mermin et Wagner resta le seul admis pendant presque 40 ans. Rétrospectivement, on peut affirmer que pour la première fois, cette première expérience montrait un mélange de flocons de graphène constitués de simple et de multi-couches. Cependant, à cette époque les sondes d'imagerie capables d'une résolution atomique comme la microscopie TEM de haute résolution n'en étaient qu'à leurs débuts sans parler de la microscopie à effet tunnel électronique, STM, qui n'était pas encore inventée. Alors des études intensives plus approfondies n'ont pas été menées sur ce type d'échantillons laissant l'affirmation de Mermin et Wagner [90] comme un principe dans la tête des scientifiques.

Tandis que pendant une grande période, le graphite ainsi que le plan basal du graphite constituaient des objets modèles dans de nombreuses études théoriques cherchant à comprendre des propriétés électroniques fondamentales [30, 31], il a fallu

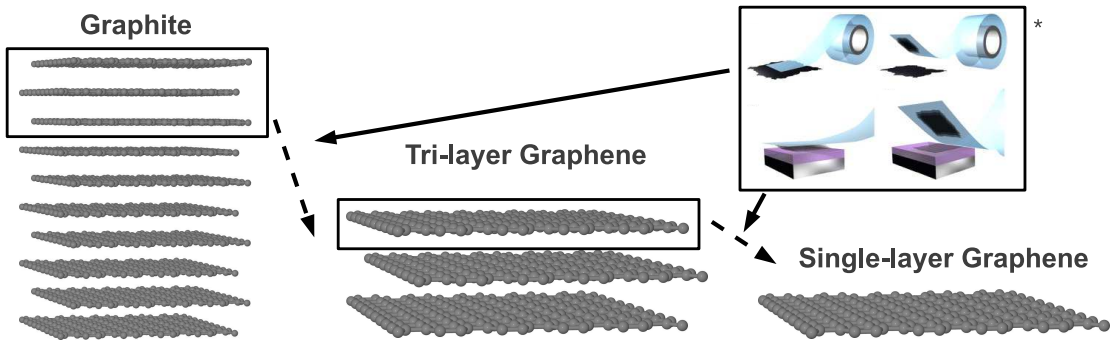

FIGURE 7 – Du graphite au graphène en utilisant la méthode de bande adhésive. (* Image adaptée de [96])

attendre 2004 et une idée très simple pour que le graphène devienne accessible [14]. Un groupe de recherche autour des deux physiciens Andre Geim et Konstantin Novoselov de l'Université de Manchester ont développé une méthode facile pour isoler des feuillets uniques de graphène à partir de blocs de graphite à l'aide de bandes adhésives. En retirant une bande adhésive collée ultérieurement sur un échantillon de graphite, une fine couche repose sur la bande. En répétant cette opération sur la bande, elle même, l'épaisseur de la fine couche se réduit d'itération en itération jusqu'à obtenir une épaisseur de quelques Å (voir Figure 7). Ces couches minces ont ensuite été analysées par microscopies électroniques, SEM et HRTEM ; des premières mesures de transport sont reportées l'année suivante [92, 93]. La discussion de savoir si cette découverte de 2004 infirme le théorème de Mermin-Wagner reste ouverte ; en effet, cette expérience d'isolement d'un feuillet ne correspond pas à une croissance libre (non supportée par un substrat) d'un cristal pur 2D, mais seulement à une forme d'exfoliation à partir d'une structure 3D préexistante comportant des feuillets empilés. De plus, un autre point intéressant dans cette discussion provient de l'observation des feuillets de graphène suspendus qui ont tendance à ne pas à adopter une forme parfaitement 2-dimensionnelle plane. Récemment des ondulations et des distorsions «hors plan» à l'échelle de l'Å ont été identifiées expérimentalement [94]. Notons aussi que des fluctuations de hauteur par rapport au plan moyen du feuillet, d'origine thermique, ont été calculées lors de simulations atomistiques de Monte-Carlo [95].

En plus des exfoliations mécanique (méthode de la bande adhésive) et chimique (procédé par étape d'intercalation à partir de solutions liquides suivie d'exfoliation pour diviser le matériau de graphite 3D [97]), la croissance contrôlée de graphène sur substrat a gagné en importance. Aujourd'hui, il est possible de faire croitre une monocouche et des multi-couches de graphène sur différents types de substrats, comme SiC [98] ou Cu [99]. Ces procédés de croissance ont été développés ces dernières années en utilisant les méthodes établies de Chemical-Vapor-Deposition, Plasma-Vapor-Deposition ou encore Molecular-Beam-Epitaxy.

Les formes dérivées du graphène appelées, oxyde de graphène (OG) et oxyde de graphène réduit (r-OG), ont été intensivement étudiées depuis de nombreuses décennies, en raison notamment de leurs préparations chimiques simples et peu chères [100]. Il a également été suggéré que le travail de Boehm en 1962 [91] avait produit la forme d'oxyde de graphène réduit plutôt que directement des flocons de pure graphène [100]. Même si les propriétés électroniques des oxydes de graphène sont moins attrayantes que celles du graphène, il existe de nombreuses possibilités d'utiliser cet OG comme brique de construction de certains composites à base de carbone [101]. Un autre domaine pourrait venir de la transformation des OG facilement dispersés et peu chers en couches de graphène, comme il vient d'être démontré récemment, avec du papier graphène conducteur et souple [102].

Le feuillet de graphène peut être considéré comme la brique structurale de base utilisable pour décrire diverses formes allotropiques de carbone vues comme l'enroulement, le pliage ou la torsion d'un feuillet en 2 dimensions dans la troisième dimension (voir aussi Figure 8). En outre, de la découpe du réseau infini hexagonal 2D on peut obtenir par exemple des nanorubans ou des boites quantiques. La plupart des formes possibles, qui ont été récemment imaginées, est résumée par Suarez-Martinez *et al.* [103] ; la Figure 9 en donne une vue d'ensemble.

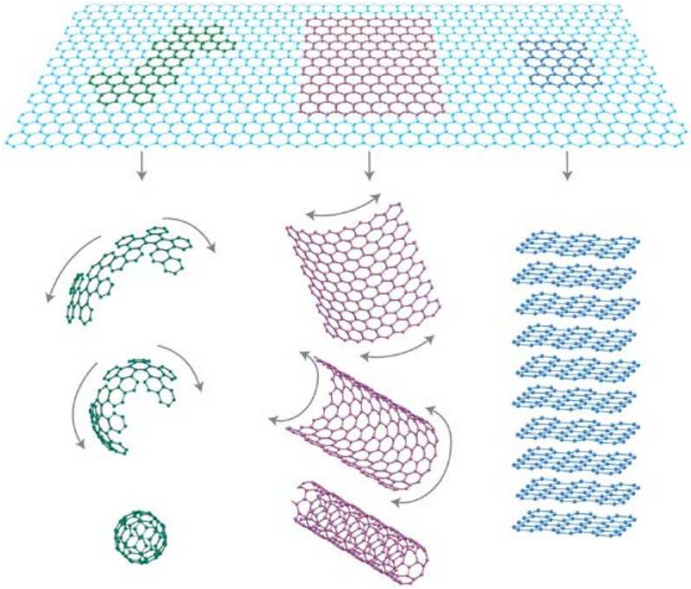

FIGURE 8 – Une feuille de graphène est l'élément de base de nombreuses formes allotropiques du carbone, telles que les fullerènes, les nanotubes de carbone et le graphite. (Image de [22])

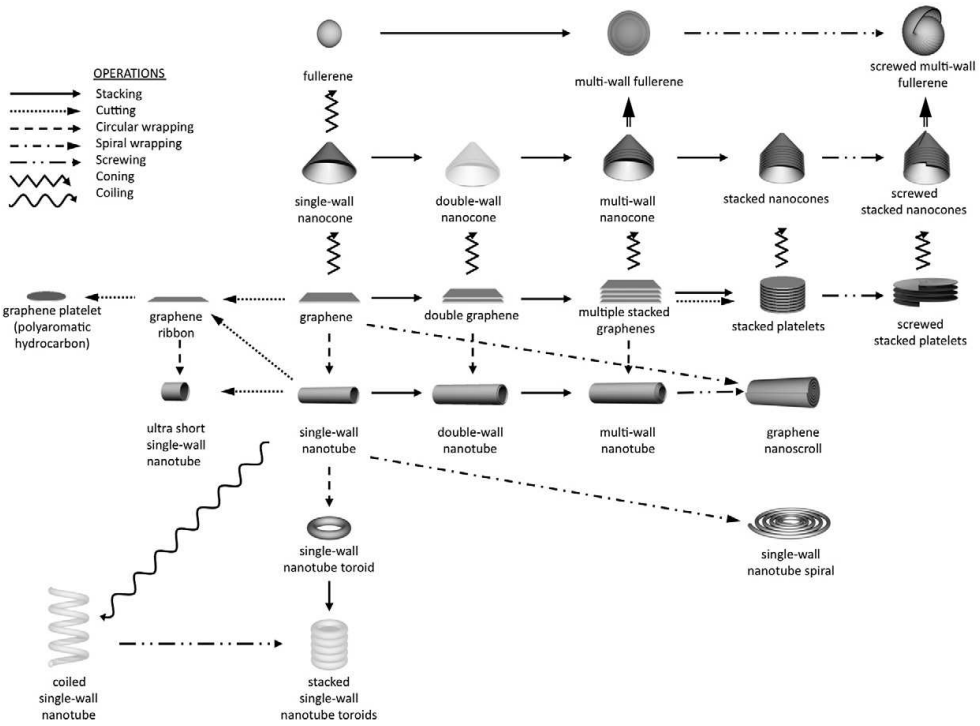

FIGURE 9 – Vue d'ensemble des différentes formes allotropiques de carbone à base de graphène, soulignant les relations topologiques entre elles. (Image de [103])

Les propriétés électroniques exceptionnelles (effet Hall quantique, transport balistique en théorie), combinés à une méthode simple de préparation (l'exfoliation mécanique) ont donné lieu à un très grand nombre de publications concernant le graphène [22]. En particulier, la haute mobilité électronique μ mesurée pour des feuillets de graphène suspendus qui atteint plus de 200.000 cm^2 V^{-1} s^{-1} [33], l'extraordinaire valeur du module d'Young «dans-le-plan» de $\approx$ 1 TPa [104, 105], la haute conductivité thermique $K \approx$ 5000 W m^{-1} K^{-1} à température ambiante [106] et une aire spécifique élevée de 2630 m^2/g [107] font du graphène un candidat prometteur pour le développement de nouveaux dispositifs électroniques [14, 108, 109], ou photoniques ou encore opto-électroniques [110]. Après un 20ème siècle dominé par une technologie fondée sur le silicium, le 21ème siècle pourrait bien être celui d'une technologie de type nanotechnologie fondée sur des structures de graphène et structures dérivées du carbone.

Les propriétés structurales du graphène

La structure du feuillet de graphène est celle du plan de base décrite ci-dessus pour le graphite. Les atomes de carbone sont disposés en un réseau hexagonal bi-dimensionnel, avec trois voisins proches par atome de carbone. La longueur de la liaison C-C est similaire à celle obtenue dans le graphite d_{C-C} = 1,42 Å. La maille unitaire hexagonale ne contient que 2 atomes, avec un paramètre de maille de a = 2,4612 Å (voir Figure 10 (a)). La structure graphène est obtenue en superposant deux réseaux hexagonaux décalés **A** et **B**, dont un atome de chacun est représenté dans la maille primitive. L'espace réciproque des vecteurs k est bi-dimensionnel avec également une structure hexagonale tournée de 30 degrés (voir Figure 10 (b)). Les atomes forment un système de hybridisation de type sp^2. Dans le plan, les atomes de carbone forment de fortes liaisons σ. Les orbitales p_z sont orientées hors du plan et constituent la base de description du nuage électronique π.

L'empilement «AB stacked» de deux feuillets est constitué de deux couches décalées de $\vec{s}$, avec $\vec{s} = \frac{1}{3}(\vec{a}_1 + \vec{a}_2)$. La distance inter-couche est similaire à celle mesurée dans le graphite à 3,35 Å. Ces couches ne sont donc que faiblement liées [111], ce

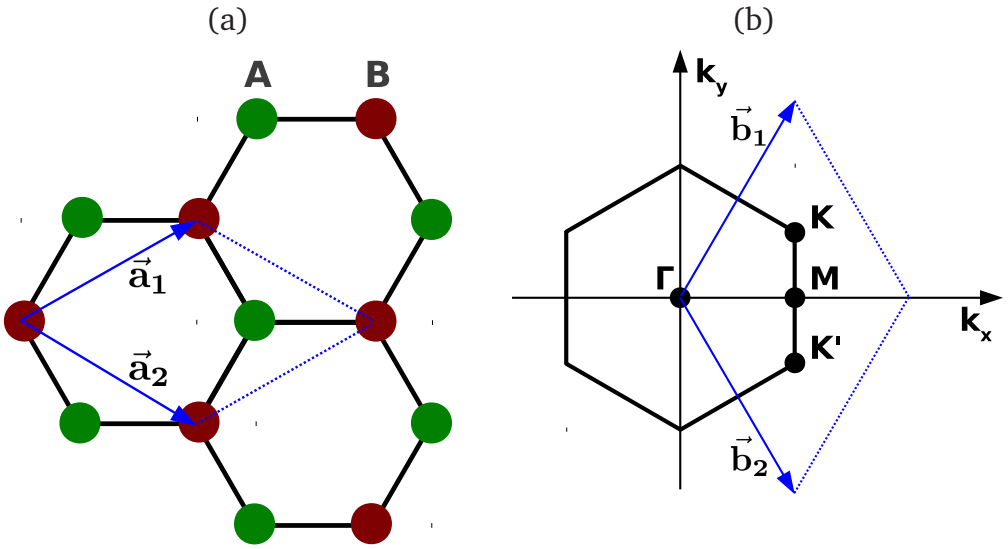

FIGURE 10 – (a) Réseau en nid d'abeille du feuillet de graphène avec les vecteurs de base $\vec{a}_1$ et $\vec{a}_2$ (tous deux = 2,4612 Å). La maille primitive élémentaire est représentée en bleu, et les sous-réseaux de graphène en rouge et vert. (b) L'espace réciproque bi-dimensionnel des vecteurs k soulignant les points importants pour la structure du graphène : Γ, M et K. La première zone de Brillouin est colorée en noir, avec les vecteurs $\vec{b}_1$ et $\vec{b}_2$ de la maille réciproque en bleu.

qui nous imposera d'être prudent lors du choix de la grille du pseudo-potentiel et des points k pour nos calculs LDA-DFT. Ce comportement est en effet mal décrit en général par des calculs LDA-DFT. Pour tester cela, nous avons testé et comparé une structure bi-couche de graphène à la structure du graphite, en utilisant le pseudo-potentiel $pdddp$ (38 fonctions de base) pour le carbone et une fine grille de points k. La comparaison des courbes donnant la variation d'énergie totale par atome en fonction de la distance inter-feuillets pour les deux structures, «AB stacked» bi-couche du graphène et du graphite, montre dans les deux cas une distance inter-couches de 3,33 Å, voir Figure 11. Ce résultat est en bon accord avec la valeur expérimentale de 3,35 Å, et nous considérons que la distance inter-couche est suffisamment bien décrite par ce pseudo-potentiel avec l'approche LDA-DFT. Nous notons en passant que pour la bi-couche de graphène, les couches sont moins fortement liées (moins énergétiquement stable) que dans le cas du graphite, et que la courbure de la courbe autour du minimum est plus faible.

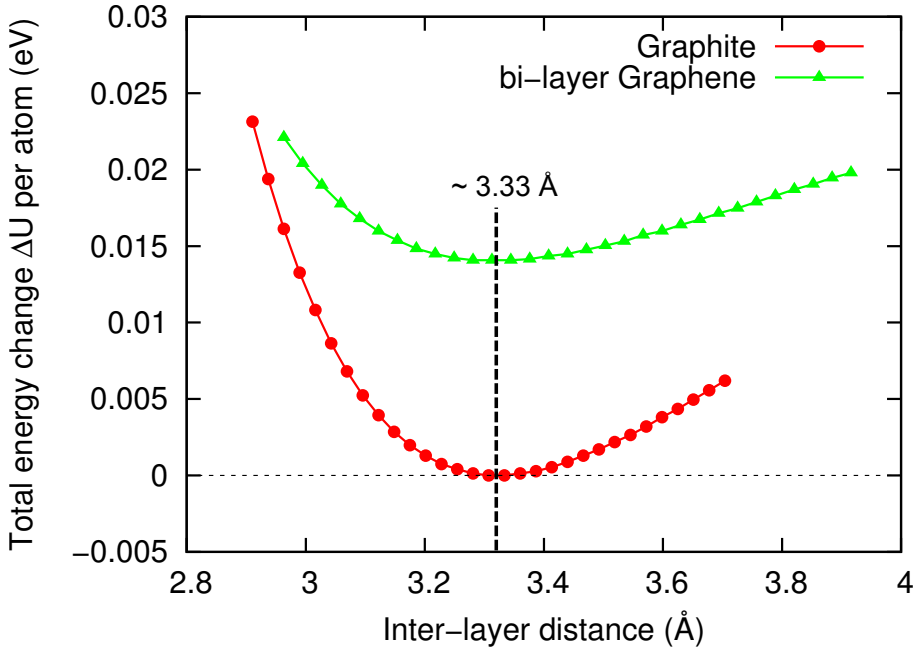

FIGURE 11 – Évolution de l'énergie totale par atome de carbone en fonction de différentes distances inter-couches, calculées avec l'approche LDA pour le graphène et le graphite dans le cas d'empilements «AB stacked» pour les deux structures, graphène bi-couche et graphite. Le pseudo-potentiel (HGH) combine avec un ensemble de functions de base $pdddp$, une grille de $20 \times 20 \times 8$ points k de graphite (ou une grille de $20 \times 20 \times 1$ points k pour la bi-couche de graphène), et une cellule unitaire hexagonale comprenant 4 atomes de carbone, ont été utilisés. Dans le cas de la bi-couche de graphène, la distance à la structure suivante est plus de 12 Å pour éviter des interactions graphène-graphène supplémentaires.

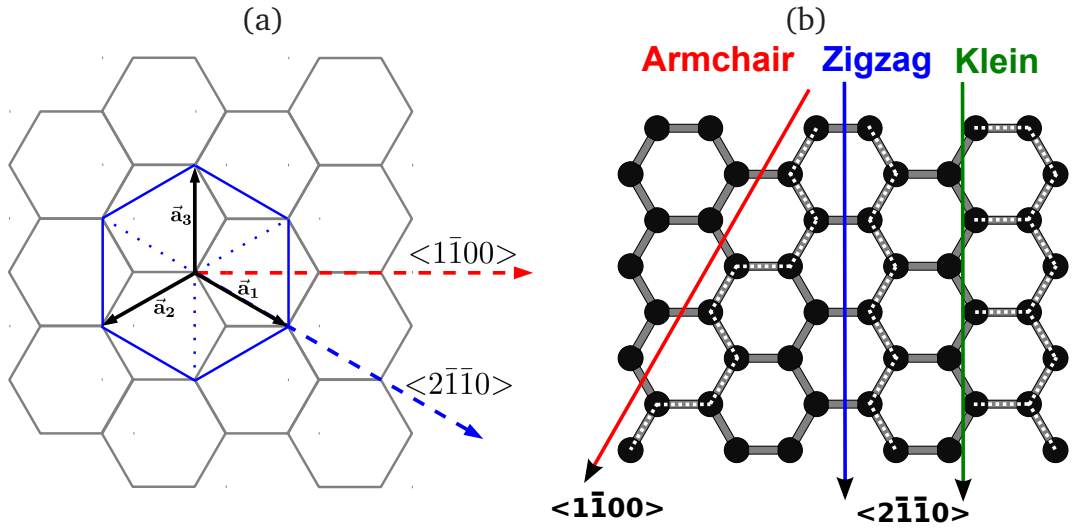

FIGURE 12 – (a) Definition des deux directions pricipales dans le plan de graphène. (b) Trois axes possibles de coupe d'un feuillet de graphène (ou de dézippage d'un nanotube de carbone vers un nano-ruban de graphène) pour créer des bords purs en «Armchair» (rouge), «Zigzag» (bleu) ou «Klein» (vert). Les configurations de bords obtenues sont marquées par des lignes pointillées blanches à la droite de chaque axe de coupe.

Les bords de feuillet du graphène

Le feuillet de la structure graphène peut présenter trois types de bords, appelés «armchair» (fauteuil), «zigzag» et «Klein» [112–115]. Ces trois types de bords peuvent être obtenus en coupant un feuillet de graphène suivant deux familles principales de directions, le $<1\bar{1}00>$ et le $<2\bar{1}\bar{1}0>$, comme schématisé dans la Figure 12, dans une vue du dessus. Ce découpage donne toujours deux bords, sur chacune des deux parties du feuillet, exactement similaires.

Au cours de la dernière décennie, les bords des feuillets dans les structures de graphite et de graphène ont été étudiés intensément à l'aide des techniques STM et TEM (corrigée des aberrations) [114–120]. Soit des trous dans un feuillet de graphène soit des bords extérieurs d'un feuillet de graphène ont été sondés à l'aide de ces techniques de microscopie modernes. Les configurations les plus courantes dans des conditions d'ultra-vide correspondent aux bords en armchair et zigzag. Les

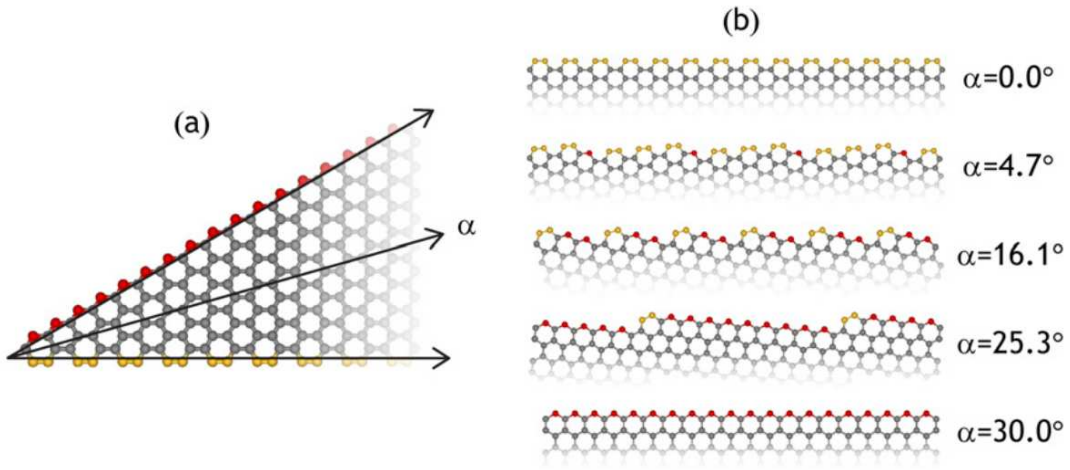

FIGURE 13 – Bords chiraux de la structure armchair (jaune) et zigzag (rouge). (a) Définition de l'angle α donnant l'orientation dans le plan du feuillet de graphène. (b) Différents bords de graphène chiraux sans reconstruction, avec des sections armchair et en zigzag soulignées respectivement en jaune et rouge pour guider l'œil. (Images de [49])

nombreuses études théoriques des propriétés de bord d'un feuillet se sont principalement concentrées sur des bords atomiquement parfaits [48, 49, 113, 121–123]. La question de savoir si d'autres configurations de bords pouvaient exister, par exemple des bords reconstruits, a cependant été posée. Des calculs récents ont prédit des configurations stables reconstruites [48, 124]. En revisitant des études de microscopie TEM, certains types de bords reconstruits sont proposés, en particulier des bords de type zigzag reconstruits en (5-7), ont été confirmés [125].

A partir de compositions de parties en armchair et en zigzag, le long d'un bord de feuillet droit, divers bords chiraux deviennent alors possibles. Une façon de les décrire est obtenue par Branicio *et al.* [49] en utilisant l'angle d'orientation α, illustré en Figure 13. Des premiers articles de revue concernant les structures de bords de graphène sans terminaison et non fonctionnalisés ont été récemment publiés [126, 127], donnant au lecteur un premier aperçu de certaines parties de la chimie et de la physique des bords de feuillets de graphène (principalement) non reconstruits et seulement simple hydrogénés.

Propriétés électroniques du graphène

Les liaisons σ sont très fortes dans le plan du feuillet, les orbitales π sont à moitié remplies, conduisant à un comportement semi-métallique (ou «semi-conducteur avec une bande interdite de zero») du graphène. La structure de bande du graphène avait déjà été étudiée en 1947 par Wallace [30], qui reportait pour la première fois une inhabituelle relation de dispersion linéaire près du point K (Figure 14 (a)), avec des électrons dits de Dirac. Une intersection linéaire des bandes de conduction et de valence est trouvée pour les faibles énergies autour du point K, créant ce qu'on appelle un cône de Dirac (voir la Figure 14 (b)). Le niveau de Fermi (qui définit le potentiel chimique) se trouve directement au point de Dirac, point de croisement des deux bandes, indiquant le centre du cône de Dirac. Cette exceptionnelle relation linéaire de dispersion permet de décrire les excitations de basse énergie des fermions sans masse de Dirac, par une approche d'électrodynamique quantique. Dans le graphène, ces fermions sans masse de Dirac se déplacent 300 fois moins vite que la lumière dans le vide, c'est à dire avec une vitesse de Fermi $v_F \approx 10^6$ m/s [128]. La description de ces fermions de Dirac fait apparaître un autre aspect intéressant, appelé paradoxe de Klein [36], qui décrit des probabilités égales à 1 de traverser (sans perte) de petites régions interdites dans une description classique. Cela se traduit dans le cas du graphène par le fait que les électrons sont capables de se propager sur de grandes zones (de l'ordre du μm) sans subir de diffusion [14], même en présence de potentiels électrostatiques générés par exemple par des défauts. Ceci conduit vers un comportement de transport balistique (avec une mobilité des électrons μ infinite) ; μ mesurée pour le graphène supérieure à 200.000 $cm^2\ V^{-1}\ s^{-1}$ [33].

En pratique, le désordre ne peut être évité dans des systèmes réels ; les défauts, impuretés, atomes de surface, molécules adsorbées à la surface ou déformations de la structure (par exemple des ondulations dans le graphène) ne peuvent pas être totalement absents [23, 94]. Devant ce constat, le transport du graphène est très prometteur pour l'intégration des couches de graphène dans des dispositifs pour réaliser des jonctions p-n, de haute efficacité et rapides.

(a)

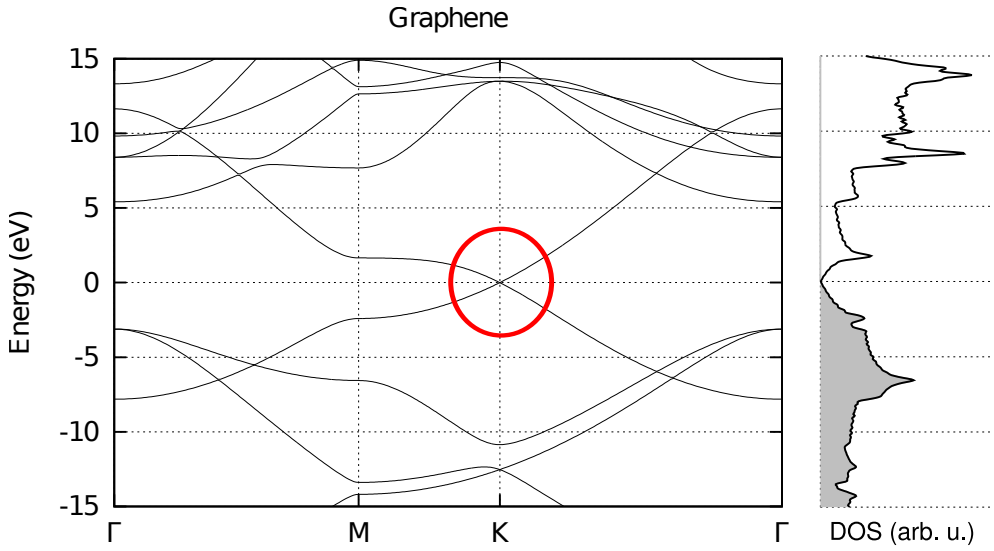

(b)

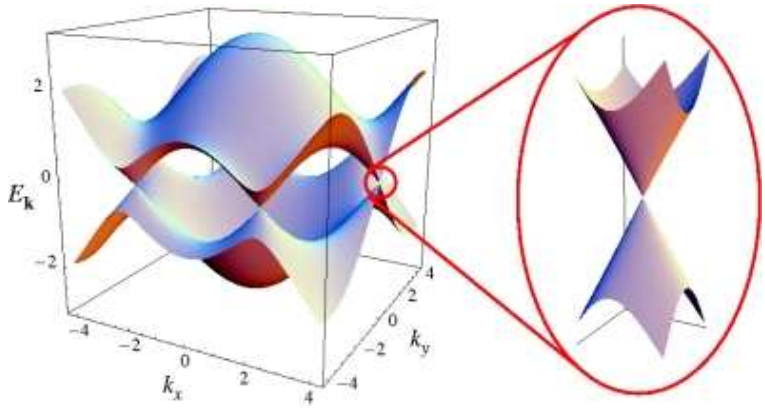

FIGURE 14 – (a) Diagramme de bandes le long de graphène $\Gamma - M - K - \Gamma$, avec, en rouge, la zone d'intersection des comportements linéaires, au niveau de Fermi. A droite le densité d'états du graphène. (b) Dispersion d'électrons du graphène caractérisée par l'intersection des bandes linéaires en K et K'. A droite, un zoom aux points K montrant un cône de Dirac. (Image (b) de [23])

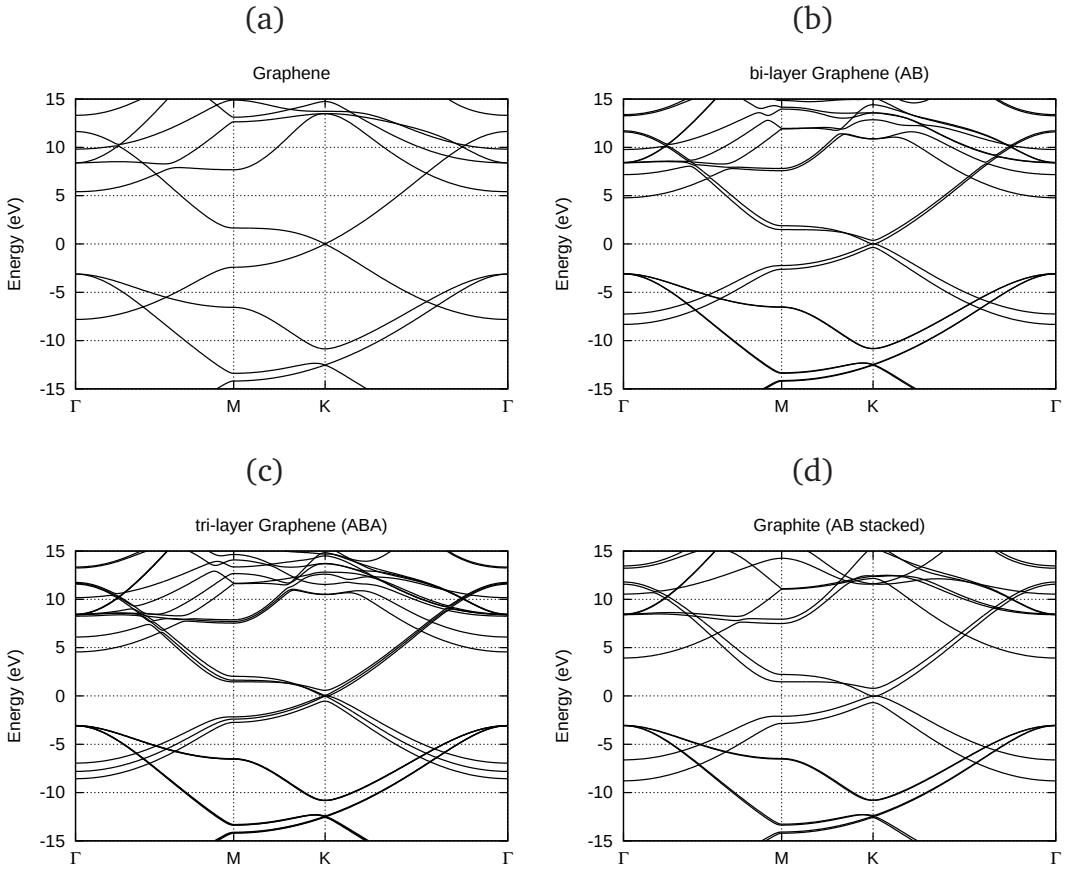

FIGURE 15 – Structure de bande (a) du feuillet isolé de graphène, (b) d'un empilement bi-couche de graphène, (c) tri-couche de graphène et (d) du matériau graphite.

L'empilement de quelques feuillets est le plus stable dans la configuration «AB-stacking», dont j'ai calculé les diagrammes de bande pour les systèmes bi-couche, tri-couche et infini, et pour le graphite. Le passage d'un seul feuillet de graphène au graphite est illustré par la Figure 15. Mes calculs sont en très bon accord avec les résultats dans la littérature de Klintenberg *et al.* [29] obtenus avec les mêmes approches DFT-LDA. Le comportement exceptionnel linéaire des bandes au point d'intersection observé au point K pour le feuillet isolé est perdu dès l'empilement de deux feuillets comme le montre son diagramme de bande où des courbures sont calculées Figure 15 (b), autour du point K. Dans le système à deux feuillets, le nombre de bandes est doublé par la contribution de quatre types d'électrons aux

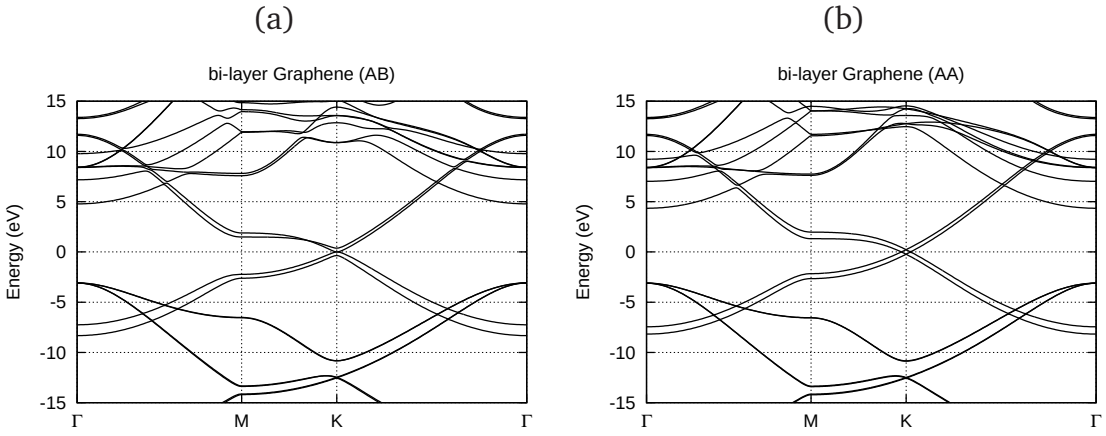

FIGURE 16 – Structures de bandes pour la bi-couche de graphène avec (a) «AB stacking» et (b) «AA stacking».

états différents p_z. En raison des interactions inter-feuillets, des éclatements des niveaux d'énergie de ces bandes apparaissent laissant seulement deux bandes près du niveau de Fermi à $E_F = 0$ eV. Le même effet est observé pour le graphène en tri-couche, où trois bandes de valence et trois de conduction sont présentes. La structure de bande d'un empilement trois feuillets peut être décrite comme une superposition des structures de bande d'une mono-couche de graphène et d'une bi-couche (voir Figure 15 (c)). En dépit de la mise en évidence d'un croisement linéaire de deux bandes, en réalité, les états excités occupés préférentiellement donnent des bandes d'énergie inférieures légèrement incurvées. La structure de bande typique du graphite ne produit pas d'intersection de bandes linéaires mais seulement une bande supplémentaire dégénérée (split), résultant de la configuration «AB stacked» combinée aux conditions aux limites périodiques dans les 3 dimensions.

En plus de l'empilement «AB stacking» discuté jusque là, la Figure 16 (b) montre le diagramme de bande calculé pour un «AA stacking» des bi-couches de graphène (avec une distance inter-couche de $\approx$ 3,59 Å dans mes calculs LDA-DFT). Nous pouvons noter que cette configuration avec les deux couches exactement l'une au-dessus de l'autre (changement de $\vec{s} = 0$ entre la couche supérieure et inférieure), est moins stable ($\sim$ +5 meV/atome, LDA-DFT) en raison de fortes répulsions entre les deux systèmes π [129]. On observe, ici aussi, une division des bandes autour

du point K, avec un caractère linéaire pour toutes les bandes. En effet, cette structure de bande pour cet empilement résulte de la superposition de deux diagrammes de bande d'un feuillet de graphène, faiblement décalés. Ce phénomène intéressant de découplage de la relation de dispersion électronique obtenu pour cet empilement bi-couche de graphène, doit être observé aussi pour l'empilement d'un feuillet de graphène sur une surface d'un échantillon de graphite ou d'autres systèmes de multi-couche graphène [130]. Ce phénomène doit être également rencontré quand l'empilement se fait avec une rotation à différents angles entre les deux feuillets, de manière énergétiquement favorable par rapport à l'empilement «AA stacked» [129, 131, 132].

Les propriétés mécaniques du graphène

La liaison C-C est l'une des plus fortes de la nature, donnant l'un des plus fort module de Young de $\approx$ 1 TPa (dans le plan) [27, 104, 133, 134] pour une seule couche de graphène. Ne considérant que de petites déformations (<5 % en tension ou en compression) de manière isotrope dans le plan, un seul module de Young peut être considéré [133, 135–137], et donc une seule valeur est indiquée. La contrainte de fracture dans le plan est mesurée à environ $\sim$ 130 GPa [12]. Le coefficient de Poisson dans le plan a été calculé à $\nu_{12} \approx$ 0,2 [27, 136]. Ces caractéristiques font du graphène un additif mécanique prometteur pour des nanocomposites à base de polymère [138] ou d'autres structures composites [11]. D'autres propriétés de composite telles que la stabilité, les propriétés de dilatation ou le comportement barrière aux gaz peuvent également être contrôlées en insérant des feuillets de graphène dans les structures de composites [12].

Les propriétés mécaniques des matériaux (dans le régime élastique) peuvent être estimées en général à l'aide des mesures du module de Young E, du coefficient de Poisson ν et du module de cisaillement G. Le module de Young donne des informations importantes lors de l'utilisation de nanomatériaux dans des composites. Dans cette thèse, j'ai mené une étude approfondie au chapitre 6 sur l'évolution du module de Young de feuillets de graphène, de nanofeuillets de formes dérivées du

graphène, ainsi que de nanotubes de carbone et de nanorubans de graphène.

Nanofeuillets	$E(c)$ (TPa)	c (e^-/a_0^3)	t (Å)	N_Q (%)	$E_{Exp.}$ (TPa)
MC-Graphène	1,059	0,00240	3,31	99,64	
BC-Graphène	1,059	0,00247	3,32	99,81	
TC-Graphène	1,058	0,00237	3,32	99,88	∼1,05 [104, 134]
4C-Graphène	1,055	0,00226	3,32	99,91	
Graphite (solide)	1,055	-	3,32	100,0	-
MC-BN	0,898	0,00268	3,19	99,60	
BC-BN	0,891	0,00288	3,19	99,78	0,6-1,5 [139]
TC-BN	0,886	0,00277	3,19	99,86	
h-BN (solide)	0,880	-	3,19	100,0	-
MC-WS_2	0,251	0,00290	6,14	99,89	-
WS_2 (solide)	0,242	-	6,17	100,0	-
MC-MoS_2	0,222	0,00293	6,12	99,85	0,2-0,4 [140, 141]
MoS_2 (solide)	0,219	-	6,14	100,0	-
MC-$MoSe_2$	0,188	0,00335	6,35	99,87	-
$MoSe_2$ (solide)	0,188	-	6,36	100,0	-
MC-$MoTe_2$	0,132	0,00329	6,87	99,87	-
$MoTe_2$ (solide)	0,132	-	6,91	100,0	-

Tableau 2 – Module de Young E dans le plan calculé pour différents nanofeuillets et leurs matériaux parents couches [27]. t indique l'épaisseur d'une seul couche d'une dalle d'un volume équivalent à celui défini par la coupure de la densité d'électrons c. $N_Q = Q(c)/Q_{total}$ donne le rapport d'électrons inclus par rapport au nombre total d'électrons dans la supercell. $E_{Exp.}$ donne des valeurs de E mesuré pour des nano-couches. (unités atomiques : e^- : électrons, a_0 : rayon de Bohr, MC : mono-couche, BC : bi-couche, TC : tri-couche, 4C : quatre couches)

Dans ce mémoire, un problème, non résolu à ce jour, a été identifié dans ce contexte : à savoir comment définir exactement un volume intrinsèque d'un nanoobjet, notamment pour pouvoir estimer le module de Young et les valeurs de E qui sont directement liés à ce volume. Le manque d'une définition commune et utilisable sur tout système explique une dispersion dans la littérature des valeurs annoncées. Avec l'établissement d'un nouveau concept du volume fondée sur la densité moyenne d'électrons pour le nanoobjet considéré, pour la première fois, une démarche transférable et fondamentale est proposée. Ainsi, cette approche permet une réelle comparaison entre systèmes, via leurs propriétés mécaniques, telles que le module de Young ; elle permet en outre d'accéder à des valeurs, par exemple le coefficient de Poisson perpendiculaire au plan d'un système 2D (applicable au graphène), ou au comportement mécanique de systèmes chargés. Enfin, cette nouvelle approche a été appliquée plus largement à une gamme de polymères dont on a calculé le module de Young, montrant l'efficacité de ce nouveau concept. Un vue d'ensemble des résultats pour les nanofeuillets est montre dans le Tableau 2.

Les propriétés mécaniques du graphène et autres structures dérivées, tels que les nanotubes de carbone et différents nanofeuillets ont été étudiés dans cette thèse avec cette nouvelle approche. Le chapitre 6 donne l'ensemble des résultats obtenus dans ce contexte et qui sont résumés en conclusion.

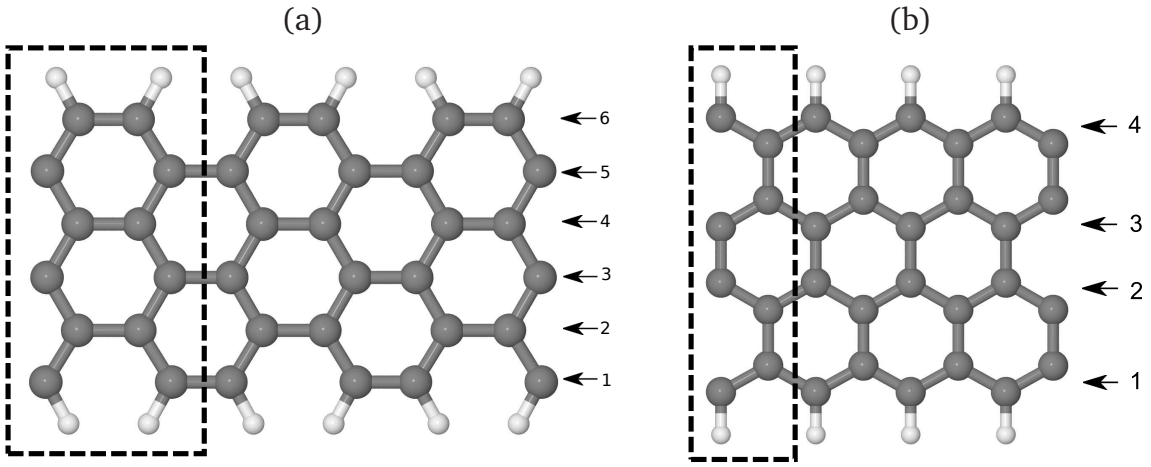

FIGURE 17 – (a) Un nanoruban de graphène armchair hydrogéné en bord, H-terminé, de largeur 6, (b) un nanoruban de graphène zigzag H-terminé de largeur 4. Pour les deux cas, la cellule de répétition la plus petite possible dans l'axe du ruban est représentée par des lignes en pointillés. La définition de la largeur des rubans armchair ou zigzag est indiquée par des chiffres introduits par Cervantes-Sodi *et al.* [143]. Les atomes de carbone sont présentés en gris et d'hydrogène en blanc.

3 Nanorubans de graphène

En pratique le feuillet de graphène n'est pas un plan infini, mais est limité par des bords. En coupant une feuille de graphène à deux reprises suivant la même direction, on obtient des structures appelées nanorubans de graphène (graphene nanoribbon : GNR). Par exemple, si on considère les bords armchair et zigzag, deux types de rubans rectilignes peuvent être construits, appelés respectivement, nanorubans de graphène armchair (armchair graphene nanoribbon : AGNR) et nanorubans de graphène zigzag (zigzag graphene nanoribbon : ZGNR), illustrés en Figure 17. Évidemment des mélanges des deux types de bord sont possibles, conduisant à ce qu'on appelle des nanorubans de graphène chiral. Si la feuille de graphène est coupée deux fois en parallèle le long d'une direction définie avec un angle d'orientation α, des bords chiraux sont obtenus. Dans le cas de nanorubans de graphène chiral, les mailles cristallographiques de répétition sont complexes et contiennent un grand nombre d'atomes et sont donc l'objet de relativement peu d'études théoriques [123], bien que ces bords soient observés expérimentalement [142].

Les nanorubans de graphène possèdent des propriétés différentes de celles du matériau infini. En particulier, ils sont caractérisés par un zone interdite de bande finie en fonction de la largeur du ruban et de l'orientation [37, 38, 113]. Ceci peut s'expliquer par l'effet physique de confinement quantique produit par largeur étroite du ruban et par les conditions de périodicité uniquement valables dans la direction le long du ruban [144]. Le comportement chimique de ce type de systèmes a été prédit sur la base de la théorie sextet de Clar [145, 146].

Dans la littérature, une approche théorique simple et courante est de terminer les feuillets de graphène ou GNRs en créant des liaisons C-H, bords de graphène H-terminés [113, 121] (voir aussi la Figure 17 et le chapitre 4 de cette thèse). Cela évite d'avoir des liaisons pendantes en bord de feuillet. Cependant, vu sous un angle plus réaliste en chimie, ces bords sont aussi un moyen facilement accessible pour fonctionnaliser chimiquement les rubans de graphène et donc modifier leurs propriétés. Les nanostructures finies de graphène à une dimension (1D) nanorubans ou zéro-dimensionnel (0D) de flocons de graphène, possèdent des propriétés de bord intéressantes, comme en témoignent les nombreuses études récentes dans la littérature sur ce sujet [105, 121, 122, 147]. Le comportement physique et chimique des bords 1D se superpose pour l'essentiel à celui du graphène à deux dimensions. Les travaux réalisés dans cette thèse sont donc consacrés à une étude minutieuse des bords de graphène pour nous permettre de définir et de concevoir des propriétés de nanorubans de graphène [105]. De manière analogue aux ondulations présentes dans les feuillets de graphène, les nanorubans de graphène 1D offrent la potentialité d'avoir d'autres modes de déformations tels que des torsions, des ondulations de bords, des pliages ou flambages qui sont examinés en détail dans le chapitre 5 de cette thèse.

Production des nanorubans de graphène

Les nanorubans de graphène peuvent être produits à partir du «dézippage» de nanotubes de carbone [39, 148–152], de procédés de lithographie [40, 153], ou de gravure [154] et de méthodes chimiques contrôlées dans une approche «bottom-

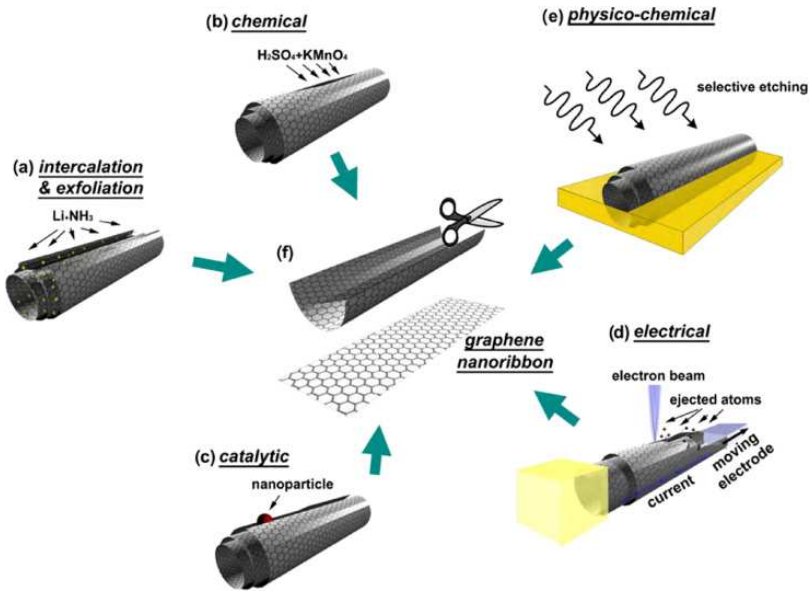

FIGURE 18 – Vue d'ensemble des différentes méthodes pour «dézipper» les NTC : (a) l'intercalation-exfoliation par voie chimique de MWCNTs, associant des traitements à l'ammoniaque, NH_3 liquide et Li, et exfoliation ultérieure à l'aide de HCl et de traitements thermiques, (b) des réactions acides oxydantes attaquant les liaisons carbone-carbone (par exemple, en utilisant H_2SO_4 et $KMnO_4$ comme agents oxydants), (c) des approches catalytiques, où des nanoparticules métalliques «coupent» le nanotube longitudinalement comme une paire de ciseaux, (d) électriquement par le passage d'un courant électrique à travers un nanotube et (e) la méthode physico-chimique en intégrant les tubes dans une matrice polymère suivi d'un traitement par plasma Ar. Les structures résultantes sont des GNRs ou des feuillets de graphène (f). (Image de [155, 156])

up» [41]. «Dézipper» des NTC est notamment devenu un sujet brûlant, depuis que le contrôle de la production et la manipulation des NTC sont maîtrisés, après d'intenses recherches depuis deux décennies. De nombreuses méthodes pour dézipper les NTC ont été appliquées avec succès, offrant différentes possibilités lors du traitement des nanorubans. Les techniques utilisées couvrent un large spectre de procédés allant de méthodes chimiques et catalytiques à des procédés utilisant un faisceau d'électrons en guise de «ciseaux» pour «dézipper» les nanotubes de carbone (voir Figure 18) [155].

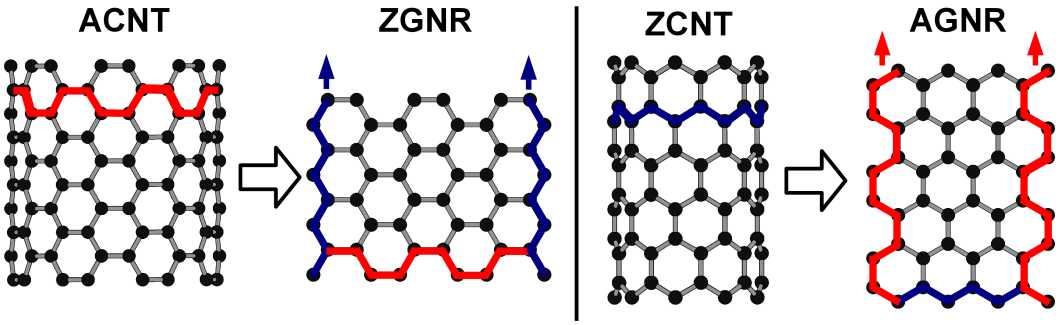

FIGURE 19 – NTC armchair (ACNTs) et NTC zigzag (ZCNTs) avec leurs transformations en nanorubans de graphène (GNRs) après dézippage le long de l'axe du tube : ACNT $\rightarrow$ ZGNR and ZCNT $\rightarrow$ AGNR.

Dézipper de nanotubes de carbone (ou seulement le tube extérieur d'un système multiparoi) donne des rubans des largeurs compris dans la gamme de 10 à 40 nm [39, 150, 152]. Dans cette gamme de taille, les effets de confinement quantique 1D latéraux sont faibles et aucune ouverture importante de bande interdite n'est attendue. En outre, le contrôle des bords n'est pour l'instant pas précis dans ces expériences de dézippage des NTC et différents types de bords peuvent être trouvés. Il est donc avantageux de tenter des croissances «bottom-up», dans des conditions contrôlées par un procédé utilisant des molécules organiques qui s'auto-assembleraient [41, 42]. Sur des surfaces Cu(111) et Au(111), la croissance d'un nanoruban de graphène armchair avec une largeur atomique de 7 précisément contrôlée a été démontrée. Les bords des rubans ainsi que la terminaison hydrogénée sont contrôlées avec précision et une bande interdite de $\sim$ 2,3 eV a été mesurée sur Au(111) [42].

Notons que la définition de la chiralité pour des nanorubans de graphène (graphene nanoribbon : GNR) peut prêter à confusion par rapport à celle adoptée pour les NTC, car ici la définition se fonde sur les bords parallèles à l'axe du ruban. Ainsi deux définitions basées sur des orientations orthogonales les unes aux autres sont utilisées dans la description des deux types de systèmes. Ainsi un NTC zigzag dézippé donne un GNR armchair et un NTC armchair un GNR zigzag (voir aussi la Figure 19).

Ces nouveaux nanorubans de graphène 1D, dans le meilleur des cas de nanostructures finement définies à l'échelle atomique, offrent un grand potentiel pour la nanoélectronique [157], l'optoélectronique [147, 158, 159] et les (nano-) composites [160]. Les nanorubans de graphène moins finement définis sur leurs bords, par exemple avec des bords chiraux, peuvent être suffisants dans un premier temps pour construire de nouveaux transistors rapides, pas chers et efficaces comme il a été montré par les simulations préliminaires de Yoon et Guo [161].

4 Matériaux parents à une seule couche

De nombreux matériaux stratifiés existent avec seulement des interactions faibles entre feuillets, par exemple des couches de graphite, de h-BN ou MoS2, des oxydes, des halogénures, des argiles et des composés du ciment [162–165]. Les solutions chimiques d'exfoliation adoptées pour le graphite pour produire un seul feuillet du matériau ont récemment été étendues avec succès à d'autres couches de matériaux tels que BN, MoS_2, WS_2, $MoSe_2$, $MoTe_2$ et $NiTe_2$ [164]. Des structures mono- ou quelques-couches comme h-BN sont aussi produits par les procédés de croissance, MBE et CVD [166].

Sur la base de ces nouveaux composites nanofeuillets à une seule couche, il devient possible d'accorder les propriétés mécaniques, électroniques ou optiques à une demande de propriétés. Si une seule couche (nanofeuillets cristaux bi-dimensionnels) offre de nouvelles propriétés, alors créer des hétérostructures de matériaux différents empilées devrait amplifier la gamme de possibilités [96, 166]. Les premières expériences montrent que le graphène et h-BN donne un couple très prometteur lorsqu'ils sont empilés. Le feuillet h-BN est une nanofeuille atomiquement lisse 2D avec des constantes de réseau très similaires à celle du modèle de sous-réseau du graphène AB. Comme h-BN est un isolant à bande interdite large, le graphène empilé sur ce h-BN, conserve ses propriétés uniques autour du point K [167]. Une autre façon intéressante de combiner différents matériaux 2D entre eux est de concevoir dans le même plan des hétéro-structures, dans une seule et même couche. Par exemple, on peut imaginer des flocons de graphène de type «boites quantiques» intégrés dans un feuillet de h-BN comme l'a proposé récemment Li et Shenoy [168]. Notons que tous les modules de Young de ces matériaux stratifiés, comprenant le graphène, h-BN, MoS_2, WS_2, $MoSe_2$ et $MoTe_2$, sont étudiés dans le chapitre 6 de la thèse.

5 Conclusions et perspectives

Les propriétés structurales, électroniques et chimiques de feuillets infinis de graphène ont déjà été modélisées et décrites théoriquement dans la littérature depuis les années 1940, en commençant par l'étude d'un seul feuillet de l'empilement donnant le graphite. Après la première obtention expérimentale très médiatisée de feuillets isolés de graphène en 2004, ce nouveau matériau bi-dimensionel (2D) a rapidement inspiré une grande communauté de chercheurs dans le monde entier. Peu de temps après, d'autres nanostructures de graphène comme les nanorubans (1D) ou les points quantiques «semblables à des paillettes» (0D) sont devenus des sujets d'actualité. Plus les nanostructures de graphène 2D sont petites et délimitées, plus le ratio bord/surface augmente et plus les bords et les effets de confinement quantique gagnent en importance. En changeant la terminaison des bords des feuillets de graphène, les propriétés de ces nanoobjets peuvent être radicalement modifiées, ouvrant de nouveaux moyens d'agir sur la conception et la manipulation de ces matériaux, notamment sur leur bande interdite. Une connaissance approfondie de l'effet de structure de bord sur les propriétés du graphène se révèle par conséquent très opportune. En particulier aujourd'hui, où de nouvelles voies expérimentales pour produire des nanostructures de graphène via la chimie de synthèse «bottom-up» sont en plein essor permettant l'élaboration précise à l'échelle atomique de nanorubans de graphène.

Le travail de modélisation présenté dans ce mémoire met l'accent sur les propriétés structurales, électroniques et chimiques de bords de feuillet de graphène non-terminés et hydrogénés, ainsi que de nanorubans de graphène avec des bords fonctionnalisés avec des groupes chimiques plus complexes. De plus, les propriétés mécaniques de graphène et systèmes connexes de basse dimensionalité (nanotubes de carbone, polymères organiques, d'autres nanofeuillets 2D) ont été étudiés, notamment le module de Young. Les techniques LDA-DFT, telles que celles transposées dans le code *AIMPRO*, ont été utilisées dans le cadre de cette thèse pour modéliser l'ensemble des structures concernées.

Ce travail de thèse aboutit aux conclusions principales suivantes pour les trois grandes thématiques abordées ici :

– **Bords de feuillet de graphène, non-terminés ou à liaisons pendantes, «en tube» et hydrogénés**

  Différents bords de type «armchair», «zigzag» et «Klein» ont été étudiés. La modélisation des bords de feuillets de graphène découplés et individuels, de larges nanorubans (largeur d'environ 50 Å) a été menée. En plus de ces trois types de bords «standards», d'autres reconstructions thermodynamiquement favorables ont été inclues dans cette étude, par exemple la reconstruction en zigzag (5-7) ou celle en bord de Klein. Notons que ce travail a rigoureusement abordé pour la première fois les bords de type «Klein» et «Klein reconstruit».

  Dans l'ensemble des bords non terminés de feuillets de graphène, les bords armchair et zigzag reconstruit (5-7) sont les plus stables, en bon accord avec la littérature.
  Cependant, uniquement dans le cas des matériaux 2D, notre travail identifie une nouvelle configuration stable thermodynamiquement de bord replié «en tube», en plus des types de bords plats non-terminés. Dans ce cas, le bord du feuillet non-reconstruit se replie sur le plan du graphène, liant le bord «libre» initial sur la feuille de graphène, formant une ligne d'atomes liés en sp^3. Un nanotube de carbone à section en forme de goutte est alors formé le long du bord de graphène. La stabilité de cette structure de bord dépend du diamètre du tube. Ainsi pour les tubes les plus grands (diamètre $\geq$ 11 Å), cette structure de bord est plus stable que toutes les autres configurations connues sans terminaison. Les propriétés électroniques des éléments du graphène et de nanotubes ont été trouvées se superposer.

  Lors de la passivation des bords de feuillet de graphène avec des atomes d'hydrogène, les principales configurations stables connues pour les bords armchair et zigzag ont été calculées dans ma approche donnant des résultats similaires à

ceux rapportés dans les études antérieures. Une nouvelle configuration armchair à haute densité d'atomes d'hydrogène a été trouvée, consistant en une ondulation périodique des groupes du bord «hors plan». De nouvelles configurations stables de bords hydrogénées basées sur les bords de Klein et de Klein reconstruits ont étonnamment pu être identifiées. Contrairement aux bords hydrogénés à base zigzag, les bords hydrogénées à base de Klein ont des énergies de formation comparable à celles obtenues pour des bords hydrogénés de type armchair. Dans ces nouveaux cas, les lignes en zigzag «backbone» ont un comportement similaire aux bords hydrogénés de type zigzag classiques. Ainsi, les structures électroniques sont similaires entre les bords hydrogénés les plus stables de types zigzag, Klein et Klein reconstruits. Contrairement aux études de la littérature montrant des possibles états magnétiques pour des nanorubans de graphène aux bords hydrogénées de type zigzag, les calculs LDA-DFT de mon travail montrent que toutes les configurations de bords hydrogénés les plus stables évitent les états magnétiques autour du niveau de Fermi aboutissant à un comportement non-magnétique et ceci quel que soit le type de bord.

En résumé, pour les bords hydrogénés de feuillets de graphène, les tendances suivantes ont été identifiées :

- Les atomes de carbone du bord préfèrent une coordination sp^3 pour les bords soit totalement armchair soit totalement Klein, en formant des liaisons simples avec la feuille de graphène «backbone».
- Les bords hydrogénés le long de l'orientation $<2\bar{1}\bar{1}0>$ (zigzag et Klein) sont plus stables avec des périodes composées d'un atome de carbone en configuration sp^3 et de deux en sp^2 le long de la dernière ligne complètement en zigzag du «backbone».
- Les densités plus élevées d'hydrogène sont plus stables lorsque des ondulations «hors plan» se forment le long du bord, ceci pour tous les types de bords.
- La tension de bord induite par des densités élevées d'hydrogène est compensée par la création d'ondulations périodiques de déformations «hors plan» du bord.

– Toutes les configurations de bord hydrogénées de graphène les plus stables montrent un comportement non magnétique, sans états fluctuants au niveau de Fermi.
– Les nanorubans plus minces de graphène montrent une bande interdite, avec un gap plus faible pour les nanorubans zigzag et Klein reconstruits, que pour les nanorubans armchair.
– Lors de la synthèse expérimentale, la stabilité des bords hydrogénés sera fortement dépendante des conditions de croissance (par exemple la pression partielle d'hydrogène, la température, les interactions de surface du substrat avec le graphène), et plusieurs différents types de bords hydrogénées sont susceptibles d'être obtenus.

Sur la base de ces nouveaux résultats concernant les bords hydrogénés de graphène, de nouveaux modèles plausibles de croissance du graphène ont été proposés. Tous les modèles impliquent des dimères de carbone hydrogénés, comme par exemple des groupes éthylène, se liant aux bords des feuillets. Mon modèle montre que les dimères de carbone peuvent être les briques de base de construction de croissance pour les deux types de bords en structures «armchair» et «zigzag». En outre, ce travail montre que les stabilités de bord de type similaire sont très proches, selon les conditions expérimentales de croissance (température, pression, etc), modélisées dans ce travail en faisant varier le potentiel chimique de l'hydrogène. Mes résultats confortent le modèle d'une croissance des bords zigzag avec des configurations intermédiaires de bords hydrogénés et des rotations de liaisons.

Cependant, lors de la croissance de graphène sur des substrats, des effets de surface doivent être pris en compte. Récemment dans la littérature, il a été montré que la croissance CVD de feuillets de graphène à partir d'éthylène sur du cuivre, serait caractérisée par des barrières d'activation provenant de la déshydrogénation de l'éthylène catalysée par la surface et de la construction des feuillets de graphène. Ceci est en bon accord avec les nouveaux modèles de croissance proposés dans ce mémoire.

– **Nanorubans de graphène avec des bords fonctionnalisés**

Cette étude fondamentale des bords de nanorubans de graphène fonctionnalisés fournit une première image de la physique sous-jacente induite par l'addition de groupes fonctionnels complexes sur les bords du nano-feuillet de graphène, en particulier dans le cas des bords armchair. Dans ce travail, en plus des simples terminaisons par des atomes d'hydrogène, des groupes fonctionnels de bord -F, -Cl, -Br, -SH et en particulier -OH (hydroxyle), tapissant des nanorubans fins de graphène (de largeur inférieure à 25 Å) ont été étudiés.

En général, la présence de groupes fonctionnels sur les bords des feuillets les plus grands ne provoque pas de fortes tensions dans les nanorubans de graphène, car la tension est compensée par la formation d'ondulations statiques le long du bord du ruban. On peut imaginer différents processus pour contrebalancer la tension de la ligne 1D le long du bord de ruban par une tension en surface 2D dans le plan de base. Dans le cas du feuillet de graphène, caractérisé par un module de Young dans le plan calculé à environ $\sim$ 1,06 TPa, la résistance dans le plan de tension est élevée et la déformation de bord est une solution énergétiquement favorable, entraînant la formation d'une structure statique ondulée en bord de feuillet. Le coût énergétique associé à la perturbation induite par l'ondulation du réseau π de graphène impose aux ondulations de rester localisées à proximité du bord de ruban, réduisant cependant la largeur effective du plan de base du ruban. Ces ondulations se forment pour la majorité des chiralités de bords de rubans et des groupes fonctionnels examinés dans cette thèse. Ceci laisse suggérer que les bords (du ruban) plats observés pour l'hydrogénation simple est en réalité une exception. Comme ce comportement d'ondulation statique de la structure de bord semble être une réponse fondamentale d'un système 2D à plat à une contrainte 1D des bords, il est également susceptible d'être important pour toute la gamme en cours de développement de nouveaux matériaux 2D en monocouche tels que BN, MoS_2, $MoSe_2$, $MoTe_2$ ou WS_2. En outre la compensation de tension par les ondulations est susceptible de jouer aussi un rôle important aux interfaces des feuillets comme dans les joints de grains.

Ces résultats excluent la possibilité que les groupes fonctionnels de bords induisent de fortes tensions dans le plan de graphène de base. Pour la première fois, j'ai calculé le module de Young pour les nanorubans fins de graphène armchair avec des terminaisosn -H et -OH, me permettant de montrer que des ondulations de bord peuvent réduire considérablement, jusqu'à 40 %, le module de Young. Je crois que ce changement des propriétés mécaniques en fonction de la fonctionnalisation du bord pourrait avoir un impact direct sur l'ingénierie de dispositifs à base de matériaux composites intégrant des nanorubans fins de graphène ou des nanostructures 2D dérivées.

En outre, les ondulations statiques locales sur les bords des feuillets changent la réactivité chimique du ruban. La périodicité de cette ondulation par superposition à celle du réseau sous jacent, peut donner lieu à l'existence de superréseaux, illustrée par exemple par l'adsorption sélective d'atomes métalliques près du bord ondulé des feuillets. En ce qui concerne les propriétés électroniques des nanorubans de graphène armchair, j'ai trouvé que la bande interdite est étonnamment insensible aux ondulations statiques, mais peut changer jusqu'à 50 % en fonction de la nature du groupe de bord fonctionnel et de la largeur du ruban.

– **Propriétés mécaniques du graphène et des nanomatériaux connexes**

Sur la base de mon étude approfondie du module de Young de système 2D, ce module a été étudié pour divers nanoobjets, notamment des nanostructures telles que des nanofeuillets 2D (graphène, BN, MoS_2 ...), des nanotubes de carbone et des polymères organiques conjugués.

Pour calculer le module de Young, un volume ou une section transversale de l'objet doivent être définis. Jusqu'à présent, dans toutes les études de la littérature, les volumes des nanoobjets ont été estimés sur des simples approximations géométriques ou des modèles de sphère atomique, comme le rayon Van der Waals. Ces valeurs conduisent alors à des valeurs de module de Young très dispersées, interdisant la comparaison entre différentes nanostructures. L'étude bibliographique de mon travail montre l'absence dans la littérature d'une définition de vo-

lume transférable, géométrique indépendante et conviviale, nécessaire pour des nano-objets de basse dimension caractérisés par un ratio surface/volume élevé. Par conséquent une première étape a consisté à développer un nouveau concept de volume adapté pour les nanoobjets en fonction de la densité électronique moyenne. Ma proposition est d'utiliser la densité électronique moyenne (donc la densité de charge moyenne) de structures 3D connexes (composition similaire et configuration de liaison), comme par exemple le graphite → graphène → nanotubes de carbone ou la structure h-BN en volume vers → nanofeuillets BN → nanotubes de BN. Pour les systèmes 3D apparentés (graphite, h-BN ...), la densité moyenne des électrons est clairement définie sur la maille primitive, et cette valeur peut être utilisée pour calculer les volumes associés aux nanofeuillets individuels ou des nanotubes.
Ce nouveau concept de volume pour les nanoobjets a ensuite été appliqué avec succès aux calculs de différentes propriétés mécaniques et en particulier le module de Young du graphène, des nanotubes de carbone à simple paroi et d'autres nanofeuillets isolés récemment. Les systèmes à quelques nanofeuillets de graphène et de BN jusqu'à 4 couches ont été étudiés dans ce contexte.

Le concept nouveau de volume permet maintenant la comparaison directe des valeurs de module de Young pour des nanoobjets de différentes formes, par exemple entre des nanotubes de carbone et graphène, avec une extrapolation correcte vers des valeurs de volume de systèmes 3D apparentés (le graphite pour le graphène). Il est à noter que toutes les valeurs calculées pour des nanofeuillets infinis et les nanotubes sont en bon accord avec la valeur «dans-le-plan» du module de Young des matériaux 3D apparentés. Pour la première fois, nous disposons ici d'un ensemble de calculs fondés sur une seule et même méthode transférable.
Enfin, pour la première fois, les coefficients de Poisson «dans-le-plan» et «hors plan» du graphène ont été calculés, à l'aide du nouveau concept de volume proposé dans ce mémoire. Dans les deux cas, les coefficients de Poisson du graphène sont similaires à ceux du graphite.

Cette nouvelle approche utilisant un volume défini fondé sur la densité électronique permet en outre d'étudier des systèmes dont le volume varie, en changeant par exemple le niveau de Fermi, comme ce travail l'illustre pour la première fois dans le cas du graphène.

Perspectives

Nous espérons que les résultats de cette thèse stimulerons à la fois de futurs travaux expérimentaux et théoriques sur le graphène et les matériaux connexes. Ce travail illustre la transition actuellement en cours d'une époque où les variations dans la structure de bord ajouté à la complexité ne pouvaient pas être décrites, où la fonctionnalisation bord est décrite et contrôlée, donnant accès ainsi à un nouvel outil puissant pour définir le comportement de graphène.

Dans un avenir proche, de nouvelles expériences vont caractériser les bords de graphène encore plus en détail, y compris les bords hydrogénés et fonctionnalisés. Notamment, des études non destructives de bords des feuillets du graphène, en utilisant par exemple la spectroscopie Raman, pourraient contribuer à confirmer et identifier les configurations de bords stables et les terminaisons proposées ici. Cette thèse pourrait donc servir comme guide à ces études des bords de feuillet. Notamment à partir de mes résultats, les modes vibrationnels caractéristiques des structures de bord peuvent maintenant être calculés théoriquement.
En outre, la croissance à des précisions atomiques de nanorubans se développe rapidement et la fonctionnalisation contrôlée complexe par des groupes des bords de ruban va bientôt devenir réaliste. Mon travail explore différents groupes fonctionnels de bord en étudiant leurs influences et indique des expériences pouvant être conçues sur la base des nouvelles informations obtenues et de la compréhension approfondie ici. Il sera très intéressant de caractériser les nanorubans obtenus expérimentalement et de comparer leurs propriétés avec les résultats modélisés dans ce travail.
Ce mémoire souligne l'importance des bords en «zigzag» et de «Klein reconstruits», qui vont être intéressants aussi si ils sont fonctionnalisés par des groupes com-

plexes. Les ondulations «hors plan» devraient être étudiées en détail dans l'avenir, notamment leurs conséquences attendues et inattendues sur les propriétés électroniques, chimiques et magnétiques.

Expérimentalement, les nanostructures de graphène sont généralement obtenues et caractérisées en couche directement adsorbées sur des surfaces (principalement métalliques). Mon travail théorique sur des bords «libres» doit donc être prolongé pour tenir compte des interactions supplémentaires avec une surface métallique. Une étape importante sera de comparer plus en détail les modèles de croissance de feuillets de graphène à base d'éthylène avec l'expérience. Ces types de calculs, tenant compte d'un environnement de substrat réaliste, nécessitent des systèmes de très grande taille avec plusieurs centaines d'atomes et devraient être coûteux en temps utilisant des approches DFT.

Dans le cadre de travail de cette thèse, des calculs préliminaires de nanorubans de graphène simples hydrogénées et hydroxylés de largeur 7 sur une surface de Cu(111) ont été effectuées. Ces calculs préliminaires indiquent que les bords hydroxylés et ondulés semblent être stables sur les surfaces, avec en particulier une distance graphène-substrat augmentée par rapport au structures simplement hydrogénées. En outre, l'ondulation des bords de feuillets introduit de manière alternative des groupes en interaction ou non avec la surface. D'autres tendances intéressantes apparaissent concernant l'orientation des nanorubans fins de graphène fortement influencée par les bords fonctionnalisés et ondulés avec la possibilité d'orientation de réseau du feuillet de graphène, dissociée de l'orientation du substrat. L'orientation fortement influençable par le choix de la nature du groupement fonctionel de bord pourrait aboutir à des alignements intéressants de ces nanostructures de graphène vis à vis des surfaces ou des marches. Cela suggère qu'il pourrait être possible d'utiliser la fonctionnalisation de bord pour maitriser l'orientation du graphène/substrat, plutôt que de tenter de maitriser l'alignement des réseaux graphène/substrat. Notamment, l'aménagement et la connectivité entre nanostructures de graphène pourraient être maitrisés à l'avenir grâce à une fonctionnalisation des bords de feuillets de graphène.

Dans l'avenir, les travaux théoriques de systèmes de grandes tailles deviendront plus facilement accessibles grâce à la mise au point récente d'une nouvelle méthode de «filtration» pour les calculs DFT. Cette extension importante est déjà implémentée dans le code *AIMPRO* et sera totalement utilisable après la phase actuelle de tests intensifs. Cela offrira de nouvelles opportunités pour modéliser d'autres distorsions topologiques (par exemple torsion) et peut-être même de petits systèmes complets de transistors sur la base de graphène, sans perdre la précision de l'approche DFT.

Des nouveaux matériaux composites de graphène seront également explorés et ce travail peut aider pour guider les efforts dans cette direction, influencés par l'utilisation de la définition prometteuse universelle transférable du volume de nano-objet proposée. En outre, la convergence et le chevauchement du graphène avec la science des polymères sera riche et ouvrira de nouveaux défis dans le domaine des nanosciences, ou physique et chimie deviennent imbriqués.

En ce qui concerne les nouveaux circuits intégrés basés sur des nanorubans de graphène et les nouvelles avancées de matériaux composites comprenant du graphène, je suis fortement convaincu que le contrôle et la conception de la fonctionnalisation de surface et de bord jouera un rôle clé. Si les efforts dans la recherche du graphène et dans l'ingénierie se poursuivent au même rythme que ces dernières années, on peut attendre beaucoup de ce fantastique matériau dans le 21ème siècle.

Références

[1] J. S. Kilby, “Turning Potential into Reality : The Invention of the Integrated Circuit”, Nobel Lecture (2000).

[2] P. O. Hahn, “The 300 mm silicon wafer — a cost and technology challenge”, Microelectronic Engineering, **56**, 3 (2001).

[3] M. Watanabe and S. Kramer, “450 mm Silicon : An Opportunity and Wafer Scaling”, ECS - Interface, **15**, 28 (2006).

[4] H. Iwai and S. Ohmi, “Silicon integrated circuit technology from past to future”, Microelectronics Reliability, **42**, 465 (2002).

[5] K. Jeong and A. Kahng, “A power-constrained MPU roadmap for the International Technology Roadmap for Semiconductors (ITRS)”, SoC Design Conference (ISOCC) 2009, 49 (2009).

[6] H. Iwai, “Roadmap for 22 nm and beyond”, Microelectron. Eng., **86**, 1520 (2009).

[7] R. Van Noorden, “Chemistry : The trials of new carbon”, Nature News, **469**, 14 (2011).

[8] K. S. Novoselov, V. I. Fal’ko, L. Colombo, P. R. Gellert, M. G. Schwab, and K. Kim, “A roadmap for graphene”, Nature, **490**, 192 (2012).

[9] M. S. P. Shaffer and A. H. Windle, “Fabrication and Characterization of Carbon Nanotube/Poly(vinyl alcohol) Composites”, Adv. Mater., **11**, 937 (1999).

[10] O. Breuer and U. Sundararaj, “Big returns from small fibers : A review of polymer/carbon nanotube composites”, Polym. Compos., **25**, 630 (2004).

[11] S. Stankovich, D. A. Dikin, G. H. B. Dommett, K. M. Kohlhaas, E. J. Zimney, E. A. Stach, R. D. Piner, S. T. Nguyen, and R. S. Ruoff, “Graphene-based composite materials”, Nature, **442**, 282 (2006).

[12] R. J. Young, I. A. Kinloch, L. Gong, and K. S. Novoselov, “The mechanics of graphene nanocomposites : A review”, Composites Sci. Tech., **72**, 1459 (2012).

[13] S. Iijima, “Helical microtubules of graphitic carbon”, Nature, **354**, 56 (1991).

[14] K. Novoselov, A. Geim, S. Morozov, D. Jiang, Y. Zhang, S. Dubonos, I. Grigorieva, and A. Firsov, "Electric field effect in atomically thin carbon films", Science, **306**, 666 (2004).

[15] A. K. Geim, "Random walk to graphene", Nobel Lecture (2010).

[16] M. Ohring, *Engineering Materials Science* (Academic Press, San Diego, 1995).

[17] C. Kittel, *Introduction to Solid State Physics*, 7th ed. (Wiley, New York, 1996).

[18] D. Chung, "Review Graphite", J. Mater. Sci., **37**, 1475 (2002).

[19] P. J. F. Harris, *Carbon Nanotubes and Related Structures : New Materials for the Twenty-first Century* (Cambridge University Press, 2004).

[20] M. Grundmann, *The Physics of Semiconductors : An Introduction Including Devices and Nanophysics* (Springer, Berlin, 2006).

[21] S. M. Sze and K. K. Ng, *Physics of Semiconductor Devices*, 3rd ed. (Wiley-Interscience, Hoboken, New Jersey, 2007).

[22] A. K. Geim and K. S. Novoselov, "The rise of graphene", Nature Mater., **6**, 183 (2007).

[23] A. H. Castro Neto, F. Guinea, N. M. R. Peres, K. S. Novoselov, and A. K. Geim, "The electronic properties of graphene", Rev. Mod. Phys., **81**, 109 (2009).

[24] M. J. Allen, V. C. Tung, and R. B. Kaner, "Honeycomb Carbon : A Review of Graphene", Chem. Rev., **110**, 132 (2010).

[25] Y. Zhu, S. Murali, W. Cai, X. Li, J. W. Suk, J. R. Potts, and R. S. Ruoff, "Graphene and Graphene Oxide : Synthesis, Properties, and Applications", Adv. Mater., **22**, 3906 (2010).

[26] C. Stampfer, S. Fringes, J. Güttinger, F. Molitor, C. Volk, B. Terrés, J. Dauber, S. Engels, S. Schnez, A. Jacobsen, S. Dröscher, T. Ihn, and K. Ensslin, "Transport in graphene nanostructures", Front. Phys., **6**, 271 (2011).

[27] Ph. Wagner, V. V. Ivanovskaya, M. J. Rayson, P. R. Briddon, and C. P. Ewels, "Mechanical properties of nanosheets and nanotubes investigated using a new geometry independent volume definition", J. Phys. : Condens. Matter, **25**, 155302 (2013).

[28] B. Partoens and F. M. Peeters, "From graphene to graphite : Electronic structure around the K point", Phys. Rev. B, **74**, 075404 (2006).

[29] M. Klintenberg, S. Lebègue, C. Ortiz, B. Sanyal, J. Fransson, and O. Eriksson, "Evolving properties of two-dimensional materials : from graphene to graphite", J. Phys. : Condens. Matter, **21**, 335502 (2009).

[30] P. R. Wallace, "The Band Theory of Graphite", Phys. Rev., **71**, 622 (1947).

[31] J.-C. Charlier, J.-P. Michenaud, and X. Gonze, "First-principles study of the electronic properties of simple hexagonal graphite", Phys. Rev. B, **46**, 4531 (1992).

[32] M. S. Dresselhaus and G. Dresselhaus, "Intercalation compounds of graphite", Adv. Phys., **51**, 1 (2002).

[33] S. V. Morozov, K. S. Novoselov, M. I. Katsnelson, F. Schedin, D. C. Elias, J. A. Jaszczak, and A. K. Geim, "Giant Intrinsic Carrier Mobilities in Graphene and its Bilayer", Phys. Rev. Lett., **100**, 016602 (2008).

[34] X. Du, I. Skachko, A. Barker, and E. Y. Andrei, "Approaching ballistic transport in suspended graphene", Nature Nanotech., **3**, 491 (2008).

[35] Z. Jiang, Y. Zhang, Y.-W. Tan, H. Stormer, and P. Kim, "Quantum Hall effect in graphene", Solid State Commun., **143**, 14 (2007).

[36] M. I. Katsnelson, K. S. Novoselov, and A. K. Geim, "Chiral tunnelling and the Klein paradox in graphene", Nature Phys., **2**, 620 (2006).

[37] V. Barone, O. Hod, and G. E. Scuseria, "Electronic Structure and Stability of Semiconducting Graphene Nanoribbons", Nano Lett., **6**, 2748 (2006).

[38] Y.-W. Son, M. L. Cohen, and S. G. Louie, "Energy Gaps in Graphene Nanoribbons", Phys. Rev. Lett., **97**, 216803 (2006).

[39] L. Jiao, L. Zhang, X. Wang, G. Diankov, and H. Dai, "Narrow graphene nanoribbons from carbon nanotubes", Nature, **458**, 877 (2009).

[40] L. Tapaszto, G. Dobrik, P. Lambin, and L. P. Biro, "Tailoring the atomic structure of graphene nanoribbons by scanning tunnelling microscope lithography", Nature Nanotech., **3**, 397 (2008).

[41] J. Cai, P. Ruffieux, R. Jaafar, M. Bieri, T. Braun, S. Blankenburg, M. Muoth, A. P. Seitsonen, M. Saleh, X. Feng, K. Mullen, and R. Fasel, "Atomically precise bottom-up fabrication of graphene nanoribbons", Nature, **466**, 470 (2010).

[42] P. Ruffieux, J. Cai, N. C. Plumb, L. Patthey, D. Prezzi, A. Ferretti, E. Molinari, X. Feng, K. Müllen, C. A. Pignedoli, and R. Fasel, "Electronic Structure of Atomically Precise Graphene Nanoribbons", ACS Nano, **6**, 6930 (2012).

[43] P. Hohenberg and W. Kohn, "Inhomogeneous Electron Gas", Phys. Rev., **136**, B864 (1964).

[44] W. Kohn and L. J. Sham, "Self-Consistent Equations Including Exchange and Correlation Effects", Phys. Rev., **140**, A1133 (1965).

[45] M. J. Rayson and P. R. Briddon, "Highly efficient method for Kohn-Sham density functional calculations of $500 - 10\,000$ atom systems", Phys. Rev. B, **80**, 205104 (2009).

[46] M. J. Rayson, "Rapid filtration algorithm to construct a minimal basis on the fly from a primitive Gaussian basis", Comput. Phys. Commun., **181**, 1051 (2010).

[47] P. R. Briddon and M. J. Rayson, "Accurate Kohn-Sham DFT with the speed of tight binding : Current techniques and future directions in materials modelling", Phys. Status Solidi B, **248**, 1309 (2011).

[48] V. V. Ivanovskaya, A. Zobelli, Ph. Wagner, M. I. Heggie, P. R. Briddon, M. J. Rayson, and C. P. Ewels, "Low-Energy Termination of Graphene Edges via the Formation of Narrow Nanotubes", Phys. Rev. Lett., **107**, 065502 (2011).

[49] P. S. Branicio, M. H. Jhon, C. K. Gan, and D. J. Srolovitz, "Properties on the edge : graphene edge energies, edge stresses, edge warping, and the Wulff shape of graphene flakes", Modell. Simul. Mater. Science Engineering, **19**, 054002 (2011).

[50] J. W. Patrick, ed., *Porosity in Carbons : Characterization and Applications*, 1st ed. (Halsted Press, 1994).

[51] E. Frieden, "Chemical Elements of Life", Scientific American, **227**, 52 (1972).

[52] S. J. Sque, *Bulk and transfer doping of diamond*, Phd thesis, University of Exeter, UK (2005).

[53] A. Fukumoto, "First-principles pseudopotential calculations of the elastic properties of diamond, Si, and Ge", Phys. Rev. B, **42**, 7462 (1990).

[54] H. J. McSkimin and W. L. Bond, "Elastic Moduli of Diamond", Phys. Rev., **105**, 116 (1957).

[55] C. A. Klein and G. F. Cardinale, "Young's modulus and Poisson's ratio of CVD diamond", Diamond Relat. Mater., **2**, 918 (1993).

[56] F. Szuecs, M. Werner, R. S. Sussmann, C. S. J. Pickles, and H. J. Fecht, "Temperature dependence of Young's modulus and degradation of chemical vapor deposited diamond", J. Appl. Phys., **86**, 6010 (1999).

[57] S. V. Kidalov and F. M. Shakhov, "Thermal Conductivity of Diamond Composites", Materials, **2**, 2467 (2009).

[58] T. Evans and P. F. James, "A Study of the Transformation of Diamond to Graphite", Proc. Royal Soc. London, Series A, **277**, 260 (1964).

[59] A. Mainwood, "Theoretical modelling of dopants in diamond", J. Mater. Sci. : Mater. Electron., **17**, 453 (2006).

[60] V. N. Mochalin, O. Shenderova, D. Ho, and Y. Gogotsi, "The properties and applications of nanodiamonds", Nature Nanotech., **7**, 11 (2012).

[61] J. D. Bernal, "The Structure of Graphite", Proc. Royal Soc. London, Series A, **106**, 749 (1924).

[62] R. E. Franklin, "The structure of graphitic carbons", Acta Cryst., **4**, 253 (1951).

[63] J. C. Slonczewski and P. R. Weiss, "Band Structure of Graphite", Phys. Rev., **109**, 272 (1958).

[64] J.-C. Charlier, X. Gonze, and J.-P. Michenaud, "First-principles study of the electronic properties of graphite", Phys. Rev. B, **43**, 4579 (1991).

[65] N. B. Hannay, T. H. Geballe, B. T. Matthias, K. Andres, P. Schmidt, and D. MacNair, "Superconductivity in Graphitic Compounds", Phys. Rev. Lett., **14**, 225 (1965).

[66] S. M. Heald and E. A. Stern, "Extended-x-ray-absorption-fine-structure study of the Br_2-graphite system", Phys. Rev. B, **17**, 4069 (1978).

[67] A. Yaya, C. P. Ewels, I. Suarez-Martinez, Ph. Wagner, S. Lefrant, A. Okotrub, L. Bulusheva, and P. R. Briddon, "Bromination of graphene and graphite", Phys. Rev. B, **83**, 045411 (2011).

[68] H. W. Kroto, J. R. Heath, S. C. O'Brien, R. F. Curl, and R. E. Smalley, "C60 : Buckminsterfullerene", Nature, **318**, 162 (1985).

[69] H. W. Kroto, A. W. Allaf, and S. P. Balm, "C60 : Buckminsterfullerene", Chem. Rev., **91**, 1213 (1991).

[70] www.ewels.info (2012).

[71] www.de.wikipedia.org/wiki/Fullerene (2012).

[72] W. Krätschmer, L. D. Lamb, K. Fostiropoulos, and D. R. Huffman, "Solid C60 : a new form of carbon", Nature, **347**, 354 (1990).

[73] P. W. Dunk, N. K. Kaiser, C. L. Hendrickson, J. P. Quinn, C. P. Ewels, Y. Nakanishi, Y. Sasaki, H. Shinohara, A. G. Marshall, and H. W. Kroto, "Closed network growth of fullerenes", Nature Comm., **3**, 855 (2012).

[74] N. Gonzalez Szwacki, A. Sadrzadeh, and B. I. Yakobson, "B_{80} Fullerene : An Ab Initio Prediction of Geometry, Stability, and Electronic Structure", Phys. Rev. Lett., **98**, 166804 (2007).

[75] S. Iijima and T. Ichihashi, "Single-shell carbon nanotubes of 1-nm diameter", Nature, **363**, 603 (1993).

[76] X. Zhao, Y. Liu, S. Inoue, T. Suzuki, R. O. Jones, and Y. Ando, "Smallest Carbon Nanotube Is 3 Å in Diameter", Phys. Rev. Lett., **92**, 125502 (2004).

[77] P. M. Ajayan, "Nanotubes from Carbon", Chem. Rev., **99**, 1787 (1999).

[78] www-ibmc.u-strasbg.fr/ict/article83.html ?lang=fr (2012).

[79] P. J. F. Harris, *Carbon Nanotube Science* (Cambridge University Press, UK, 2009).

[80] M. Dresselhaus, G. Dresselhaus, and R. Saito, “Physics of carbon nanotubes”, Carbon, **33**, 883 (1995).

[81] J. P. Lu, “Elastic Properties of Carbon Nanotubes and Nanoropes”, Phys. Rev. Lett., **79**, 1297 (1997).

[82] S. Gupta, K. Dharamvir, and V. K. Jindal, “Elastic moduli of single-walled carbon nanotubes and their ropes”, Phys. Rev. B, **72**, 165428 (2005).

[83] E. W. Wong, P. E. Sheehan, and C. M. Lieber, “Nanobeam Mechanics : Elasticity, Strength, and Toughness of Nanorods and Nanotubes”, Science, **277**, 1971 (1997).

[84] M. Yu, B. S. Files, S. Arepalli, and R. S. Ruoff, “Tensile Loading of Ropes of Single Wall Carbon Nanotubes and their Mechanical Properties”, Phys. Rev. Lett., **84**, 5552 (2000).

[85] J. N. Coleman, U. Khan, W. J. Blau, and Y. K. Gun’ko, “Small but strong : A review of the mechanical properties of carbon nanotube-polymer composites”, Carbon, **44**, 1624 (2006).

[86] M. Terrones, “SCIENCE AND TECHNOLOGY OF THE TWENTY-FIRST CENTURY : Synthesis, Properties, and Applications of Carbon Nanotubes”, Annu. Rev. Mater. Res., **33**, 419 (2003).

[87] B. J. Landi, M. J. Ganter, C. D. Cress, R. A. DiLeo, and R. P. Raffaelle, “Carbon nanotubes for lithium ion batteries”, Energy & Environmental Science, **2**, 638 (2009).

[88] K. Kostarelos, A. Bianco, and M. Prato, “Promises, facts and challenges for carbon nanotubes in imaging and therapeutics”, Nature Nanotech., **4**, 627 (2009).

[89] J.-C. Charlier, L. Arnaud, I. V. Avilov, M. Delgado, F. Demoisson, E. H. Espinosa, C. P. Ewels, A. Felten, J. Guillot, R. Ionescu, R. Leghrib, E. Llobet, A. Mansour, H.-N. Migeon, J.-J. Pireaux, F. Reniers, I. Suarez-Martinez, G. E. Watson, and Z. Zanolli, “Carbon nanotubes randomly decorated with gold clusters : from nano 2 hybrid atomic structures to gas sensing prototypes”, Nanotechnology, **20**, 375501 (2009).

[90] N. D. Mermin and H. Wagner, “Absence of Ferromagnetism or Antiferromagnetism in One- or Two-Dimensional Isotropic Heisenberg Models”, Phys. Rev. Lett., **17**, 1133 (1966).

[91] H. P. Boehm, A. Clauss, G. O. Fischer, and U. Hofmann, "Dünnste Kohlenstoff-Folien", Zeitschrift für Naturforschung B, **17**, 150 (1962).

[92] K. S. Novoselov, A. K. Geim, S. V. Morozov, D. Jiang, M. I. Katsnelson, I. V. Grigorieva, S. V. Dubonos, and A. A. Firsov, "Two-dimensional gas of massless Dirac fermions in graphene", Nature, **438**, 197 (2005).

[93] Y. Zhang, Y.-W. Tan, H. L. Stormer, and P. Kim, "Experimental observation of the quantum Hall effect and Berry's phase in graphene", Nature, **438**, 201 (2005).

[94] J. C. Meyer, A. K. Geim, M. I. Katsnelson, K. S. Novoselov, T. J. Booth, and S. Roth, "The structure of suspended graphene sheets", Nature, **446**, 60 (2007).

[95] A. Fasolino, J. H. Los, and M. I. Katsnelson, "Intrinsic ripples in graphene", Nature Mater., **6**, 858 (2007).

[96] K. S. Novoselov and A. H. Castro Neto, "Two-dimensional crystals-based heterostructures : materials with tailored properties", Phys. Scripta, **T146**, 014006 (2012).

[97] Y. Hernandez, V. Nicolosi, M. Lotya, F. M. Blighe, Z. Sun, S. De, I. T. McGovern, B. Holland, M. Byrne, Y. K. Gun'Ko, J. J. Boland, P. Niraj, G. Duesberg, S. Krishnamurthy, R. Goodhue, J. Hutchison, V. Scardaci, A. C. Ferrari, and J. N. Coleman, "High-yield production of graphene by liquid-phase exfoliation of graphite", Nature Nanotech., **3**, 563 (2008).

[98] W. A. de Heer, C. Berger, X. Wu, P. N. First, E. H. Conrad, X. Li, T. Li, M. Sprinkle, J. Hass, M. L. Sadowski, M. Potemski, and G. Martinez, "Epitaxial graphene", Solid State Commun., **143**, 92 (2007).

[99] L. Gao, J. R. Guest, and N. P. Guisinger, "Epitaxial Graphene on Cu(111)", Nano Lett., **10**, 3512 (2010).

[100] D. R. Dreyer, R. S. Ruoff, and C. W. Bielawski, "From Conception to Realization : An Historial Account of Graphene and Some Perspectives for Its Future", Ang. Chem. Intern. Edition, **49**, 9336 (2010).

[101] O. C. Compton and S. T. Nguyen, "Graphene Oxide, Highly Reduced Graphene Oxide, and Graphene : Versatile Building Blocks for Carbon-Based Materials", Small, **6**, 711 (2010).

[102] C. Vallés, J. David Núñez, A. M. Benito, and W. K. Maser, "Flexible conductive graphene paper obtained by direct and gentle annealing of graphene oxide paper", Carbon, **50**, 835 (2012).

[103] I. Suarez-Martinez, N. Grobert, and C. P. Ewels, "Nomenclature of sp^2 carbon nanoforms", Carbon, **50**, 741 (2012).

[104] C. Lee, X. Wei, Q. Li, R. Carpick, J. W. Kysar, and J. Hone, "Elastic and frictional properties of graphene", Phys. Status Solidi B, **246**, 2562 (2009).

[105] Ph. Wagner, C. P. Ewels, V. V. Ivanovskaya, P. R. Briddon, A. Pateau, and B. Humbert, "Ripple edge engineering of graphene nanoribbons", Phys. Rev. B, **84**, 134110 (2011).

[106] A. A. Balandin, S. Ghosh, W. Bao, I. Calizo, D. Teweldebrhan, F. Miao, and C. N. Lau, "Superior Thermal Conductivity of Single-Layer Graphene", Nano Lett., **8**, 902 (2008).

[107] M. D. Stoller, S. Park, Y. Zhu, J. An, and R. S. Ruoff, "Graphene-Based Ultracapacitors", Nano Lett., **8**, 3498 (2008).

[108] C. Berger, Z. Song, T. Li, X. Li, A. Y. Ogbazghi, R. Feng, Z. Dai, A. N. Marchenkov, E. H. Conrad, P. N. First, and W. A. de Heer, "Ultrathin Epitaxial Graphite : 2D Electron Gas Properties and a Route toward Graphene-based Nanoelectronics", J. Phys. Chem. B, **108**, 19912 (2004).

[109] Y.-M. Lin, C. Dimitrakopoulos, K. A. Jenkins, D. B. Farmer, H.-Y. Chiu, A. Grill, and P. Avouris, "100-GHz Transistors from Wafer-Scale Epitaxial Graphene", Science, **327**, 662 (2010).

[110] F. Bonaccorso, Z. Sun, T. Hasan, and A. C. Ferrari, "Graphene photonics and optoelectronics", Nature Photonics, **4**, 611 (2010).

[111] J.-C. Charlier, X. Gonze, and J.-P. Michenaud, "Graphite Interplanar Bonding : Electronic Delocalization and van der Waals Interaction", Europhys. Lett., **28**, 403 (1994).

[112] D. Klein, "Graphitic polymer strips with edge states", Chem. Phys. Lett., **217**, 261 (1994).

[113] K. Nakada, M. Fujita, G. Dresselhaus, and M. S. Dresselhaus, "Edge state in graphene ribbons : Nanometer size effect and edge shape dependence", Phys. Rev. B, **54**, 17954 (1996).

[114] C. Girit, J. Meyer, R. Erni, M. Rossell, C. Kisielowski, L. Yang, C. Park, M. Crommie, M. Cohen, S. Louie, and A. Zettl, "Graphene at the edge : stability and dynamics", Science, **323**, 1705 (2009).

[115] K. Suenaga and M. Koshino, "Atom-by-atom spectroscopy at graphene edge", Nature, **468**, 1088 (2010).

[116] Y. Kobayashi, K. Fukui, T. Enoki, K. Kusakabe, and Y. Kaburagi, "Observation of zigzag and armchair edges of graphite using scanning tunneling microscopy and spectroscopy", Phys. Rev. B, **71**, 193406 (2005).

[117] Y. Kobayashi, K.-i. Fukui, T. Enoki, and K. Kusakabe, "Edge state on hydrogen-terminated graphite edges investigated by scanning tunneling microscopy", Phys. Rev. B, **73**, 125415 (2006).

[118] X. Jia, M. Hofmann, V. Meunier, B. G. Sumpter, J. Campos-Delgado, J. M. Romo-Herrera, H. Son, Y.-P. Hsieh, A. Reina, J. Kong, M. Terrones, and M. S. Dresselhaus, "Controlled Formation of Sharp Zigzag and Armchair Edges in Graphitic Nanoribbons", Science, **323**, 1701 (2009).

[119] J. Tian, H. Cao, W. Wu, Q. Yu, and Y. P. Chen, "Direct Imaging of Graphene Edges : Atomic Structure and Electronic Scattering", Nano Lett., **11**, 3663 (2011).

[120] T. Enoki, S. Fujii, and K. Takai, "Zigzag and armchair edges in graphene", Carbon, **50**, 3141 (2012).

[121] T. Wassmann, A. P. Seitsonen, A. M. Saitta, M. Lazzeri, and F. Mauri, "Structure, Stability, Edge States, and Aromaticity of Graphene Ribbons", Phys. Rev. Lett., **101**, 096402 (2008).

[122] C. K. Gan and D. J. Srolovitz, "First-principles study of graphene edge properties and flake shapes", Phys. Rev. B, **81**, 125445 (2010).

[123] L. Sun, P. Wei, J. Wei, S. Sanvito, and S. Hou, "From zigzag to armchair : the energetic stability, electronic and magnetic properties of chiral graphene nanoribbons with hydrogen-terminated edges", J. Phys. : Condens. Matter, **23**, 425301 (2011).

[124] P. Koskinen, S. Malola, and H. Häkkinen, "Self-Passivating Edge Reconstructions of Graphene", Phys. Rev. Lett., **101**, 115502 (2008).

[125] P. Koskinen, S. Malola, and H. Häkkinen, "Evidence for graphene edges beyond zigzag and armchair", Phys. Rev. B, **80**, 73401 (2009).

[126] M. Acik and Y. J. Chabal, "Nature of Graphene Edges : A Review", Jap. J. Appl. Phys., **50**, 070101 (2011).

[127] X. Jia, J. Campos-Delgado, M. Terrones, V. Meunier, and M. S. Dresselhaus, "Graphene edges : a review of their fabrication and characterization", Nanoscale, **3**, 86 (2011).

[128] M. Katsnelson and K. Novoselov, "Graphene : New bridge between condensed matter physics and quantum electrodynamics", Solid State Commun., **143**, 3 (2007).

[129] J. Berashevich and T. Chakraborty, "On the Nature of Interlayer Interactions in a System of Two Graphene Fragments", J. Phys. Chem. C, **115**, 24666 (2011).

[130] G. Li, A. Luican, and E. Y. Andrei, "Scanning Tunneling Spectroscopy of Graphene on Graphite", Phys. Rev. Lett., **102**, 176804 (2009).

[131] J. Hass, F. Varchon, J. E. Millán-Otoya, M. Sprinkle, N. Sharma, W. A. de Heer, C. Berger, P. N. First, L. Magaud, and E. H. Conrad, "Why Multilayer Graphene on 4H-SiC(0001^{-}) Behaves Like a Single Sheet of Graphene", Phys. Rev. Lett., **100**, 125504 (2008).

[132] J. M. B. Lopes dos Santos, N. M. R. Peres, and A. H. Castro Neto, "Graphene Bilayer with a Twist : Electronic Structure", Phys. Rev. Lett., **99**, 256802 (2007).

[133] F. Liu, P. Ming, and J. Li, "Ab initio calculation of ideal strength and phonon instability of graphene under tension", Phys. Rev. B, **76**, 064120 (2007).

[134] C. Lee, X. Wei, J. W. Kysar, and J. Hone, "Measurement of the Elastic Properties and Intrinsic Strength of Monolayer Graphene", Science, **321**, 385 (2008).

[135] I. G. Masters and K. E. Evans, “Models for the elastic deformation of honeycombs”, Composite Struc., **35**, 403 (1996).

[136] F. Scarpa, S. Adhikari, and A. Srikantha Phani, “Effective elastic mechanical properties of single layer graphene sheets”, Nanotechnology, **20**, 065709 (2009).

[137] H. Zhao, K. Min, and N. R. Aluru, “Size and Chirality Dependent Elastic Properties of Graphene Nanoribbons under Uniaxial Tension”, Nano Lett., **9**, 3012 (2009).

[138] L. Gong, R. J. Young, I. A. Kinloch, I. Riaz, R. Jalil, and K. S. Novoselov, “Optimizing the Reinforcement of Polymer-Based Nanocomposites by Graphene”, ACS Nano, **6**, 2086 (2012).

[139] L. Song, L. Ci, H. Lu, P. B. Sorokin, C. Jin, J. Ni, A. G. Kvashnin, D. G. Kvashnin, J. Lou, B. I. Yakobson, and P. M. Ajayan, “Large Scale Growth and Characterization of Atomic Hexagonal Boron Nitride Layers”, Nano Lett., **10**, 3209 (2010).

[140] S. Bertolazzi, J. Brivio, and A. Kis, “Stretching and Breaking of Ultrathin MoS2”, ACS Nano, **5**, 9703 (2011).

[141] A. Castellanos-Gomez, M. Poot, G. A. Steele, H. S. J. van der Zant, N. Agraït, and G. Rubio-Bollinger, “Elastic Properties of Freely Suspended MoS2 Nanosheets”, Adv. Mat., **24**, 772 (2012).

[142] C. Tao, L. Jiao, O. V. Yazyev, Y.-C. Chen, J. Feng, X. Zhang, R. B. Capaz, J. M. Tour, A. Zettl, S. G. Louie, H. Dai, and M. F. Crommie, “Spatially resolving edge states of chiral graphene nanoribbons”, Nature Phys., **7**, 616 (2011).

[143] F. Cervantes-Sodi, G. Csányi, S. Piscanec, and A. C. Ferrari, “Edge-functionalized and substitutionally doped graphene nanoribbons : Electronic and spin properties”, Phys. Rev. B, **77**, 165427 (2008).

[144] M. Ezawa, “Peculiar width dependence of the electronic properties of carbon nanoribbons”, Phys. Rev. B, **73**, 045432 (2006).

[145] M. Baldoni, A. Sgamellotti, and F. Mercuri, “Electronic properties and stability of graphene nanoribbons : An interpretation based on Clar sextet theory”, Chem. Phys. Lett., **464**, 202 (2008).

[146] T. Wassmann, A. P. Seitsonen, A. M. Saitta, M. Lazzeri, and F. Mauri, "Clar's Theory, π-Electron Distribution, and Geometry of Graphene Nanoribbons", J. Am. Chem. Soc., **132**, 3440 (2010).

[147] D. Prezzi, D. Varsano, A. Ruini, A. Marini, and E. Molinari, "Optical properties of graphene nanoribbons : The role of many-body effects", Phys. Rev. B, **77**, 041404 (2008).

[148] D. V. Kosynkin, A. L. Higginbotham, A. Sinitskii, J. R. Lomeda, A. Dimiev, B. K. Price, and J. M. Tour, "Longitudinal unzipping of carbon nanotubes to form graphene nanoribbons", Nature, **458**, 872 (2009).

[149] L. Jiao, X. Wang, G. Diankov, H. Wang, and H. Dai, "Facile synthesis of high-quality graphene nanoribbons", Nature Nanotech., **5**, 321 (2010).

[150] A. L. Elías, A. R. Botello-Méndez, D. Meneses-Rodríguez, V. Jehová González, D. Ramírez-González, L. Ci, E. Munoz-Sandoval, P. M. Ajayan, H. Terrones, and M. Terrones, "Longitudinal Cutting of Pure and Doped Carbon Nanotubes to Form Graphitic Nanoribbons Using Metal Clusters as Nanoscalpels", Nano Lett., **10**, 366 (2010).

[151] K. Kim, A. Sussman, and A. Zettl, "Graphene Nanoribbons Obtained by Electrically Unwrapping Carbon Nanotubes", ACS Nano, **4**, 1362 (2010).

[152] L. Xie, H. Wang, C. Jin, X. Wang, L. Jiao, K. Suenaga, and H. Dai, "Graphene Nanoribbons from Unzipped Carbon Nanotubes : Atomic Structures, Raman Spectroscopy, and Electrical Properties", J. Am. Chem. Soc., **133**, 10394 (2011).

[153] A. Fasoli, A. Colli, A. Lombardo, and A. C. Ferrari, "Fabrication of graphene nanoribbons via nanowire lithography", Phys. Status Solidi B, **246**, 2514 (2009).

[154] J. Bai, X. Duan, and Y. Huang, "Rational Fabrication of Graphene Nanoribbons Using a Nanowire Etch Mask", Nano Lett., **9**, 2083 (2009).

[155] H. Terrones, R. Lv, M. Terrones, and M. S. Dresselhaus, "The role of defects and doping in 2D graphene sheets and 1D nanoribbons", Rep. Prog. Phys., **75**, 062501 (2012).

[156] M. Terrones, A. R. Botello-Méndez, J. Campos-Delgado, F. López-Urías, Y. I. Vega-Cantú, F. J. Rodríguez-Macías, A. L. Elías, E. Munoz-Sandoval, A. G. Cano-Márquez, J.-C. Charlier, and H. Terrones, "Graphene and graphite nanoribbons : Morphology, properties, synthesis, defects and applications", Nano Today, **5**, 351 (2010).

[157] Z. Chen, Y. Lin, M. J. Rooks, and P. Avouris, "Graphene nano-ribbon electronics", Physica E, **40**, 228 (2007).

[158] L. Yang, M. L. Cohen, and S. G. Louie, "Excitonic Effects in the Optical Spectra of Graphene Nanoribbons", Nano Lett., **7**, 3112 (2007).

[159] V. Ryzhii, V. Mitin, M. Ryzhii, N. Ryabova, and T. Otsuji, "Device Model for Graphene Nanoribbon Phototransistor", Appl. Phys. Express, **1**, 063002 (2008).

[160] Q. Su, S. Pang, V. Alijani, C. Li, X. Feng, and K. Mullen, "Composites of Graphene with Large Aromatic Molecules", Adv. Mater., **21**, 3191 (2009).

[161] Y. Yoon and J. Guo, "Effect of edge roughness in graphene nanoribbon transistors", Appl. Phys. Lett., **91**, 073103 (2007).

[162] D. Cochin, M. Passmann, G. Wilbert, R. Zentel, E. Wischerhoff, and A. Laschewsky, "Layered Nanostructures with LC-Polymers, Polyelectrolytes, and Inorganics", Macromolecules, **30**, 4775 (1997).

[163] D. W. Kim, J. Kumar, and A. Blumstein, "Ordered assembly of conjugated ionic polyacetylenes within clay nanoplatelets : layer-by-layer assembly and intercalative polymerization", Appl. Clay Sci., **30**, 134 (2005).

[164] J. N. Coleman, M. Lotya, A. O'Neill, S. D. Bergin, P. J. King, U. Khan, K. Young, A. Gaucher, S. De, R. J. Smith, I. V. Shvets, S. K. Arora, G. Stanton, H. Kim, K. Lee, G. T. Kim, G. S. Duesberg, T. Hallam, J. J. Boland, J. J. Wang, J. F. Donegan, J. C. Grunlan, G. Moriarty, A. Shmeliov, R. J. Nicholls, J. M. Perkins, E. M. Grieveson, K. Theuwissen, D. W. McComb, P. D. Nellist, and V. Nicolosi, "Two-Dimensional Nanosheets Produced by Liquid Exfoliation of Layered Materials", Science, **331**, 568 (2011).

[165] H. Manzano, A. N. Enyashin, J. S. Dolado, A. Ayuela, J. Frenzel, and G. Seifert, "Do Cement Nanotubes exist ?", Adv. Mater., **24**, 3239 (2012).

[166] A. H. C. Neto and K. Novoselov, “New directions in science and technology : two-dimensional crystals”, Rep. Prog. Phys., **74**, 082501 (2011).

[167] C. R. Dean, A. F. Young, I. Meric, C. Lee, L. Wang, S. Sorgenfrei, K. Watanabe, T. Taniguchi, P. Kim, K. L. Shepard, and J. Hone, “Boron nitride substrates for high-quality graphene electronics”, Nature Nanotech., **5**, 722 (2010).

[168] J. Li and V. B. Shenoy, “Graphene quantum dots embedded in hexagonal boron nitride sheets”, Appl. Phys. Lett., **98**, 013105 (2011).

UNIVERSITÉ DE NANTES

Ab initio modelling of graphene

Philipp Wagner

THÈSE DE DOCTORAT

April 2013

Université de Nantes, France

Institut des Matériaux Jean Rouxel (IMN), CNRS UMR 6502

Declaration

I hereby declare that this thesis has not been and will not be submitted in whole or in part to another University for the award of any other degree. I certify that all material in this thesis which is not my own work has been identified.

Philipp Wagner

April, 2013

Abstract

In this thesis graphene and related nanostructures were studied, using density functional *ab initio* modelling techniques.

The influence of different edge terminations has been investigated for typical pristine graphene edges (armchair, zigzag and Klein) and several reconstructed edge configurations. For unterminated graphene edges a new stable folded back edge has been identified, creating a nanotube along the graphene edge. A systematic study of hydrogenated edges was performed, and new favourable reconstructed Klein edge configurations were found. Furthermore hydrogenated edges are expected to play an important role for graphene growth processes, and thus possible adapted growth models via carbon dimer addition are proposed.

Next more complex edge functionalisations such as hydroxylated (-OH) edges were studied, in particular modelling thin 4 - 25 Å wide armchair graphene nanoribbons. Notably the influence on structural, electronic, chemical and mechanical properties has been investigated. This promises new routes towards controlled design of specific nanoribbon properties.

Finally the in-plane Young's modulus of various nanosheets (including graphene, BN, MoS_2, $MoTe_2$ etc.) were calculated. In this context a new geometry independent volume definition for nanoobjects has been developed, based on the average electron density. This new approach offers a transferable underlying framework to calculate the Young's modulus, and thus values correctly extrapolate for example between graphene, carbon nanotubes and bulk graphite. The concept was further extended to organic polymers.

List of Publications

1. Hydrogenated Klein and reconstructed Klein graphene edges
   Ph. Wagner, C. P. Ewels, V. V. Ivanovskaya, P. R. Briddon, B. Humbert,
   in preparation

2. Mechanical properties of nanosheets and nanotubes investigated using
   a new geometry independent volume definition,
   Ph. Wagner, V. V. Ivanovskaya, M. J. Rayson, P. R. Briddon, C. P. Ewels,
   J. Phys.: Condens. Matter 25, 155302, 2013

3. Graphene edge structures: Folding, scrolling, tubing, rippling and twisting,
   V. V. Ivanovskaya, **Ph. Wagner**, A. Zobelli, I. Suarez-Martinez, A. Yaya, C. P. Ewels,
   Springer book series "Carbon Nanostructures", GraphITA 2011, 75-85, 2012

4. A comparative study of density functional and density functional tight binding
   calculations of defects in graphene,
   A. Zobelli, V. Ivanovskaya, **Ph. Wagner**, I. Suarez-Martinez, A. Yaya, C. P. Ewels,
   Phys. Status Solidi B 249, 276-282, 2012

5. Ripple edge engineering of graphene nanoribbons,
   Ph. Wagner, C. P. Ewels, V. V. Ivanovskaya, P. R. Briddon, A. Pateau, B. Humbert,
   Phys. Rev. B 84, 134110, 2011

6. Low-Energy Termination of Graphene Edges via the Formation of
   Narrow Nanotubes,
   V. V. Ivanovskaya, A. Zobelli, **Ph. Wagner**, M. Heggie, P. R. Briddon, M. J. Rayson,
   C. P. Ewels,
   Phys. Rev. Lett. 107, 065502, 2011

7. Tetrahedral Chalcopyrite Quantum Dots for Solar-Cell Applications,
   J. Ojajärvi, E. Räsänen, S. Sadewasser, S. Lehmann, **Ph. Wagner**,
   M. Ch. Lux-Steiner,
   Appl. Phys. Lett. 99, 111907, 2011

8. Purification of single-walled carbon nanotubes,
   A. Yaya, C. P. Ewels, **Ph. Wagner**, I. Suarez-Martinez, A. G. Tekley, L. R. Jensen,
   EPJ AP 54, 10401, 2011

9. Behavior of hydrogen ions, atoms, and molecules in α-boron studied using density functional calculations,
   Ph. Wagner, C. P. Ewels, I. Suarez-Martinez, V. Guiot, S. F. J. Cox, J. S. Lord, P. R. Briddon,
   Phys. Rev. B 83, 024101, 2011

10. Bromination of graphene and graphite,
    A. Yaya, C. P. Ewels, I. Suarez-Martinez, **Ph. Wagner**, S. Lefrant, A. Okotrub, L. Bulusheva, P. R. Briddon,
    Phys. Rev. B 83, 045411, 2011

11. Structure and vibrational properties of oxohalides of vanadium,
    V. Guiot, I. Suarez-Martinez, **Ph. Wagner**, J. Goss, P. Briddon, A. W. Allaf, C. P. Ewels,
    Inorg. Chem. 48, 3660-3666, 2009

12. Muonium in boron,
    S. F. J. Cox, J. S. Lord, A. D. Hillier, S. P. Cottrell, **Ph. Wagner**, C. P. Ewels,
    Physica B 404, 841-844, 2009

Publications 2, 3, 4, 5 and 6 are partly directly quoted in the thesis.

During the thesis I participated at 14 international conferences and workshops, with 7 oral presentations and 7 poster contributions. Further I participated twice at the "Journées de l'Ecole Doctorale 3MPL", 2011 in Le Mans and 2012 in Nantes, and won 2011 the Poster prize for the best poster and poster presentation.

Acknowledgements

I would like to thank the french ANR project “NANOSIM-GRAPHENE” for funding my thesis. The CNRS Institut des Matériaux Jeau Rouxel (IMN) and the Université de Nantes I would like to thank for making this work possible, and for providing such a positive, friendly and well organized environment.

Special thanks to my supervisor Chris Ewels. With all his time, encouragement, support and never ending enthusiasm he made this three years during my thesis in Nantes very exciting, humorous and very fruitful. I had the chance to learn and work on an interesting, modern and fast developing topic. Furthermore I was able to travel and meet many great and interesting researchers and PhD students all over Europe. I’m also very thankful and appreciate a lot Chris’s constant efforts making conferences and workshops possible, from the first day on.

Many thanks go also to Bernard Humbert, my co-supervisor, for his open ear at any moment and his useful and positive advice during the whole time. I further much appreciated having Olivier Chauvet and Irene Suárez-Martínez as members of my "comité de suivi de thèse".

Also thanks to all the members of the PMN group, and everyone from the other IMN groups for the friendly, helpful and supportive atmosphere. Especially I would like to thank all current and former PhD students of the IMN, for the warm welcome, all the science discussions, unforgettable evenings, and the pétanque and football matches in Nantes during the last three years.

I had further the privilege and pleasure to work, discuss or meet with Abu, Vika, Jean-Jo, Alberto, Patrick, John, Malcolm, Irene, Greg and the Brussels guys, Wolfgang and his "gang" from Zaragossa, Vojislav and his group from Dublin, Alain and his group from Bordeaux and Nicole with her students from Oxford. I felt the international research community added many positive, chummy, creative, propulsive and unforgettable moments and influences to my PhD time.

Finally many thanks for all their support to my parents, my brother, my girlfriend with her family and all friends. Even if they often hadn't got a clue what I was talking about, when asking me what I'm "really" doing.

"Men love to wonder, and that is the seed of science."
Ralph Waldo Emerson

Contents

List of Figures

List of Tables

Abbreviations and Symbols

DFT	Density Functional Theory
LDA	Local Density Approximation
GGA	Generalized Gradient Approximation
TB	Tight Binding
SCC	Self Consistency Cycle
AIMPRO	Ab Initio Modelling Program
NT	Nanotube
CNT	Carbon Nanotube
SWCNT	Single-Wall Carbon Nanotube
MWCNT	Multi-Wall Carbon Nanotube
ACNT	Armchair Carbon Nanotube
ZCNT	Zigzag Carbon Nanotube
GNR	Graphene Nanoribbon
AGNR	Armchair Graphene Nanoribbon
ZGNR	Zigzag Graphene Nanoribbon
CGNR	Chiral Graphene Nanoribbon
RKGNR	Reconstructed Klein Graphene Nanoribbon
GO	Graphene Oxide
r-GO	Reduced Graphene Oxide

SPM	Scanning Probe Microscope
TEM	Transmission Electron Microscope
SEM	Scanning Electron Microscope
STM	Scanning Tunnelling Microscope
STS	Scanning Tunnelling Spectroscopy
AFM	Atomic Force Microscope
MBE	Molecular Beam Epitaxy
CVD	Chemical Vapor Deposition
PVD	Physical Vapor Deposition
UHV	Ultra High Vacuum
MOSFET	Metal Oxide Semiconductor Field Effect Transistor
CMOS	Complementary Metal Oxide Semiconductor
PMOS	p-channel Metal Oxide Semiconductor

RT	Room Temperature
BZ	Brillouin Zone
DOS	Density of States
FM	Ferromagnetic
AFM	Anti-Ferromagnetic
NM	Non-Magnetic
HOMO	Highest Occupied Molecular Orbital
LUMO	Lowest Unoccupied Molecular Orbital
a.u.	atomic units
Ha	Hartree energy (atomic units)
a_0	Bohr radius (atomic units), lattice parameter
SL	single-layer
BL	bi-layer
TL	tri-layer

e	elementary charge
m_e	electron mass
h	Planck constant
$\hbar = h/(2\pi)$	reduced Planck constant
$\hat{H}$	Hamiltonian operator
Ψ	wavefunction
n	charge density
ρ	average charge density
E	energy, Young's modulus
B	bulk modulus
G	shear modulus
T	kinetic energy
U, E	internal system energy
F	force
P	pressure
$V(\vec{r})$, V_{XC}, V_{x-y}	potentials
V, V_{BZ}	volumes
μ	charge carrier mobility, chemical potential
K	thermal conductivity
E_{tot}	total energy
E_{form}	formation energy
ϵ	strain
ν	Poisson's ratio
μ_B	Bohr magneton
v_F	Fermi velocity

Chapter 1

Introduction

Today nanotechnology is present in many situations in modern day life. We use mobile telephones and portable computers everyday, and have become used to 3D computer games with realistic graphics and communicate via email or video using the internet. This is only possible because in the 20th century the semiconductor material silicon has been intensively studied. This enabled profitable manufacturing of silicon based (integrated) electronic circuits composed of electronically connected transistors, resistors, capacitor or diodes. Computers, portable telephones (smartphones), tablets, TVs, cars, aircrafts, Si-photovoltaic applications, digital photo cameras, different sorts of detectors or medical systems are all using silicon based electronics, thus computer chips. This growing intense influence of electronic devices in modern life has created over the last 30 years a huge silicon market and industry, with a total revenue in 2012 of about 300 billion US dollars.

The history of modern computer chips started in 1958 by Jack S. Kilby [1] with the invention of the "Integrated Circuit" in a lab at Texas Instruments, USA. It took until 1971 when Intel made the first commercial available Si-based computer chips using a PMOS-technology and transistors with 10 μm gate-length (2300 transistors on one chip). Commercial Si-based chips are (mass-) produced using silicon wafers, highly pure and nearly defect free single crystalline silicon discs with diameter up to 450 mm ("18 inch") and thickness up to 925 μm [2, 3]. On the wafers many integrated circuits are produced in parallel and the wafers are cut afterwards

[4]. Today powerful chips can contain several billion transistors. In 2012 the most advanced chips were routinely produced using a CMOS-technology with 22 nm gate-length, and roadmaps for chips with gate-lengths down to less than 10 nm are sighted [5, 6]. While near 5 nm the physical limits of silicon based chips will be reached, in the same time new materials such as Si-nanowires, carbon nanotubes and graphene are promising candidates for future integrated circuits [6]. For the Si-nanowires some known processing techniques can be adopted, and this favours these structures to follow today's chip architectures. But a real performance boost for new future computer chips is predicted when integrating carbon materials such as carbon nanotubes or graphene.

21st century technology will be very probably dominated by new carbon nanomaterials, such as fullerenes, carbon nanotubes (CNTs) and graphene [7], leading to new high performance electric circuits, stronger, more intelligent materials and composites, and new bio-electronic systems, mentioning only a few of the great possibilities offered by these materials [8]. To realise these goals, big investments have been made in the field of nanotechnology research, as besides developing the new carbon nanomaterials themselves, new efficient production methods have to be established. Regarding the huge and still increasing 300 billion dollar market (2012) for Si-based electronics, the future perspective is very good for graphene (and related carbon materials) to enter this market [7].

Besides electronics, carbon nanomaterials can also be used to remove heat or to mechanically support composite materials. An early example are polymer-CNT composites [9, 10] and also polymer-graphene materials have been investigated [11, 12]. These multiple possibilities are a main advantage compared to other materials, and offer many different applications. Additionally it has to be reminded that the element carbon is very common on earth and thus prices are more independent than for rare elements used in *e.g.* III-V semiconductors such as indium, gallium or arsenic.

Today most big technology companies are already investing, in the field of carbon nanomaterial research. At the same time, industry is still very interested in the fun-

damental understanding of the underlying physics and chemistry of these materials [7]. Especially recently, graphene has become popular as a subject of fundamental study at Universities and Research Laboratories worldwide, while parallel research into carbon nanotubes and fullerenes is ongoing.

Both of these currently favoured carbon nanomaterials are rather new: CNTs were discovered in 1991 [13] and free-standing graphene first investigated in 2004 [14]. This already shows the extreme fast dynamics in the ongoing innovation cycles launched based on graphene, given that the material was first experimentally fabricated only 9 years ago. Another big step forward for the today hyped "miracle material" graphene has been with no doubt as well the Noble Prize in Physics for Andre Geim and Konstantin Novoselov from the University of Manchester in 2010 [15]. They were honoured for their fundamental work on graphene, showing experimentally for the first time the great potential regarding electronic, thermal, optical and mechanical properties of graphene. The properties of graphene can lead theoretically to far superior device performances than it is possible with materials in use today such as graphite, silicon or copper. An overview comparing these materials is given in Table 1.1.

Graphene - the nanomaterial of the 21st century?

The nanomaterial graphene is a single, only one atom thick layer, with carbon atoms arranged in a two-dimensional (2D) honeycomb lattice. When wrapping this unique structure carbon nanotubes (1D) and fullerenes (0D) can be created, while stacking the layers leads to graphite (3D). Therefore graphene can be seen as the "mother" material for all graphitic carbon materials [16].
To distinguish between 2D materials and 3D materials, one can consider up to 10 stacked graphene layers as still essentially 2D materials [16–18]. Thus these materials are named in the following thesis (single-layer) graphene, bi-layer graphene, tri-layer graphene etc.

	Graphene	Graphite	Silicon	Copper
Dimensions	2D	3D	3D	3D
	(thickness $\approx$ 3.3 Å)	(bulk)	(bulk)	(bulk)
Density ρ at RT (g cm^{-3})	$\sim$ 2.25	2.27	2.33	8.95
Melting point (K)	-	3925 **	1683	1358
Young's modulus E (TPa)	1.06	0.35 - 1.06 *	0.13 - 0.18	0.11 - 0.13
Poisson's ratio ν	0.0 / 0.2 *	0.0 / 0.2 *	0.2 - 0.3	$\sim$ 0.34
Thermal conductivity K (W m^{-1} K^{-1})	$\sim$ 5000	25 - 1000 *	$\sim$ 150	$\sim$ 400
Electron mobility μ (cm^2 V^{-1} s^{-1})	5000 - > 200,000	3 - 15,000 *	$\leq$ 1400	$\sim$ 20,000
Resistivity at RT (Ω m)	$\sim 1 \cdot 10^{-8}$	$3 \cdot 10^{-6}$ - $3 \cdot 10^{-3}$ *	$\sim 6.4 \cdot 10^{2}$	$\sim 1.7 \cdot 10^{-8}$
Bandgap (eV)	-	-	1.12	-
	(semimetal)	(semimetal)	(semiconductor)	(metal)

*: Note that graphene and graphite are strongly anisotropic, *e.g.* perpendicular and parallel to the basal plane(s).

**: Direct sublimation.

Table 1.1: Summary of the basic properties of graphene, graphite, crystalline silicon and crystalline copper. (Most values for graphite, silicon and copper can be found in standard literature [19–24]. For graphene please see [8, 12, 16, 25–29] and also Chapter 3.)

The electronic properties of graphene are exceptional. For many decades the materials has been the subject of theoretical studies [30–32], often described using terms such as “2D graphite”. Pristine, defect-free single-layer graphene is a semimetal (also described as semiconductor with zero bandgap) and thus does not show a energy gap in the band structure. The region in the electronic band structure around the Fermi level at the K-point is of particular interest, as here the valence and conduction band cross linearly, forming a so called “Dirac cone”. While electrons are normally described with the Schrödinger equation, this linearity of the bands means that electrons in this region are described through the relativistic Dirac equation and thus represent relativistic quasiparticles, so called massless Dirac fermions [16]. In other words, near the Fermi level (at the K-point) the electrons move like massless particles with a speed of $v_F \approx 10^6$ m/s (Fermi velocity) in the graphene lattice. These properties of graphene were confirmed experimentally in 2004 by Novoselov *et al.* [14], nearly 60 years after their theoretical prediction, as extremely high carrier mobilities have been measured. Electron mobility μ values over 200,000 $cm^2\ V^{-1}\ s^{-1}$ were measured for free-standing single-layer graphene in follow up studies [33], approaching ballistic transport behaviour [34]. Further a Quantum Hall effect behaviour was induced applying an external magnetic field [35].

Paired with a high in-plane Young’s modulus of 1.06 TPa and an extraordinarily high thermal conductivity of $\sim 5000\ W\ m^{-1}\ K^{-1}$ graphene is predestined for the next generation of electronic circuits and devices. Even low defect densities in the graphene plane do not strongly influencing the Dirac fermions due to the Klein-Paradox [36] and therefore do not significantly degrade the electronic properties.

For electronic applications with on-off characteristics, such as field effect transistors in computer chips, a moderate bandgap is normally needed. To achieve this the intrinsic graphene properties have to be modified or redesigned. One possibility to introduce a bandgap is tailoring graphene into thin strips, so called graphene nanoribbons (GNRs). Here, a quantum confinement parallel to the ribbon reduces the dimensions to a 1D object. Dependent on the edge properties and ribbon thick-

ness a significant bandgap opening has been predicted for narrow ribbons (< 20 Å) [37, 38]. Various routes to produce GNRs were proposed and realized in recent years, including unzipping carbon nanotubes [39], cutting graphene with an electron beam [40] or molecular bottom-up self-assembling of organic precursors [41]. While ribbon width plays a crucial role, to date only atomically precise armchair GNRs of width 7 ($\sim$ 7.3 Å, see also Chapter 3) have been successfully reproduced, showing a bandgap around 2.3 eV on Au(111) [42]. While the growth of GNRs is very complex, ways to change the electronic properties keeping one precise ribbon width are becoming increasingly interesting.
Prior to this thesis, calculations to date on GNRs in the literature had not yet sufficiently studied the edge properties of GNRs and of graphene sheets in general. Graphene edges are chemically more reactive than the flat 2D honeycomb lattice due to dangling bonds, and thus offer an accessible and hopefully good controllable way to design the electronic properties of GNRs.

Objectives of the thesis

The primary aim of this thesis was to investigate systematically the behaviour of graphene and graphene edge properties for different possible shaped edges (armchair, zigzag, chiral and Klein edges, including several reconstructed edge configurations), combined with various realistic edge termination groups. Furthermore mechanical properties of nanosheets, nanotubes and organic polymers have been studied, using on a new developed volume concept.

I modelled these systems using calculations based on density functional theory within the local density approximation, as implemented in the *AIMPRO* code. A brief description of the important basic underlying theoretical concepts is given in Chapter 2, including details relevant for the *AIMPRO* code.
Chapter 3 gives an overview of recent developments and investigations in the field of carbon research. All for this thesis important carbon allotropes are described, including in detail graphene and graphene nanoribbons.

In Chapter 4 of this manuscript I describe the systematic investigation of unterminated and hydrogenated graphene edges configurations. Surprisingly, in this very general study, some new stable graphene edge configurations were identified, for example the "tubed" edges or the hydrogenated reconstructed Klein edge.

In Chapter 5, I focus on thin armchair graphene nanoribbons, and explore the effect of attaching different functional groups such as monoatomic -F, -Cl and -Br groups and further complex functional groups such as -OH and -SH groups. Special attention was given to the case study of -OH terminated armchair GNRs in a width range from 4 - 25 Å, investigated in detail. Here the influence of the different edge terminations on the properties of the armchair graphene nanoribbons were studied, including structural, electronic, chemical and mechanical properties.

Finally in Chapter 6, mechanical properties such as the Young's modulus and the Poisson's ratio were calculated for infinite graphene and related nanosheets, armchair GNRs, carbon nanotubes and relevant common organic conjugated polymers. Notably a new concept to define the volume independent of a given nanoobject geometry for such surface dominated nanostructures was developed and successfully applied.

A short conclusion and an outlook deliberating on the work done in this thesis can be read in Chapter 7.

Chapter 2

Theoretical background

This chapter introduces the theoretical background to understand the kind of calculations performed in this thesis. The first sections discuss very fundamental concepts starting from the Schrödinger equation, and further explaining basic solutions and useful approximations. The second half is more focused on applied concepts implemented in the used *ab initio AIMPRO* code. Still more details about Density Functional Theory based calculations are discussed, but more linked to the type of calculations made in this thesis. Regarding that today a lot different literature is available introducing in deep and very detailed to Density Functional Theory based modelling [43–48]; this chapter aims to give the reader a brief overview on fundamental concepts and theorems to be able understanding the further chapters, and the calculations done therein.

2.1 The Schrödinger equation

Classical mechanics based on Newton's equation of motion $\vec{F} = m\vec{a}$ (Newton's second law) can be used to describe the movement of macroscopic mechanical systems. For molecular, atomic and subatomic systems (with dimensions of typically less than 100 nm) the classical approach is not sufficient and a quantum mechanical description is necessary. Based on quantum mechanics, mainly established in the first half of 20th century [49], the *time-dependent Schrödinger equation* (2.1) can be formulated [50, 51], comparable to Newton's equation of motion in classical mechanics. The Schrödinger equation uses the wavefunction Ψ and the Hamiltonian operator $\hat{H}$ to describe a defined system.

$$i\hbar\frac{\delta}{\delta t}\Psi(\vec{r},t) = \hat{H}\Psi(\vec{r},t) \tag{2.1}$$

If the Hamiltonian operator $\hat{H}$ is not explicitly time dependent, the wavefunction $\Psi(\vec{r},t)$ is separable and can be written as $\Psi(\vec{r},t) = \Psi(\vec{r})e^{-iEt/\hbar}$, leading to the *time-independent Schrödinger equation* (2.2). Solving this equation gives the energy eigenstate state of the system with eigenvalue E, the energy.

$$E\Psi(\vec{r}) = \hat{H}\Psi(\vec{r}) \tag{2.2}$$

Using the concept of the wavefunction as variable to describe a system an analytical solution of (2.2) can be found for systems with only one electron, *e.g.* the hydrogen atom. For the case of a *non-relativistic single particle* the *time-independent Schrödinger equation* (2.2) can be written for as follow:

$$E\Psi(\vec{r}) = \left(\frac{-\hbar^2}{2m}\nabla^2 + V(\vec{r})\right)\Psi(\vec{r})\ . \tag{2.3}$$

An example of (2.3) could be a single electron moving in an electric field. For more complex systems the Schrödinger equation becomes insoluble, in other words a many-body problem, and approximations have to be made.

2.2 The Born-Oppenheimer approximation

To tackle the problem of the insolubility for many electron/nuclei systems of the non-relativistic time-independent Schrödinger equation, we have to describe in more detail the Hamiltonian operator $\hat{H}$. First, we can rewrite $\hat{H}$ in terms for electrons (e) and nuclei (n), to separate the kinetic energy terms (T) and electrostatic interactions (V) between charged particles. Considering a system with N electrons with mass m_e and M nuclei with mass M and charge Z, $\hat{H}$ can be expressed as follows:

$$\begin{aligned} \hat{H} &= T_e + T_n + V_{e-n} + V_{n-n} + V_{e-e} \\ &= -\frac{\hbar^2}{2m_e}\sum_i \nabla_i^2 - \frac{\hbar^2}{2}\sum_A \frac{1}{M_A}\nabla_A^2 - \frac{e^2}{4\pi\epsilon_0}\sum_{i,A}\frac{Z_A}{r_{iA}} + \frac{e^2}{4\pi\epsilon_0}\sum_{A<B}\frac{Z_A Z_B}{r_{AB}} + \frac{e^2}{4\pi\epsilon_0}\sum_{i<j}\frac{1}{r_{ij}} \,. \end{aligned} \tag{2.4}$$

Here the labels i, j refer to electrons and respectively A, B to nuclei, at sites $\vec{r}_x$ and distances $r_{xy} = |\vec{r}_x - \vec{r}_y|$. We always sum over the total number of electrons N, respectively the total number of nuclei M (a sum with two indices can also be written as two nested sums (*e.g.* $\sum_{A<B} = \sum_{A=1}^{M}\sum_{B>A}^{M}$)).

Regarding the movement of electrons and nuclei, now we can first assume that they are decoupled. This is a reasonable approach as the electrons move much faster compared to nuclei as a consequence of the much larger nuclear masses ($M >> m$). The *Born-Oppenheimer approximation* now considers the nuclei to be static (adding a constant potential) [52], while electrons move and react instantly on the time scale seen by a nuclei. Therefore the kinetic energy of the nuclei is zero ($T_n = 0$) and the nuclei-nuclei interaction is constant ($V_{n-n} = const.$). This leads to a reduced Hamiltonian operator $\hat{H}_{BO}$:

$$\begin{aligned} \hat{H}_{BO} &= T_e + V_{e-n} + V_{e-e} \\ &= -\frac{\hbar^2}{2m_e}\sum_i \nabla_i^2 - \frac{e^2}{4\pi\epsilon_0}\sum_{i,A}\frac{Z_A}{r_{iA}} + \frac{e^2}{4\pi\epsilon_0}\sum_{i<j}\frac{1}{r_{ij}} \,. \end{aligned} \tag{2.5}$$

The non-relativistic time-independent Schrödinger equation with this reduced Hamiltonian operator $\hat{H}_{BO}$ is unfortunately still analytically not solvable as the motion of the electrons is strongly correlated with the electrostatic electron-electron interaction V_{e-e}.

2.3 Electron-Electron interaction

The electron-electron interactions are difficult to treat, as these are strongly coupled with the motion of all electrons and therefore presents a many-body problem. Considering a uniform electron gas of N electrons with each the elementary charge e, we can calculate the average charge density $\rho = (N \cdot e)/V$ in a defined volume V. But there is also repulsive interaction between electrons resulting from the same negative charge state. Secondly, the spin interaction has to be taken into account following the Pauli exclusion principle, stating that electrons with parallel spin avoid each others and electrons with inverse spin can occupy the same energy state. This underlying effects lead to a changing local charge density $n(\vec{r})$ for real systems.

2.3.1 The Hartree and Hartree-Fock method

One early approach to handle the problem of electron-electron interaction is the *Hartree method*. First the wavefunction Ψ of the whole system can be considered as the product of all single electron wavefunctions Ψ_λ, including the spin s:

$$\Psi(\vec{r}_1 s_1, \vec{r}_2 s_2, ...\vec{r}_N s_N) = \Psi_1(\vec{r}_1 s_1)\Psi_2(\vec{r}_2 s_2)...\Psi_N(\vec{r}_N s_N) \tag{2.6}$$

The non-relativistic time-independent Schrödinger equation can now be written for every single electron (in the following *atomic units* (a.u.) are used, simplifying $m_e = e = \hbar = 4\pi\epsilon_0 \equiv 1$):

$$\begin{aligned} E\Psi_\lambda &= \hat{H}\Psi_\lambda \,, \\ E\Psi_\lambda(\vec{r}) &= \left(-\frac{1}{2}\nabla^2 + V(\vec{r})\right)\Psi_\lambda(\vec{r}) \,. \end{aligned} \tag{2.7}$$

Further Hartree proposed to replace the potential $V(\vec{r})$ with a effective potential $V_{eff}(\vec{r})$ which directly includes the mean electrostatic potential from all electrons [53].

$$V_{eff}(\vec{r}) = V_{ext}(\vec{r}) + \int \frac{n(\vec{r}^{\,\prime})}{|\vec{r} - \vec{r}^{\,\prime}|} dr^{\prime} \tag{2.8}$$

$V_{ext}(\vec{r})$ is the external potential, mostly likely the Coulomb interaction of electrons and nuclei, but can also include for example electrical fields in the background. This leads to a new form of the Schrödinger equation using (2.7) and (2.8):

$$E\Psi_\lambda(\vec{r}) \;=\; \left(-\frac{1}{2}\nabla^2 + V_{ext}(\vec{r}) + \int \frac{n(\vec{r}^{\,\prime})}{|\vec{r}-\vec{r}^{\,\prime}|}dr^{\prime}\right)\Psi_\lambda(\vec{r})\;. \tag{2.9}$$

But still the Pauli principle is not satisfied, as there is nothing to stop more than one electron from occupying an energy state. To improve the influence of electron exchange the many-body electronic wavefunction can be expressed via the *Hartee-Fock theory* in a Slater determinant [54, 55]. Here the spin is taken into account. As one of the first solutions of the Schrödinger equation, the *Hartree-Fock method* is a good first approximation and useful for many different systems.
Still there is a lack of electron correlation and therefore causes problems in metallic systems, or shows a strong over estimation of the bandgap in semiconductors. Another critical parameter is the scaling of the calculation size, which limits this approach to smaller systems.
One approach to include the electron correlation is used in Density Functional Theory (DFT), building on the Hohenberg-Kohn theorem and the Kohn-Sham equations explained in the following sections and building the underlying fundamentals for all calculations in this thesis.

2.4 Density Functional Theory

2.4.1 The Hohenberg-Kohn theorem

The Hohenberg-Kohn theorem [56] has given the fundamental basis for DFT:

The ground state of a defined system can be completely described using the charge density $n(\vec{r})$, equivalent to the description with a non-degenerate non-polarised ground state wavefunction $\Psi(\vec{r})$.

To make the proof we can write the Hamiltonian $\hat{H}$ for N spinless electrons in a external potential V_{ext}, normally the Coulomb interaction with the nuclei:

$$\hat{H} = T_e + V_{e-e} + V_{ext} \; . \tag{2.10}$$

In (2.10) T gives the kinetic energy and V_{e-e} the electron-electron interaction, and the Born-Oppenheimer approximation has been used. The charge density $n(\vec{r})$ can be written as

$$n(\vec{r}) = N \int |\Psi(\vec{r}, \vec{r}_2, ...\vec{r}_N)|^2 d\vec{r}_2 ... d\vec{r}_N \; . \tag{2.11}$$

We can consider now a second Hamiltonian $\hat{H}^{'}$ with a different external potential $V_{ext}^{'}$, where $V_{ext} - V_{ext}^{'} \neq const.$, and the ground state wavefunction $\Psi^{'}$. If we now assume that the ground state charge densities for both Hamiltonians are equal $n(V_{ext}) = n^{'}(V_{ext'})$ we get the following inequality:

$$E^{'} = \langle \Psi^{'} | \hat{H}^{'} | \Psi^{'} \rangle < \langle \Psi | \hat{H}^{'} | \Psi \rangle = \langle \Psi | \hat{H} + V_{ext}^{'} - V_{ext} | \Psi \rangle \tag{2.12}$$

$$E^{'} < E + \int (V_{ext}^{'}(\vec{r}) - V_{ext}(\vec{r})) n(\vec{r}) d\vec{r} \, . \tag{2.13}$$

However, this expression is equally valid for E,

$$E < E^{'} + \int (V_{ext}(\vec{r}) - V_{ext}^{'}(\vec{r})) n(\vec{r}) d\vec{r} \, . \tag{2.14}$$

This leads to a contradiction when adding (2.13) and (2.14):

$$E^{'} + E < E + E^{'}. \tag{2.15}$$

As the energies are discrete values for the ground states, (2.15) is wrong. This shows as *reductio ad absurdum* that our assumption of the same charge densities $n(V_{ext}) = n^{'}(V_{ext'})$ for two different ground state wavefunctions Ψ and $\Psi^{'}$ cannot exist. *Only a single and specific external potential V_{ext} can give rise to a system charge density $n(\vec{r})$ (Hohenberg-Kohn theorem)*, and therefore $n(\vec{r})$ contains all the information about the system, equivalent to the ground state wavefunction Ψ. This has reduced now the many-body problem of N electrons of the order of $4N$ for the Schrödinger equation to 3 Cartesian coordinates variables ($\vec{r}$), plus the spin state. Secondly, it makes now bigger systems computational less costly, a key argument regarding the big success of the DFT approach in theoretical solid state physics. Using the charge density as variable to characterise a system we need in addition the Kohn-Sham equations, which offer a iterative way to solve the problem.

2.4.2 The Kohn-Sham equations

To really use the charge density to describe a ground state of a system, Kohn and Sham reformulated the problem in the so-called Kohn-Sham equations [57]. Using atomic units, the following three self consistent equations have been given by Kohn and Sham:

$$\underbrace{\left[-\frac{1}{2}\nabla^2 + \int \frac{n(\vec{r'})}{|\vec{r} - \vec{r'}|} d\vec{r} + V_{ext}(\vec{r}) + V_{XC}(\vec{r})\right]}_{\hat{H}_{KS_\lambda}} \Psi_\lambda(\vec{r}) = E_\lambda \Psi_\lambda(\vec{r}) \tag{2.16}$$

$$n(\vec{r}) = \sum_{\lambda}^{N} |\Psi_\lambda(\vec{r})|^2 \tag{2.17}$$

$$V_{XC}(\vec{r}) = \frac{\delta E_{XC}\left[n(\vec{r})\right]}{\delta n(\vec{r})} \tag{2.18}$$

The ground state charge density can be represented as the sum over one-electron orbitals (2.17), assuming non-interaction for N electrons. The so called Kohn-Sham

orbitals Ψ_λ are the states of the Schrödinger equation (2.16) for every electron. Regarding the new Kohn-Sham Hamiltonian $\hat{H}_{KS_\lambda}$, there are still further approximation needed to describe the exchange correlation potential $V_{XC}(\vec{r})$. $E_{XC}\left[n(\vec{r})\right]$ is called the exchange correlation energy used in (2.18) to describe the exchange correlation potential.

Using (2.16), (2.17) and (2.18), the total energy of the system can be efficiently iteratively minimized to find the ground state, stating with a first guessed charge density distribution. The variational principle can be applied to find the charge density $n(\vec{r})$, knowing that the correct charge density represents the ground state with the minimum energy of the system.

The Local Density Approximation (LDA) has been used as approximation in this thesis to describe the exchange correlation potential $V_{XC}(\vec{r})$ and will be explained in the following section. The variational principle has been applied in the so called "Self Consistency Cycle" to find iteratively the minimum energy of the system, and therefore the ground state charge density, as implemented in the *AIMPRO* code used in this study.

2.4.3 The Local Density Approximation

The Local Density Approximation (LDA) builds on the idea of a homogeneous electron gas with a uniform charge density n. Even if for real systems the charge density is not uniform, to approximate systems with slowly varying charge densities with a homogeneous electron gas has been one of the first applicable solutions to the exchange correlation in the Kohn-Sham equations. Using the Local Density Approximation, the exchange correlation energy $E_{XC}\left[n(\vec{r})\right]$ can be written as,

$$E_{XC}^{LDA}\left[n(\vec{r})\right] = \int n(\vec{r})\epsilon(n(\vec{r}))d\vec{r}\,. \tag{2.19}$$

In (2.19), $\epsilon(n)$ gives the exchange correlation term for the homogeneous electron gas of charge density n. In other words, the exchange correlation energy using the LDA has locally the same dependence upon the charge density as a homogeneous electron gas. When performing DFT-LDA calculations, an expression for this homo-

geneous electron gas exchange correlation is still needed. Here later on a lot of important work has been done [58–61], and the parametrised description developed by Ceperley and Alder [58] through Monte Carlo simulations has been used initially in the *AIMPRO* code. Today, the PW92 [61] representation of the correlation energy is implemented, and has been used in this work.
In spite of its simplicity, the LDA leads to good results compared with experimental values. Surprisingly, also for systems with rapidly varying charge densities reasonable results can be achieved. In general, when using LDA we should keep in mind that ground state energies and ionisation energies are underestimated, while binding energies tend to be over predicted and bond lengths shorter than experimentally measured.

This mathematical approximation has been proposed right after the formulation of the Kohn-Sham equations in the 1960's as well by Kohn and Sham, and helped fundamentally to launch the big story of success for DFT calculations.

GGA and Hybrid Functionals

Further attempts to improve the LDA have been made by adding in principle, gradient corrections, called the Generalized Gradient Approximation (GGA). This approximation should be able to better represent the non-uniform charge density distribution. But still no long range interactions such as Van-der-Waals forces are explicitly included.
Therefore today many attempts have been made to establish so called "Hybrid Functionals" to include such kinds of long range interactions and improve for example the prediction of correct band gaps. A commonly used functional is the B3LYP [62–64], including a combination of weighted exchange correlation energies form Hartee-Fock, LDA and GGA (In general the exchange correlation can be split further into a exchange part and a correlation part, $E_{XC}\left[n(\vec{r})\right] = E_X\left[n(\vec{r})\right] + E_C\left[n(\vec{r})\right]$). To evaluate the weighting parameters, this combination of exchange correlation energies was fitted to experimental values such as atomization energies, ionization potentials, proton affinities and total atomic energies [64].

Still a key point when comparing these methods is the fast increasing computational cost when using higher developed approximations. LDA up to date shows still clear advantages when calculating for example bigger systems. The challenge to give a sufficient description of the exchange correlation potential $V_{XC}(\vec{r})$ is still going on, and a detailed recent review to this problematic and further challenges for DFT calculations has been written by Cohen *et al.* [48].

2.5 DFT calculations using the *AIMPRO* code

2.5.1 Short history of the *AIMPRO* code development

The abbreviation *AIMPRO* stand for "**A**b **I**nitio **M**odelling **Pro**gram" and is coded mainly in the programming language Fortran. In general an *ab initio* method is, except from predefined atom species, only based on a theoretical approach. In the case of *AIMPRO* the underlying approach to calculate structural, electronic or vibrational properties is based on Density Functional Theory (DFT).

The story of *AIMPRO* has begun at the Exeter University (UK) under supervision of Prof. Robert "Bob" Jones in the 1980's [65] working on defects in diamond. Since these days the code was developed continuously by Dr. Patrick Briddon, since a while lecturer at the Newcastle University (UK). Today new implementations and developmental work is mainly done by Dr. Briddon and Dr. Mark Rayson (when writing the thesis, working at the Luleå University of Technology, Sweden). These two are only the main persons who are keeping the code together, and are trying to release stable versions more or less regularly. Many other people have contributed since the first *AIMPRO* runs with helpful implementations, scripts and tutorials and are not all listed by name, but won't be forgotten. A good overview of current developments and a state of the art discussion of the *AIMPRO* code can be read elsewhere [66–68]. Regarding the successes of *AIMPRO*, it is used today with many different materials (carbon based, silicon, zeolites etc.) at about 10 different Labs and Universities in 5 different European countries.

2.5.2 Pseudopotentials

When running a DFT calculation, a further speed up of the calculation is to split the electrons into strongly bound core electrons and valence electrons. Assuming that core electrons are strongly localised at the core region, the chemical bonding behaviour between atoms is mostly characterised by the valence electrons. It is further assumed that the core states are unaffected when changing the local

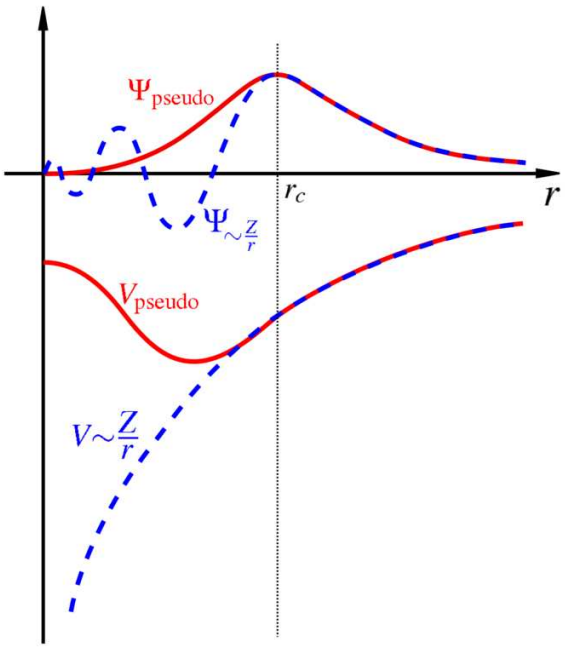

Figure 2.1: Comparison of a wavefunction in the exact potential of the nuclei (blue) to the one in the pseudopotential (red). The real and the pseudo wavefunction and potentials match above a certain cut-off radius r_c. (Image from [72])

atomic environment, also called *frozen-core approximation*. Also the overlap between core and valence states is assumed to be negligible, to enable the approximation $E_{XC}(n_{core}(\vec{r}) + n_{valence}(\vec{r})) = E_{XC}(n_{core}(\vec{r})) + E_{XC}(n_{valence}(\vec{r}))$. As the cost of a calculations scales with the number of electrons, core electrons can then be included to the nuclear potential leading to a effective screened potential [69–71], a so called pseudopotential.

The influence of this approximation shall remain very localised at the atom cores and therefore the electron wavefunction far away from the core should remain the same as for a all-electron system. Therefore a cut-off radius r_c has been defined. Inside r_c , the former complex core wavefunction is replaced by a smooth node-less function. This function can easily be implemented numerically. The new pseudo-wavefunction remain equal to the former all-electron wavefunctions outside radius r_c, but has been simplified using pseudopotentials to a simple, smooth function in the core region (see Figure 2.1). For norm conversation, the integrated core

charge densities for the all-electron and the pseudo wavefunction have to be equal. This implies a correct total charge in the core region. The choice of r_c defines the accuracy, meaning choosing a larger value for r_c results in higher speed up but lower accuracy of the calculation. Reducing r_c increases the quality of the core potential. It is important to remember that these pseudopotentials differ for all elements. Therefore, a basis of pseudopotentials has been created for the AIMPRO code, using three different techniques. In this thesis relativistic, separable, dual-space Gaussian pseudopotentials created with the Hartwigsen, Geodecker, Hutter (HGH) [73] scheme have been used. This type of Gaussian pseudopotentials offer especially advantages in combination with Gaussian basis sets, as solutions of Gaussian type orbitals can easily be evaluated analytically. Other pseudopotentials where created by Bachelet, Hamann and Schlüter (BHS) [74] and by Troullier and Martins (TM) [75] but haven't been used in this work.

2.5.3 Basis sets - Gaussian type orbitals

When solving the Schrödinger equation, the solution of the electron wavefunction $\Psi_\lambda(\vec{r})$ is a continuous function. These function can be expanded in a series of known functions $\Phi_i(\vec{r})$,

$$\Psi_\lambda(\vec{r}) = \sum_{i=1}^{N} c_i^\lambda \Phi_i(\vec{r}) \ . \tag{2.20}$$

c_i^λ are called the expansion coefficients which can be stored by a computer much more easily compared to a continuous function. The functions $\Phi(\vec{r})$ are *the basis functions* and as there are N functions we talk about a set of N basis functions, *the basis set*. The basis set functions in the *AIMPRO* code are Gaussian type orbitals [76, 77]. Other common used types are plane-wave or Slater orbitals basis sets.

Plane waves can be expressed using a complex exponential function of type $\exp(i\vec{k}\vec{r})$, whereas Gaussian type orbitals have a $\exp(-\alpha r^2)$ part. The exponent α in the Gaussian exponential function controls the width of the Gaussian function. Matrix elements of many operators can be calculated analytically using Gaussian functions,

offering a big advantage. Using a Gaussian basis set, we can expand the wavefunction of one electron as,

$$\Psi_\lambda(\vec{r}) = \sum_i c_i^\lambda \exp\left[-\alpha_i(\vec{r} - \vec{R}_i)^2\right] \ . \tag{2.21}$$

The Gaussian orbitals are centred around $\vec{R}_i$, normally the nuclei position. The basis functions are conventionally generated to form Cartesian Gaussian functions:

$$\Phi_i(\vec{r} - \vec{R}_i) = (x - R_{ix})^{n_1}(y - R_{iy})^{n_2}(z - R_{iz})^{n_3} \exp\left[-\alpha_i(\vec{r} - \vec{R}_i)^2\right] \ . \tag{2.22}$$

The exponents n_1, n_2 and n_3 are integers and characterise the symmetry of the Cartesian Gaussian orbital. For example, if we set $n_1 = n_2 = n_3 = 0$ than the resultant Gaussian has s-orbital character. When setting $n_1 + n_2 + n_3 = 1$ gives a p-orbital in ether x-, y- or z-direction. This case is 3-fold degenerate as there are 3 p-orbitals possible and therefore we take 3 Gaussian functions into account. For $n_1 + n_2 + n_3 = 2$, this generates a 5-fold degenerate d-orbital plus one s-orbital. The basis sets can be generated for every element by varying the exponents α_i and the number of total functions by defining up to what orbital type per exponent [77]. For carbon atoms I used in this work for example a $pdddp$ basis set, which consist of 38 Gaussian functions ($s/\mathbf{p} = 4$, $s/p/\mathbf{d} = 10$) and 5 different exponents α_i. In general, the more functions are added the better the description of the wavefunction, but at the same time the computational cost increases quickly. When starting a calculation using *AIMPRO* the basis sets are given, that means the type of basis set (*e.g.* $pdddp$) and the corresponding exponents α. The coefficients c_i^λ are then determined in the calculation, using the variational principle to find the minimum energy of the system. Element specific basis sets are used for all atoms in the calculation, using their atomic positions $\vec{R}$.

Regarding the Hamiltonian of the Schrödinger equation, Gaussian basis sets offer a second big advantage as they decay more quickly compared to the true wave functions. For the Hamiltonian, this reduces longer range interactions, and therefore the matrix elements, to zero. This is especially relevant for bigger system and offers a big gain in speed. In general, far fewer functions are needed for an accurate

description of the system when using Gaussian basis sets compared to plane-wave basis sets.

2.5.4 The reciprocal space - k-point sampling

In this work, all calculations have been performed using periodic boundary conditions. A cell with lattice vectors $\vec{a}_1$, $\vec{a}_2$ and $\vec{a}_3$ comprising the repeating structure is also called a supercell. When solving the Kohn-Sham equations for a supercell this usually takes place in the *reciprocal space* [20], also called k*-space*. This virtual space is orthogonal to the real space and new reciprocal vectors $\vec{a}_1^{\,\prime}$, $\vec{a}_2^{\,\prime}$ and $\vec{a}_3^{\,\prime}$ can be defined, based on the relation $\vec{a}_i \cdot \vec{a}_j^{\,\prime} = 2\pi\delta_{ij}$ (δ_{ij} is the Kronecker delta). Taking the picture of a plane wave for a free electron the wave vector $\vec{k}$ can be identified via the general relation $\Psi_{\vec{k}}(\vec{r},t) = A \cdot \exp(i(\vec{k}\vec{r} - \omega t))$, A represents an amplitude and ω the angular frequency. $\vec{k}$ describes the periodicity of the propagating wave. The energy of a free electron can be determined through the relation $E(\vec{k}) = \frac{\hbar^2\vec{k}^2}{2m}$. This relation represents the well known dispersion relation for a free electron.
In the case of a periodic crystal, where the electrons move in a periodic potential, the time independent wavefunction can be written using the *Bloch function* $u_{\lambda,\vec{k}}(\vec{r})$ to handle the periodicity, based on the *Bloch theorem*:

$$\Psi_{\lambda,\vec{k}}(\vec{r}) = u_{\lambda,\vec{k}}(\vec{r}) \cdot \exp(i\vec{k}\vec{r}) \ . \tag{2.23}$$

The *Bloch theorem* [78] states that the energy eigenvalues remain the same when translated with periodicity $\vec{P}$, a reciprocal vector in k-space, *i.e.* $E_\lambda(\vec{k}) = E_\lambda(\vec{k}+\vec{P})$. Characterising the reciprocal space, the first Brillouin zone is identified as the space where the eigenstates of the electrons from the unit cell are represented [20, 79]. The shape of this first Brillouin zone is directly derived from the real space crystal symmetry. In general, the periodic dispersion relations $E(\vec{k})$ for periodic systems (solids) are plotted only in the first Brillouin zone, and are called the band structure or band diagram.

To calculate the charge density we have to integrate all N wavefunctions over the first Brillouin zone (BZ),

$$n(\vec{r}) = \frac{1}{V_{BZ}} \sum_{\lambda=1}^{N} \int_{BZ} |\Psi_{\lambda,\vec{k}}(\vec{r})|^2 d\vec{k} \, . \tag{2.24}$$

In (2.24), V_{BZ} defines the volume of the Brillouin zone. In practice a complete integration of the k-space for every point $\vec{r}$ is too time demanding. Thus instead of a full integration, the k-space is normally just sampled over a defined point grid. Monkhorst and Pack [80] proposed an equidistant point grid along the axis of the unit cell in k-space to sample the Brillouin zone, and this approach is widely applied in DFT calculations. Here only a defined number of points are calculated and then summed to get the charge density (2.25). For correct summation the k-points have to be weighted correctly (weighting factors $\omega_{\vec{k}}$), to reflect the lattice symmetry.

$$n(\vec{r}) = \sum_{\lambda=1}^{N} \sum_{\vec{k}} \omega_{\vec{k}} |\Psi_{\lambda,\vec{k}}(\vec{r})|^2 \tag{2.25}$$

The number of k-points chosen is strongly related to the accuracy of the calculation. If not enough k-points have been set than the energy is not correctly converged. For small supercell dimensions more k-points are needed than for very large cells. This also implies that the density of k-points along the reciprocal lattice vectors should be roughly the same (more points for short real space lattice vectors, fewer points for larger real space lattice vectors). On the other hand, an increasing number of k-points also increases the computational cost. In this work, k-point sampling has been checked carefully for every calculation. For example to reproduce correctly the semimetal system graphene with it's characteristic *Dirac cone* (see also Chapter 3), it is important that the K-point in the reciprocal space is included in the k-point grid.

2.5.5 The Self Consistency Cycle

In Figure 2.2, a schematic of the Self Consistency Cycle (SCC) is shown, used to find the charge density and the energy of the ground state for a given system. In other

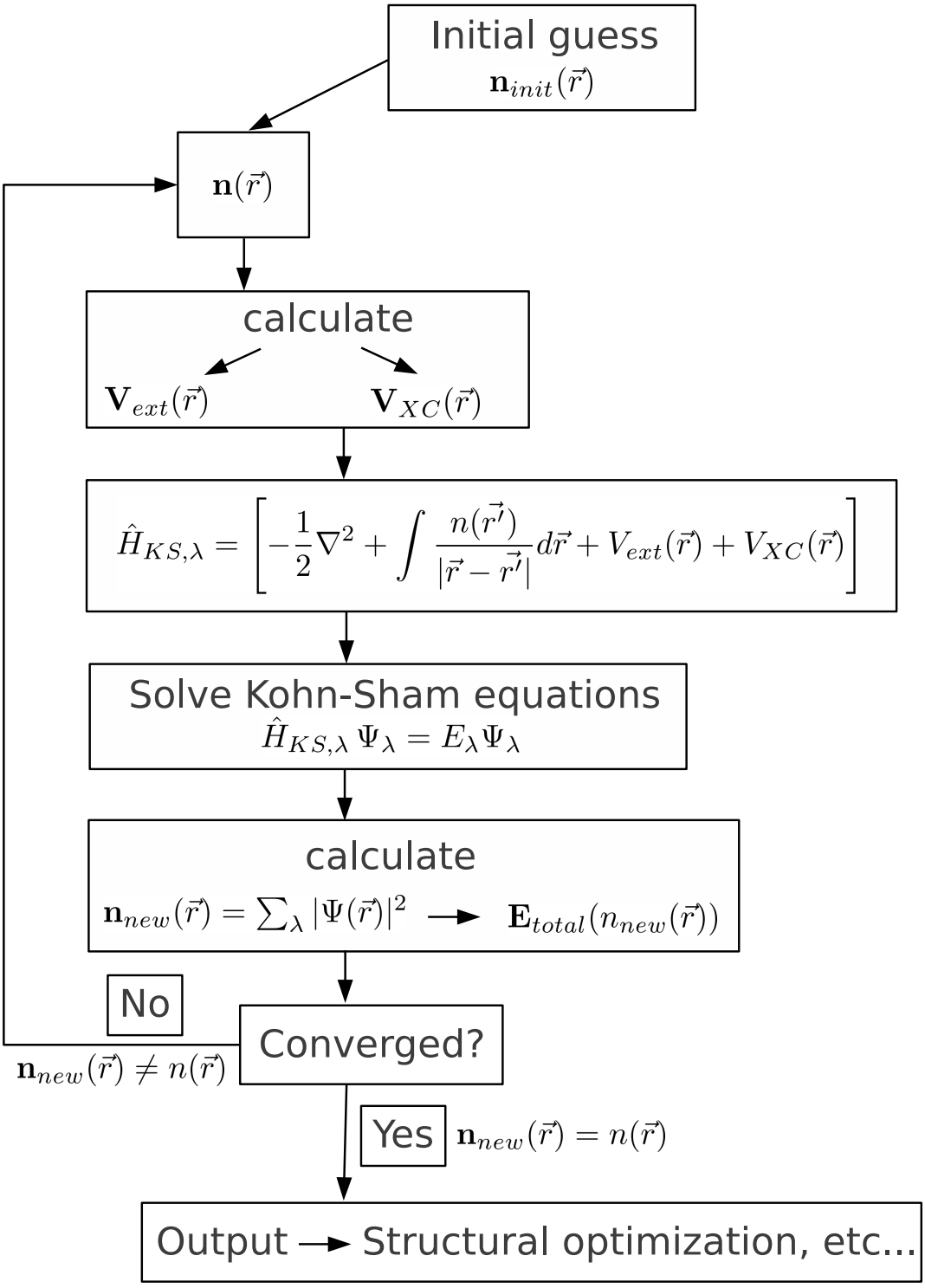

Figure 2.2: Schematic of the Self Consistency Cycle (SCC) for a typical DFT calculation using the *AIMPRO* code, solving the *Kohn-Sham equations* to get the ground state charge density and energy.

words, the electrons are iteratively redistributed, while lowering the total system energy, until the energy converges to a minimum, and the ground state charge density distribution has been found. The SCC solves iteratively the self-consistent *Kohn-Sham equations* (Section 2.4.2). The initial guess charge density $n_{init}(\vec{r})$ is usually constructed using the charge density taken from the neutral atoms. During structural optimization this is taken from the previous iteration. In the simplified Figure 2.2, the new charge density $n_{new}(\vec{r})$ is taken as the new input charge density. In reality, the new input charge density is calculated as a weighted combination of the charge density from multiple previous iterations. This increases the efficiency and stability of the SCC and leads normally to a faster convergence.
In *AIMPRO*, the SCC is normally repeated until the difference in energy regarding the input and new output charge density is smaller than 10^{-5} - 10^{-8} Ha (atomic unit of energy: **Ha**rtree), as default tolerance parameter 10^{-5} Ha is set. Lowering the tolerance can increase the accuracy, depending on the chosen pseudopotentials and basis sets, but is also computationally more costly, as is takes usually more cycles to converge. Once converged the resultant charge density and total energy can be used to obtain the forces and structural optimization can be done.

2.5.6 Structural optimisation method in *AIMPRO*

After running the Self Consistency Cycle, the total system energy is found based on the charge density, and the force on every atom can be calculated based on the Hellman-Feynman theorem [81, 82].

$$F_{X,A} = -\frac{\partial E}{\partial X_A} \tag{2.26}$$

In (2.26), $F_{X,A}$ gives the force component on atom A in direction X. The forces on every atom are used to move the atoms before repeating again the SCC. This process is repeated iteratively towards a system energy minimum until either a tolerance in total system energy change is reached, or the forces and therefore the displacement of the atoms is smaller than a tolerance parameter. Attention has to be paid, that depending on the initial structure, it is not known if the global or only

a local minima has been found as stable structure. Here, a critical view of the user is often needed to find the most stable structure (global energy minimum), trying different starting positions.

The underlying mathematical optimization method implemented in the *AIMPRO* code is the conjugate gradient method [83, 84], *i.e.* the atoms are moved in a direction weighted between forces calculated over multiple previous iterations.

Chapter 3

Graphene and related structures

In this chapter, first the main structures, known so far, including only carbon atoms are introduced. After regarding the element of carbon and its fundamental influence in our life, general descriptions of the allotropes relevant for this thesis are given, *i.e.* diamond, graphite, fullerenes and nanotubes. Following these more general sections, the fundamental properties of graphene are discussed in detail. Recent new structures like graphene nanoribbons and other single-layer materials are introduced at the end of this chapter.

3.1 Carbon allotropes

Historically, carbon is one of the few elements know already since Antiquity, *e.g.* used to manufacture bronze by Egyptians and Sumerians about 5000-6000 years ago [85]. The main early used form was as charcoal for heating. Later first applications in medicine had been recorded for coal, and had been also used for water purification. The English name *carbon* can be derived ether from the french expression for charcoal "charbon", or from the Latin word "carbo" for coal and charcoal. The element carbon (**C**) has the atomic number 6 and can be found in group 14 of the Periodic Table. It shows the electron configuration $[1s^2 2s^2 2p^2]$. Therefore the isolated carbon atom has two core electrons forming the $1s$ orbital and four valence electrons (two forming the $2s$ orbital and two occupying the $2p$ orbital). Carbon can form strong single, double and triple bonds with other carbon atoms or other elements. Today there are around ten million different carbon based compounds known, forming even its own class of chemistry, called organic chemistry. Due to its bonding flexibility, the element carbon has several allotropes such as diamond, graphite / graphene, amorphous carbon, graphyne, schwarzites and nanotubes / fullerenes.

Carbon is present in all life forms discovered to date, *e.g.* in the human body around 18 % of the total mass consists of carbon [86]. As one key element in the universe, carbon seems to be part of the chemical basis necessary for all known life.

3.1.1 Diamond

In diamond, a carbon atom has four nearest neighbours, also carbon atoms, placed in a regular tetrahedral coordination. To all four neighbour carbon atoms strong bonds are formed using one valance electron from each C atom, which are all sp^3 hybridised. In total, with the electrons form the surrounding carbon atoms four σ bonds are formed. Arranged in this way, the bulk material forms the so called "diamond structure", a face centred cubic (fcc) lattice, with a basis of 2 atoms at each lattice point (positions at $(0,0,0);(\frac{1}{4},\frac{1}{4},\frac{1}{4})$ in fractions of lattice vectors). In Fig-

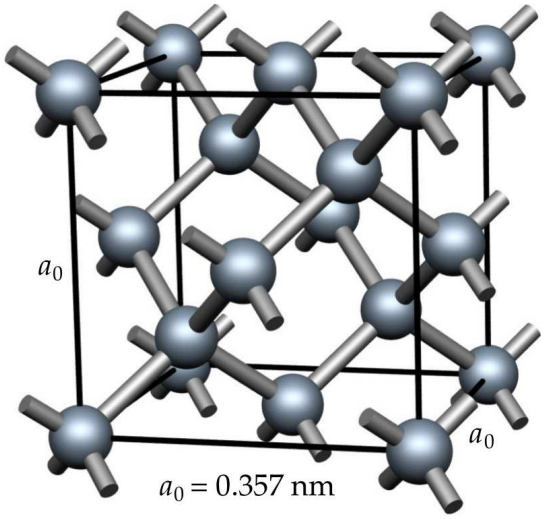

Figure 3.1: Schematic of the conventional fcc unit cell of diamond, with a_0 the cubic lattice parameter. Shiny gray ball are carbon atoms, while gray lines symbolise bonds. (Image from [88])

ure 3.1, the conventional unit cell of the diamond structure is schematically shown with the cubic lattice parameter a_0 = 3.57 Å = 0.357 nm at 300 K [23, 24, 87]. The bond length of a C-C bond is $d_{C-C} = \frac{\sqrt{3}}{4}a_0 \approx 1.54$ Å [20, 88] with a C-C-C bond angle of 109.5°.

Diamond is a semiconductor with a large indirect gap of 5.45 - 5.47 eV at 300 K [23, 24]. This causes that very pure diamonds are highly transparent, and can in some cases be used as electrical insulator. Diamond is further known for its extreme hardness, compared to many other materials. Even if the Young's modulus is not completely isotropic, the values are impressively high from around 1.05 TPa in the (100) plane up to around 1.22 TPa in the (111) plane respectively [89–91]. In addition, the thermal conductivity is very high for diamond at room temperature (293.15 K) up to 2200 W m^{-1} K^{-1} [92], meaning several times higher than for metals (copper $\approx$ 400 W m^{-1} K^{-1} [92]). Further diamond can be heated up to about 2000 K in an inert atmosphere and still remains stable [93].

All these properties make diamond a very interesting material for applications. For

many decades, the mechanical and thermal properties of diamonds have been used in sawing blades for stone, metal and ceramic cutting, as heatspreaders, in windows or surgical blades. Furthermore, big potential was predicted in the 1990s for semiconductor devices, by doping diamond to change the electronic properties, *e.g.* creating a smaller band gap. Although this has been found to be difficult especially for shallow p-type dopants [94]. Today, nanodiamonds and diamond quantum dots are promising future research areas [95]. But to date, the big industrial breakthrough of diamond in the semiconductor industry is missing, while carbon allotropes, such as graphene, are rivaling.

3.1.2 Graphite

Graphite is another carbon allotrope, but compared to diamond the atoms are sp^2 hybridised and bonded in trigonal coordination. The atoms are arranged in stable flat layers (basal planes), where the layers contain the sp^2 carbon network. In every layer a carbon atom has 3 nearest neighbours arranged in a hexagonal structure (also called "honeycomb" lattice, see Figure 3.2). The in-plane atoms are strongly bonded via covalent σ bonds, and form an additional π-bond system (using the free $2p$ electron) with strong metallic character. The layers interact weakly by Van der Waals forces and weak bonding induced by the overlapping p_z-orbitals of neighbouring planes [21]. In the most stable configuration of graphite, the layers are stacked in a A-B-A-B pattern along the out of plane axis (see Figure 3.2). This is called "AB stacking" or "Bernal stacking". J. D. Bernal first discovered the structure via X-ray analysis of graphite in 1924 [96]. The C-C bond length in the basal plane is $d_{C-C} = 1.42$ Å, and the interlayer spacing has been measured to be around 3.35 Å [22, 97]. The conventional unit cell in Figure 3.2 of AB stacked graphite contains 4 atoms.

Graphite is a semi-metal, as the band overlap is nearly zero (only 0.03 eV reported by Chung [21]). The bands nearest to the Fermi level are generated from the π- and π^*-bonds, while the σ- and σ^*-bonds in the basal plane show a large separation, similar to diamond. The band diagram shown in Figure 3.3 has been calcu-

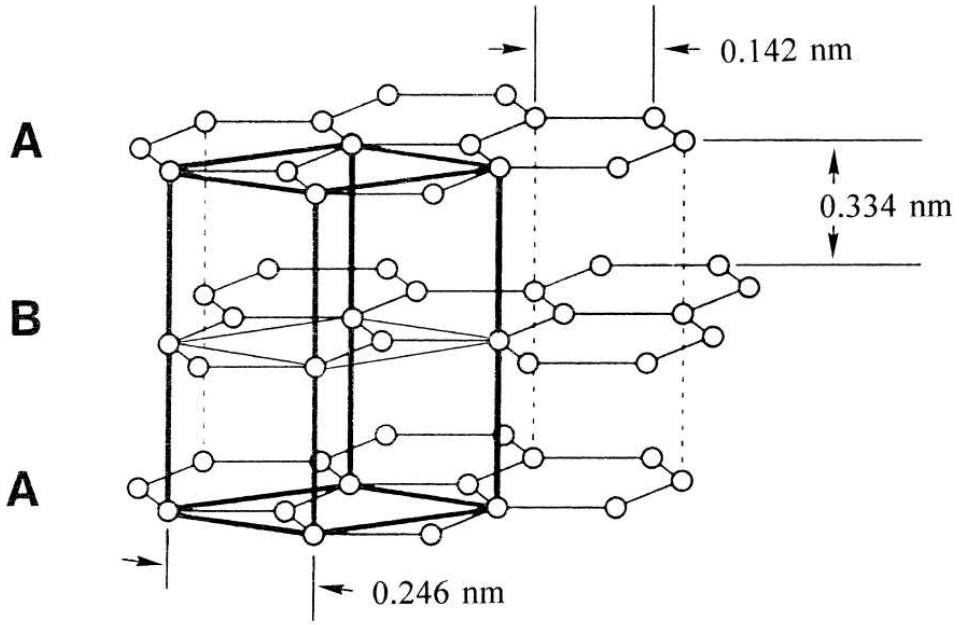

Figure 3.2: Schematic of graphite with the conventional unit cell and the AB stacking pattern. White circles symbol carbon atoms, while thin black lines represent bonds. (Image from [22])

lated using the *AIMPRO* code (LDA-DFT), and shows nice agreement with results in the literature (Tight-Binding [98], LDA-DFT [18, 99]). This continuum of states around the Fermi level means graphite appears black to the human eye. Due to the metallic bond character of the π-bonds, the in-plane electrical conductivity is very high (similarly for the thermal conductivity due to a large mean free path of the in-plane phonons). Although perpendicular to the basal plane the conductivities are much weaker [21]. This demonstrates the highly anisotropic behaviour of graphite.

Graphite is a more common naturally occurring mineral than diamond and is comparatively cheap. It is used for example in steel-making, as anodes in batteries, in parts for heavy brakes or as lubricant. Graphite powders are used as dry lubricators. Another common application is in pencils, writing with graphite mixed with clay as a black pigment. Today, synthetic graphite is produced, to get highly pure material. This offers other possibilities to the use of graphite for example in fusion rectors as neutron moderators, or in the oil industry.

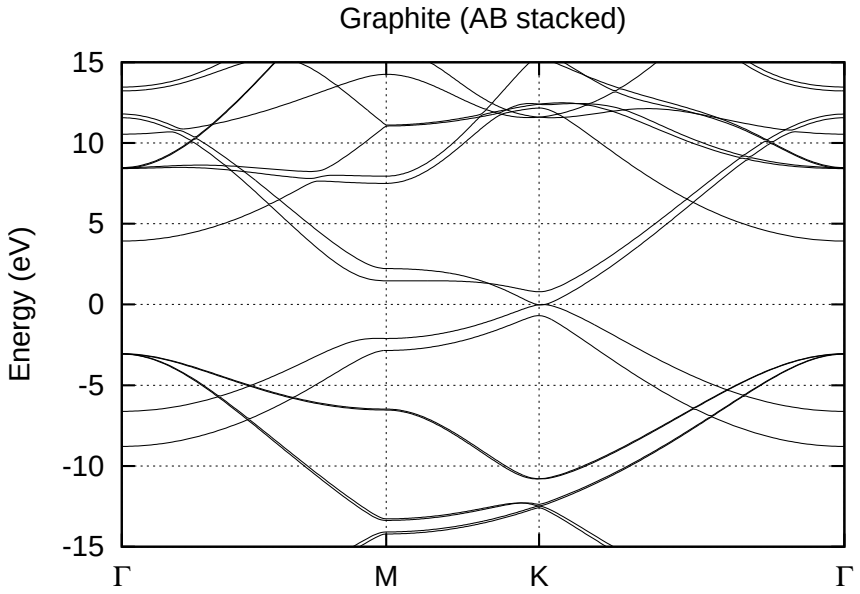

Figure 3.3: Band diagram around the Fermi level for AB stacked graphite in reciprocal space along $\Gamma - M - K - \Gamma$ using LDA-DFT calculations. (See Figure 3.10 (b) for the first in-plane Brillouin zone)

Graphite intercalation compounds

Graphite also offers great possibilities in combination with intercalated species. This means that atoms or small molecules are inserted between the graphite layers, causing an expansion of the inter-layer distance. Intercalation provides ways to change the electronic, chemical, thermal and magnetic properties of the graphite [32]. A prominent example is stage 1 intercalation of potassium (C_8K, K atoms between every graphite layer) forming a low temperature (< 1 K) superconductor [100]. In the case of molecules, intercalation of, for example, Br_2 has been investigated [101, 102]. Especially the acceptor or donor behaviour of intercalated species in graphite and the induced charge transfer with the π-system attracts much attention.

3.1.3 Fullerenes

After decades of carbon research on pure carbon bulk systems, in 1985 the discovery of C_{60} (also known as “Buckminsterfullerene”, “Buckyball” or “Fullerene”)

(a) (b)

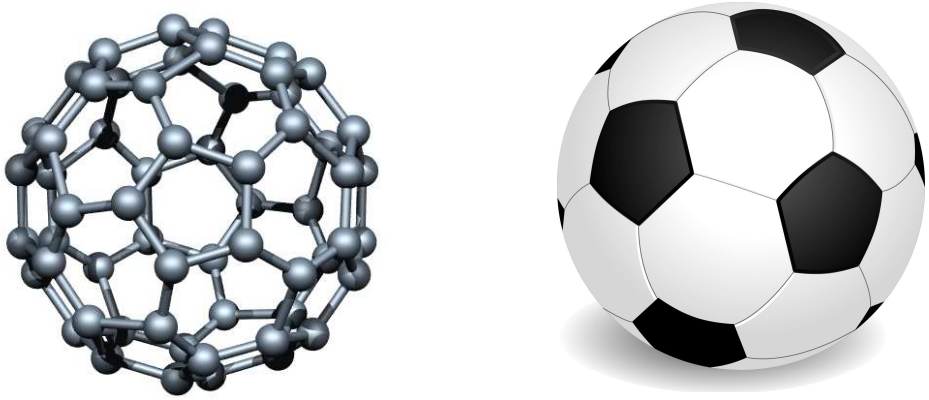

Figure 3.4: (a) C_{60} Buckminsterfullerene and (b) a football with the same symmetry. (Images from (a): [105], (b): [106])

was announced [103, 104]. By vaporizing graphite using a powerful Nd:YAG Laser small carbon clusters were produced. Mass spectrometry showed a dominant species containing exactly 60 carbon atoms. The explanation was a new very stable and highly symmetric spherical structure shown in Figure 3.4 (a), reminiscent of a classic football (Figure 3.4 (b)). C_{60} contains 20 carbon hexagons and 12 carbon pentagons rings, with a C-C bond length of $d_{C-C} = 1.39$ Å for a pure hexagon-hexagon bond and $d_{C-C} = 1.43$ Å for a hexagon-pentagon bond [104].

Today, even more fullerene types can be produced (C_{20},..,C_{70}, C_{76}, C_{82},...) and more methods, for example using an electric arc to evaporate graphite, have been established [107]. Recently, the fundamental growth mechanism of these structures has been explained [108]. After the development of new large scale production methods, it is today possible to produce large amounts of fullerenes to use in devices. A commercial breakthrough is not clearly visible yet, but interest in using fullerenes for organic solar cells, drug delivery and as image contrast agents in MRI are under development [7]. It can be stated that the discovery paved the way for new 0-, 1- and 2-dimensional forms based on carbon and related materials (e.g. carbon nanotubes and the boron B_{80} fullerene [109]).

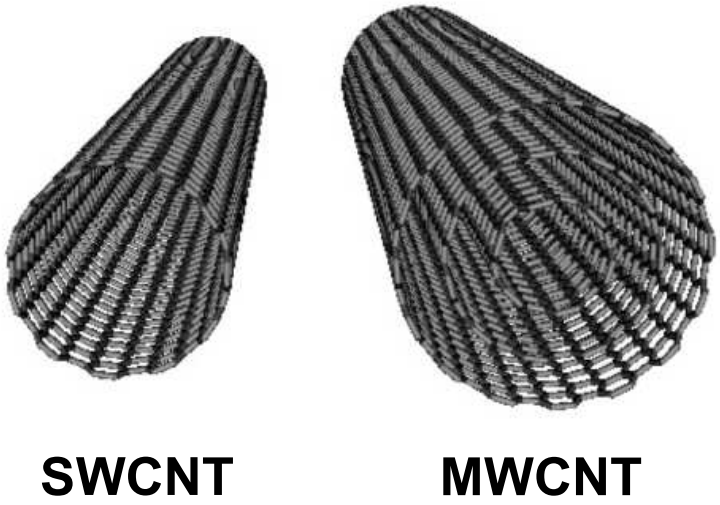

Figure 3.5: Two types of carbon nanotubes, single-wall CNTs and multi-wall CNTs. (Image from [113])

3.1.4 Carbon nanotubes

In 1991, Iijima [13] reported "Helical microtubules of graphitic carbon", today known as carbon nanotubes (CNTs). In TEM images he was able to see long structures with curved surfaces of carbon produced by arc-evaporation similar to that for fullerenes [107]. Carbon nanotubes are built on a hexagonal carbon network like graphite, but rolled to a cylinder. First only nanotubes with walls containing several carbon layers were found, called multi-wall carbon nanotubes (MWCNTs). In 1993, additional pure single-wall carbon nanotubes (SWCNTs) were found [110]. The general two types of CNTs are shown in Figure 3.5. All nanotubes seen were capped on the ends by fullerene like structures, both SWCNTs and MWCNTs. The diameter of the tubes can range for SWCNTs from around 3 - 20 Å [111, 112] and for MWCNTs between 20 - 250 Å [112].

To define the structure of a (SW)CNT we can start from the graphite layer basal plane [114], demonstrated in Figure 3.6. $\vec{a}_1$ and $\vec{a}_2$ are defining the hexagonal unit cell of the basal plane containing 2 atoms (see also Figure 3.2). Next, we can construct the vector $\vec{C}_h = n\vec{a}_1 + m\vec{a}_2$, when adding n times vector $\vec{a}_1$ and m times vector

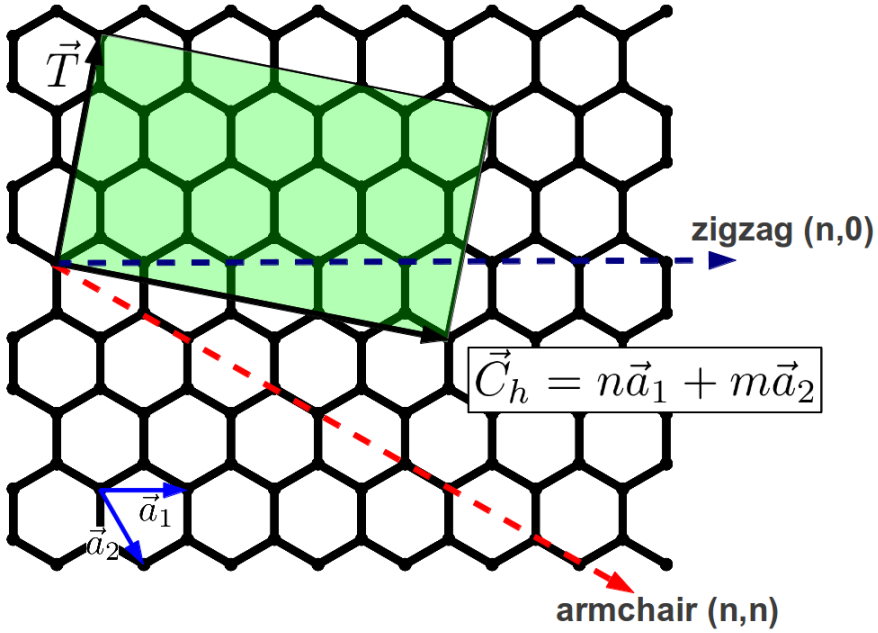

Figure 3.6: Definition of the nanotube chirality (n,m), based on a rolled-up graphene sheet by connecting the two ends of vector $\vec{C}_h$. $\vec{T}$ points along the tube axis, its length shows the smallest repeating cell.

$\vec{a}_2$, with $n, m = 0, 1, 2, \ldots$. When we next roll up the sheet, by connecting the end and the beginning of vector $\vec{C}_h$ to form a tube. This directly delivers the circumference of the tube $L = |\vec{C}_h| = a\sqrt{n^2 + m^2 + nm}$ and the diameter $d = L/\pi$. The two parameters (n,m) are a exact definition of the tube symmetry, also called *chirality*. In case of $n = m$, vector $\vec{C}_h$ points along the armchair direction of the basal plane, thus this CNTs are called armchair CNTs (ACNTs). For chiralities with $m = 0 \neq n$ vector $\vec{C}_h$ points along the zigzag direction, and these CNTs are therefore called zigzag CNTs (ZCNTs). $\vec{T}$ defines the translational vector, the length of one unit cell along the tube axis [114]. This theoretical description shows that there are many different possibilities to form a CNT, and shows the difficulty to detect the chirality in TEM images.

CNTs have attracted much interest since their discovery, because of their extraordinary electronic, thermal and mechanical properties. When bending a graphite basal plane to get a tube, we reduce the dimensions of the material from 2D to

1D. In the quantum mechanics picture, this changes the boundary conditions and we get chirality specific dispersion relations, only along the CNT axis. CNTs can be metallic, semi-metallic or semiconducting [115]. It has been found that if $n-m$ is a multiple of 3 than the tube shows metallic conduction. Roughly speaking that gives one third of possible chiralities are metallic and two third are semi-conducting or semi-metallic.
Also the transport behaviour of CNTs is very interesting. While in normal material the resistance increases with the length, due to scattering, in CNTs it stays constant. Electrons are in the regime of ballistic transport, what offers great possibilities in devices. They can conduct large currents without loss and heat production [114].
CNTs have an in-plane Young's modulus similar to graphite with high rigidity along the tube axis from around $\sim$ 1 TPa [116–120]. No strong chirality dependence has been found for mechanical properties. Like the electronic properties, this behaviour is reduced to the dimension along the CNT. CNTs are very elastic perpendicular to the tube axis, and thus can bend easily. Especially for composites engineering, the mechanical behaviour of CNTs is very interesting.

Discovered in 1991, CNTs can be produced in large scale today. This offers now the possibility for industrial use, and it seems as if CNTs can open new avenues [121]. CNTs are used today in carbon lightweight construction (in form of CNTs bundles or CNT carpets), in batteries [122], are candidates to held in drug delivery medicine [123], or gas sensors [124] and many more potential is getting explored in the field of electronic circuits [114].

While the key molecular forms of C, *i.e.* fullerenes and CNTs, have been briefly introduced here, many other forms exist (such as carbon nanocones) and new ones are continually being discovered.

3.2 Graphene - Fundamental properties

Graphene is a monolayer of sp^2 bonded carbon atoms, arranged in a 2-dimensional hexagonal lattice equivalent to one isolated basal plane of graphite. That a single-layer of this thinnest imaginable material can exist was long time not believed, mainly based on a theoretical study of Mermin and Wagner [125] from 1966. In this study it had been "rigorously proved" the absence of ferro- and anti-ferromagnetism in 1- or 2-dimensional systems built on the isotropic Heisenberg model. This suggested that pure 1- or 2-dimensional crystals cannot exist. Even the documented ultra-thin graphite flakes, and also the mention of single-layer graphene sheets isolated by Boehm *et al.* [126] already in 1962 in a solution, had not changed this point of view for nearly 40 years. Looking back, this probably was the first documented experiment including a mix of single- and few-layer graphene flakes. At that time, imaging probes capable of atomic resolution such high resolution TEM were only in their infancy and the STM had not been invented. So further intensive studies were not performed and the statement of Mermin and Wagner [125] stayed in the heads of scientists.

While graphite and also the graphite basal plane have been used by theoreticians for a long time as example systems to develop understanding of basic electronic properties [30, 31], a quite simple idea had to come across until graphene became accessible in 2004 [14]. A research group around the two physicists Andre Geim and Konstantin Novoselov at the University of Manchester had developed an easy method of isolating single graphene sheets from graphite blocks using adhesive (sticky) tape. When pulling off the tape from a graphite block, they observed a fine layer resting on the tape. By repeating this pulling off the tape also from the fine layer, they were able to shrink the layer thickness down to few Å (see Figure 3.7). These thin layers were then analysed using SEM and HRTEM and first transport measurements were performed [127, 128]. There is a lot discussion till today if this discovery from 2004 is consistent with the Mermin-Wagner-Theorem. But it can be interpreted as if the free growth (not supported by a substrate) of a pure 2D

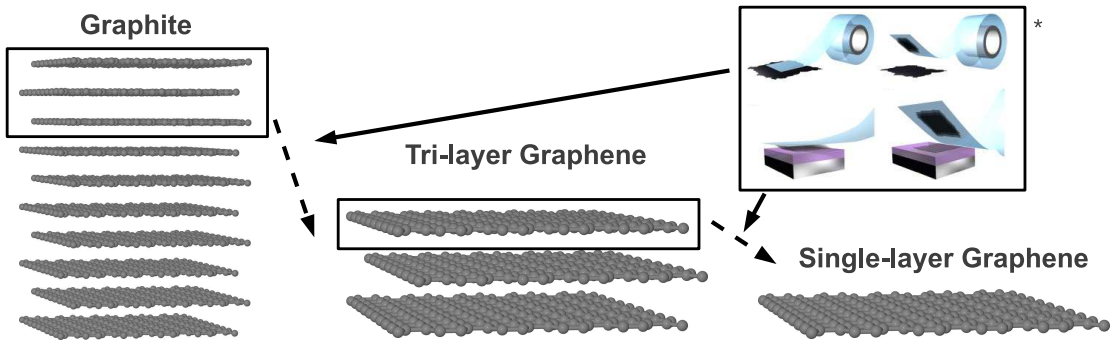

Figure 3.7: From graphite to graphene using the adhesive tape method. (* Image adapted from [131])

crystal is not possible. But by using the adhesive tape method nothing is growing, as pre-existing layers are exfoliated. Another interesting insight is that suspended graphene sheets tend to be not perfect 2-dimensionally flat. Recently ripples and out-of-plane distortion in the Å-range have been found experimentally [129] and additional thermally induced height fluctuations have been reported using atomistic Monte-Carlo simulations [130].

Besides mechanical exfoliation (adhesive tape method) or chemical exfoliation (using liquid solutions to intercalate and then split graphite [132]), the controlled growth of graphene on substrates has gained importance. Today it is possible to grow single- and few-layer graphene on different types of substrates, *e.g.* SiC [133] or Cu [134]. These growth processes have been developed in recent years using established CVD, PVD or MBE setups.

Graphene oxide (GO) and reduced graphene oxide (r-GO) have been intensively studied for many decades, due to simple and cheap chemical preparation methods [135]. It was further suggested that Boehm *et al.* [126] had produced r-GO rather than pristine graphene flakes [135]. Even if the electronic properties of GO are less attractive than graphene, there are many possibilities to use GO for example as building blocks for carbon-based composites [136]. Another research area is the transformation of easily dispersible and cheap GO layers to graphene, as demonstrated recently with flexible conductive graphene paper [137].

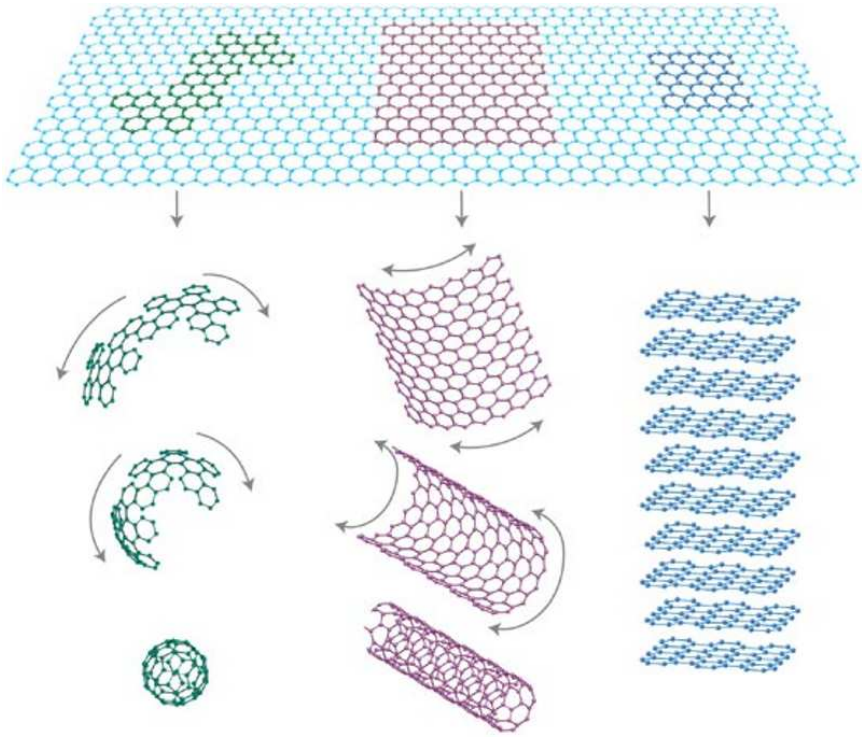

Figure 3.8: A graphene sheet is the underlying basic element for many carbon allotropes, such as fullerenes, CNTs and graphite. (Image from [16])

Graphene can be seen as the basic underlying building block which can be used to form various different carbon allotropes when rolling, folding or twisting the 2-dimensional sheet into the third dimension (see Figure 3.8). Additionally, the 2D hexagonal lattice can be tailored when cutting it for example into nanoribbons or quantum dots. Many of the possible constructed forms have been recently summarised by Suarez-Martinez *et al.* [138] and an overview is shown in Figure 3.9.

The exceptional semi-metallic properties and the well described electronic behaviour (*e.g.* Quantum-Hall-Effect, ballistic transport behaviour) combined with a simple method for preparation (for scientific use first based on mechanical exfoliation) started the new hype of graphene [16]. Especially the high electron mobility μ measured free-standing to reach over 200,000 $cm^2\ V^{-1}\ s^{-1}$ [33], the high in-plane Young's modulus value of $\approx$ 1 TPa [139, 140], the high thermal conductivity $K \approx$ 5000 $W\ m^{-1}\ K^{-1}$ at room temperature [141] and a high specific surface area of

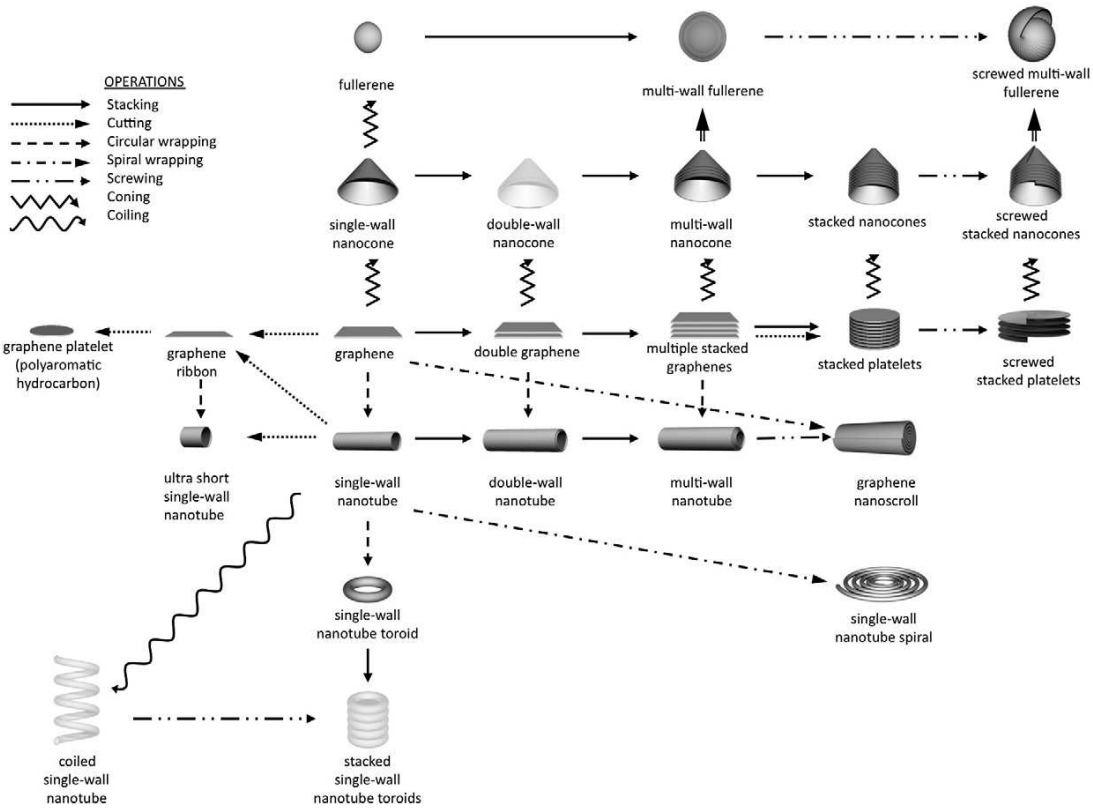

Figure 3.9: Overview of different carbon allotropes based on graphene, showing the topological relationships between them. (Image from [138])

2630 m^2/g [142] makes graphene a very promising candidate for the developmental of new electronic devices [14, 143, 144], as well as photonics and optoelectronics [145]. After the 20th century dominated by silicon based technology, the next big technology step in the 21st century could be a nanotechnology based on graphene and related carbon structures.

3.2.1 Structural properties of graphene

The structure of graphene is that of the basal plane of graphite (see section 3.1.2). The carbon atoms are arranged in a 2-dimensional hexagonal lattice, with 3 nearest neighbours each. The C-C bond length is similar to graphite $d_{C-C} = 1.42$ Å. The smallest possible hexagonal unit cell contains only 2 atoms, the lattice parameter is $a = 2.4612$ Å (see Figure 3.10 (a)). Graphene can be regarded as two overlaying hexagonal lattices **A** and **B**, one atom of each represented in the unit cell. The

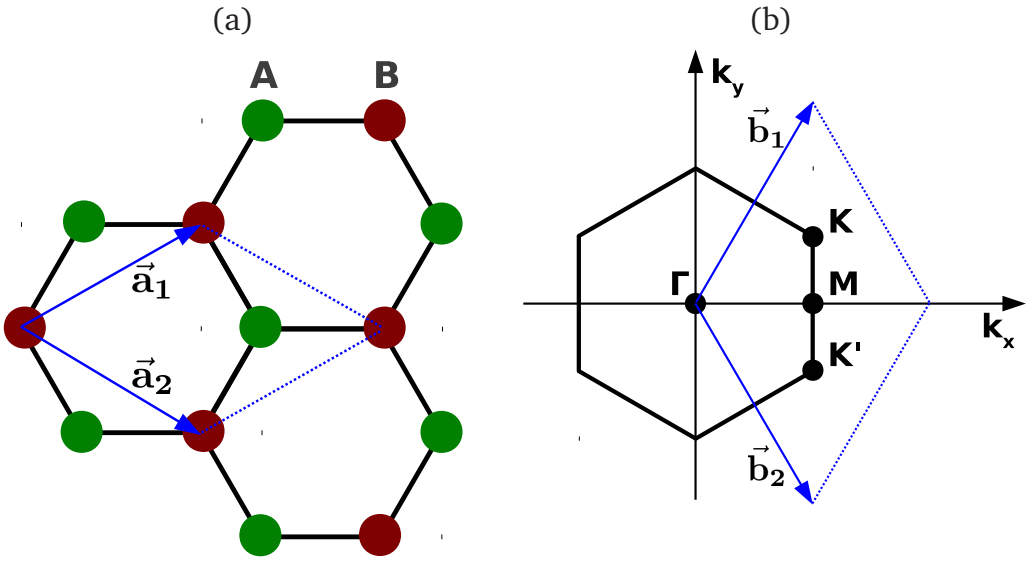

Figure 3.10: (a) Honeycomb lattice of graphene with the lattice unit vectors $\vec{a}_1$ and $\vec{a}_2$ (both = 2.4612 Å). Unit cell shown in blue, sublattices of graphene shown by red and green coloured carbon atoms. (b) 2-dimensional k-space of graphene with important points Γ, M and K in the first Brillouin zone (coloured black). The reciprocal unit cell and reciprocal lattice vectors $\vec{b}_1$ and $\vec{b}_2$ are shown in blue.

k-space is also 2-dimensional and the hexagonal structure is preserved, but rotated 30 degree (see Figure 3.10 (b)). The atoms form a sp^2 hybridised system. In-plane the atoms form strong σ bonds. The p_z orbital is oriented out-of-plane, forming with the last electron a π-cloud.

The AB stacked bi-layer consists of 2 layers shifted by $\vec{s}$, with $\vec{s} = \frac{1}{3}(\vec{a}_1 + \vec{a}_2)$. The inter-layer distance is similar to graphite 3.35 Å. When choosing the pseudo-potential, basis sets and k-point grid for a DFT-LDA run, we have to be careful, as these layers are only weakly bonded [146]. This behaviour is in general not well described by LDA-DFT calculations. To test this, bi-layer graphene and graphite were tested using the $pdddp$ basis set (38 basis functions) for carbon and a fine k-point grid. Comparing the total energy change per atom versus the inter-layer distance for both graphite and AB stacked bi-layer graphene an inter-layer distance of 3.33 Å in both cases is found, see Figure 3.11. This is in good agreement with the experimental value of 3.35 Å , and we consider the inter-layer distance as suf-

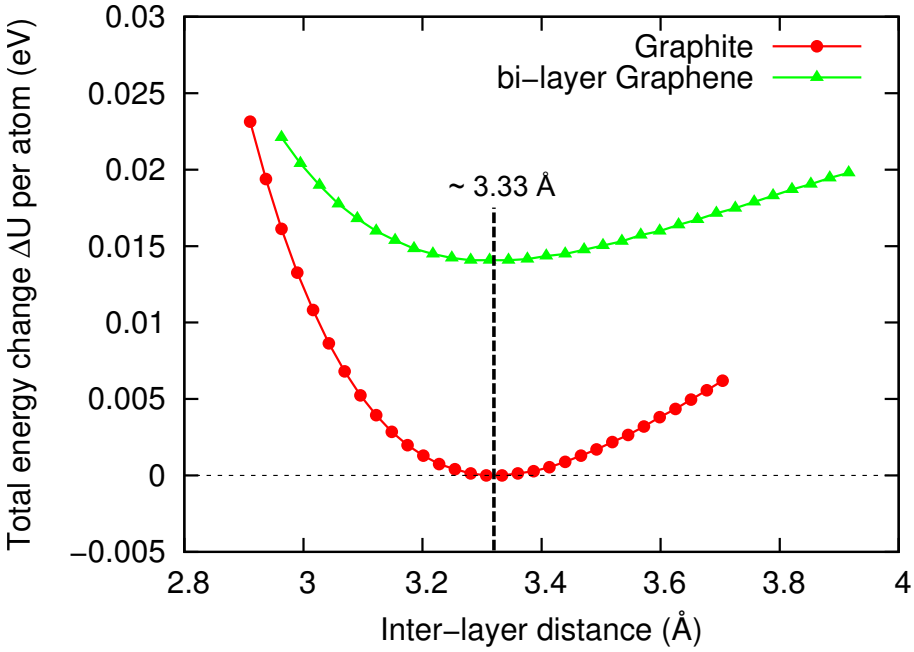

Figure 3.11: Total energy change per atom when using different inter-layer distances calculated with the LDA for graphite and bi-layer graphene both AB stacked. HGH pseudo-potential with $pdddp$ basis set, $20 \times 20 \times 8$ k-point grid for graphite ($20 \times 20 \times 1$ k-point grid for bi-layer graphene), and a hexagonal unit cell including 4 carbon atoms have been used in both cases. In the case of bi-layer graphene, the distance to the next structure was more than 12 Å to avoid interactions.

ficiently good using this basis set and the LDA-DFT approach. We note that for bi-layer graphene the layers are less strongly bond than in graphite and the energy curvature with distance is smoother.

Graphene edges

For graphene, three basic edge types exist, called armchair, zigzag and Klein edges [147–150]. All three edge types can be created by cutting the graphene sheet along two primary families of directions, the $<1\bar{1}00>$ and the $<2\bar{1}\bar{1}0>$ (see Figure 3.12 (a)). From a top view perspective, this is demonstrated in Figure 3.12 (b). We note that always two exactly similar edges are created on both graphene parts, when cutting the graphene sheet.

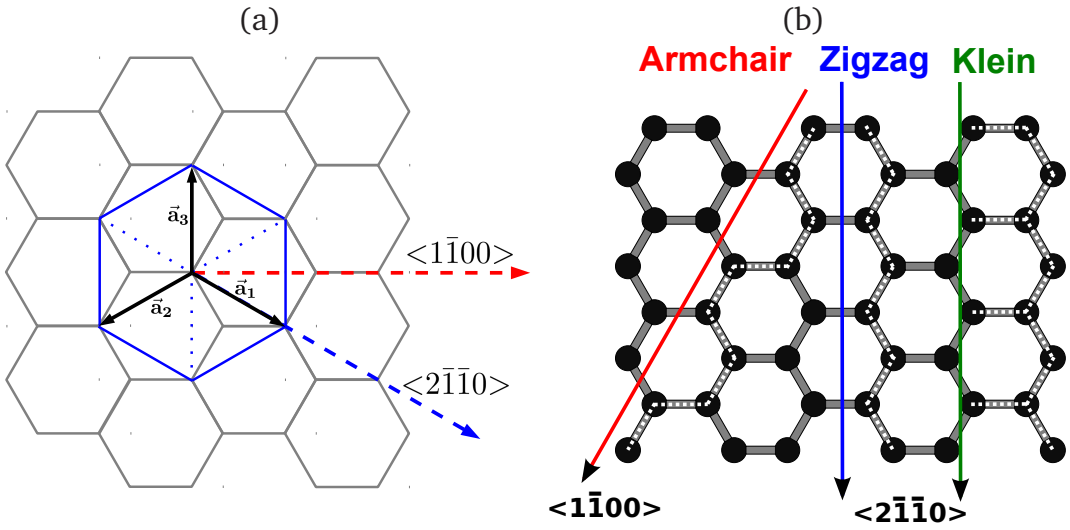

Figure 3.12: (a) Hexagonal graphene lattice with the characteristic <1$\bar{1}$00> and <2$\bar{1}\bar{1}$0> directions. (b) Possible orientations to cut a graphene sheet (or unzip a nanotube into a graphene nanoribbon) to create pure straight armchair (red), zigzag (blue) or Klein edges (green). The resulting atomic edge structures are marked via dotted white lines to the right of each cutting axis.

Over the last decade, graphite and graphene edges have been studied intensively using STM and (today normally aberration-corrected) TEM techniques [149–155]. Either holes in a graphene sheet or the outer edges of single- and few-layer graphene have been probed using modern microscopy techniques. Considering a planar graphene sheet, armchair and zigzag edges are the most common observed configurations under UHV conditions (an example of a TEM study from Girit *et al.* [149] is shown in Figure 3.13). At the same time, the edge properties of graphene have been subject of many theoretical studies, mostly focused on perfect armchair or zigzag edges [148, 156–160].

But the question came up if also other edge configurations could exist, for example reconstructed edges. Recent calculations have predicted stable reconstructed graphene edge configurations [160, 161]. Revisiting TEM studies, some proposed edge types, especially the (5-7) reconstructed zigzag edge, were confirmed [162].

In this thesis, different possible unterminated and hydrogenated graphene edge configurations are studied in detail, including rigorously for the first time the Klein and reconstructed Klein edges. Results can be found in Chapter 4.

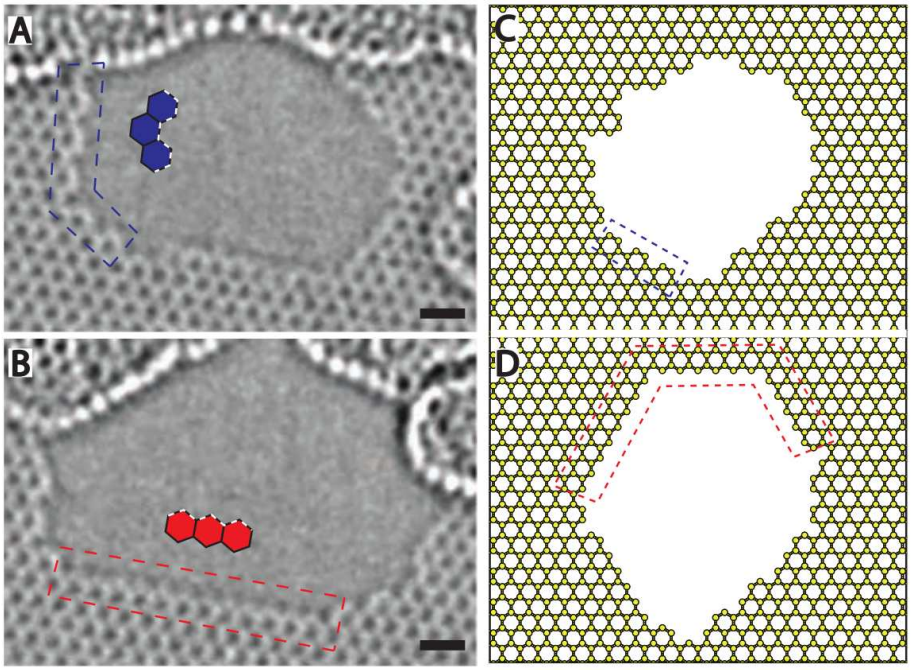

Figure 3.13: (A) and (B) show typical aberration-corrected TEM images of two different holes in graphene. (C) and (D) show two simulated graphene holes with a high degree of ordered edges. In blue armchair edges and in red zigzag edges are marked as guide for the eye. (Images from [149])

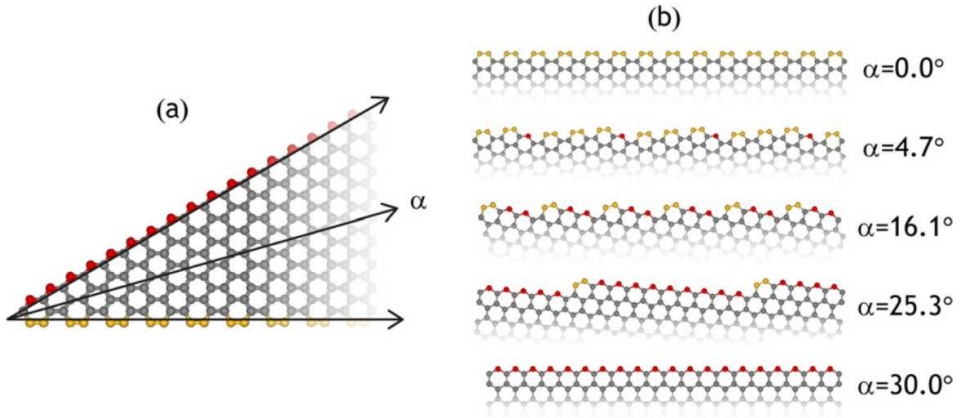

Figure 3.14: Chiral edges from armchair (yellow) to zigzag (red). (a) Definition of the orientation angle α in the graphene sheet plane. (b) Different chiral unreconstructed graphene edges, with armchair and zigzag sections marked in yellow and red as guide for the eye. (Images from [158])

Considering mixed parts of armchair and zigzag along one straight edge, various chiral graphene edges are possible. One possibility to describe these is given by Branicio *et al.* [158] using the orientation angle α [158], illustrated in Figure 3.14. Additionally, first reviews about unterminated and unfunctionalized graphene edges were published recently [163, 164], giving the reader a first overview to parts of the chemistry and physics of (mainly) unreconstructed and only simple hydrogenated graphene edges.

3.2.2 Electronic properties of graphene

While the strong σ bonds are responsible for the high in-plane strength, the π bonds are half filled and lead to the semi-metallic behaviour of graphene. Already in 1947, the band structure of graphene had been studied by Wallace [30], reporting for the first time the unusual linear dispersion relation near the K-point (Figure 3.15 (a)), with the so called Dirac electrons. A linear crossing of the conduction- and valence band can be found for low energies at the K-point, leading to the so called Dirac cone (see Figure 3.15 (b)). The Fermi level (chemical potential) lies directly at the Dirac point (crossing point of the two bands), marking the center of the Dirac cone. This exceptional linear dispersion relation leads, for low-energy excitations, to massless Dirac fermions as described by quantum electrodynamics. But different to photons in graphene, the massless Dirac fermions move 300 times slower that the speed of light in vacuum, with a Fermi velocity $v_F \approx 10^6$ m/s [165]. Regarding Dirac fermions another interesting aspect concerns the Klein-Paradox [36], the probability of 1 to pass (lossless) small classical forbidden regions. In other words, in graphene electrons are able to propagate large sections (in the μm range) without scattering [14], even in the presence of disordered electrostatic potentials generated e.g. by defects. This can lead to ballistic transport behaviour (infinite electron mobility μ); recently high values of μ with over 200,000 cm^2 V^{-1} s^{-1} [33] were probed.

In general, disorder cannot be avoided in real systems, as the control of defects, impurities, surface adatoms, adsorbed molecules on the surface or structural defor-

(a)

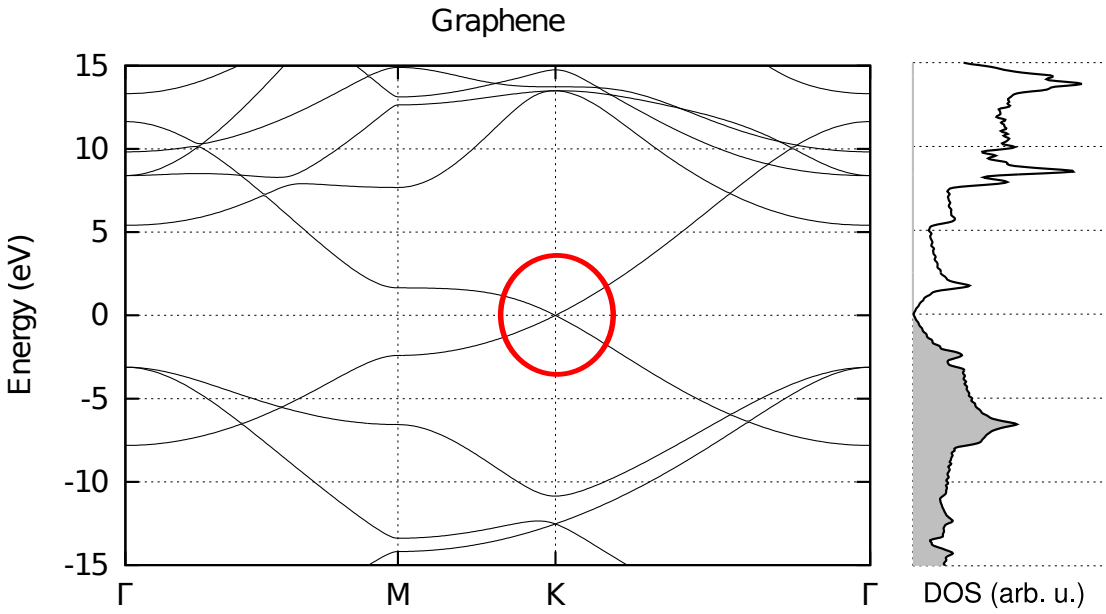

(b)

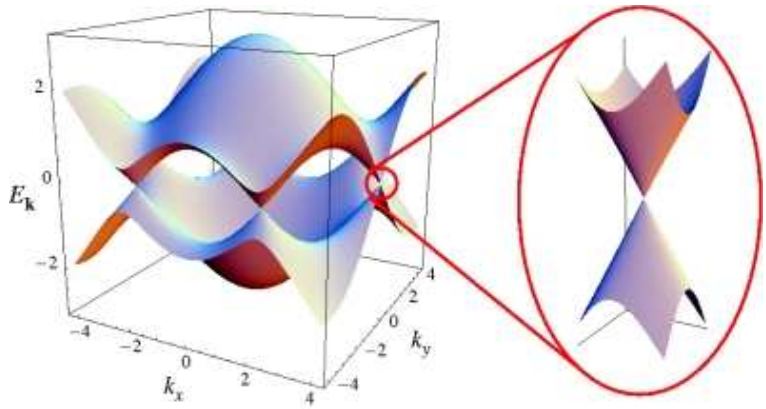

Figure 3.15: (a) Band diagram of graphene along $\Gamma - M - K - \Gamma$, with marked region of linear crossing at the Fermi level in red. On the right the density of states (DOS) of graphene is plotted. (b) Electron dispersion of graphene with linear band crossing at K and K'. In the zoom one of the K points to show the Dirac cone. (Image (b) from [25])

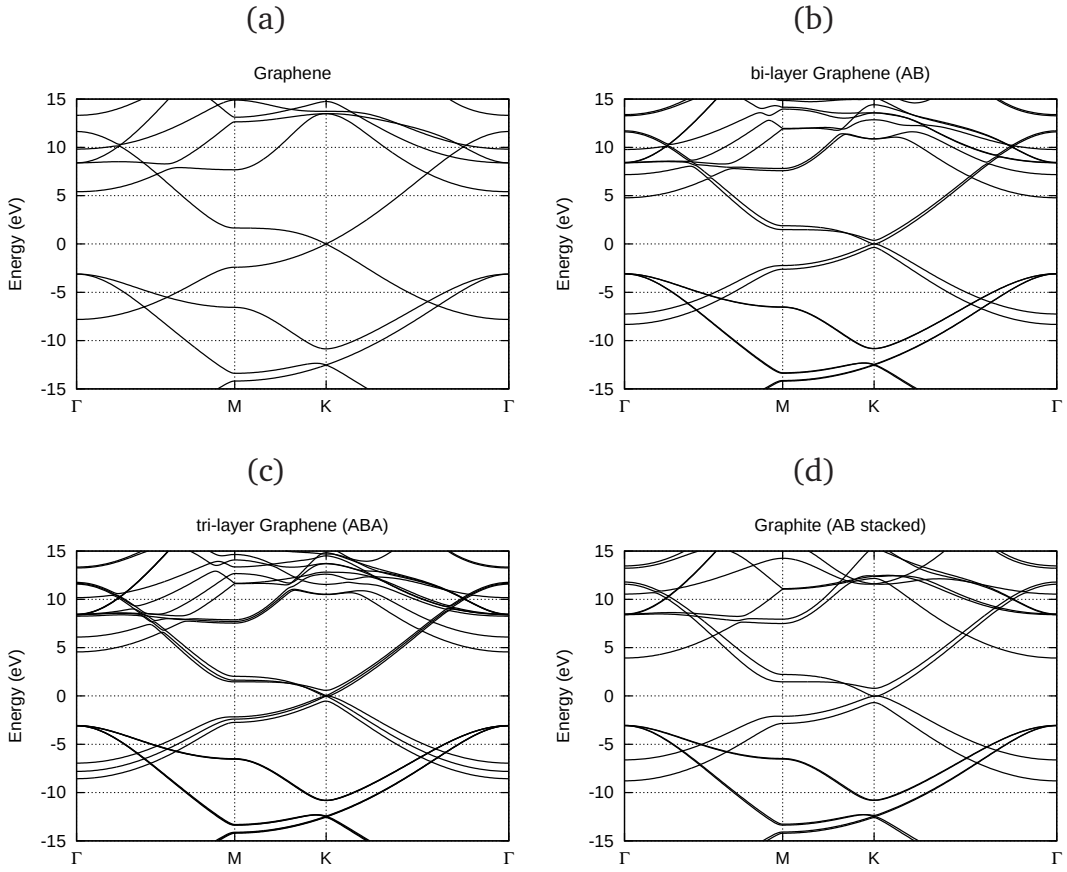

Figure 3.16: Bandstructures for (a) graphene, (b) bi-layer graphene, (c) tri-layer graphene and (d) the graphite bulk material.

mations (*e.g.* ripples in graphene) is limited [25, 129]. This still somehow robust transport behaviour of graphene is very promising for the integration of graphene layers in devices to realise, for example, highly efficient and fast p-n junctions.

Regarding the addition of graphene layers in the most stable stacking order of the AB pattern, we can additionally calculate the band diagrams for bi-layer, tri-layer and graphite. The transition from a single-graphene layer to graphite is shown in Figure 3.16. My calculations are in very good agreement with a published article by Klintenberg *et al.* [18] using similar LDA-DFT calculations. The transition to graphite can be well observed at the characteristic K-point in the band diagram. While for single-layer (SL) graphene a linear band crossing can be found, this exceptional behaviour vanishes already for bi-layer (BL) graphene, Figure 3.16 (b),

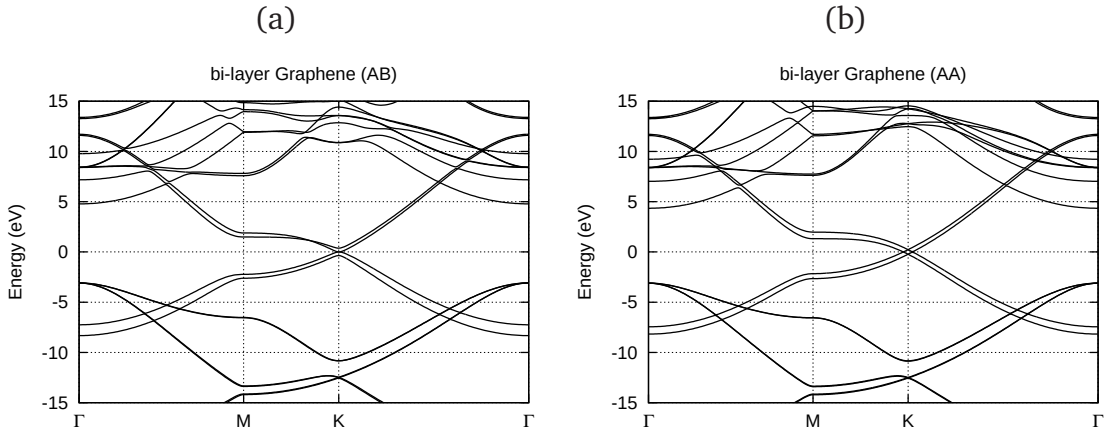

Figure 3.17: Bandstructures for bi-layer graphene with (a) AB stacking and (b) AA stacking.

showing smooth curvature around the K-point. The number of bands has doubled for BL-graphene as there are contributing now 4 electrons form 4 different p_z states. Due to inter-layer interaction, these bands split and only two bands are near the Fermi-level $E_F = 0$ eV. The same effect can be observed for TL-graphene, three valence- and three conduction bands can be observed. For three layers, the band structure can be described as a superposition of the SL-graphene band structure and the BL-graphene one (see Figure 3.16 (c)). There is a linear crossing of two bands visible, but in reality excited states will preferably occupy the energetically lower smoothly curved bands. For graphite the typical band structure occurs with no linear band crossings and only one additional degenerate (split) band, resulting from the AB stacking pattern combined with periodic boundary conditions in all 3 dimensions.

Thus far, only straightforward the AB stacking has been discussed. Figure 3.17 (b) shows the calculated band diagram for AA stacked BL-graphene (inter-layer distance $\approx$ 3.59 Å for my LDA-DFT calculations). I note that this configuration with the two layers exactly on top of each other (shift $\vec{s} = 0$ between the top and bottom layer), is less stable ($\sim$ +5 meV/atom, LDA-DFT) due to strong repulsion of the π systems [166]. Here also a splitting of the bands around the K-point can be observed, but additionally all bands keep their linear character. This can be simply described as the superposition of two sightly off set SL-graphene band

diagrams. This decoupling of the electron dispersion relation is a very interesting phenomenon for BL-graphene, but also possibly for graphene on graphite or other few-layer graphene systems [167]. It can be also observed for different angles between two rotated layers (also called “turbostratic graphite”), all energetically favourable compared to AA stacked graphene [166, 168, 169].

3.2.3 Mechanical properties of graphene

The C-C bond is one of the strongest in nature, resulting in one of the highest known Young’s modulus of $\approx$ 1 TPa (in-plane) [29, 139, 170, 171] for single-layer graphene. Considering only small deformations ($<$ 5 % strain or compression) an isotropic in-plane behaviour of the Young’s modulus can be considered [170, 172–174], and therefore only one value is stated. The in-plane strength is measured to be around 130 $\pm$10 GPa [12]. The in-plane Poisson’s ratio has been caculated to be $\nu_{12} \approx 0.2$ [29, 173]. Thus graphene is very promising as mechanical additive for polymer-based nanocomposites [175] or other composite structures [11]. Other properties such as stability, expansion or gas barrier behaviour can also be controlled by inserting graphene structures into composites [12].
The mechanical properties of graphene and other related structures such as CNTs and different nanosheets have been studied extensively in this thesis and more can be read in Chapter 6.

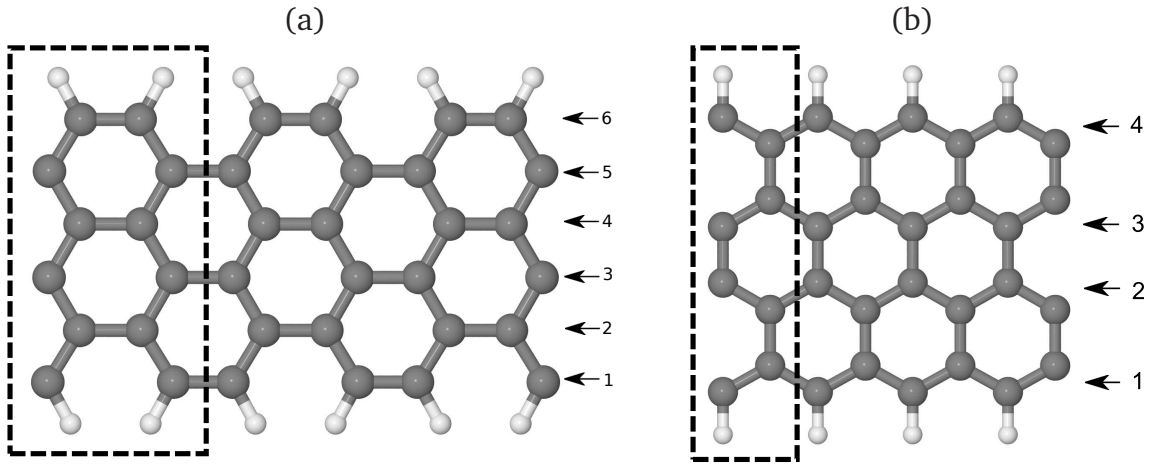

Figure 3.18: (a) H-terminated armchair graphene nanoribbon of width 6, (b) H-terminated zigzag graphene nanoribbon of width 4. For both cases the smallest possible repetition cell along the ribbon axis is shown with dotted lines. The definition of width for straight armchair or zigzag ribbons is indicated with numbers introduced by Cervantes-Sodi *et al.* [177]. C atoms are shown grey and H atoms are white.

3.3 Graphene nanoribbons

In reality, graphene is not an infinite plane but is constrained by edges. By cutting a graphene sheet twice parallel along the same direction, so called graphene nanoribbons (GNRs) can be tailored. Considering the common armchair or zigzag edges directly two types of straight ribbons can be build, called armchair graphene nanoribbons (AGNRs) and zigzag graphene nanoribbons (ZGNRs) as shown in Figure 3.18. Additionally a mix of both edge types is possible, leading to so called chiral GNRs (CGNRs). Here the graphene sheet is cut twice parallel along a certain direction defined for example with the orientation angle α (see section 3.2.1), leading to chiral edges. For CGNRs the repetition cells are more complex, normally containing a large number of atoms, and therefore relatively few theoretical studies exist to date [159], but such edges are seen experimentally [176].

Graphene nanoribbons (GNRs) have different properties from the infinite bulk material, notably they can display a finite band gap as a function of ribbon width and

orientation [37, 38, 148]. This can be explained physically by the quantum confinement effect due to a narrow ribbon width and periodic conditions only in the direction along the ribbon [178]. From a more chemistry based point of view this behaviour has been similarly predicted based on Clar sextet theory [179, 180].

A simple and widely used theoretical approach to terminate a graphene sheet or GNRs is to use H-terminated graphene edges [148, 156] (see also Figure 3.18). This satisfies the dangling bonds of the edge carbon atoms in a classical theoretical manner well known from organic chemistry. However seen from a more chemically realistic point of view, these edges are an easily accessible way to chemically functionalise the graphene ribbons and hence modify its properties. Regarding finite graphene nanostructures such as well defined one-dimensional (1D) nanoribbons or zero-dimensional (0D) graphene flakes, the edge properties appear to be very important, as demonstrated by the many recent literature studies [140, 156, 157, 181]. The physical and chemical behaviour of the 1D edges will be superimposed on that of the two-dimensional graphene. Therefore, careful design of graphene edges allows us to define and design the graphene nanoribbon properties as has been shown in work done in this thesis [140]. Analogous to ripples in graphene sheets, 1D GNRs offer additional potential deformations modes such as twisting, edge-rippling, buckling or folding which are discussed detailed in Chapter 5.

3.3.1 Producing graphene nanoribbons

GNRs can be produced by unzipping carbon nanotubes [39, 182–186], lithography [40, 187], etching [188] and controlled chemical bottom-up methods [41]. Unzipping CNTs has notably became a hot topic, as the control of producing and handling CNTs is now well understood after intense investigation for two decades. Many different approaches to unzip CNTs have been successfully applied, offering different possibilities when processing the nanoribbons afterwards. The applied techniques cover a brought range from chemical or catalytic methods to methods using an electron beam as “scissor” to unzip the CNTs (see Figure 3.19) [189].

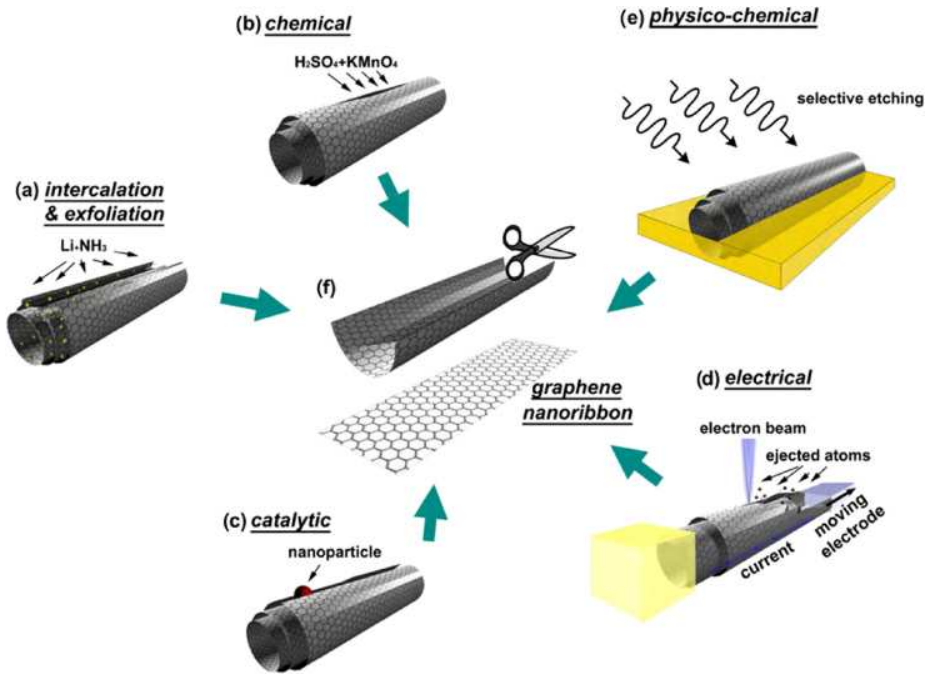

Figure 3.19: Overview of different methods to unzip CNTs: (a) Intercalation-exfoliation of MWCNTs, involving treatments in liquid NH_3 and Li, and subsequent exfoliation using HCl and heat treatments, (b) chemical route involving acid reactions that break carbon-carbon bonds (e.g. using H_2SO_4 and $KMnO_4$ as oxidizing agents), (c) catalytic approaches, in which metal nanoparticles “cut" the nanotube longitudinally like a pair of scissors, (d) electrically by passing an electric current through a nanotube and (e) physicochemical method by embedding the tubes in a polymer matrix followed by Ar plasma treatment. The resulting structures are either GNRs or graphene sheets (f). (Image from [189, 190])

Through unzipping of CNTs (also possible with the outer tube of MWCNTs) normally ribbons in the width range of 10 - 40 nm width are produced [39, 184, 186]. In this nm range the lateral 1D quantum confinement effects are weak and no significant band gap opening is expected. Additionally, the control of the edges is not precise in the CNT unzipping experiments to date, and various edge types can be found.

Here the clear advantage of the bottom-up growth is visible, using temperature controlled self-assemble processes of organic precursor molecules [41, 42]. On

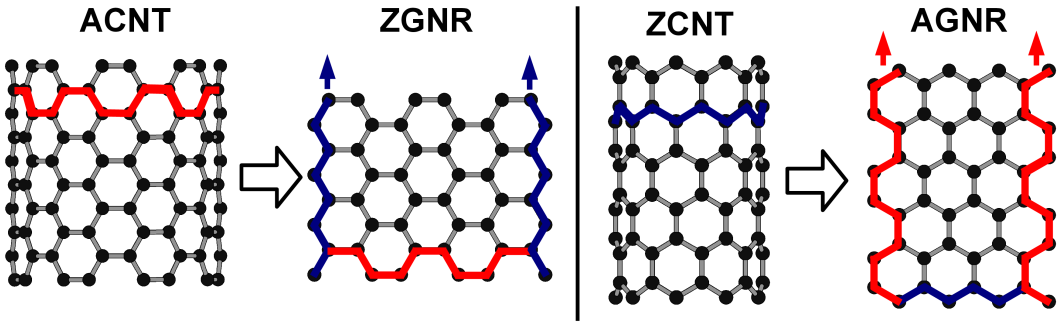

Figure 3.20: Armchair CNTs (ACNTs) and zigzag CNTs (ZCNTs) and their transformations to GNRs when unzipping along the tube axis: ACNT $\rightarrow$ ZGNR and ZCNT $\rightarrow$ AGNR.

Cu(111) and Au(111) surfaces the growth of an atomically precise width 7 armchair GNR was demonstrated. The edges on this ribbons and the edge H-termination are precisely controlled, and a band gap of $\sim$ 2.3 eV was measured [42].

The definition of the chirality of a CNT is chosen to be the carbon arrangement perpendicular to the tube axis for armchair and zigzag CNTs. For GNRs this can lead to confusion as here the definition is based on the edges parallel to the ribbon axis, *i.e.* the two definitions are based on orientations orthogonal to each other. Thus unzipping a ZCNT results in a AGNR and an unzipped ACNT gives a ZGNR (see also Figure 3.20).

These new 1D graphene nanoribbons, in the best case atomically sharp defined nanostructures, offer great potential for nanoelectronics [191], optoelectronic [181, 192, 193] and (nano-) composites [194]. Even GNRs with less precise controlled edges, *e.g.* chiral edges, could be sufficient as a first step to built new fast, cheap and efficient transistors as preliminary simulations from Yoon and Guo [195] show.

3.4 Related single layer materials

Many layered materials exist with only weak interactions between the individual layers *e.g.* graphite, h-BN or MoS_2, also oxides, halides and many clay and cement materials [196–199]. Chemical solution based graphite exfoliation to produce single-layer material has recently been successfully extended to other layered bulk materials such as BN, MoS_2, WS_2, $MoSe_2$, $MoTe_2$ and $NiTe_2$ [198]. Single- or few-layered structures such as h-BN can be additional produced by MBE and CVD growth [200]. The case of an isolated MoS_2 nanosheet is shown in Figure 3.21, as well as the parent layered bulk material. The single-layer structure is not atomically flat as in the case of graphene, and the stacking orientations is more complex.
For new composites, these single-layered nanosheets offer various possibilities to tune mechanical, electronic or optical properties. Single-layer nanosheets (two-dimensional crystals) offer new properties themselves, and can also be used to create controlled hetero-structures of different stacked materials [131, 200]. First experiments show that graphene and h-BN could be a very promising couple when stacked. h-BN is an atomically smooth 2D nanosheet with very similar lattice constants and AB sublattice pattern as graphene. As h-BN is a large bandgap insulator, graphene maintains its unique properties around the K-point, when lying on top of h-BN [201]. Another interesting way to combine different 2D materials is the design of in-plane hetero-structures, within one single-layer, for example graphene quantum dots embedded in a h-BN sheet as proposed recently [202].

The in-plane Young's modulus of layered materials, including graphene, h-BN, MoS_2, WS_2, $MoSe_2$ and $MoTe_2$, is studied in Chapter 6.

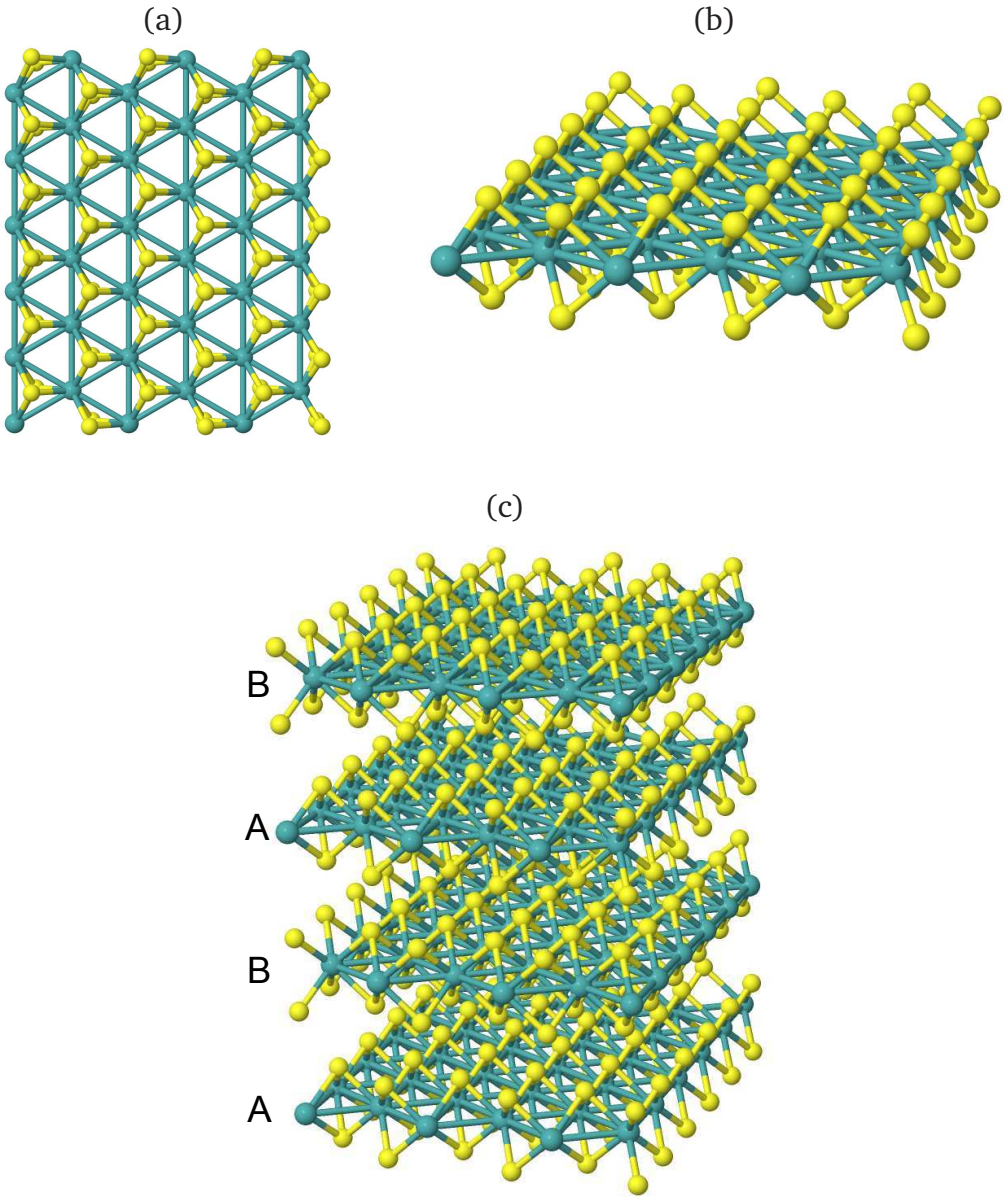

Figure 3.21: (a) Top view of an isolated single MoS_2 nanosheet, (b) perspective view of the MoS_2 nanosheet, (c) layered MoS_2 bulk with "AB" stacking pattern. Mo atoms are shown cyan and S atoms are yellow.

Chapter 4

Graphene edges: unterminated and hydrogenated

This chapter concentrates on graphene edges and the influence of different hydrogen edge configurations. In sections 4.1 and 4.2, I report results of systematically studied unterminated graphene edges, aiming to give a reasonable overview of possible realistic unterminated graphene edge configurations. Therefore the armchair, the zigzag and the Klein edge are discussed as the basic structures to start with (see also Chapter 3 section 3.2.1). Next, a new edge termination unique for 2D materials, undergoing a folding back of the unterminated edge on the graphene sheet, is reviewed and studied. While the formation energy is dependent on the edge "nanotube" diameter, it was found that large tube diameter configurations are more thermodynamically favourable compared to all other possible flat unterminated configurations.

Notably less attention has been paid so far in the literature to the Klein edge. This is an important fact, as for more complex hydrogenated edge configurations I find the Klein edge plays an important role.
Investigating hydrogenated graphene edges, I found new possible stable hydrogenated edge configurations of CH_3 type, both for armchair and zigzag edges, not reported in the literature in this detailed manner. Furthermore in this chapter, I present for the first time hydrogenated reconstructed Klein edges, which could play

an important role in the graphene growth mechanism. Based on the new findings, possible growth mechanisms are proposed, related to experimental observations.

Results for unterminated pristine graphene edges are directly comparable to experimental clean conditions performed in ultra high vacuum (UHV) as for STM or TEM measurements. Thus for direct experimental comparison, high resolution transmission electron microscopy (HRTEM) images have been simulated by Alberto Zobelli using a full dynamical multi-slice method as implemented in the *SimulaTEM* code [160, 203] (relevant for Figures 4.1 and 4.4).

All structures presented here have been modelled using a LDA-DFT approach as implemented in the *AIMPRO* code (see also Chapter 2). Graphene edges in section 4.1, 4.2, 4.3, 4.4 and 4.5 are modelled using GNR with width ~ 50 Å in orthogonal supercells. In all cases, both opposed GNR edges are modelled with similar edge configurations. Supercell sizes have been checked carefully and chosen to be sufficiently large, considering a vacuum distance in all directions between the ribbons of > 12 Å, avoiding interactions with neighbouring GNRs. More computational details are given in section 4.8.

4.1 Unterminated flat graphene edges

While pristine armchair and zigzag edges have been widely studied, for unterminated flat edges more configurations can exist [161]. In Figure 4.1, the typical most stable unterminated graphene edge configurations have been modelled. Edge formation energies per unit length (eV/Å), also referred to simply as "edge energy", are calculated as followed:

$$E_{form} = \frac{E_{tot} - n_C \cdot E_C}{2L} \,, \tag{4.1}$$

where E_{tot} gives the total internal energy of a system with n_C carbon atoms, E_C is the total energy associated with a single carbon atom of a perfect graphene sheet and L is the ribbon edge length (see also [156, 160]).

Figure 4.1 clearly shows that the armchair and the (5-7) reconstructed zigzag edges represent the most stable configurations (around $E_{form} \approx +1.1$ eV/Å). This result is in excellent agreement with previous calculations performed by Koskinen *et al.* [161]. The Klein edge [147] can be identified as least stable configuration, with unsaturated single edge carbon atoms. More interest attracts the reconstructed Klein edge studied the first time in the literature [160] (see bottom right Figure 4.1 (f)), gaining around 0.7 eV/Å compared to the pristine Klein edge through rebonding in pairs. Still with an edge formation energy of $E_{form} = +1.5$ eV/Å it is energetically far less stable than the armchair, (5-7) reconstructed zigzag or zigzag edge. But as "transition" configuration this could lower the energy barriers for fluctuations under the electron beam. Segments of the unreconstructed Klein edge were recently reported using annular dark field microscopy [150, 204]. It can be speculated, considering its general instability, that the observed Klein edges might been partly hydrogenated, what is not detectable by annular dark field microscopy. As a possible variation for the armchair edge, the (5-6) reconstructed configuration has been modelled (Figure 4.1 (d)), resulting in $E_{form} = +1.63$ eV/Å. In literature also the (6-7-7) armchair reconstructions is discussed, with $E_{form} = +1.23$ eV/Å calculated edge formation energy [161], but all armchair reconstructions are generally found to be less stable configuration compared to the pristine armchair edge.

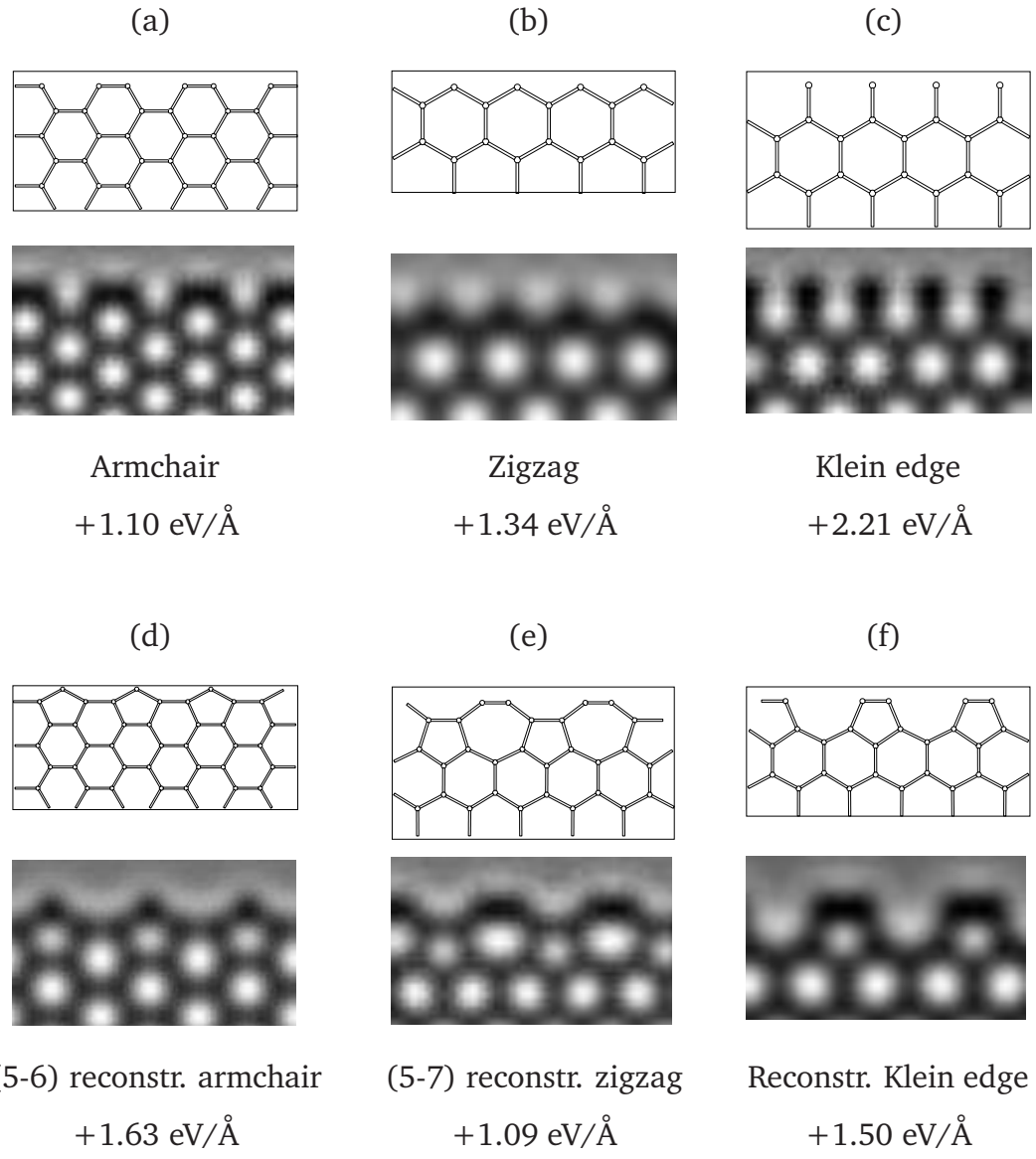

Figure 4.1: Calculated edge formation energies and corresponding simulated HRTEM images for: Upper panel (a)-(c), the three pristine flat unterminated graphene edge configurations. Lower panel (d)-(f), one possible edge reconstructions for each pristine type above. (Images from [160])

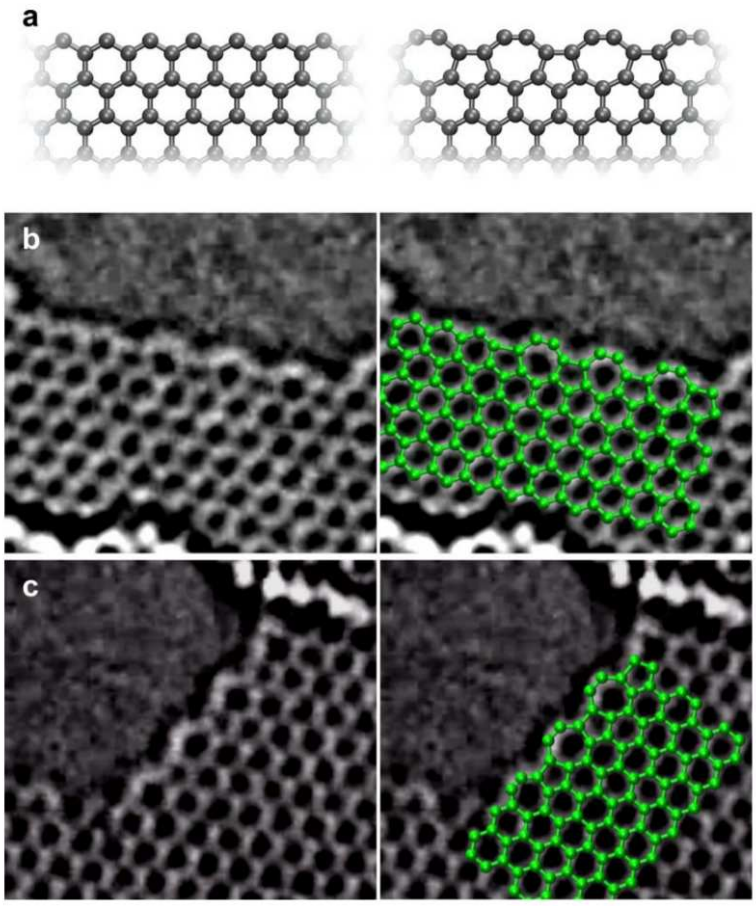

Figure 4.2: (a) left: normal zigzag edge, right: (5-7) reconstructed zigzag edge, (b) left: zigzag edge reconstruction from TEM film taken by [149], right: highlighted assigned reconstructed structure, (c) left: another reconstructed zigzag edge from [149], right: highlighted assigned reconstructed structure. (Images from [162])

Realistically in TEM experiments under an electron beam, unterminated edge configurations are fluctuating as shown via short films by Girit *et al.* [149]. These films taken during the TEM measurements have been revisited later by Koskinen *et al.* [162], and they found the (5-7) zigzag reconstructions shown in Figure 4.2, as theoretically predicted before. Thus it can be concluded that graphene edges in general tend to reconstruct continuously to energetically similar or more stable configurations, while performing TEM studies.
Additional to this flat basic unterminated edge configurations, another stable possible configuration has been identified, discussed in the next section.

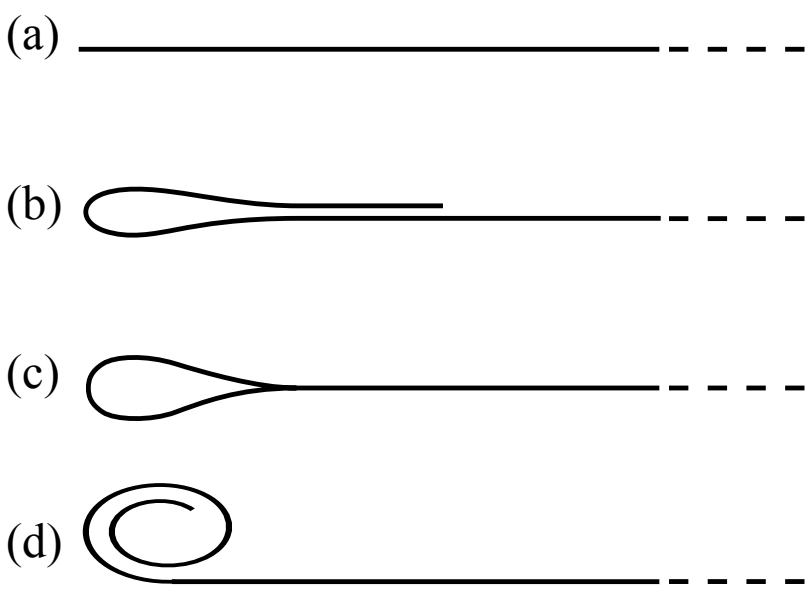

Figure 4.3: Schematic cross-section showing four possible out-of-plane distortions of graphene sheet edges orthogonal to the edge line: (a) flat, (b) folded, (c) folded and rebonded (tubing) and (d) scrolled edges. (Image from [205])

4.2 Folded and tubed graphene edges

First it has to be remembered, that some possible edge distortions have no direct analogy in surface termination of three-dimensional materials, *i.e.* these edge types are unique to two-dimensional layered materials. Keeping that in mind, looking now at a graphene edge in cross-section, there are four distinct classes of edge distortion possible. The first in Figure 4.3 (a) is to simply remain planar, as discussed before for unterminated edges. However, if we consider a thought experiment where the edge is now pulled up out of the graphene plane and back above the graphene layer, there are three possible structures depending on the angle at which the edge then approaches the graphene surface below it. If the approach angle is less than 90° the edge folds back on itself, resulting in a bi-layer structure shown in Figure 4.3 (b). If the approach angle is 90° the edge will bond into the sheet below (Figure 4.3 (c)), creating a "drop-shaped" nanotube at the graphene edge. If the approach angle is greater than 90° the edge folds back in on itself, creating a scroll (Figure 4.3 (d)).

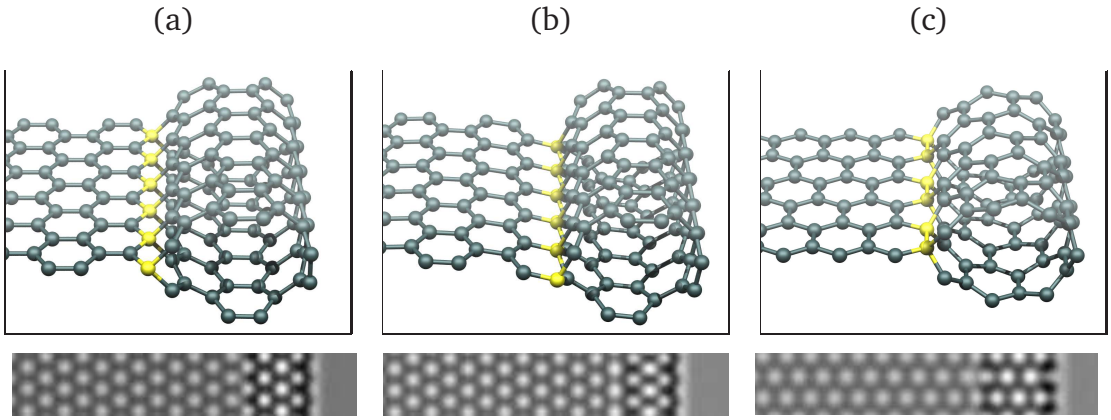

Figure 4.4: Upper panel: structure of (4,4) armchair (a), (4,4) armchair-like (b) and (8,0) zigzag (c) nanotube terminated graphene sheet. sp^3-like coordinated carbon atoms are marked in yellow. Bottom panel: corresponding simulated HRTEM images. (Images from [160])

While scrolling, and folding at graphene edges have been already known in literature [149, 204, 206–208], a new type of termination leading to the stabilization of the edge can be achieved by taking an unreconstructed free edge, folding it back on itself and bonding the edge dangling bonds to a line of basal graphene atoms. A rolled zigzag edge can bond into the graphene plane in two configurations: either above what would be zigzag edge atoms or Klein edge atoms. Rolled armchair edges can only bond to equivalent armchair edge atoms. Drawing on carbon nanotube nomenclature, it will be referred to these new edge types as armchair nanotube terminated (Figure 4.4 (a)), armchair-like nanotube terminated (Figure 4.4 (b)), and zigzag nanotube terminated (Figure 4.4 (c)) respectively. In all cases the line of carbon atoms bridging the tube and graphene layer adopts an sp^3-like hybridization with average bond lengths ($\sim$ 1.50 Å) and angles ($\sim$ 108°) close to those of diamond. Locally, the structure is similar to the core of the zigzag prismatic dislocation in AA graphite [209]. The sp^3-like bonding allows the tube to localise strain, resulting in a “drop”-shaped cross-section (Figure 4.3 (c)).

As next step the edge formation energies (or simply referred to as “edge energy”) of different unterminated edge configurations are compared to a range of armchair, armchair-like and zigzag nanotube terminated edges. Figure 4.5 presents edge en-

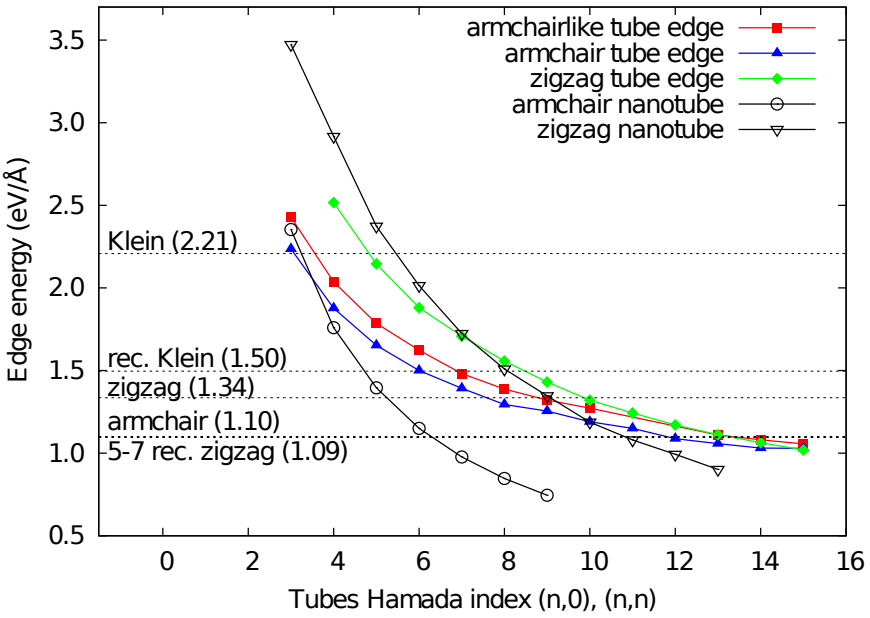

Figure 4.5: Edge formation energy (eV/Å) for different graphene edges (dashed lines indicated on the figure: Klein, reconstructed Klein, zigzag, armchair and (5-7) reconstructed zigzag, see Figure 4.1), free standing zigzag and armchair tubes, armchair-, armchair-like-, and zigzag-tube terminated edges. (Image from [160])

ergies for different types of free and tube terminated edges as a function of the Hamada index (n,0) and (n,n) of the tube. For comparison, the values for free-standing isolated armchair and zigzag nanotubes are included. Consistent with an earlier study [210], free standing small tubes with diameters below 4 Å (i.e. (3,3) and (5,0) and below) are unstable compared to a flat graphene sheet. This means that it is thermodynamically preferable to split these tubes open creating two armchiar / (5-7) reconstr. zigzag edges, even with unfunctionalised edges. Indeed experimentally these small radii nanotubes have not been observed on their own but may exist as inner tubes in large multiwalled nanotubes [211, 212].

It can be seen here, however, that such small nanotubes are more stable when formed on graphene ribbon edges, through localisation of the nanotube strain along the sp^3-coordinated tetrahedral bonding line, e.g. a (3,3) armchair tube and all zigzag tubes up to (7,0). Comparing to free zigzag edge configurations, graphene edges become more stable when rolled in tubes above (8,8). Rolled

(tubed) graphene armchair edges have a lower energy than free edges when forming nanotubes larger than (14,0). For the largest presented tube terminated edges (for all tubed graphene edge types), formation energies are lower than any of the previously proposed free edge configurations.
When extrapolating this further to larger diameter tubes it might be expected that they collapse due to Van der Waals interactions between walls to a dog-bone cross-section [213]. However, the droplet cross-section induced by the line of sp^3-like carbon atoms naturally induces a "local collapse", and this pinched region extends further as the tube diameter increases. Thus for large diameters, rolled edges converge to a classical folded edge which then terminate some distance from the actual edge via a line of sp^3-like bonds. It can be noted that in no case is the combination of a free tube and graphene edge more stable than the nanotube terminated edge [214] *i.e.* there will be no thermodynamic driving force for nanotube production from rolled edges (see Figure 4.3).

4.2.1 Electronic properties of GNRs with tubed edges

Next the effect of tubed graphene edges on the electronic properties of graphene ribbons is going to be examined. In Figure 4.6, the electronic density of states for the (8,8) and (8,0) tube terminated edges are plotted. This plot shows an interesting combination of the graphene and nanotube behaviour. In spite of different electronic character of free standing (8,8) and (8,0) tubes, *i.e.* metallic and semiconducting, in both cases the composite system has a non-zero density of states at the Fermi level. For a zigzag tube termination, the background density of states around the Fermi level rises smoothly, reflecting the graphene density of states, overlaid on which there is a series of peaks reminiscent of Van Hove singularities, characteristic of a nanotube. For the armchair-tube terminated edge, *i.e.* a rolled zigzag graphene edge, there is a sharp peak at the Fermi level similar to that seen for flat non-magnetic unterminated zigzag edges [161, 215, 216]. Such Fermi level peaks can lead to magnetic instability and indeed, the spin-polarized calculations show a ferromagnetic configuration to be the lowest energy state (slightly lowering

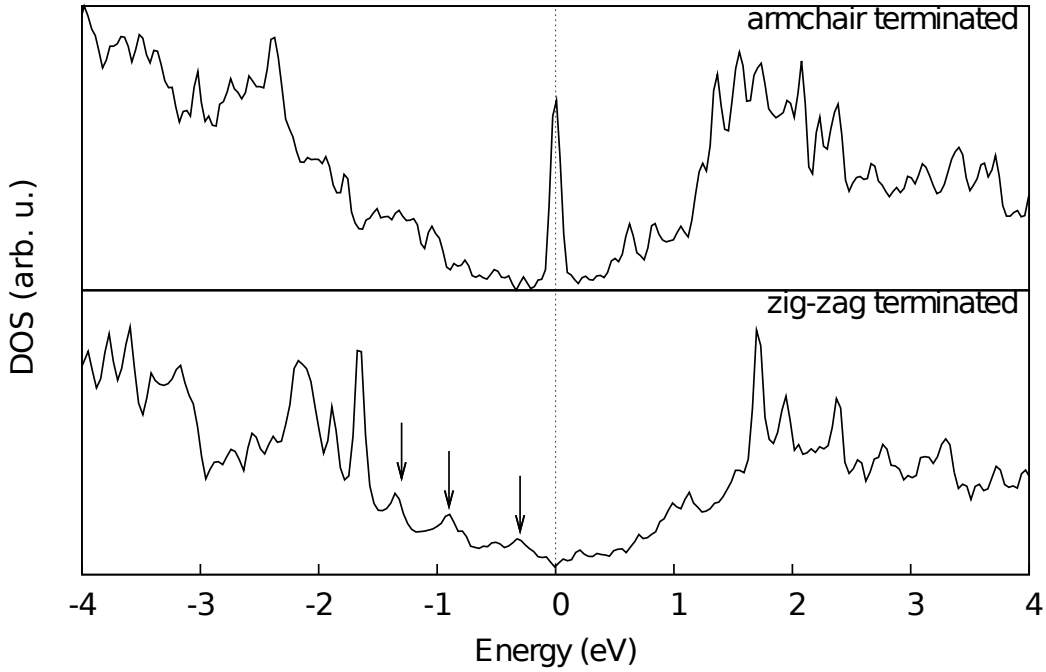

Figure 4.6: Calculated density of states for (a) (8,8) armchair- and (b) (8,0) zigzag-nanotube terminated graphene edge. The Van Hove singularities are marked by arrows. (Image from [160])

the edge energy of the system by only 20 meV/Å, see also Figure 4.13), although this must be treated with caution given the use of the local density approximation. Notably LDA-DFT calculations tend often to (energetically) favour configurations with higher spin moments.

The peak consists of two degenerate states which can be seen in the associated band structure (Figure 4.7 (a)) as involving a mixing of several bands. Plotting these states at the Γ and X point (Figure 4.7 (b)) shows that the Fermi level spike is localised mainly on the row of graphene atoms next to the sp^3-carbon atoms, mirroring the edge state seen in flat zigzag terminated graphene [156, 216, 217], whereas at the X-point the highest occupied state comes from dispersive edge states located in the nanotube segment along the junction. This convergence of three zigzag edges at the line of sp^3-bonded carbon atoms suggests possible interesting magnetic behaviour under an applied field.

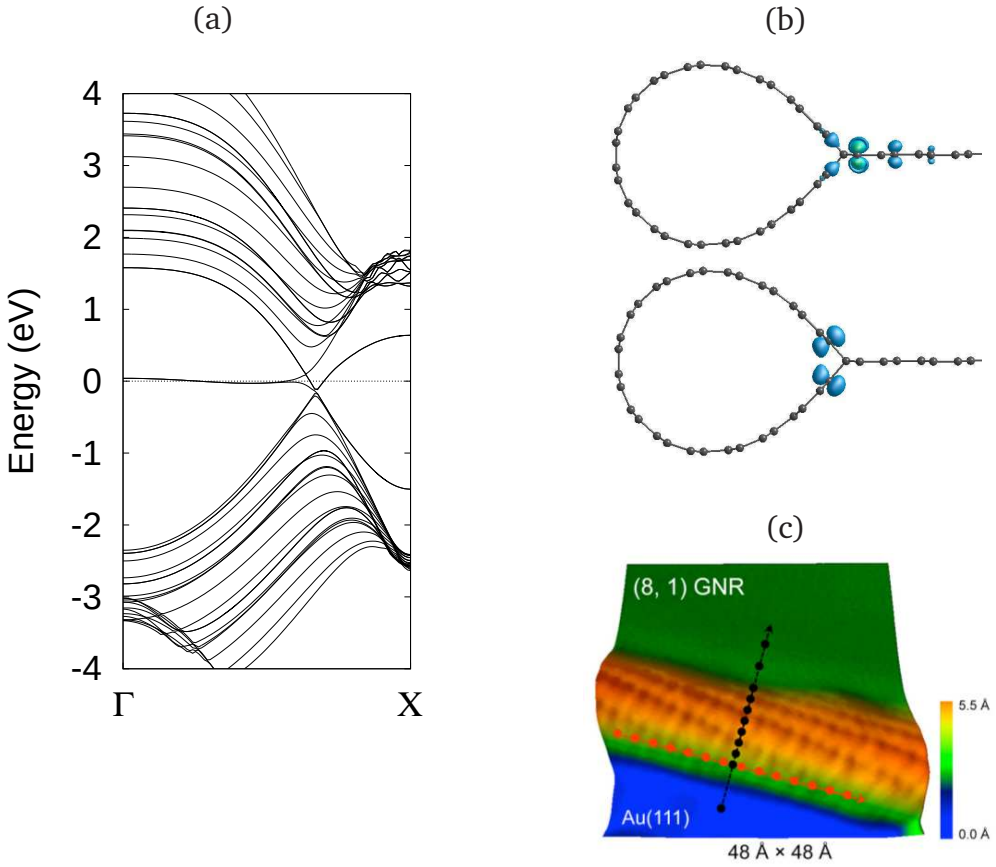

Figure 4.7: (a) Band structure for (8,8) armchair-nanotube terminated edges, and (b) distribution of highest occupied state at the Γ-point (upper) and X-point (lower). (c) Showing a atomically-resolved topography of a GNR edge taken from [176], described therein as (8, 1) chiral edge, but could as well be a tubed graphene edge. (Images (a) and (b) from [160])

It can be noted that the zigzag metallic edge state is preserved in this configuration, and unlike the unterminated simple zigzag edge, it will also be partially protected from environmental attack, since all neighbouring atoms are fully coordinated. Notably it might be expected to be stable in air. These states also suggest intriguing transport behaviour, with possible conduction channels both along the edge of the graphene and in the edge states in the nanotube segment.

First experimental data of graphene edges supports the new tubed edge configurations [176] (see Figure 4.7 (c)), and the results should be revisited with this new insights.

4.3 Hydrogenated armchair graphene edges

Considering different H-terminated graphene edge configurations the edge formation energies have been calculated similar to (4.1), but now also including n_H hydrogen atoms:

$$E_{form,H_2} = \frac{E_{tot} - n_C \cdot E_C - n_H \cdot E_H}{2L} \ . \tag{4.2}$$

In (4.2), $E_H = \frac{1}{2}E_{tot,H_2}$ gives the energy of one H atom in an isolated H_2 molecule. E_{tot} is the total internal energy of the wide nanoribbon system, calculated using a orthorhombic supercell. L is the length of the repeated nanoribbon segment in the supercell with two identical edge configurations. Similar to the unterminated edges, nanoribbons of width $\sim$ 50 Å have been used to model different uncoupled H-terminated edge configurations [216]. A discussion of the hydrogen chemical potential μ_{H_2} follows in section 4.7.

To define and differentiate the different hydrogenated edge configurations (see Figures 4.8, 4.12 and 4.15), I follow here the nomenclature introduced by Wassmann *et al.* [156], extended by the Klein and the reconstructed Klein edge (a: armchair, z: zigzag, k: Klein and rk: reconstr. Klein edge). The subscript numbers are defining the number of hydrogen atoms on every edge carbon atom, in a edge repeating segment. u and d stands for "up" and "down" in the superscript, when the edge carbon atoms are not found to stay flat in-plane (also marked directly in the relevant schematic figures).

For all hydrogenated edge configurations studied on armchair, zigzag, Klein and reconstr. Klein edges, the strain of the hydrogenated GNRs along the ribbon axis compared to pristine graphene has been found to be only very small ($< \pm$ 0.3 %). Preliminary calculations show as well that for small GNR widths the strain increases only slightly, remaining in all cases less than $\pm$ 1 %.

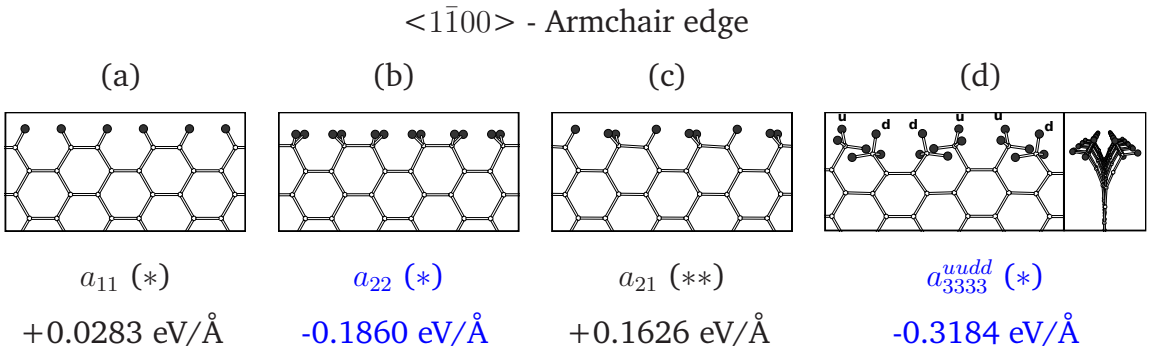

Figure 4.8: (a)-(d) Edge formation energies of hydrogenated armchair edges, (d) with side view. H atoms are schematic represented by black spheres. Energetically favourable edges are highlighted blue. (∗): Non-magnetic, (∗∗): Magnetic.

4.3.1 Stability of hydrogenated pristine armchair edges

I started calculating the edge formation energies of different possible hydrogenated edge configurations for pristine armchair edges shown in Figure 4.8. My calculations are in good agreement with previous calculations in the literature [156, 161]. In general, hydrogenated reconstructed armchair edges, *e.g.* the (5-6) or (6-7-7) reconstruction, do not show any important additional stable configurations as predicted in the literature [156], and thus are not recalculated here.

While in literature so far always the a_{22} edge is declared as the most stable hydrogenated armchair edge, I found additionally the high hydrogen density a_{3333}^{uudd} edge configuration (Figure 4.8 (d)). The new a_{3333}^{uudd} edge configuration is with E_{form,H_2} = -0.3184 eV/Å significantly more stable than the armchair a_{22} edge with E_{form,H_2} = -0.1860 eV/Å . While two hydrogen atoms per edge carbon atom (a_{22}) stabilise the pristine armchair edge, by adding one additional hydrogen per edge carbon atom the former C-C edge bond can break, forming now CH_3 groups bond to the next inner armchair line. The CH_3 edge groups are most stable in an up-up-down-down ("$uudd$") edge configuration, relieving edge strain due to steric hindrance. This rippled graphene edge configuration has been identified to be characteristic for the armchair edge and is discussed in detail in Chapter 5.

It should be noticed that in the most stable configurations the armchair edge tries to provide single bonded edge carbon atoms to the carbon honeycomb network. In both stable armchair edge configurations a_{22} and a_{3333}^{uudd}, the edge carbon atoms are sp^3-like hybridized, forming single bonds with all four neighbouring atoms, thus as well to the armchair backbone line.

While in general all my calculated edge energies for H-terminated armchair edges reflect the same tendencies as calculated by Wassmann *et al.* [156], it should be mentioned that the a_{22} edge from [156] shows less stability with a edge formation energy of E_{form,H_2} = -0.071 eV/Å (this work E_{form,H_2} = -0.1860 eV/Å), while all other values are in a similar range compared to my values. A possible explanation, beside the plane-wave code used by Wassmann *et al.* [156], could be the use of smaller supercells in this earlier study, with only 8.5 Å vacuum distance between two graphene layers, and 9.5 Å vacuum distance between the edges [156]. In my calculations for all hydrogenated edges in each direction a vacuum distance of 15 Å or larger has been used to avoid interactions. Ribbon interactions could therefore give rise to the less stable edge formation energy of E_{form,H_2} = -0.071 eV/Å for the a_{22} armchair edge in this former study, as the out-of-plane hydrogen atoms sticking to the edge carbon atoms reduce the vacuum distance about 1.72 Å. Another difference are my ribbon widths of $\sim$ 50 Å , thus about twice as large as in the literature calculations.

4.3.2 Electronic properties of hydrogenated pristine armchair edges

A typical band diagram with the corresponding density of states (DOS) of an AGNR is shown in Figure 4.9 (a). The AGNR shows a small finite bandgap at Γ, due to the lateral quantum confinement. Changing the edge configuration to a_{22} as shown in Figure 4.9 (b) slightly enlarges the energy gap at Γ. It can be further noted that the bands close to the Fermi level are paired together for the a_{22} configuration, but else the band diagram is similar to the a_{11} case.

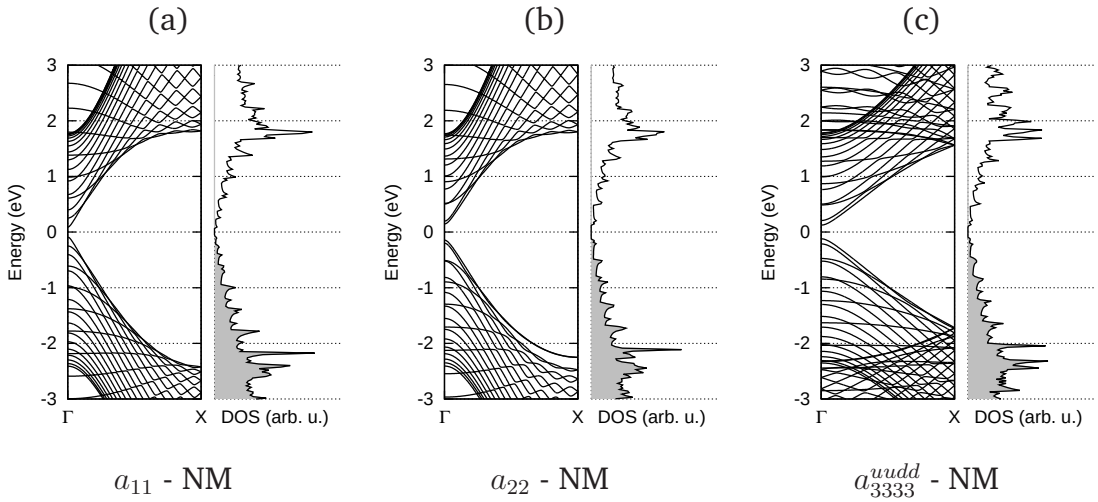

Figure 4.9: Band diagram and DOS of AGNRs with symmetric edge configurations (a) a_{11}, (b) a_{22} and (c) a_{3333}^{uudd}. A ribbon width of 42 (50.07 Å) has been used in all cases, modelling always the smallest possible unit cell. (NM: Non-magnetic)

In Figure 4.9 (c), the band diagram of the new most stable a_{3333}^{uudd} edge configuration is plotted. No significant changes in the band diagram or the DOS near the Fermi level at Γ are visible compared to Figure 4.9 (a) and (b). As well compared to the a_{22} configuration, no new edge states near the Fermi level appear. However, deeper levels are induced around $\sim$ -2.5 eV and $\sim$ +2.0 eV, probably related to the single bonded CH_3 edge groups. Coupling between the opposed edges is negligible for those wide AGNRs. Thus the relatively large gain in stability for the a_{3333}^{uudd} configuration can mainly be explained through strain relief via neighbouring up and down bended edges carbon atoms.

AGNRs with different opposed edge hydrogenation

Additional to a symmetrical H-terminated GNR, I tested further the mix of a_{11} on one ribbon edge and a_{22} on the other ribbon edge of AGNRs. For AGNRs of different widths the bandgap shows a $3N$ periodicity calculated in different studies [37, 140, 179, 180], but only considering a_{11} hydrogenated edges (-H termination in Figure 4.10). The a_{11} configuration keeps all edge carbon atoms in the sp^2 hybridization, typical for graphene. But if changing the edge termination to a_{22} (-2H

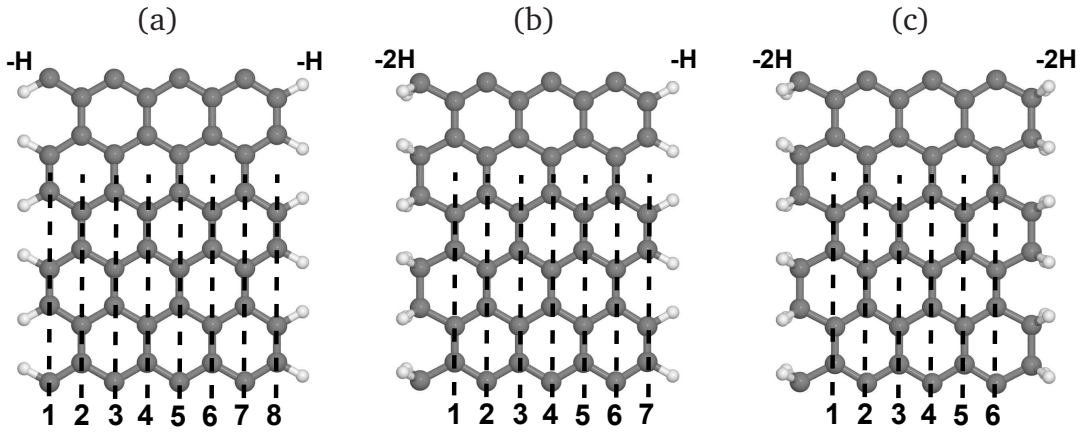

Figure 4.10: (a)-(c) Shifting the effective AGNR width $n_{effective}$ via different -H (a_{11}) and -2H (a_{22}) armchair edge configurations. The number of carbon atoms is in all cases constant. Through changing the edge functionalization to -2H, the edge carbon dimer row is not counted. On the top the edge termination is stated as -H and -2H, on the bottom $n_{effective}$ is shown as guide for the eye.

termination in Figure 4.10), the two hydrogen atoms and the edge carbon atom form sp^3-like hybridized orbitals. This breaks the aromaticity in the edge honeycomb armchair structure and reduces the effective ribbon width n by one dimer row $n_{effective} = n - 1$ (see Figure 4.10). As shown already by Koskinen *et al.* [161], unterminated graphene edges are decoupled in terms of edge formation energy down to very narrow ribbons < 10 Å. Following this idea of uncoupled edges leads to the possibility that both edges could be terminated independently from each other. In Figure 4.11 (a), I have calculated the bandgap for the three possible cases considering a_{11} (-H) and a_{22} (-2H) edge termination of narrow AGNRs. The shift of the periodic bandgap behaviour is clearly visible for -H/-2H $\rightarrow n_{effective} = n - 1$ and for -2H/-2H $\rightarrow n_{effective} = n - 2$.

While writing the chapter, I discovered a recently published article regarding this effect in the same way [218] for classic ribbon width [177] 7, 8 and 9, confirming exactly my calculations and interpretations. This finding highlights an interesting point: shifting the bandgap only through different edge hydrogenation. Especially as recently the width 7 a_{11} terminated AGNR has been grown atomically precise

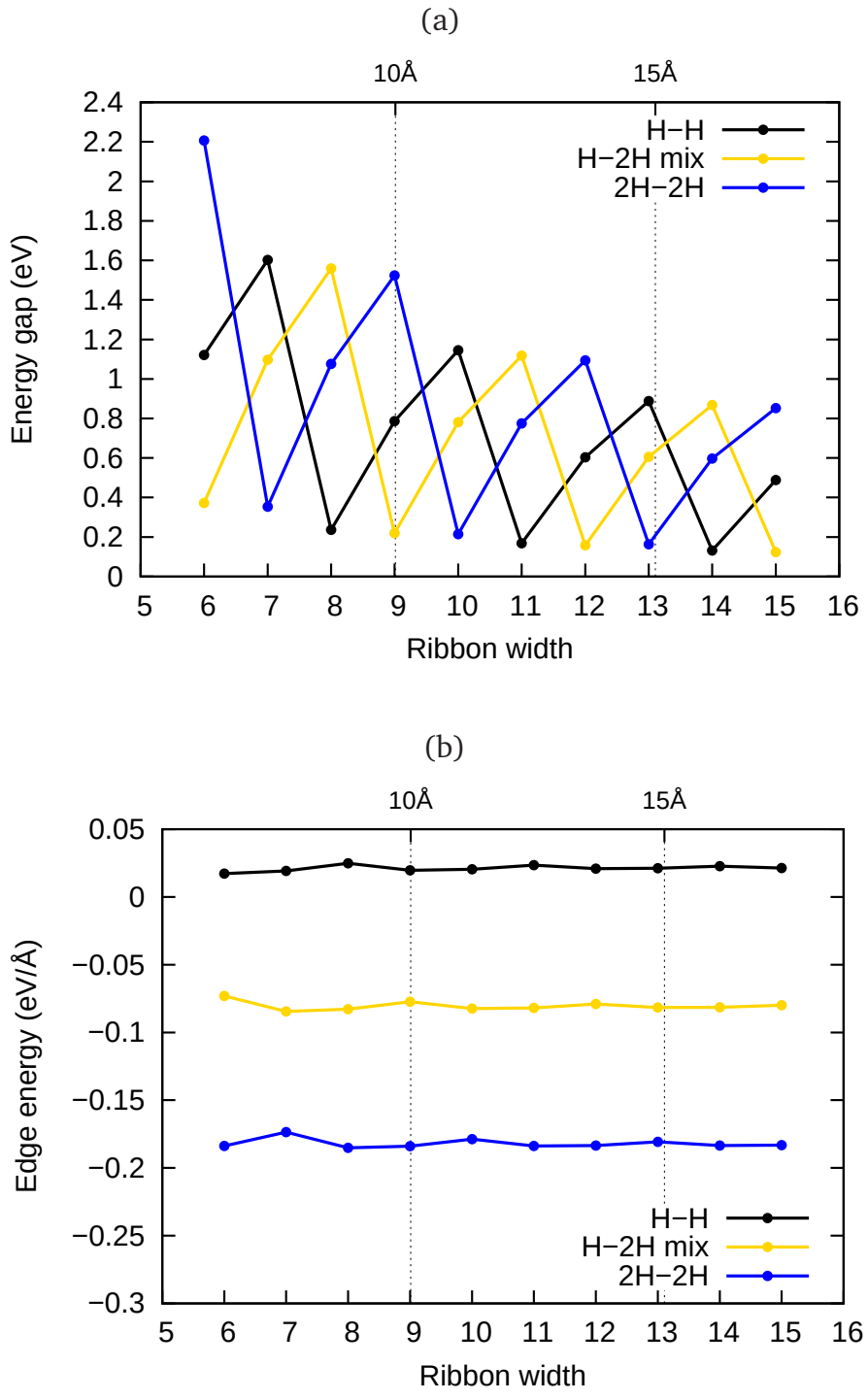

Figure 4.11: (a) Shifting the $3N$ periodicity, respectively the effective AGNR width $n_{effective}$, for AGNRs via different edge H-terminations. (b) Edge formation energy for different H-terminated edge configurations versus ribbon width. (The ribbon width on the x-axis in both graphs gives the classic defined width [177] for pure -H/-H terminated AGNRs, *i.e.* as in Figure 4.10 (a)).

[41, 42], using a promising bottom-up self-assembly approach on copper surfaces. It could be therefore possible to adapt the procedure and create other edge hydrogen terminations. As Figure 4.11 (a) shows, for a width 7 AGNR, the bandgap could be tuned massively ($\sim$ 1.6/1.1/0.35 eV) by changing the effective ribbon width. The bandgaps values are quantitatively underestimated as typical for LDA-DFT calculations. Nevertheless the change in bandgap permits a qualitative interpretation, and the same behaviour should be found using more adapted approximations. A first experimental value of the bandgap of a -H/-H terminated width 7 AGNR on Au(111) has recently been measured around 2.3 eV [42].

In Figure 4.11 (b), the edge energy is plotted for all three cases showing only small changes for very narrow ribbons. In general, decoupling of the armchair edges for small ribbon width is given by a constant edge energy over the whole range of tested AGNRs widths. This shows in more detail the edge decoupling of narrow AGNRs edges compared to the work of Koskinen *et al.* [161], whose calculations consider mainly GNRs with larger widths.

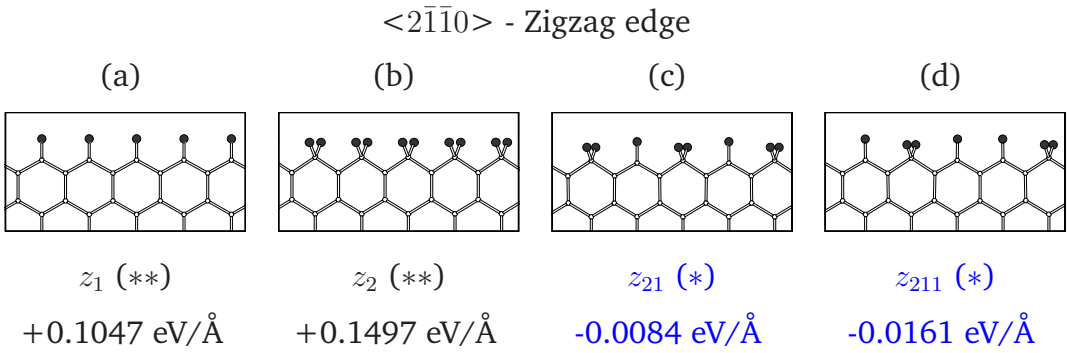

Figure 4.12: Edge formation energies of hydrogenated (a)-(d) armchair and (e)-(h) zigzag edges. H atoms are schematic represented by black spheres. Energetically favourable edges are highlighted blue. (∗): Non-magnetic, (∗∗): Magnetic.

4.4 Hydrogenated zigzag graphene edges

Similar to the previous sections for hydrogenated armchair edges, (4.2) is used to describe the edge stability per length.

4.4.1 Stability of hydrogenated pristine zigzag edges

Here I modelled different possible hydrogenated edge configurations starting with pristine zigzag edges shown in Figure 4.12. The energetic stabilities are in good agreement with previous calculations [156, 161, 216]. Similar to the armchair edges, reconstructed zigzag edges such as the (5-7) reconstruction are not recalculated here, as they don't show any important additional stable configuration [156]. The most stable hydrogenated pristine zigzag edge has been identified as the non-magnetic (NM) z_{211} configuration (Figure 4.12 (d)). Periodically one z_2 sp^3 and two z_1 sp^2 coordinated carbon atoms are present at the pristine zigzag edge. Predicting the z_{211} configuration most stable is in perfect agreement with other literature results [156, 216]. The stability of the z_{211} configuration can be explained using Clar's sextet rule for benzenoid aromatic rings [156, 179, 180, 219–221]. While the Clar's sextet rule is derived from chemistry fundamentals, a more physical explanation is given when studying the electronic properties in terms of band structure and the corresponding density of states (DOS).

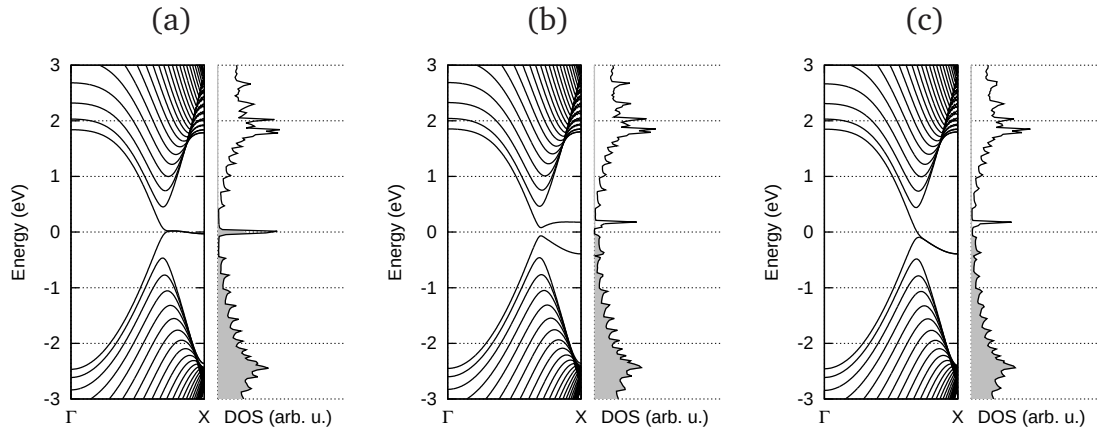

z_1 - NM	z_1 - AFM	z_1 - FM
0.0 μ_B/unit cell	0.0 μ_B/unit cell	0.611 μ_B/unit cell
+4.082 meV/unit cell	+0.0 meV/unit cell	+0.272 meV/unit cell

Figure 4.13: Band diagram and DOS of the possible magnetic states for a z_1 hydrogenated ZGNR, (a) non-magnetic (NM), (b) anti-ferromagnetic (AFM) and (c) ferromagnetic (FM). All cases are modelled for a width 25 (51.54 Å) ZGNR (50 carbon atoms, 2 hydrogen atoms). The structure and lattice parameter were optimised in a non spin-polarized calculation (NM). The unit cell size along the ribbon has been found 2.44 Å. Net spin magnetic moments and the energy difference respective to the AFM ground state (b) are given.

4.4.2 Electronic properties of hydrogenated pristine zigzag edges

In the literature, the anti-ferromagnetic (AFM) state has been predicted to be most stable in the case of simple hydrogenated (z_1) ZGNRs [222], with spin “up" states on one edge, coupling ferromagnetic locally along the edge, and spin “down" states on the opposed edge. In Figure 4.13, I have calculated the band diagram and the corresponding density of states (DOS) for the three possible magnetic states using a perfect z_1 hydrogenated wide ZGNR, with results in very good agreement to the literature [156, 215, 222, 223]. (In addition to the AFM configuration, AFM coupling locally along the edge carbon atoms within the same edge has been tested, but found less stable than edge carbon atoms coupling ferromagnetic by +65.44 meV/unit cell.) The net spin magnetic moment for the used cell is given in Bohr magnetons $\mu_B = \frac{e\hbar}{2m_e}$. In the NM and AFM case, the total net spin magnetic

moment is by definition zero, while for the FM case 0.611 μ_B/unit cell has been calculated. This value is in a similar range as 0.46 μ_B/unit cell using a width 8 ZGNR by Lee and Cho [215]. However, Jiang *et al.* [224] showed a slight increase of the net spin magnetic moment with increasing ribbon width calculating very small ZGNRs (width 4/5/6: 0.396/0.436/0.470 μ_B/unit cell). Tests for this smaller widths agree with the literature results (width 4/5/6/8: 0.432/0.438/0.440/0.446 μ_B/unit cell). Thus such a trend suggests to lead to increased values for wider ZGNRs.

Energy differences of the FM and the AFM configurations are very small (+0.272 meV/unit cell) for the width 25 ZGNR, close to the noise in the energy of the calculation. The energy difference of the AFM case with the NM is slightly larger at +4.082 meV/unit cell. These energy differences are very small compared to thinner ZGNRs used in the literature (width from 4 - 12) [216, 222, 224]. This can be explained with a decreasing coupling of the opposed edges with increasing ribbon width, due to a finite decay length of the magnetic edge states interaction range. A decay proportional to $\sim$ (width)$^{-1}$ has been theoretically proposed [225], and ZGNRs of width 12 are already considered as having largely decoupled edges [216]. Additionally, all DFT based calculations discussed here are ground state calculations at 0 K, thus not directly applicable to experiments performed normally at higher temperatures. The decay length measured via STM and STS methods has been found to be around 12 Å for zigzag edges mixed with some armchair sections on HOPG [226]. Thus both theory and first experimental results suggest electronically decoupled edges in the $\sim$ 50 Å width ZGNRs used here.

For graphene edges on larger graphene flakes or sheets, magnetic edge states therefore can be considered as decoupled, with the FM, AFM and NM configuration energetically close together. However, certain edge configurations such as the z_{211} clearly show non-magnetic (NM) properties. This can be physically well explained from the band diagram and density of states (DOS) in Figure 4.14 at the Fermi level (E_F = 0.0 eV). In the NM case of the z_1 edge, electronic states exist at the E_F with the DOS showing a sharp, half filled peak. This configuration is metastable, and as shown for the case of z_1 in Figure 4.13 before, transforming to a energetically

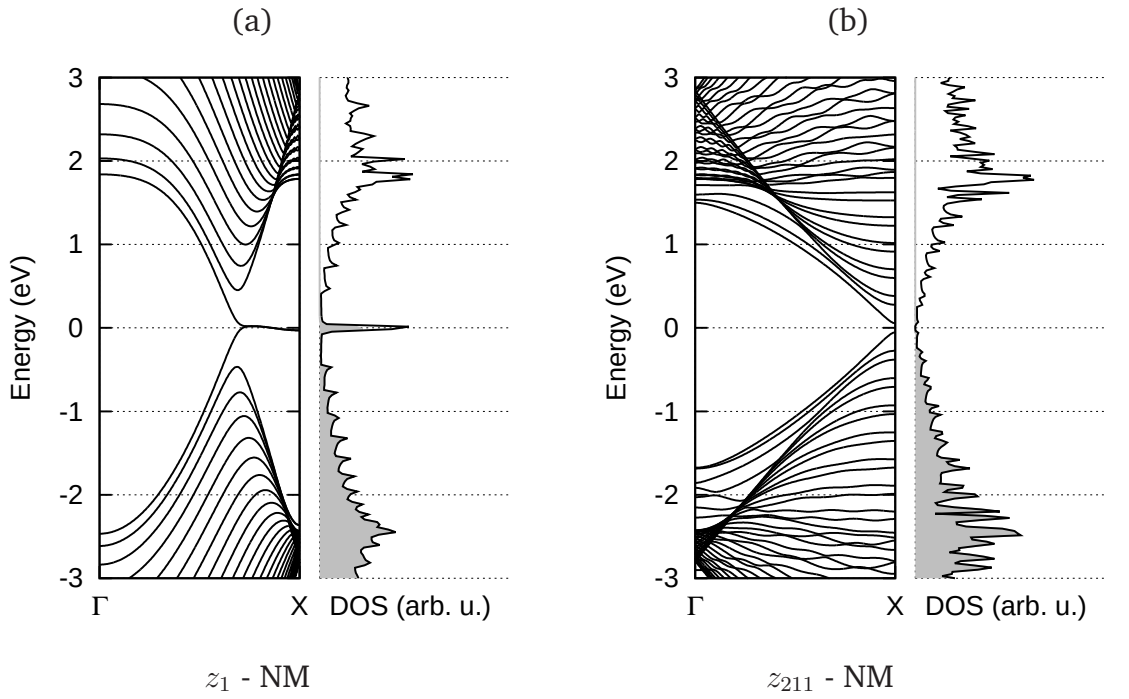

Figure 4.14: Band diagram and DOS of ZGNRs with symmetric edge configurations (a) z_1 and (b) z_{211}. In both cases the non-magnetic (NM) state is shown. A ribbon width of 25 (51.54 Å) has been used, modelling always the smallest possible unit cell.

favourable AFM or even FM magnetic state. But changing the edge hydrogen termination from $z_1 \rightarrow z_{211}$, the NM configuration gains stability through stabilizing the edge states, thus avoiding metastable edge states at the Fermi level. The very small gap ($\sim$ 0.11 eV) for this stable NM wide zigzag ribbon results from quantum confinement, and is expected to be more prominent for smaller widths.

As the states near the Fermi level are induced by magnetic instability at the edges, every stable hydrogenated edge configuration for zigzag edges is expected to be non-magnetic. This leads to the conclusion that all narrow ZGNRs under real conditions containing hydrogen should show weak semi-conducting behaviour, with small energy gaps dependent on the ribbon width. First studies of z_{211} hydrogenated ZGNR showed bandgaps in a similar range as AGNRs (width 12 ZGNR: $\sim$ 0.61 eV [216]). A detailed study based on Clar's sextet rule for narrow ZGNRs could help to predict ZGNR bandgaps.

4.5 Hydrogenated Klein and reconstructed Klein edges

Surprisingly, the other possibilities of hydrogenated graphene edge configurations, such as for example the Klein [147] and the reconstructed Klein edge [160] along the $<2\bar{1}\bar{1}0>$ orientation (comparable to the zigzag orientation, see Figure 3.12), have been skipped by all studies in literature so far. To address this, I have calculated different possible hydrogenated Klein and reconstructed Klein edge configurations as shown in Figure 4.15.

4.5.1 Stability of hydrogenated Klein and reconstructed Klein edges

As expected from the non-terminated edges (see Figure 4.1, Section 4.1), the Klein edge configurations k_1 and k_2 are energetically unfavourable with edge formation energies calculated more than $E_{form,H_2} > +0.47$ eV/Å (Figure 4.15 (a), (b)). But similar to the armchair case, CH_3 edge groups in configurations k_{33}^{ud} and k_{32} add stability (Figure 4.15 (c), (d)). Comparing these results with the z_{211} pristine zigzag edge leads logically to structures such as k_{332} and $k_{33}^{ud} + z_2$, built on the Clar's rule [156, 219] for the backbone zigzag GNR. While the k_{332} is energetically unstable ($E_{form,H_2} = +0.4900$ eV/Å) and unable to avoid strong repulsion of the Klein edge groups, $k_{33}^{ud} + z_2$ is with E_{form,H_2} = -0.1910 eV/Å (Figure 4.15 (f)) the most stable hydrogenated Klein edge configuration found in this work, more stable than any zigzag edge structure.

Regarding the reconstructed Klein edges under hydrogen termination (Figure 4.15 (g)-(k)), the hydrogenated rk_{22} configuration shows a stable edge formation energy of E_{form,H_2} = -0.0295 eV/Å. And even more stable the $rk_{22} + z_2$ has been calculated with E_{form,H_2} = -0.1069 eV/Å. Here, the same underlying Clar's rule can be applied to explain the gain in stability, showing the same single-single-double bond termination of the outer most complete zigzag edge, similar to the z_{211}.

Summarizing for all H-terminated unreconstructed zigzag and reconstructed Klein

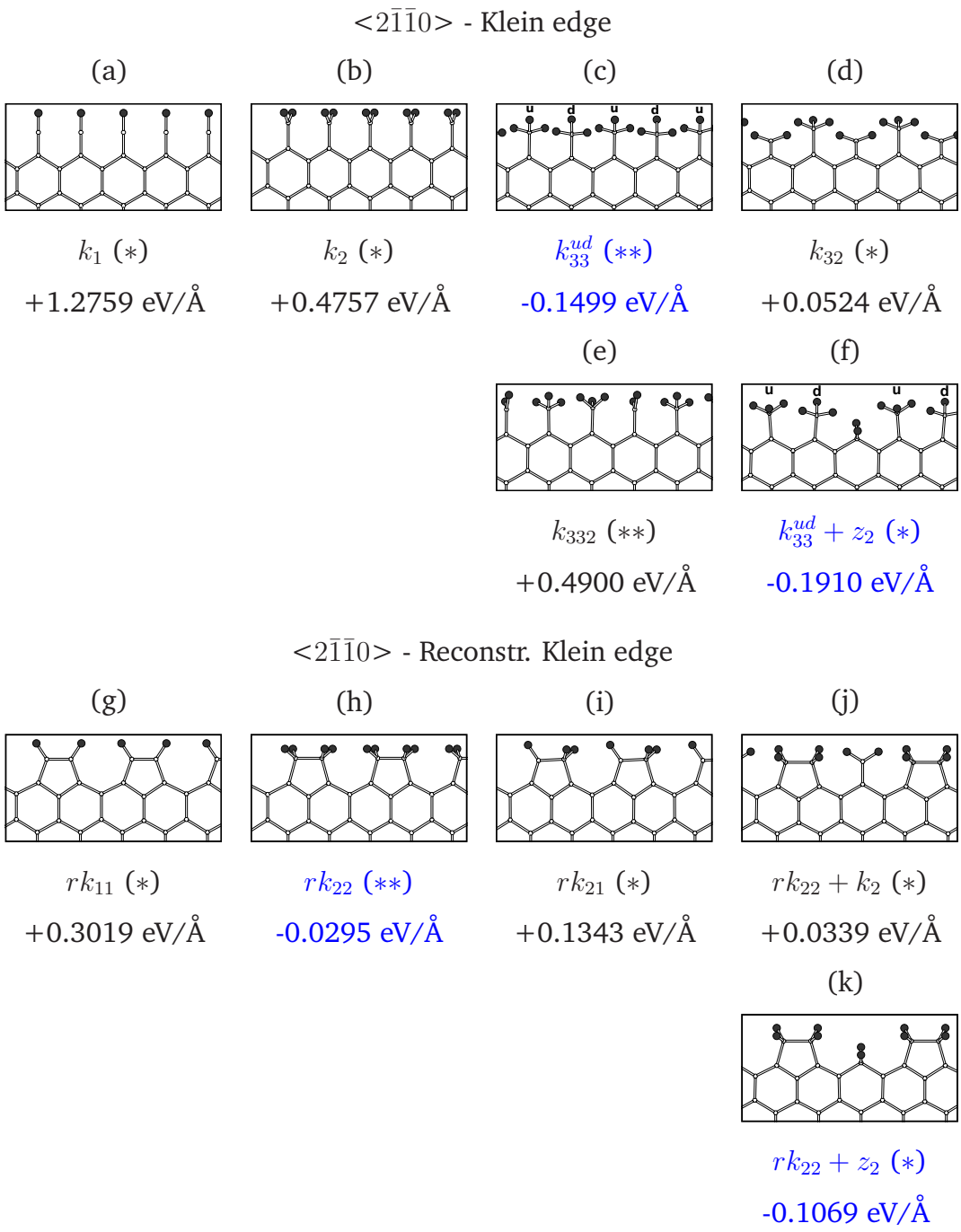

Figure 4.15: Edge formation energies for different hydrogen passivated (a)-(f) Klein and (g)-(k) reconstructed Klein edges. Most stable configurations are marked in blue. (∗): Non-magnetic, (∗∗): Magnetic.

edges, the $k_{33}^{ud} + z_2$ edge configuration is actually the most stable. This configuration is much more stable that the z_{211} edge with E_{form,H_2} = -0.0161 eV/Å edge formation energy, considered the most stable hydrogenated $<2\bar{1}\bar{1}0>$ edge state to date [156, 216] (see also Figure 4.12 (d)).
In general, many of the hydrogenated Klein and reconstructed Klein based edges have lower formation energies than zigzag edges, and may be expected to be the prominent $<2\bar{1}\bar{1}0>$ orientated edge types.

In summary for zigzag and related Klein edges, the z_{211} configuration (Figure 4.12 (d)) is preferred from the zigzag backbone honeycomb network. In other words periodically one sp^3 and two sp^2 coordinated carbon atoms on the last straight and complete zigzag line parallel to the $<2\bar{1}\bar{1}0>$ direction are most stable. But beside the underlying fundamental Clar's sextet rule, (physically speaking, avoiding states near the Fermi level induced by the edge configuration), other clear tendencies are visible for zigzag, Klein and reconstr. Klein edges. Steric hindrance on the edge termination groups lowers the edge stability. This can either be avoided through out-of-plane distortions (as seen in the a_{3333}^{uudd} armchair edge case), forming a rippled edge as in the case of k_{33}^{ud}, or through mixing with the z_2 configuration. For any kind of zigzag $<2\bar{1}\bar{1}0>$ edge, regarding the last complete zigzag edge line, a periodic sp^3 configuration is preferred realized through direct H-bonding (z_2) and the single bonds tend to be most stable through single C-C bonds.

4.5.2 Electronic properties of hydrogenated Klein and reconstructed Klein edges

In Figure 4.16 (a), the NM state of a rk_{22} ZGNR is shown. Here, the characteristic half filled peak at the Fermi level for the NM state has been found indicating the instability of this configuration, trying to avoid the Fermi level states through switching to a magnetic configuration similar to the case study with z_1 edges (see section 4.4.2). Again in Figure 4.16 the structural transition from (a) $\rightarrow$ (b) shows

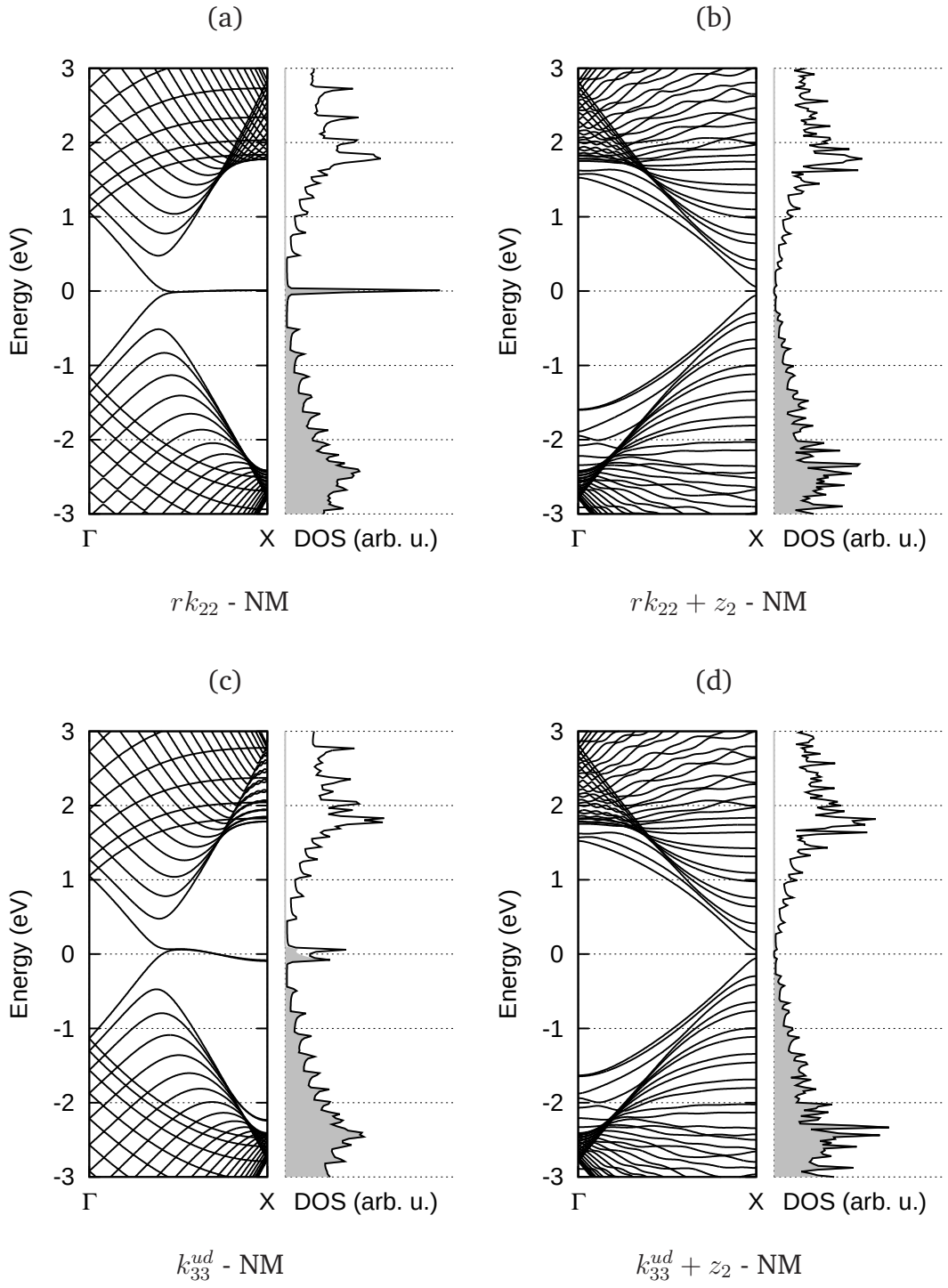

Figure 4.16: Band diagram and DOS of Klein and reconstr. Klein ZGNRs with symmetric non-magnetic (NM) edge configurations (a) rk_{22}, (b) $rk_{22} + z_2$, (c) k_{33}^{ud} and (d) $k_{33}^{ud} + z_2$. Ribbon widths $\sim$ 50 Å have been used, modelling the smallest possible unit cell.

the stabilisation through avoiding states around the Fermi level, *i.e.* the peak at E = 0 eV in the DOS disappears. Here the insertion of one z_2 group between each reconstructed Klein pair adds massive stability, a logical consequence similar to that found for the pristine zigzag edges.
Further a new CH_3 containing rippled edge configuration k_{33}^{ud} has been identified for the Klein edges, which can be easily stabilized in the same way (Figure 4.16) (c) $\rightarrow$ (d)). The most stable configuration is achieved by adding one z_2 unit to form the non-magnetic $k_{33}^{ud} + z_2$ edge configuration. Again, as for the armchair a_{3333}^{uudd} case in the DOS additional deeper states due to the sp^3 hybridisation CH_3 edge group appear now around $\sim$ -2.5 eV and $\sim$ +2.0 for the $k_{33}^{ud} + z_2$ case in Figure 4.16 (d).

Based on insights from these calculations we can now generalise the classic graphene nanoribbon width definition (see Chapter 3, section 3.3, [177]), including Klein and reconstructed Klein configurations, in the next section.

4.6 Generalized effective width definition for GNRs

In order to incorporate many possible different hydrogenated edge types discussed in the previous sections, the width definition given in 2008 by Cervantes-Sodi *et al.* [177] for AGNRs and ZGNRs has to be extended and generalised. One first step towards a new effective ribbon width has already been demonstrated for armchair GNRs in section 4.3.2.

A logical way to define the width for zigzag and armchair backbone GNRs is to only count the preserved complete straight and sp^2 coordinated carbon dimer rows; as demonstrated for the first time for a rk_{22} ZGNRs (or RKGNR) and a a_{22} AGNRs in Figure 4.17. Here the new effective ribbon width $n_{effective}$ can help to compare the properties, such as for example the bandgap. Therefore GNRs with different edge hydrogenations can be better compared using this effective ribbon width.

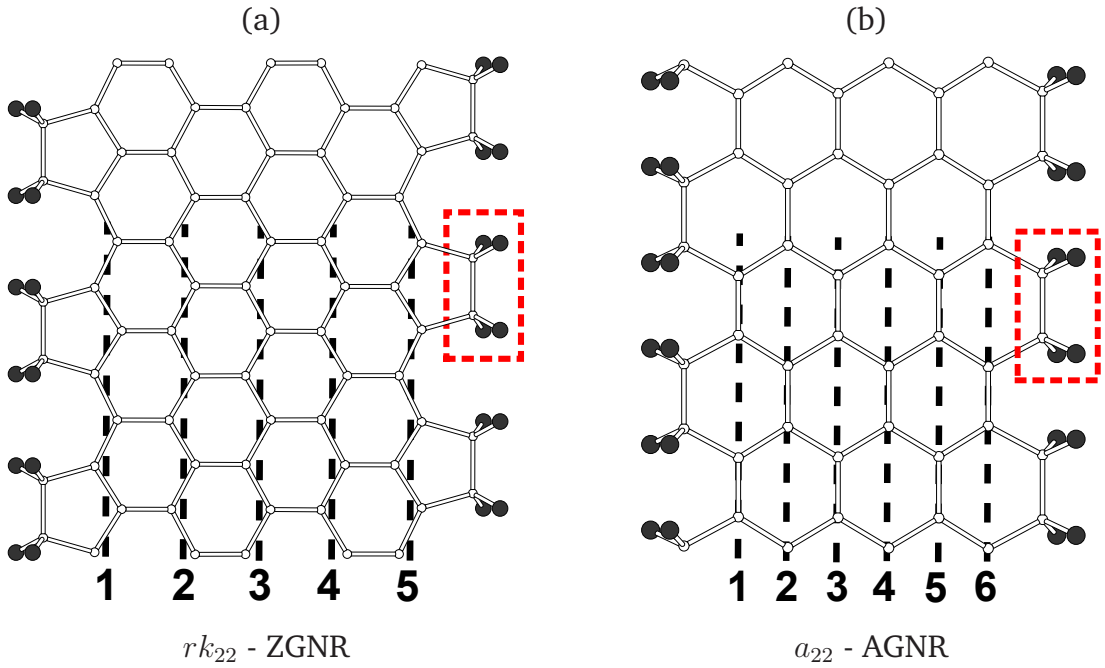

Figure 4.17: (a) Schematic ZGNR of width 5 with rk_{22} hydrogenated edges and (b) schematic a_{22} hydrogenated AGNR of width 6. In both cases an “ethylene like" edge termination group is highlighted with a red box as a guide for the eye. On the bottom for both cases the new effective width definition is demonstrated.

4.7 Graphene edges under experimental conditions

After all the calculations presented thus far considering perfect vacuum conditions around free standing GNRs, the legitimate question arises, namely what could be expected in experiments?

The most common growth method for graphene is CVD growth, using ethylene or methane as precursors. In these processes, single-layer graphene is grown on metal surfaces such as Cu, Ni, Ir or Ru [134, 227–229]. Cu-foils in particular show excellent results as substrates combined with affordable material prices. The substrate surface temperatures range from 800 °C - 1100 °C at pressures from 10^{-8} bar to 1 bar [134, 227–229]. In order to consider a molecular hydrogen gas atmosphere around a graphene edge (or GNR), the calculated total edge formation energy E_{form,H_2} (see also (4.2)),

$$E_{form,H_2} = \frac{E_{tot} - n_C \cdot E_C - n_H \cdot E_H}{2L} \ ,$$

can be compared to the hydrogen chemical potential μ_{H_2}. This results in the relative edge stability G_{H_2}, comparing E_{form,H_2} and μ_{H_2}, leading to the following expression:

$$G_{H_2} = E_{form,H_2} - \rho_H \cdot \mu_{H_2}/2 \ . \tag{4.3}$$

$\rho_H = \frac{n_H}{2L}$ gives the edge hydrogen density per (GNR) edge, with the number of hydrogen atoms n_H attached to the (ribbon) edges of length L ($2L$ for a GNR), following the same approach as Wassmann *et al.* [156]. The hydrogen chemical potential depends on the pressure and temperature of the system and can be calculated using the following formula:

$$\mu_{H_2} = H^{P_1}(T) - H^{P_1}(0) - T \cdot S^{P_1}(T) + k_B \cdot T \cdot ln\left(\frac{P_{H_2}}{P_1}\right) \ , \tag{4.4}$$

where H is the enthalpy and S the entropy at pressure P_1. Values of H and S for P_1 = 1 bar and T = 300 K can be calculated to $H(300)$-$H(0)$ = 0.05 kJ/mol and $S(300)$ = 130.9 J/mol*K as listed in thermo-chemistry data bases [230]. As an indication, at ambient conditions the chemical potential μ_{H_2} with 300 K and the partial H_2 pressure in air of $P_{H_2} \approx 5 \cdot 10^{-4}$ mbar gives $\mu_{H_2} \approx$ -0.41 eV. For both

lower H_2 pressures and increasing temperatures the chemical potential lowers. Plotting G_{H_2} over the chemical potential μ_{H_2} displays a linear relationship between the two values, see (4.3). For $G_{H_2} < 0$, the hydrogenated edge is expected to be unstable, while for $G_{H_2} > 0$, it is considered as stable. The edge configuration with the lowest G_{H_2} describes the most stable (hydrogenated) edge configuration for a given hydrogen chemical potential.
All possible hydrogenated edge configurations, discussed so far in this chapter, were plotted over a wide range of the hydrogen chemical potential, shown in Figure 4.18.

In Figure 4.18 (a), all hydrogenated armchair edges configurations (along the $<1\bar{1}00>$ direction) are plotted, with the most stable configurations indicated by sections. For hydrogenated armchair edges, the a_{3333}^{uudd} configuration is stable ($G >$ 0) for higher μ_{H_2}, but switching quickly to a_{22} and later a_{11} armchair edge configurations for lower chemical potentials. In the presence of hydrogen, a fully unterminated armchair edge is rather unstable with G_{H_2}= +1.10 eV/Å.
Figure 4.18 (b) shows hydrogenated zigzag and (reconstructed) Klein edges (along the $<2\bar{1}\bar{1}0>$ direction). The new $rk_{22} + z_2$ and $k_{33}^{ud} + z_2$ are stable for $\mu_{H_2} > \sim$ -0.65 eV, and have to be considered in future work for low temperature and high pressure experiments. For lower hydrogen chemical potentials, the z_{211} and later the z_1 edge configurations are most probable. Similarly to the $<1\bar{1}00>$ edge orientation, a fully unterminated edge such as the (5-7) reconstructed zigzag edge at G_{H_2}= +1.09 eV/Å is very unstable compared to hydrogenated edge types.

In Figure 4.18 (c), all most relevant graphene edges configuration are included. While both zigzag and armchair edge types are possible, the stability is strongly dependent on the experimental growth conditions.
In general for graphene CVD growth experiments, a prediction is complex, as additionally surface interactions should be included along with μ_{CH_4} etc. Especially the metallic character of common substrates (*e.g.* Cu) is expected to play an important role for the graphene formation process. Thus the chemical potential can be influenced, and therefore in Figure 4.18 (c) a larger region (highlighted in gray) is

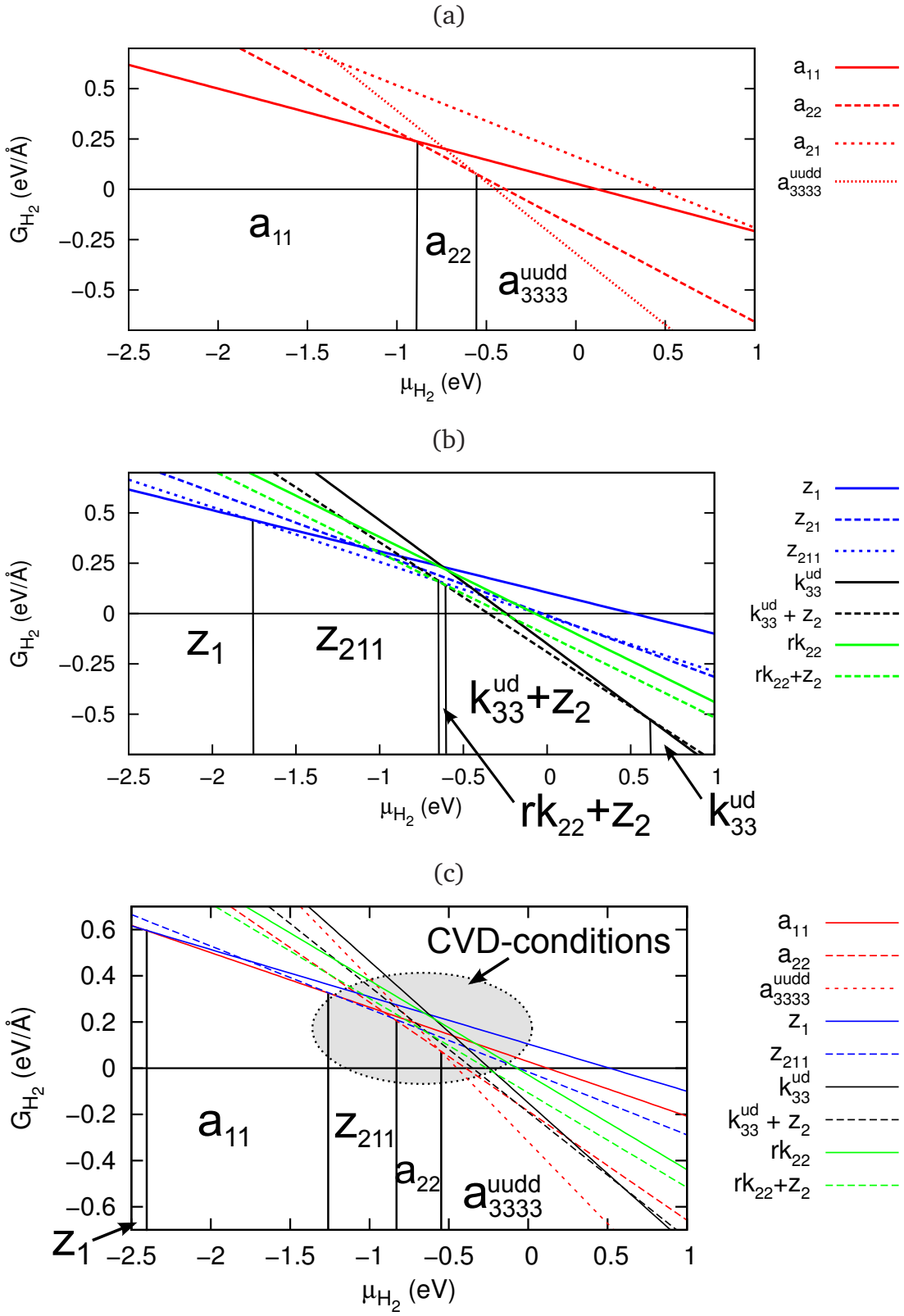

Figure 4.18: Edge stability G_{H_2} versus chemical potential μ_{H_2} for free standing graphene edges in H_2 atmosphere. (a) Hydrogenated armchair edges, (b) hydrogenated zigzag, Klein and reconstr. Klein edges. (c) Most stable hydrogenated edge configurations with possible CVD growth conditions highlighted in gray.

proposed to be relevant for CVD growth experiments. Notably this region includes several different possible edge types, all relatively close in edge energy, including the newly identified rk_{22} and k_{33}^{ud} hydrogenated edge configurations.
Under real conditions the influence of the cooling down also has to be considered, changing again the hydrogen chemical potential. Thus for example the final edge structure may not match the edge structure during growth. Further it could be speculated that the strongly rippled k_{33}^{ud} and a_{3333}^{uudd} with large CH_3 edge groups are less probable when growing graphene direct on surfaces, but these edge types could occur when exfoliating graphite mechanically.

4.7.1 Edge formation and (CVD) graphene growth models

When tailoring a graphene sheet or unzipping CNTs, both the zigzag and the Klein edge can be created through cutting along the $<2\bar{1}\bar{1}0>$ direction (see also Chapter 3 section 3.2.1 Figure 3.12). Considering additionally a hydrogen containing atmosphere while unzipping axially an armchair CNT (along the zigzag lines), leads to two possible types of GNRs, either with classic zigzag edges or terminated by recon-

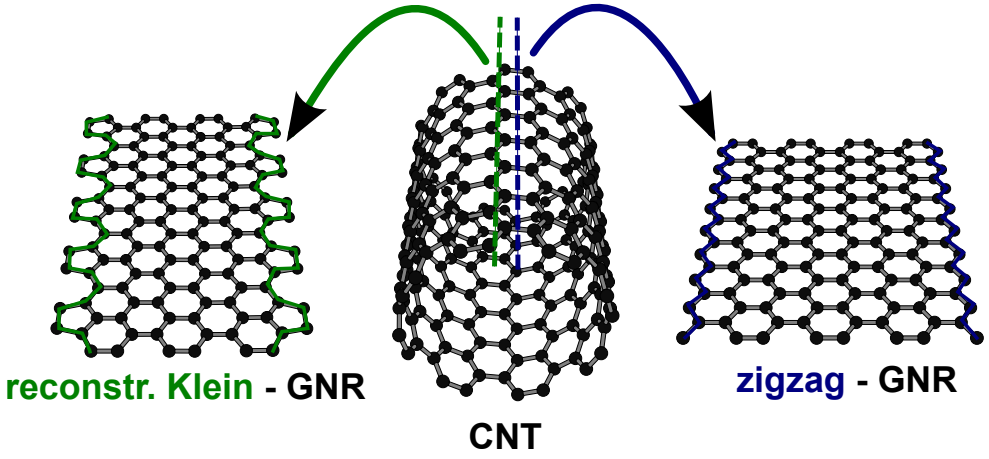

Figure 4.19: Schematic illustration of cutting carbon nanotubes (CNTs) to form well defined graphene nanoribbons (GNRs). This schematic shows that when cutting an armchair CNT, both zigzag and reconstructed Klein GNRs are possible depending on the cutting line. My calculations show that in the presence of hydrogen the reconstructed Klein GNR will be thermodynamically favoured.

structed Klein edges, as schematically shown in Figure 4.19. In terms of stability, a fully rk_{22} terminated reconstructed Klein graphene nanoribbon (RKGNR) should be $\Delta E_{form,H_2}$ = -0.0268 eV/Å more stable than a fully z_{211} hydrogenated zigzag ribbon. On the other hand, precisely controlled unzipping of CNTs is still difficult, and normally a mix of different armchair, zigzag and chiral edges is created along the edges for wide GNRs in the range of 10 - 40 nm thickness [39, 182–184, 186]. With more experience and better control of the experimental conditions, I can imagine it could be possible in the future to create well defined edges, and I would speculate that reconstructed Klein edges will in these cases be identified.

CVD-based graphene growth

Another promising synthesis route is Chemical Vapour Deposition (CVD), *i.e.* growing single-layer graphene directly on substrates. Here, recently the use of ethylene (C_2H_4) as precursor has be successfully demonstrated [229], growing graphene on copper substrates. While the addition route of C_2H_4 groups to armchair edges is rather simple (see Figure 4.20 (a)), for zigzag edges the mechanism is not directly obvious. As in experimental observations, both edges orientations are normally present, thus also on zigzag edges graphene growth should take place.
In this chapter, the new additional stable edges identified such as the hydrogenated reconstructed Klein edges could help to get a more complete picture of these CVD graphene growth processes. In Figure 4.20, three possible growth mechanisms for the armchair edge, zigzag "step" edge and the reconstructed Klein edge are illustrated. For zigzag edges, steps could be important to initialize the growth along the edge, as shown in Figure 4.20 (b). To explain the graphene growth along "straight" zigzag edges (with no steps), I propose the addition of an intermediate step, notably the formation of hydrogenated reconstructed Klein edges, followed by a Stone-Thrower-Wales rotation (Figure 4.20 (c)). In this case, two different routes can be imagined, and the activation barriers for both on surfaces have to be studied in the future. First results for unterminated and suspended edges support the possibility of Stone-Thrower-Wales rotations at zigzag edges with low energy

barriers of approximately 0.4 - 0.7 eV [161, 231, 232].

Taking the example of an ethylene-based CVD process, initially ethylene precursor groups attach to the zigzag edge, forming stable reconstructed Klein edges. In a second step, further ethylene groups attach to this edge and build a (5-7) reconstructed zigzag edge [162]. This edge can now be transformed through a Stone-Thrower-Wales rotation [233, 234] into a classic zigzag edge. Thus one line of zigzag carbon atoms was added to the graphene edge and the graphene sheet has grown. Now the growth mechanism will restart and the growth continues.
It has to be noted that for both edges, the fundamental building blocks are carbon dimers. By introducing the new (probably hydrogenated) reconstructed Klein edge, this growth mechanism is generalized, thus similar for all edge orientations.
As the graphene growth works good on metallic (*e.g.* copper) surfaces, I speculate that this could lower the activation barrier for the Stone-Thrower-Wales rotations through surface interactions. Celebi *et al.* [229] report an activation energy of about 2.46 eV needed to start graphene growth, thus this could be related to the here presented edge growth mechanism. They additionally propose ethylene surface dehydrogenation (important for the attachment a carbon dimer to the edge in my growth model) and graphene lattice constructions (*e.g.* Stone-Thrower-Wales rotations in my model) responsible for this activation barrier. More calculations have to be performed on copper surfaces, to confirm this activation barrier value.

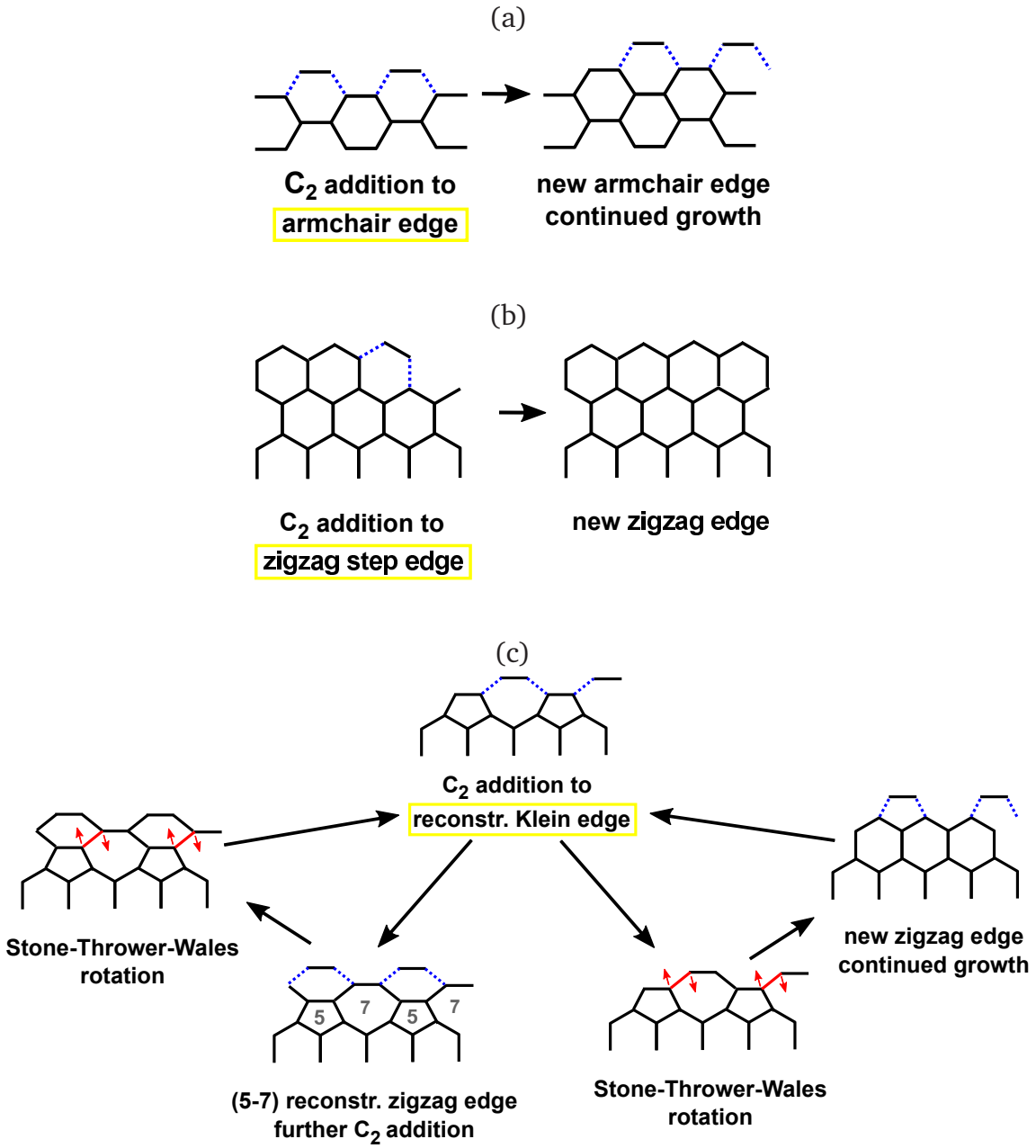

Figure 4.20: Graphene growth models: (a) armchair edge, (b) zigzag step edge and (c) reconstructed Klein edge, with carbon dimers (C_2) as fundamental building blocks, similar to C_2H_4 (ethylene) precursors used for CVD graphene growth. Carbon dimer bonding to the graphene edges with dehydrogenation of the edge atoms marked with dotted blue lines, Stone-Thrower-Wales rotations are labelled red.

4.8 Computational details

In all calculations relativistic pseudopotentials based on the Hartwigsen, Goedecker and Hutter scheme were used [73]. Atom-centred Gaussian basis functions are used to construct the many-electron wave function with angular momenta up to l=2, with 22 independent functions ($pdpp$) per C atom and 12 functions (ppp) per H atom. This basis set has been used for cases of large GNRs due to very large system sizes. I confirmed, that the optimisations of all structures were energetically converged. Electronic level occupation was obtained using a Fermi occupation function with kT = 0.04 eV. The charge density was fitted to plane waves within an energy cut-off of 150 Ha. The choice of the k-point grid was tested to give fully converged energies. The energy tolerance for the DFT calculations were set to $1 \cdot 10^{-7}$ Ha, and for the atomic positions to $1 \cdot 10^{-5}$ Bohr. Calculations in sections 4.1 and 4.2 were primarily performed by V. V. Ivanovskaya.

Chapter 5

Edge functionalized armchair graphene nanoribbons

In this chapter, the influence of edge functionalization is studied using narrow armchair graphene nanoribbons (AGNRs), whose properties are strongly dependent on width and the edge termination. The simplest way to saturate GNR edge dangling bonds is through simple hydrogen termination (see also chapter 4 section 4.3). This has been for many years the standard approach in GNR modelling [37, 148, 156, 161, 179]. However, other edge terminating heteroatoms (*e.g.* -N, -O, -F, -Cl) or functional groups (*e.g.* -OH, -SH) can be imagined, and an intriguing example of this was a recent theoretical study which found -F terminated armchair GNRs to be more stable when twisted helically [235]. Nevertheless, to develop a realistic picture of the possibilities of GNR edge chemistry, more complex termination groups have to be investigated.

A good and realistic example are hydroxyl functional groups (-OH), which as well as being bulkier than simple heteroatoms, also show more complex chemical interaction between themselves. Such groups have been proposed for AGNRs as a way to introduce strain along the graphene edge [236] in order to tune the electronic properties, similar to electronic changes predicted for strained graphene [237, 238]. Furthermore possibilities to create hetero-junctions by directly influencing the bandgap via edge functionalization on GNRs have been studied [239].

However, free standing two dimensional (2D) materials such as graphene or related nanosheets have alternative mechanisms for relieving edge-induced strain, especially through structural deformations into the third dimension via rippling, folding, twisting or buckling the 2D sheet [240]. Notably, dynamic rippling of graphene has been demonstrated via electron microscopy [129] and molecular dynamics calculations [130], and there have been first discussions of the possibility for stable static ripples in graphene [240, 241].
This additional degree of freedom adds significant richness to graphene edge chemistry, which I have investigated here for narrow infinitely long armchair graphene nanoribbons (AGNRs), discussing first in detail the example of hydroxyl (-OH) functionalization. Structural, electronic, chemical and mechanical properties have been studied [140]. From this first fundamental basic example, more results for other edge terminating heteroatoms or functional groups such as -F, -Cl, -Br or -SH can be derived and will be discussed afterwards. Especially structural properties and the bandgap behaviour has been investigated for a range of functional groups.

Finally the possibility of twisted armchair GNRs due to edge functionalization is discussed in section 5.3. Notably, the study of Gunlycke *et al.* [235], investigating -F terminated twisted AGNRs, is set in the new context of possible strain relief via localised edge rippling [140, 205].

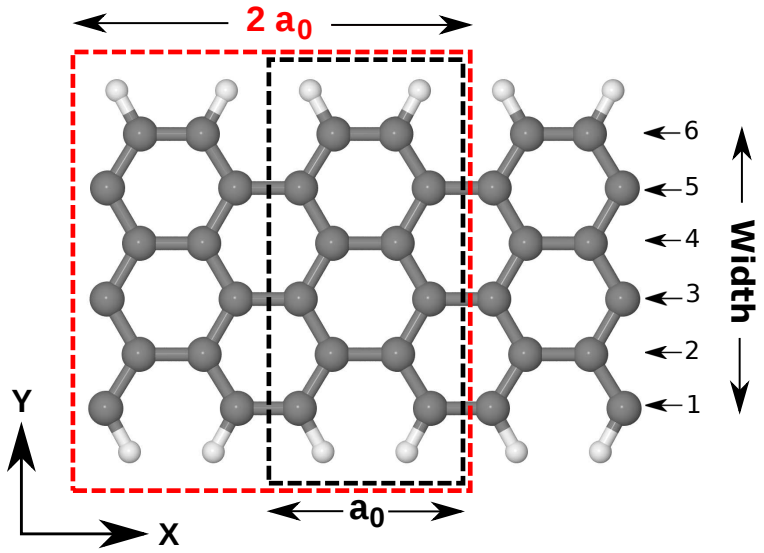

Figure 5.1: H-terminated AGNR, different unit cells (in black smallest possible unit cell, in red unit cell used for edge rippled AGNR) shown by dotted frames, classic definition of armchair ribbon width shown by numbers with width 6 [177]. C atoms are shown grey and H atoms are white.

5.1 -OH edge functionalized armchair GNR

While thin GNRs have been modelled already in recent years [37, 179, 215, 242], it is important to pay special attention to the supercell size when considering complex edge functional groups. The cost of DFT calculations is directly related to the system size, and as a result the smallest possible repeating cell along the GNR has normally been used. In the following, this important parameter is discussed, showing why it wasn't possible in earlier studies to rigorously investigate complex edge functional groups attached to GNRs.

5.1.1 Modelling thin functionalized armchair GNR

A classic definition of ribbon widths of AGNRs is given by Cervantes-Sodi *et al.* [177] and is used in the text as well as in the following figures, when regarding the width range 4 - 20 of thin AGNRs. The width definition and also the two typical unit cell sizes (with axial lengths a_0 and $2 \cdot a_0$) used in this study are shown in Figure 5.1 for a simple hydrogenated AGNR. The vacuum distance between neighbouring

ribbons has been set to larger than 12 Å in all directions, to avoid inter-ribbon interactions. A fine k-point grid was chosen of the form $12/n \times 1 \times 1$ with $n \in N$, which gives energies converged to better than 10^{-5} Ha (Ha: Hartree energy). a_0 is the length of a fundamental AGNR unit cell along the ribbon axis in the supercell (see Figure 5.1). For rippled GNRs, the unit cell was doubled along the ribbon ($2 \cdot a_0 \rightarrow n = 2$) to satisfy the periodic conditions of the supercells. Pseudo-potentials based on Gaussian functions were used; generated via the Hartwigsen-Goedecker-Hutter scheme [73]. The basis sets used for each atom type were $pdddp$ (C), ppp (H) and $dddd$ (O), resulting in 38 independent functions for carbon, 12 for hydrogen and 40 for oxygen. Here, a bigger basis set for carbon was used compared to the unterminated and hydrogenated graphene edges (modelled with $\sim$ 50 Å wide GNRs in Chapter 4, using the $pdpp$ basis set for C with 22 functions). These calculations have been possible as fewer atoms per supercell were modelled. For all structures, the atom positions and the lattice parameters were fully relaxed. Strain parallel to the ribbon axis (Figure 5.1, x-axis) was calculated using:

$$\epsilon = \frac{a_0 - a_{Graphene}}{a_{Graphene}} , \tag{5.1}$$

with $a_{Graphene}$ = 4.23 Å , my optimized LDA-DFT lattice parameter along the armchair direction of free standing pristine graphene, and a_0 the new lattice parameter for the functionalized GNRs. The calculated lattice parameter value for the pristine graphene $a_{Graphene}$ is in good agreement with experimental values of $\approx$ 4.2 Å [208].

5.1.2 Structural properties of -OH functionalized AGNRs

Larger functional groups on GNR edges can introduce a range of possible intergroup interactions, including steric hindrance, Coulombic repulsion, dipole-dipole interactions and hydrogen bonding. To get a first overview, I modelled fifteen different structural armchair -OH edge possibilities, for widths 5 - 8 and 13 - 15 in order to identify the most stable configuration (for more details see also section 5.1.2, p. 104). Now I will focus, in a first step, on three characteristic structures

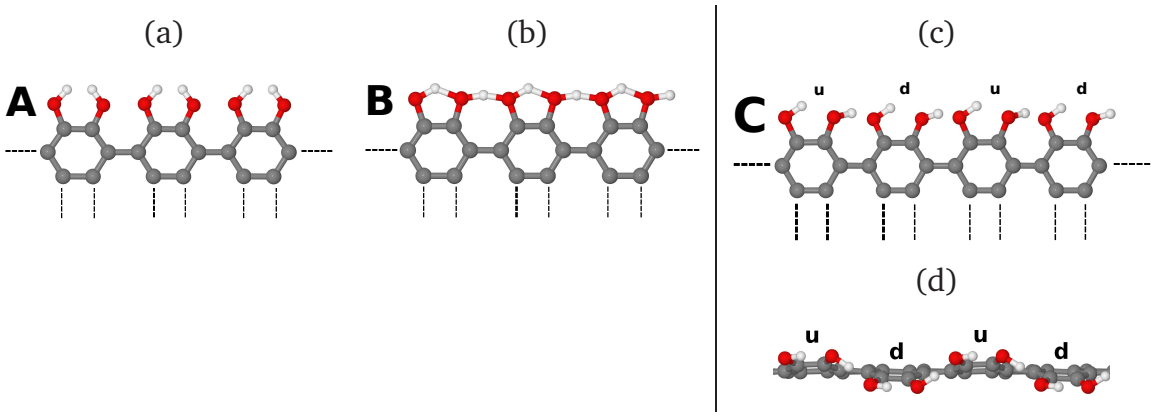

Figure 5.2: Three different -OH terminated armchair edge structures, (a) base symmetric structure A, (b) metastable structure B with hydrogen bonding. (c) and (d): Structure C, the stable ground state structure with static rippling (side view in (d)). u stands for “up" and d for “down" for the rippled edge carbon dimer with bonded -OH groups. Dotted lines are a guide to the eye for the GNR. C atoms are in grey, O atoms in red and H atoms are white (same for Figure 5.6 ,5.4, 5.5, 5.11 and Figure 5.12).

shown in Figure 5.2, further always referred to as A, B and C configurations of hydroxylated armchair graphene edges. Associated structural parameters of A, B and C are given in Table 5.1. Structure C is shown again in more detail for a larger GNR segments in Figure 5.4.

To compare these three edge configurations, thin AGNRs in the width range of 4 - 20 were modelled. A detailed comparison of total energy per unit cell and total strain of the three structures is plotted in Figure 5.3. Here, for the configuration C the total system energies were divided by 2, as the GNR segments in this unit cells ($2 \cdot a_0$) were twice as long (respectively twice as many atoms of every species) compared to configurations A and B. As ribbon segments for same widths are strained differently, this direct comparison of energies per unit cell has been chosen, as in terms of edge energy (eV/Å) strain and energy wouldn’t been separable.

Starting with structure A (Figure 5.2 (a)) where the -OH groups lie symmetrically constrained in the graphene plane with symmetrically paired -OH groups, removing any possibility for hydrogen bonding. Calculated bond lengths are d_{C-O} = 1.33 Å

Structure		d_{C-O} (Å)	d_{O-H} (Å)	$d_{O\cdots H}$ (Å)
A (flat)		1.33	0.96	-
B (flat)	width 4	1.36	1.05	1.26/1.41
	width 20	1.35	1.09	1.11/1.14
C (rippled)	width 4	1.36	1.02	1.40/1.63
	width 20	1.36	1.02	1.45/1.69
Phenol (C_6H_6O)		1.35	0.97	-

Table 5.1: Overview of calculated bond lengths of the AGNRs from width 4 - 20 for structures A, B and C. O$\cdots$H bond lengths for Structure B and C vary with ribbon width between the limits given in the table. Structure C is the most stable ground state. Calculated Phenol (C_6H_6O)) values included for comparison.

and d_{O-H} = 0.96 Å. This structure was recently discussed as a possible configuration for inducing strain in AGNRs [236]. Indeed I found that it induces strains ϵ of up to 9 % for small AGNRs (see Figure 5.3 (b)), however this structure is energetically extremely unstable (see Figure 5.3 (a)).

I next introduce hydrogen bonding between the hydroxyl groups by breaking the in-plane symmetry and rotating every second -OH group, giving the most stable planar configuration, structure B (Figure 5.2 (b)). Here d_{C-O} = 1.36 Å with hydrogen forming one strong covalent bond d_{O-H} = 1.05 - 1.09 Å and one weaker hydrogen bond $d_{O\cdots H}$ = 1.11 - 1.41 Å. This new hydrogen bond lowers the system energy by typically 3.7 eV/unit cell compared to Structure A. While it reduces slightly the induced strain, this remains still up to 6.7 % for a width 4 AGNR compared to perfect graphene, as can be seen in Figure 5.3 (b).

However, by additionally breaking the planar symmetry the energetically most stable configuration for hydroxyl terminated AGNRs can be reached, structure C (see Figure 5.2 (c)). The -OH groups displace out-of-plane pairwise, creating a static

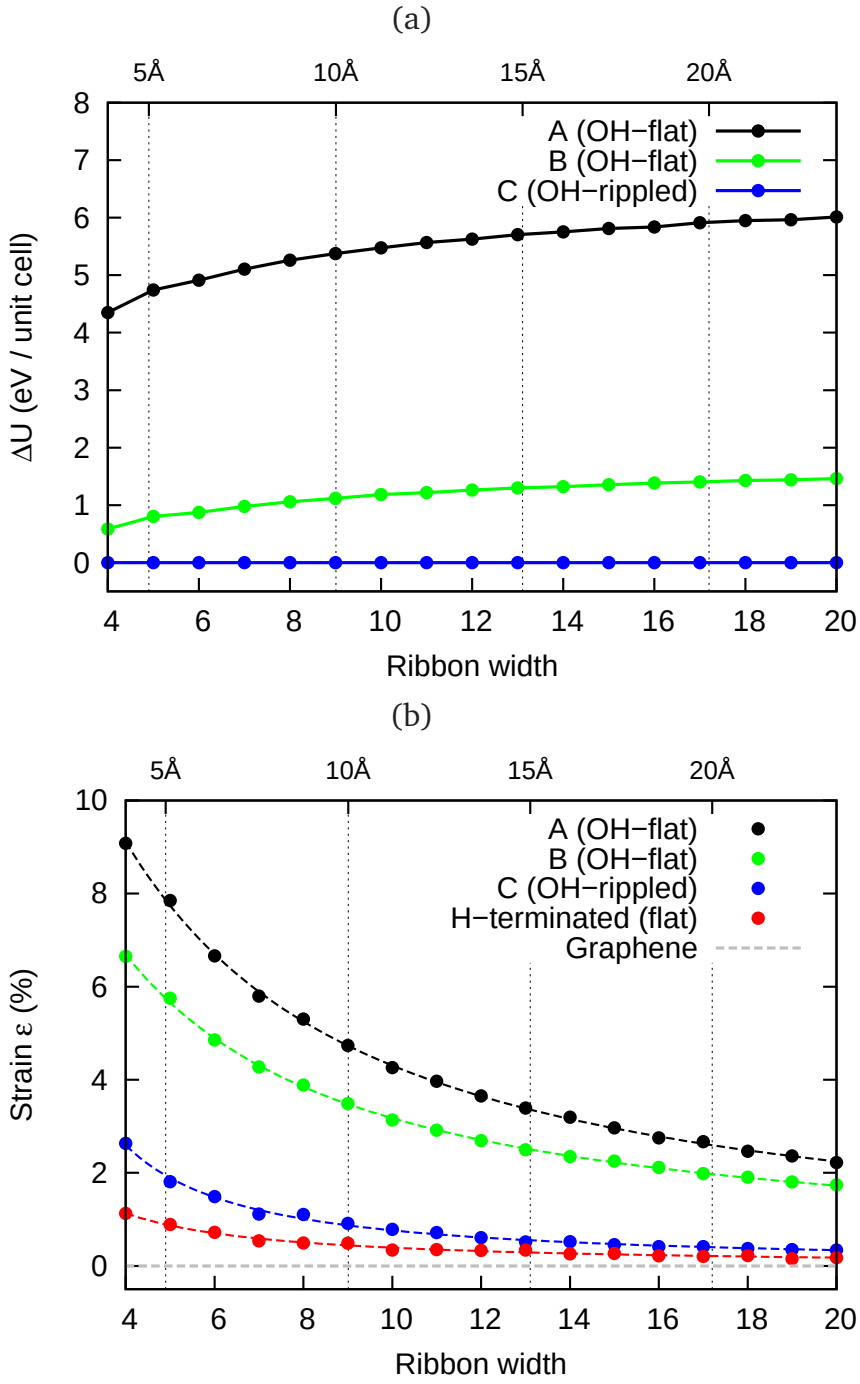

Figure 5.3: (a) Energy difference ΔU between structure A (black) and structure B (green) referring to structure C (blue) versus armchair ribbon width from 4 to 20. (b) Strain along the ribbon, strain is referenced to a perfect flat graphene sheet (ϵ = 0 %), H-termination (red), A (black), B (green) and C (blue). Fits in (b) using function $\epsilon(x) = \frac{a}{x} + \frac{b}{x^2} + c$ (see also Table 5.2). The top scale for ribbon width in Å is taken from perfect flat graphene with C-C bond lengths of d_{c-c} = 1.41 Å as guide for the eye.

Figure	Structure	a	b	c	Standard deviation
Figure 5.3 (b)	A (OH-flat)	48.154	-46.023	-0.048	0.050
	B (OH-flat)	33.149	-27.726	0.137	0.036
	C (OH-rippled)	5.760	18.369	0.004	0.048
	H-terminated (flat)	3.759	3.398	-0.018	0.031

Table 5.2: Fit parameters of function $\epsilon(x) = \frac{a}{x} + \frac{b}{x^2} + c$ when fitting to the curves of strain versus ribbon width Figure 5.3 (b).

sinosoidal ripple along the AGNR edge (perspective and side view in Figure 5.4). By displacing out-of-plane, the structure releases up to 1.46 eV/unit cell (Figure 5.3 (a)) and the strain in the ribbon is relieved (Figure 5.3 (b)), returning to values similar to hydrogen terminated AGNRs. The edge carbon pairs for each hexagonal ring are displaced up and down alternately supporting the sinusoidal ripple along the AGNR edge. This pairwise distortion appears to be characteristic for the armchair edge, as longer period oscillations were tested in supercells with $n \cdot a_0$ and $n > 2$ at a variety of ribbon widths, but were found to be energetically less stable. Thus these minimal period ripples provide the optimum distance between the -OH functional groups, gaining a maximum of stability while avoiding distortion (strain) along the ribbon. While d_{C-O} stays largely unchanged at 1.36 Å, the covalent d_{O-H} extends to 1.02 Å, while the rippling allows the hydrogen bond lengths to increase to $d_{O\cdots H}$ = 1.40 - 1.69 Å. The lengths for d_{C-O} and d_{O-H} are approaching my calculated bond lengths for isolated phenol (d_{C-O} = 1.35 Å, d_{O-H} = 0.97 Å, Table 5.1).

This out-of-plane edge deformation mode can be understood as an elastic response to a 1D edge line tension applied to an effectively rigid 2D graphene sheet (my calculated in-plane Young's Modulus for graphene (using a slab model) is 1.08 $\pm$0.03 TPa), where it is clearly energetically favourable to buckle/ripple the edge rather than stretch the whole sheet. However, non-planar sheet deformation changes (decreases) the π-orbital overlap, and this enthalpic driving force of graphene to remain flat localises the rippling along the ribbon edge for all widths. This is demon-

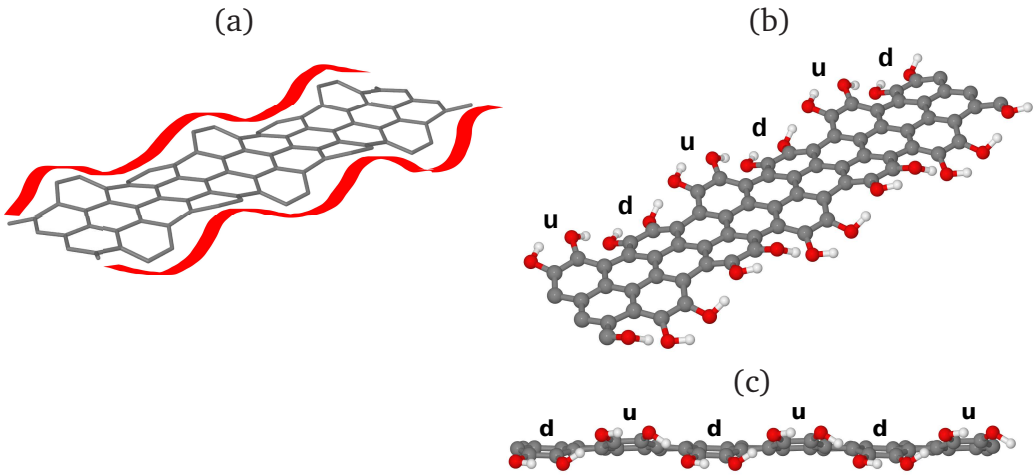

Figure 5.4: (a) Schematic of AGNR with rippled edges. On the right an optimized -OH terminated AGNR width 6 of with edge configuration C is shown, (b) perspective view of ribbon, (c) side view with clearly visible rippled edge. u stands for “up" and d for “down" for the pairwise distorted edge carbon atoms of the rippled edge.

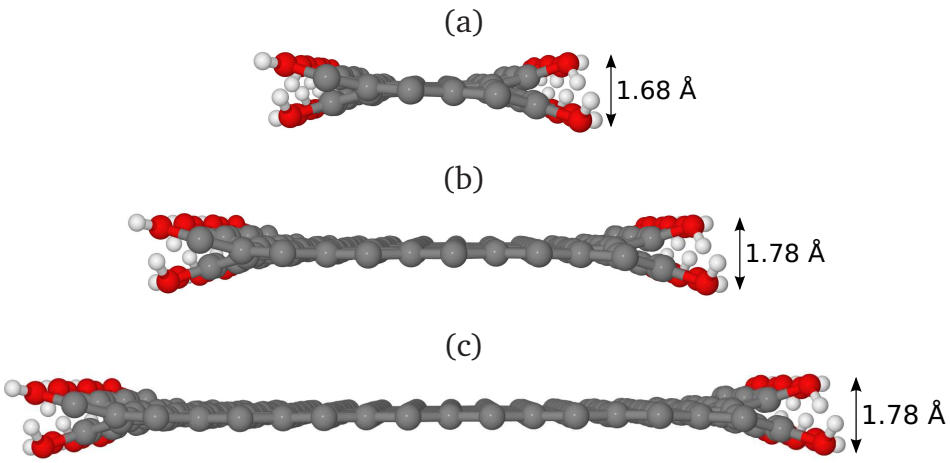

Figure 5.5: Front view of -OH terminated AGNRs forming the stable configuration C, (a) width 6, (b) width 12 and (c) width 18. Edge ripple localization within 2.3 Å is visible, and the ripple amplitude is lower for thinner ribbon with which are more strained.

strated in Figure 5.5 where the ripple amplitude increases from 1.63/2 = 0.82 Å (width = 4) to 1.78/2 = 0.89 Å for large ribbons (width $\geq$ 12), and where out-of-plane displacements remain localised within around $\sim$ 2.3 Å of the armchair graphene ribbon edge. The ripple amplitude is inversely proportional to the AGNR strain (for widths < 12) and only indirectly coupled to the width of the ribbon, consistent with a picture of a constant buckled/rippled edge length more able to dilate the graphene when its basal plane area is smaller.

Do opposed rippled armchair GNR edges couple?

Coming back to the 15 different modelled structures, mentioned at the beginning, an overview of the performed calculations is given in Figure 5.6. Out of these calculations, four different families of edge structures have been identified in terms of the total energy difference ΔU per unit cell (with length a_0) for each width and the strain ϵ along the ribbon axis (see Figure 5.6).

Configuration 1 (structure A) on the left in Figure 5.6 shows a symmetrical in-plane -OH arrangement and is the least stable arrangement (family), with repulsive -OH groups constrained to lie in the graphene plane as proposed in literature [236].
As second family (configurations 2 and 3), flat in-plane graphene configurations were classed, with -OH groups are orientated in the same way creating hydrogen bonding between neighbouring -OH groups (like edge structure B in the previous sections). In these two cases, the orientation can be varied to be symmetrical on both edges or inverse, marked with black arrows for all relevant cases in Figure 5.6, but the identical energy for 2 and 3 shows this relative orientation is not important. Both these 2 structures still show significant axial strain, as the -OH groups are too closely spaced.
As third intermediate (metastable) family, the “uu” and “ud” configurations (4 - 11) are adding stability through moderate out-of-plane rippling of the -OH groups. Due to the small repeating unit cell of the AGNR, only -OH groups are possible to arrange out-of-plane. Relaxing an edge with both -OH groups pointing upwards

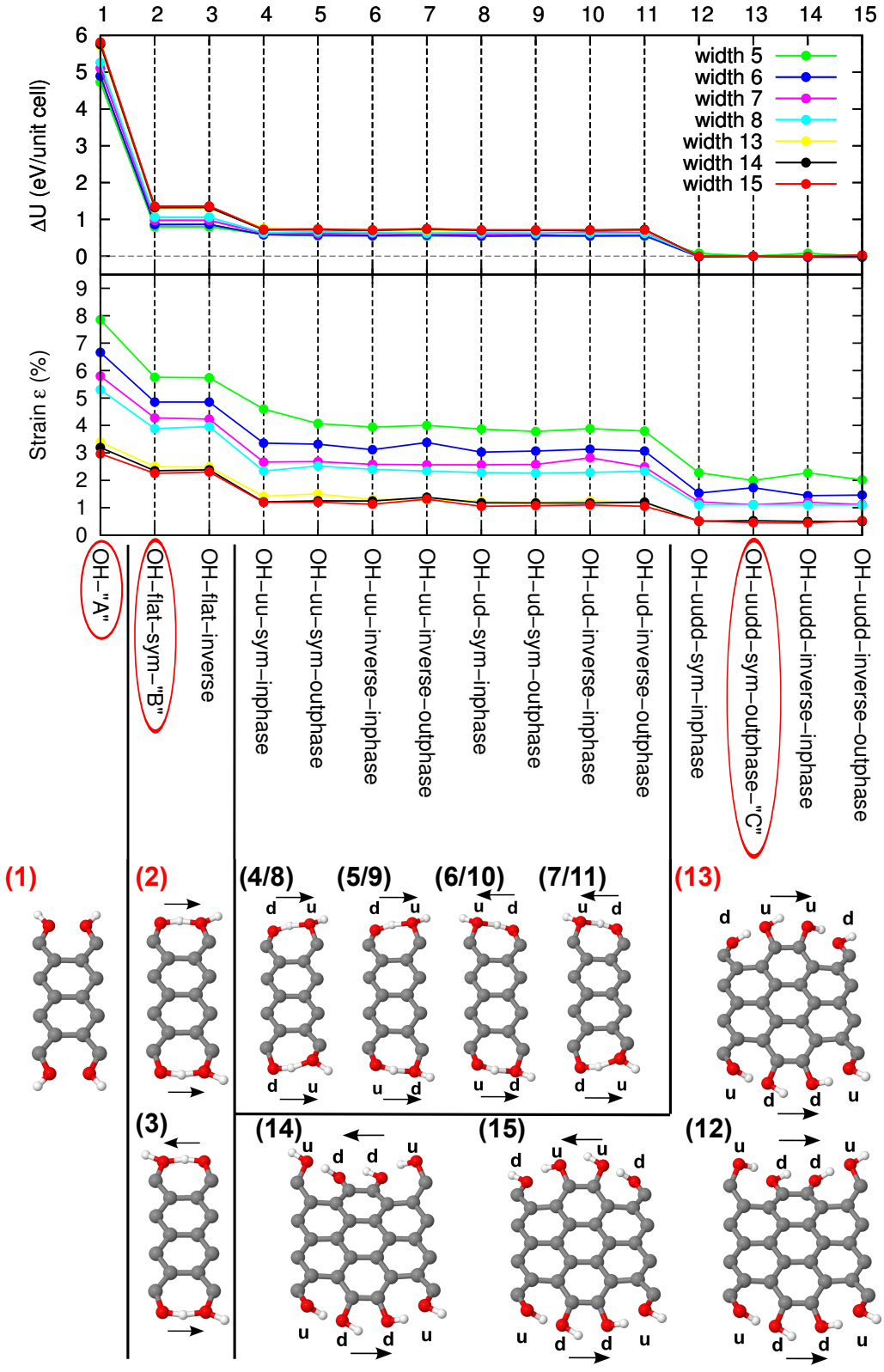

Figure 5.6: Energy and strain of 15 different GNR edge -OH configurations for width 5 - 8 and 13 - 15. Below: unit cell of a width 7 AGNR showing the specific -OH configuration. Arrows show chain orientations, u ("up") and d ("down") help to show out-of-plane edge rippling. (Configurations highlighted with red circles were discussed in the previous sections.)

on the edge ("uu" configurations 4 - 7), it was found the edge turns directly into a related "ud" configuration (8 - 11). Here, the phase of the rippling adds another degree of freedom, with either in phase (mirrored in the GNR middle) or with a phase shift between the edges. (Another phase shift is introduced directly for to the ribbon axis asymmetric edges for all $2N$ ($N = 1, 2, ...$) widths.) But also the ripple phase does not influence the total energy, and thus no coupling between these edges for GNR $\geq$ width 5 has been found.
Adding another additional freedom to the graphene armchair edges via doubling the repeating unit cell to $2 \cdot a_0$ (configurations 12 - 15, structure C), leads clearly to the most stable edge -OH terminated AGNRs family. Here, the edges form the characteristic "uudd" ripples, as already discussed in the previous sections, and also no direct coupling has been found.

Regarding the 4 different edge type GNR families, it can be noted that neither the edge -OH chain orientation nor the ripple phase between edges is changing the total energy or the induced strain. Spin-polarized calculations have been tested for width 7 - 9 for AGNR with structure C ("uudd" configuration 13), and always the non-magnetic (non spin-polarized) case was found to be the most stable configuration. Thus no electronic coupling between the armchair edges is expected down to very small ribbon widths. Comparing to the very small differences in edge energy for magnetic hydrogentaed edges (Chapter 4) in the meV scale, the comparatively large changes in energy in Figure 5.6 result clearly from the structural favourable rippled -OH group arrangement at the edge.

Slight fluctuations in energy or strain inside the four edge type families are resulting from the set default optimisation tolerances. Thus for all calculations in Figure 5.3, the tolerance of the energy convergence for one self consistency cycle has been set to 10^{-8} Ha (default 10^{-5} Ha), in order to avoid this small variations when studying in detail the edge configurations A (1), B (3) and C (13) in the previous section.

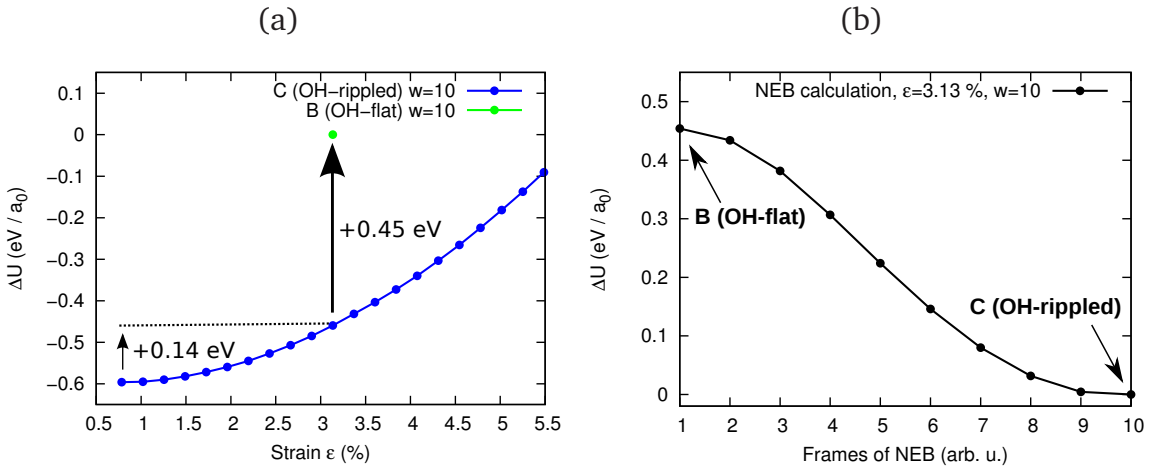

Figure 5.7: (a) Estimated energy barrier ΔU for dynamic rippling of one edge of length a_0 (see Figure 5.1) for a AGNR width 10 with ΔU = 0.14 + 0.45 = 0.59 eV/a_0. (b) No energy barrier is found (NEB-method) between hydroxyl AGNR configurations B and C for one edge with same strain (ϵ = 3.13 %), showing configuration B is a metastable maximum. Comparable to the energy difference plotted in Figure 5.3 (a) at width 10 of $\approx$ 1 eV/unit cell a_0 for both structures fully relaxed. Here additionally the energy is divided by factor 2, regarding only one edge.

Thermodynamic stability of rippled -OH functionalized edges

I further examined whether the static ripples will dynamically fluctuate at room temperature by calculating the barrier to invert the ripple. This calculation at fixed cell length show a high barrier of $\sim$ 0.59 eV/a_0 per edge, and thus suggests there will not be strong phonon coupling with these kind of edge ripples.

This static character of the rippled edges is demonstrated in Figure 5.7 (a) where an -OH terminated rippled AGNR is strained. Even straining the AGNR up to 5.5 % the ripples do not flip spontaneously to a flat structure (*e.g.* structure B). Further a nudged elastic band (NEB) calculation [243] has been performed to determine the barrier between configuration B and C, when strained to the same value as the flat configuration (Figure 5.7 (b)). No barrier has been found between the rippled C and flat B configuration, demonstrating that configuration B can only be a metastable local maximum.

Excluding any intermediate local minima, the two calculations can be summed to

estimate the ripple inversion barrier of one edge per unit cell length a_0 ($\sim$ 4.3 Å) length. As demonstrated in Figure 5.7 (a) with arrows, leading to a minimum estimated barrier of $\Delta U_{Barrier}$ = 0.59 eV/a_0 to invert one edge wave. This barrier is too high for thermal activation at room temperature ($\sim$ 0.025 eV), and therefore this rippled edge configuration is expected to be static under ambient conditions.

Why haven't these characteristic edge ripples been discussed before?

It is surprising that this edge structure hasn't been described in the literature so far. The most probable explanation is that its low symmetry requires doubling the unit cell along the ribbon, leading to expensive calculations. Still, one very recent study, additionally to this work, has studied the special case of a -OH edge terminated AGNRs of width 7 [244], confirming my results. This work shows also that a fully -OH terminated armchair GNR edge represents the most stable configuration compared to other -OH densities at the edge. Further, this study focused especially on vibrational properties, pointing out that such functionalization is potentially characterisable through vibrational spectroscopy.

The discussion so far concerns free-standing graphene, but preliminary calculations suggest that even on surfaces like Cu(111) rippled edges occur, when starting from a rippled edge configuration. On substrates, the modulating height of the hydroxylated edge ripples will result in periodic modulation in the graphene-substrate spacing and hence the substrate-induced potential felt by the nanoribbon, increasing electronic localisation effects. Variation in graphene-substrate spacing at the ribbon edge could also facilitate impurity intercalation beneath the graphene. This field especially in combination with new experimental data [42] offers many interesting questions for future investigations.

Summarizing this section, I have shown that hydroxylated AGNRs will spontaneously form static edge ripples, due to an edge-strain induced out-of-plane deformation mode. As a result, the strain induced by the rippled hydroxylated edge

of wide ribbons is less than 0.35 % (width $\geq$ 20), and very close to that of H-terminated AGNRs of the same width ($<$ 0.18 %). It can be noted that no significant interaction between the two edges of different -OH terminated AGNRs has been found (as reflected in the total energy and strain), suggesting they are largely decoupled.

Next I have investigated how static edge ripples modify the electronic properties of graphene nanoribbons, comparing structures B and C to determine the influence of rippling, and C and H-terminated AGNRs to determine the influence of the hydroxyl functional group.

5.1.3 Bandgap behaviour of -OH functionalized AGNRs

Concerning the electronic properties, the energy gap behaviour of AGNRs plays a key role for the use in electronic devices. The value of the energy gap is extracted from the band structure along the ribbon axis at Γ in the reciprocal space. Examples are plotted for AGNR widths 6 - 8 in Figure 5.8. I obtained good agreement between my calculated LDA-DFT bandgap values for flat H-terminated AGNRs and previous literature results [37, 179]. Additionally, the -OH functionalized AGNRs with edge structures C and B are calculated for the complete width range 4 - 20, studying the influence of the -OH functional group and the edge rippling. An overview of all energy gap values is given in Figure 5.9.

Generally, the bandgap for narrow AGNRs is inversely proportional to the ribbon width due to lateral quantum confinement, superimposed with a strong $3N$ periodicity. This $3N$ alternation can be explained via Clar's sextet theory as demonstrated in previous studies [179, 180], and has also been explained using approaches based on quantum confinement effects applied to the Dirac equation [245] and using a nearest-neighbour tight-binding model [178].

The calculated bandgaps for AGNRs with edge structures B and C are almost superposed plotted in Figure 5.9, clearly showing that edge rippling does not directly

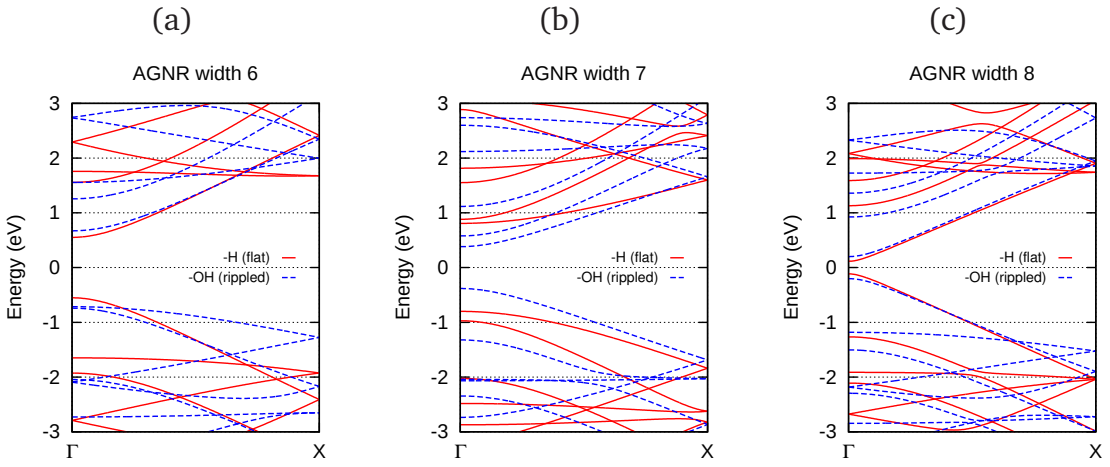

Figure 5.8: Band diagrams of AGNRs H-terminated (flat) and -OH functionalized (rippled structure C), (a) width 6, (b) width 7 and (c) width 8. For the H-terminated AGNRs, the super cell was doubled to $2 \cdot a_0$ in order to compare correctly with the -OH terminated ribbons. All calculations were non spin-polarized (NM).

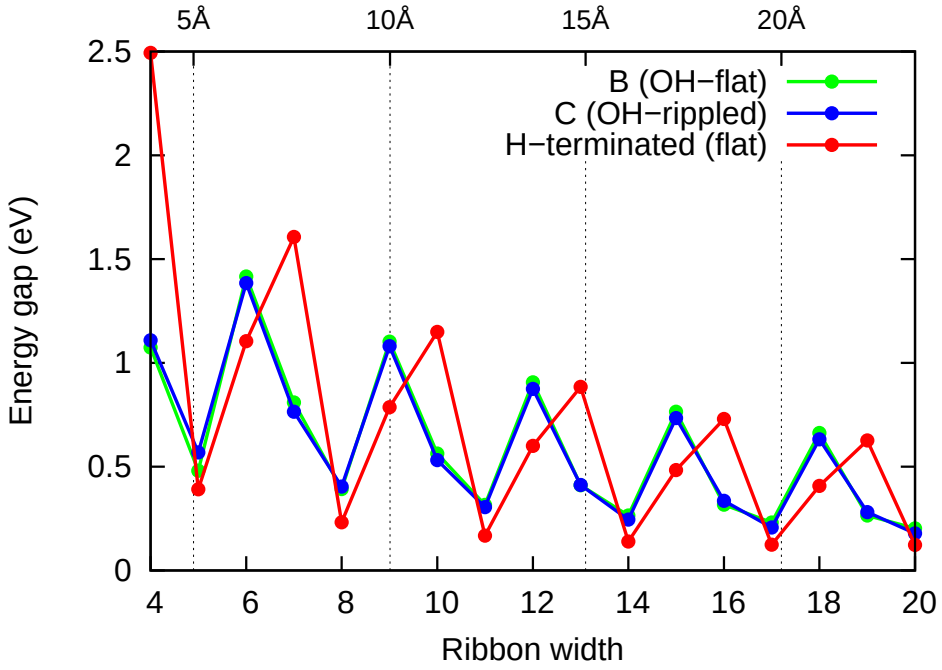

Figure 5.9: (Energy gap (bandgap) versus width for different terminated AGNR. H-terminated AGNR (red), hydroxylated structures B (green) and C (blue).

affect the gap for -OH termination. Instead, the bandgap is dominated by the choice of the edge functional group. Once again, the typical predicted $3N$ periodicity with width [179] can be observed for -OH edge functionalisation, but the difference with the H-termination case is not a simple phase shift of the periodicity (see also Chapter 4 section 4.3.2). For $3N + 2$ ($N = 1, 2, ..$) widths the bandgap is similar to the H-terminated case, but for $3N$ and $3N + 1$ the difference is significant, with bandgap fluctuations of up to 50 %.
It can be noted that AGNRs with -OH edges of structure A (found to be energetically very unstable) show as well exactly the same bandgap behaviour as AGNRs with -OH edges of structures B and C. This excludes additionally any speculations about influences on the AGNR electronic properties induced by the hydrogen bond interactions between the -OH groups (structures B and C).

These significant changes in bandgap between H-terminated and -OH terminated AGNRs of the same width are also not caused by new -OH edge states introduced near the Fermi level, directly visible at Γ in the band diagrams in Figure 5.8. It seems the bands near the Fermi level are getting squeezed (*e.g.* width 7) or stretched (*e.g.* width 6) when the ribbons are -OH terminated. The reason for these changes especially for $3N$ and $3N+1$ widths has been addressed briefly in the literature [244], proposing mechanical deformations and the change in quantum confinement boundary conditions. Still, a simple explanation for all periodicities seems not to be possible yet, and personally I think the mechanical axial deformation (strain/stress) due to edge functional groups on the AGNR is too weak to induce any detectable changes of the bandgap.
An additional possible effect could be the influence of the differences in electronegativity between the edge carbon atoms and the directly bonded atomic species (here oxygen), more studies in this direction are aimed to be done by another group (personal communication with G. van Lier and F. Martín-Martínez [246]). The same periodic bandgap behaviour is discussed later, when testing further atomic species as edge functional groups.

It is important to remember, that all bandgap values in Figures 5.8 and 5.9 are quantitatively underestimated as typical for LDA-DFT calculations. Nevertheless, the change in bandgap permits a qualitative interpretation, supported by results using other approximations such as for example PBE and HSE functionals [37, 247, 248]. Note also that all new types of functionals (PBE0, HSE, B3LYP, GW-BSE) are leading to weakly scattered results, and have to be treated carefully [247, 248].

In summary, I have shown here that bandgaps of AGNRs, especially for the widths $3N$ and $3N+1$, appear highly sensitive to choice of edge functional group. However, the gap is not sensitive to out-of-plane edge rippling for -OH termination.

5.1.4 Mechanical properties of -OH functionalized AGNRs

In this section, the changes due to edge rippling for the in-plane Young's Modulus (E) of AGNRs along their axis is determined using the approach described by Zeinalipour-Yazdi and Christofides [249]. Inducing strain up to $\pm$3 % along the ribbon, the total energies were calculated (7-points, $\pm$1, $\pm$2, $\pm$3 %). Energy difference (ΔU) vs. strain (ϵ) has been fitted with a quadratic function $\Delta U(\epsilon) = a\epsilon^2$. E is given by $E = \frac{2a}{V}$, where $V = a \cdot w \cdot t$ is the volume of the ribbon section composed of length a, width w taken in this study as the H-H distance between opposed edges and t = 3.35 Å as AGNR thickness. I calculated E for flat defect-free infinite graphene to be 1.08 $\pm$0.03 TPa using this slab model, in good agreement with theoretical literature values (1.05 TPa [170], 1.09 TPa [249], 1.11 TPa [250]). More detailed information and discussion about mechanical properties of nanostructures can be found in Chapter 6.

Interestingly, finite width H-terminated and edge-rippled -OH terminated AGNRs show significantly smaller Youngs' Modulus compared to graphene as shown in Figure 5.10. In both cases, the in-plane Young's modulus is approximately inversely proportional to ribbon width, with some non-linearity at smaller widths ($<$10) when edge effects start to dominate. Both edge terminations extrapolate to the ideal graphene value at infinite width (H-terminated: 1.05 TPa, OH-rippled: 1.03

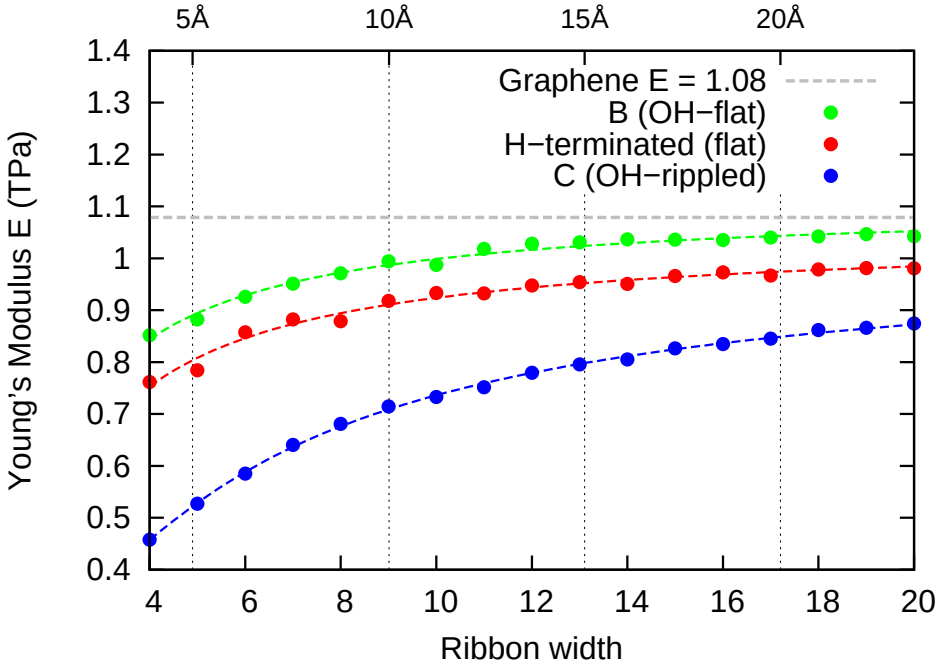

Figure 5.10: Young's Modulus E along the AGNRs (in case of graphene along the armchair direction). E fitted with $E = \frac{a}{x} + \frac{b}{x^2} + c$ as guide for the eye (fit parameter see Table 5.3).

Figure	Graph	a	b	c	standard deviation
Figure 5.10	B (OH-flat)	-1.101	0.198	1.107	0.008
	H-terminated (flat)	-1.257	0.334	1.046	0.010
	C (OH-rippled)	-3.381	4.354	1.031	0.004

Table 5.3: Fit parameters of function $E(x) = \frac{a}{x} + \frac{b}{x^2} + c$ when fitting the curves of Young's Modulus versus ribbon width in Figure 5.10. For infinite ribbon widths both the H-terminated and -OH rippled ribbons tend to the same calculated Young's Modulus of about 1.05 $\pm$0.05 TPa, in good agreement to that of graphene with 1.08 $\pm$0.03 TPa. The flat unstable -OH configuration B adds stiffness to the narrow ribbons. The non-zero coefficient for b indicates non-linear effects that become important for small ribbon widths.

TPa, presented in Table 5.3), and as expected the modulus of -H terminated AGNRs drops towards the value for cis-polyacetylene polymer chain ($[C_2H_2]_n$) at small widths (since this polymer corresponds to a width 2 AGNR, see also Chapter 6, section 6.6).

However, changing the edge functionalisation from -H to -OH groups (with rippled edges) significantly decreases the Youngs' Modulus of thin ribbons. This reduction has to be a direct result of the rippling. Indeed, calculations for the unstable flat -OH ribbons (structure B), actually show a slight increase in Young's Modulus over the -H terminated case (Figure 5.10), since in this case the ribbon is under slight tension. As for the bandgap (Figure 5.9), a slight periodicity of $3N$ can be observed in the values of E, reflecting variations in C-C bonding with width. These changes in E as a function of both ribbon width, and edge termination, will be critical in graphene nanocomposite design. Modifying ribbon edge functionalisation is an obvious way to chemically bind graphene nanoribbons into a host polymer matrix, but these results show that changing the functionalisation groups can decrease the Young's Modulus of the nanoribbon itself up to 40 % for small widths. For wider GNRs (> 5 nm) these edge effects become less important.

5.1.5 Chemical reactivity of metallic Pd adatoms on -OH functionalized AGNRs

Rippling may be expected to modify the chemical reactivity of the ribbon surface. To give first insights, I calculated possible bonding sites for a single Pd atom addition on an AGNR of width 10. Normally single Pd atoms prefer to sit above a C-C bond center as predicted in the literature [251, 252], confirmed in my calculations. In general, binding nearer the ribbon edge is more stable, regarding flat edges. For rippled -OH functionalized armchair edges, I find Pd atoms at the ribbon edge are $\sim$ 0.4 eV more stable in a concave "valley" site of an edge ripple than on the convex "ridge top" (see Figure 5.11). Indeed the concave "top" site is even $\sim$ 0.1 eV less stable than a flat site at the ribbon centre. It can be expected that with a very small activation energy, Pd atoms can migrate to the edge (diffusion

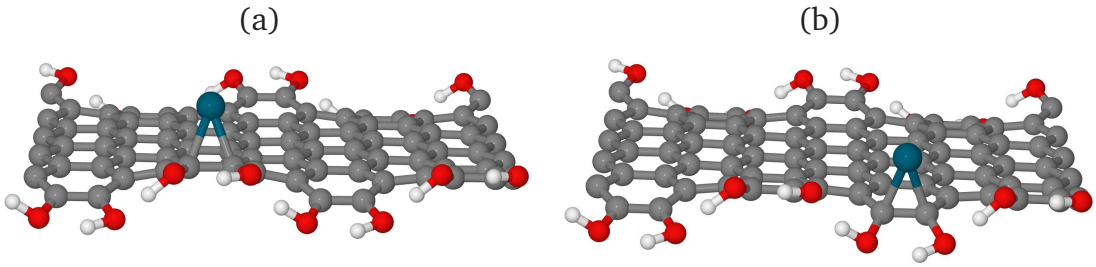

Figure 5.11: Pd atom addition to a -OH terminated AGNR (width 10). (a) “Top-ridge" site, (b) “Valley" site, which is ΔU = -0.4 eV more stable.

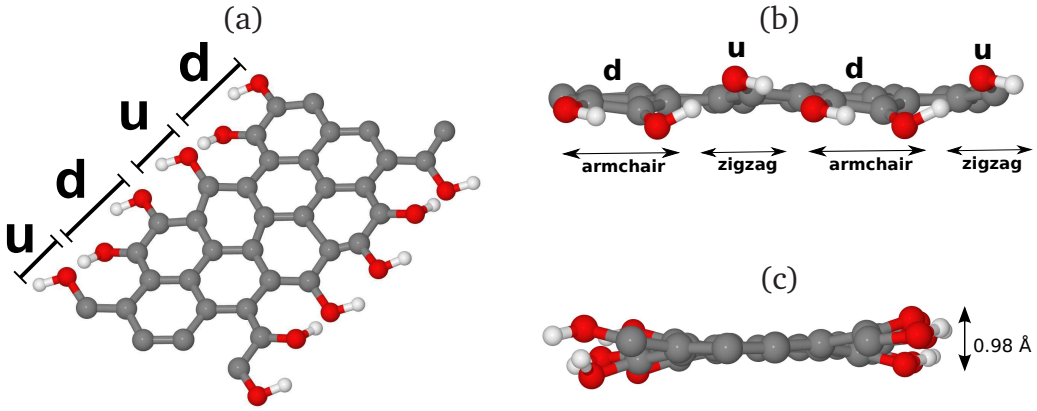

Figure 5.12: Chiral -OH terminated GNR, orientation angle α = 10.89° [158]. (a) perspective view, (b) side view, (c) front view.

barrier $<$ 0.1 eV [251]) and will sit preferentially in the valleys of the rippled edge structure. Thus the ripple-induced changes in surface curvature periodically modify the surface reactivity of the graphene. This suggests interesting changes in absorption behaviour for chemisorbed and physisorbed species, and potentially important geometric effects for metal contact deposition.

5.1.6 -OH functionalized zigzag and chiral GNRs

I find that hydroxylated zigzag GNRs (ZGNRs) do not exhibit out-of-plane edge rippling confirmed by theoretical literature results [215, 242]. The larger spacing between edge C atoms (d_{C-C} = 2.44 Å) at the zigzag edge results in sufficient spacing between the -OH groups to keep edge strain generally below $\pm$0.2 %. Additionally, the electronic properties for fully -OH edge terminated ZGNRs are similar to single H passivation (see Chapter 4 section 4.4.2), with the carbon edge atoms showing

sp^2 hybridisation [215]. Free standing zigzag edges are more likely to be oxidised rather than hydrogenated [215]. Note however this does not preclude edge rippling in ZGNRs for other larger functional groups, such as -Cl or -SH groups.
In order to determine how general the static edge rippling effect is, I next examined one example of a chiral GNR. I calculated the -OH edge configuration of a GNR cut at the orientation angle $\alpha = 10.89^\circ$ as shown in Figure 5.12. Calculations for hydroxylated chiral edges show an intermediate effect, with localised edge rippling around armchair-like sections which rapidly decays in zigzag sections of the edge as demonstrated in Figure 5.12. Thus these results show that the majority of graphene edges, when hydroxylated, will exhibit static out-of-plane rippling, as discussed in section 5.1.2. Placing functionalized chiral GNRs on surfaces could change this behaviour, dependent on the surface ribbon interactions (*e.g.* charge transfer) and orientation.

5.2 -F, -Cl, -Br and -SH edge functional groups

In order to determine the generality of this edge ripple effect, I further examined the dependence of static edge rippling at AGNRs on different functional groups, replacing -OH with -F, -Cl, -Br and -SH. In all cases, the ribbons exhibited the same characteristic periodic edge rippling as the hydroxylated edges. This is shown in Figure 5.13 for a fully -SH terminated AGNR, and in Figure 5.14 with -F termination. In all cases, the edge strain, caused by steric hindrance between the edge functional groups, is relieved through out-of-plane edge rippling. The amplitude varies depending on the functional group. In the extreme case of -SH groups, an edge ripple amplitude of 4.51 Å was calculated.

The different functional groups attached to graphene nanoribbons can be roughly ordered in two groups. First the heteroatom edge functionalization, with groups such as -F, -Cl and -Br. These atom species can all be found in group 17 of the periodic system and tend to form stable single covalent bonds with the edge carbon atoms. As second group, complex functional groups such as -OH or -SH can be identified. Here, the characteristic O or S atoms (both group 16) form strong bonds with the edge carbon atoms, while between neighbouring functional groups weak hydrogen bonds are possible. In terms of the edge structure both groups are clearly most stable in a rippled edge configuration.

Thus a key finding of this study of functionalized armchair GNRs is that flat graphene edges, often exemplified by hydrogen termination, appear to be the exception rather than the rule. The majority of graphene nanoribbon chiralities and functionalisations examined in this work undergo spontaneous out-of-plane static rippling.

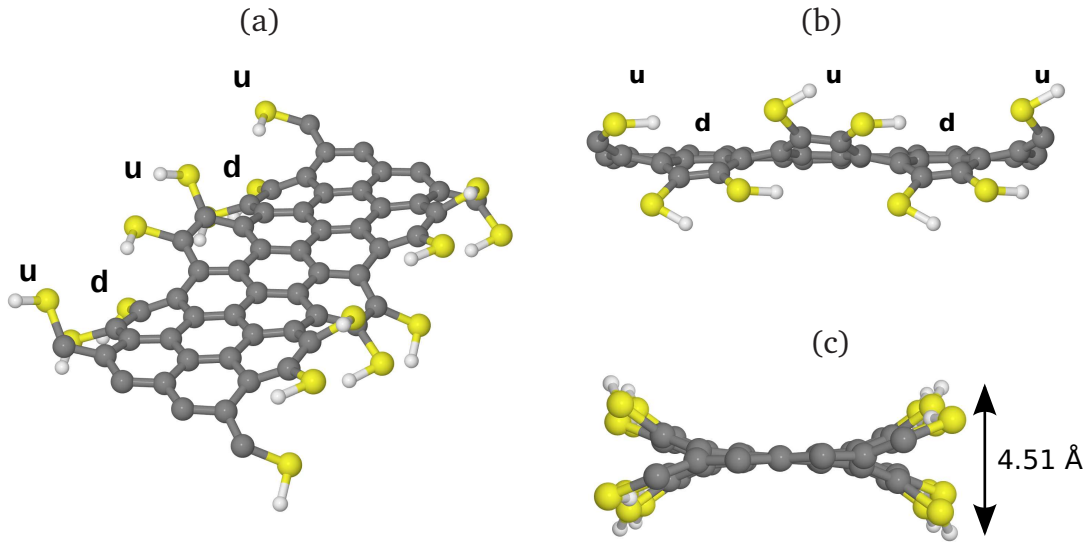

Figure 5.13: AGNR (width 7) -SH terminated. (a) perspective view, (b) side view, (c) front view. In grey C atoms are pictured, H atoms in white and S atoms in yellow. u stands for “up" and d for “down" for the rippled edge carbon dimer groups.

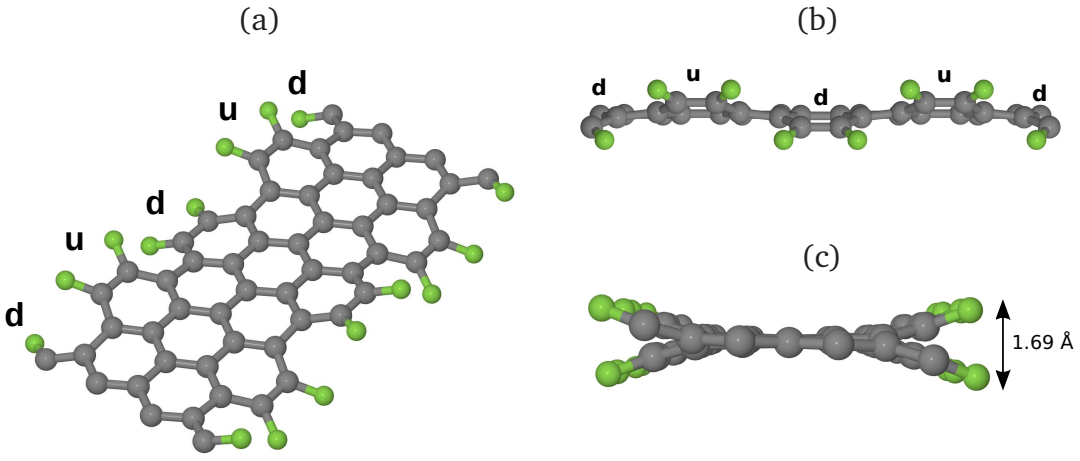

Figure 5.14: Armchair graphene nanoribbon (width 7), F-terminated. (a) perspective view, (b) side view, (c) front view. In grey C atoms are pictured, F atoms are green. u stands for “up" and d for “down" for the rippled edge carbon dimer groups.

5.2.1 Bandgap behaviour of -F, -Cl, -Br, -SH functionalized AGNRs

Aiming to used graphene and GNRs in electronic circuits, a major challenge is bandgap engineering [239]. Edges of small ribbons could be perfect to tune the bandgap using different edge functional groups. Therefore, in a next step, the influence of the edge functional groups -F, -Cl, -Br and -SH on the energy gap behaviour of the armchair graphene ribbons has been calculated. In Figure 5.15 (a) and (b), the periodic 3N variation over width for AGNRs with different functional groups is plotted.

The simpler single bonded functional groups -F, -Cl and -Br in Figure 5.15 (a) are found to show the same periodic trends as for single H-termination. A sightly different variation for -F edge termination is visible for the $3N$ and $3N+1$ widths, similar to the -OH case. It can be speculated that this effect comes from a higher electronegativity of the F atoms, but a coupling with the aromatic AGNR is not simple to prove. A detailed study of the local electron distribution (*e.g.* calculating the Mulliken populations for the HOMO and the LUMO state for the edge carbon atoms) for every single case could be one possibility to get further insights. Such studies are leading to time consuming calculations and complex statistics, and will be done certainly in future studies.

The more complex functional group -SH in Figure 5.15 (b) shows a relatively similar periodic bandgap behaviour as already studied for the -OH functionalized AGNRs (Figure 5.9). But while the $3N+1$ width is strongly influenced, the bandgap values for $3N$ widths are much closer to the simple hydrogenated case than to the -OH terminated AGNRs.

A key observation is, common to all functional groups tested, the insensitivity or constant bandgap behaviour for all the $3N+2$ widths. For these special widths the aromatic graphene network seems to be very stable, and chemical environmental changes to the edge carbon atoms do not show any significant electronic effect, in LDA-DFT calculations.

(a)

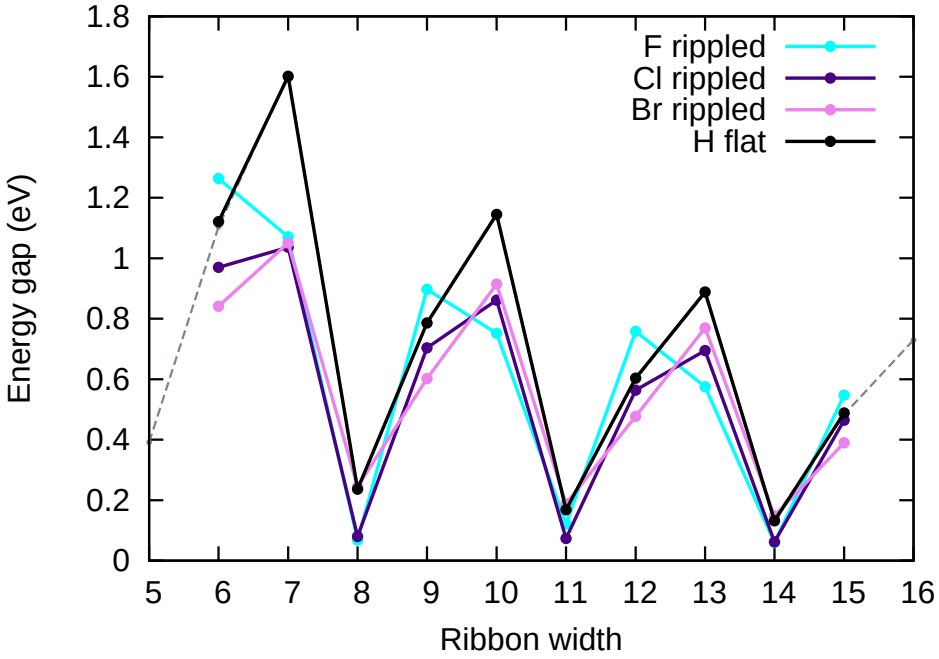

(b)

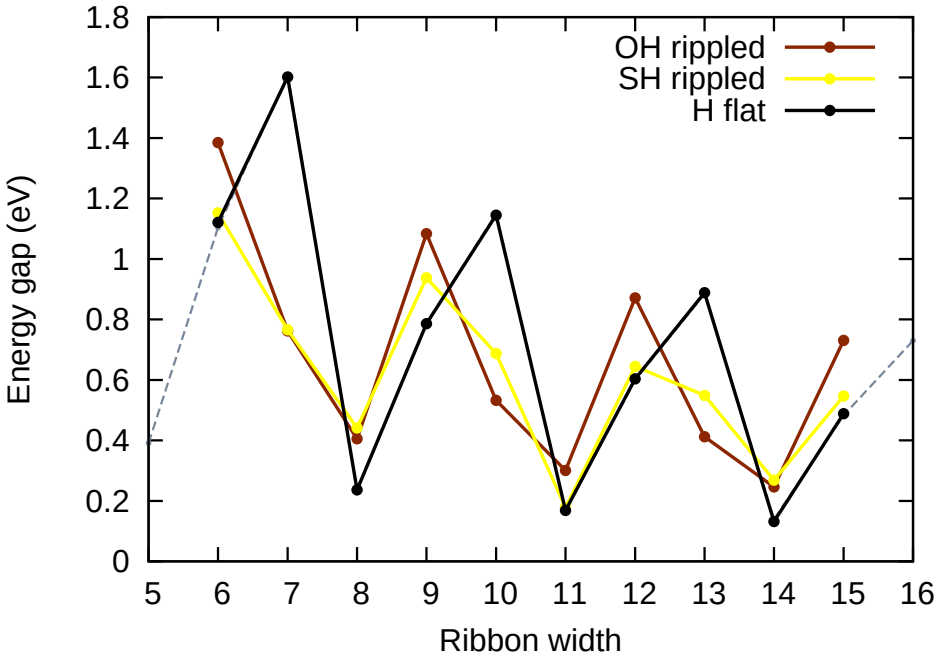

Figure 5.15: (a) Energy gap versus width for different single atom terminated AGNRs. (b) Energy gap versus width for -OH and -SH terminated AGNRs.

The influence of the LDA-DFT approach on these new energy gap values for -F, -Cl, -Br and -SH edge functionalized AGNRs is not totally clear, and has to be tested using other (hybrid) functionals, especially for periodicities $3N$ and $3N + 1$ giving sometimes close energy gap values.

Another option to get more informations about the chemical behaviour could be therefore a study of the mean bond length and ring bond dispersion, recently applied by Martín-Martínez *et al.* [246] to GNRs. While this is a purely geometrical approach, it should be noted that the geometric optimisation has to be done very precisely with high tolerances, requiring high computational costs. Note that this approach can also be indirectly influenced by the chosen functional.

5.3 Twisted graphene nanoribbons via edge functionalization?

An alternative way to relieve edge strain proposed recently is twisting of the whole graphene nanoribbon [235]. In this study, a -F edge-terminated armchair graphene nanoribbon of width 8 was twisted helically and found to be most stable with a twisting angle of 4.2° between two unit cells. The energy difference between twisted and flat was -2.3 · 10^{-3} Ha (≈ -0.0626 eV), I assume, per unit cell but this was not clearly stated in the article. In this case, the sp^2 π - system of the graphene nanoribbon is slightly distorted throughout compared to a flat graphene sheet. In the case of a simple H-terminated AGNR of width 8, no energetically more stable twisted configuration was found.

In this first literature study regarding functionalized twisted AGNRs, Gunlycke *et al.* [235] used tight binding calculations for geometrical optimisations. Only very small super cells with rotated boundary conditions were used to model the twisted systems. However, it is not obvious that the cell size was sufficiently large and how accurate the tight binding approach worked with the exotic rotated boundary conditions.

I have therefore tried to calculate the structure and energy of such -F functionalized twisted ribbons using a large orthorhombic unit cell containing 1620 atoms (ribbon width 7) performing a 360° twist in the unit cell with an angle of 4° between fundamental unit cells, using a more accurate LDA-DFT method (*AIMPRO* code). I note that this full 360° twist is necessary, since when twisting only 180° the periodic boundary conditions are not correct. The 180° twisted ribbon segment in one supercell connects to the next following ribbon segment comparable to ribbon ends connected forming a Möbius band [253]. Examples of twisted AGNRs of width 7 with -F terminated edges are schematically shown in Figure 5.16, including the identified rippled edge configuration in this work (see also Figure 5.14). Such system sizes (1000 atoms and more) are only possible due to recent development of a new filtration method for DFT calculations (for computational details see

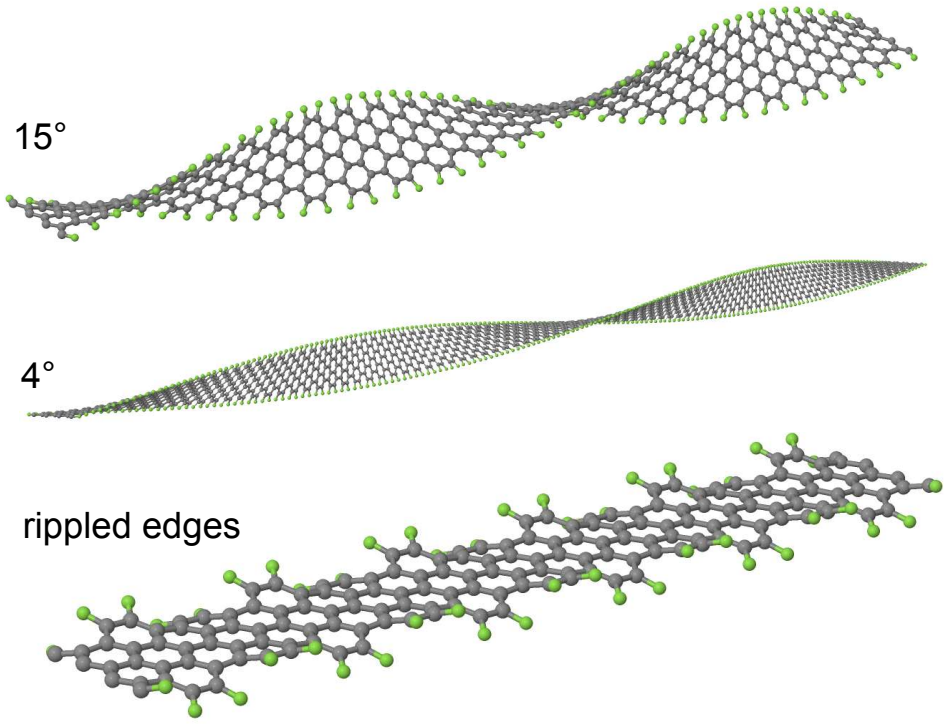

Figure 5.16: Schematic of a -F terminated twisted armchair graphene nanoribbon (width 7) twisted 15° (432 atoms/unit cell), 4° (1620 atoms/unit cell) between each original unit cell (length a_0). The flat width 7 AGNR with rippled -F terminated edges (36 atoms/unit cell) was found more stable compared with twisted configurations as preliminary calculations indicate.

[66–68]). These calculations are nonetheless very time consuming, and the new filtration algorithm has to be tested and the implementation has to be optimised. Especially for nanostructures with bigger parts of vacuum in the supercell, more development work is needed.

My first preliminary results suggest that twisted ribbons are much less stable than the flat ribbons with rippled edges [205]. This agrees with my calculations for the rippled edge configuration compared to a flat -F terminated AGNR of width 8 where gain in energy per unit cell is $\sim$ 2.42 eV. Thus the rippled edge configuration adds massive stability compared to the small energy gain reported for the investigated twisted AGNR of width 8 in literature (-0.0626 eV [235]). This seems sensible since edge rippling disturbs only the edge of the sp^2-graphene network whereas twisting

distorts the entire ribbon. Even if twisting can occur, this suggests a limitation in width where twisting can be applied before collapsing and folding, whereas rippling the edge is independent of the graphene nanoribbon width.

Thus it can be concluded that ribbon edge strain will not lead to twisting, for AGNRs functionalized with simple heteroatoms such as -F.

5.4 Computational details

In this Chapter, besides the already mentioned pseudopotentials (generated using the Hartwingster-Goedecker-Hutter scheme [73]) and the basis sets ($pdddp$) for C, (ppp) for H and ($dddd$) for O, additionally the following basis set F: ($ddpp$), Cl: ($dddd$), Br: ($fddd$) and S: ($ddpp$), were used. The charge density was fitted to plane waves within an energy cut-off of 200 Ha. Electronic level occupation was obtained using a Fermi occupation function with kT = 0.04 eV. For all structures, the atom positions and the lattice parameters have been fully relaxed. The choice of the k-point grid was always tested to give fully converged energies. The energy tolerance for the calculations were set to $1 \cdot 10^{-5}$ - 10^{-7} Ha, and for the atomic positions $1 \cdot 10^{-4}$ - 10^{-5} Bohr. For calculations in this chapter additional a energy tolerance value per SCC of $1 \cdot 10^{-8}$ Ha (default $1 \cdot 10^{-5}$ Ha) was used.

Chapter 6

Mechanical properties of graphene and related nanostructures

Mechanical properties of materials (in the elastic regime) can be determined in general by measuring the Young's modulus E, the Poisson's ratio ν and the shear modulus G. These mechanical properties can deliver important information for example when introducing novel nanomaterials, such as graphene or carbon nanotubes, in advanced composites and devices. In this chapter, the main focus is concentrated on the (in-plane) Young's modulus of graphene and related nanosheets, as well as carbon nanotubes and armchair graphene nanoribbons. In this study, a so far unsolved problem has been identified in this context, namely an exact definition of the intrinsic volume of a nanoobject. Notably the Young's modulus (normally applied to objects at the macroscopic scale) is directly related to the volume, and therefore values of E in the literature for nanoobjects are often scattered and of unclear quality. With the development of a new volume definition, based on the average electron density, for nanoobjects (mesoscopic scale), shown here for the first time, a transferable and underlying framework is given. Thus, this approach allows a better comparison of mechanical properties, such as the Young's modulus, and enables further access to values for example the out-of-plane Poisson's ratio for graphene or the mechanical behaviour of charged systems. Finally this new approach has been applied to a range of polymers calculating the Young's modulus, allowing to show the wider and very effective use of this new concept.

6.1 Defining mechanical properties of materials

6.1.1 Young's modulus and its computational realization

The Young's Modulus E, also called tensile modulus, is defined as tensile stress σ over tensile strain ϵ,

$$E = \frac{tensile\ stress}{tensile\ strain} = \frac{\sigma}{\epsilon} \ . \tag{6.1}$$

The tensile strain can be defined as the fractional change in length $\epsilon = \Delta l / l_0$ along the direction of the applied strain, where l_0 defines the length at equilibrium. The tensile stress is defined as the force F per surface area A, $\sigma = F/A$, leading to

$$E = \frac{\sigma}{\epsilon} = \frac{F \cdot l_0}{A \cdot \Delta l} \ . \tag{6.2}$$

Using DFT calculations, one easily accessible way to describe the strained system is via the total system energy U. In general $U(\epsilon)$ can be expanded in the form of a nth order polynomial,

$$U(\epsilon) = a\epsilon + b\epsilon^2 + c\epsilon^3 + ... + C \ . \tag{6.3}$$

When applying small strains the induced change in energy $\Delta U(\epsilon)$ can be expressed as difference of the total energy $U(\epsilon)$ and the equilibrium total energy $U(0)$ of the system (in (6.3) $C = U(0)$).

For small strains (typically $\leq$ 3 %), we are in the harmonic regime and $U(\epsilon)$ can be simplified to a quadratic function ($a, c, .. \approx 0$). An example is given in Figure 6.1, where the energy difference $\Delta U(\epsilon)$ (6.4) of in-plane strained graphene with a quadratic fit is shown.

$$\begin{aligned} \Delta U(\epsilon) &= U(\epsilon) - U(0) \\ &= a\epsilon + b\epsilon^2 + c\epsilon^3 + ... \approx b\epsilon^2 \ . \end{aligned} \tag{6.4}$$

Using the first derivative of the energy U, the force F can be expressed through

$$F = -\frac{\partial U(\epsilon)}{\partial l} = -\frac{\partial U(\epsilon)}{\partial l}\frac{\partial l}{\partial \epsilon\ l_0} = -\frac{\partial U(\epsilon)}{\partial \epsilon\ l_0} \ . \tag{6.5}$$

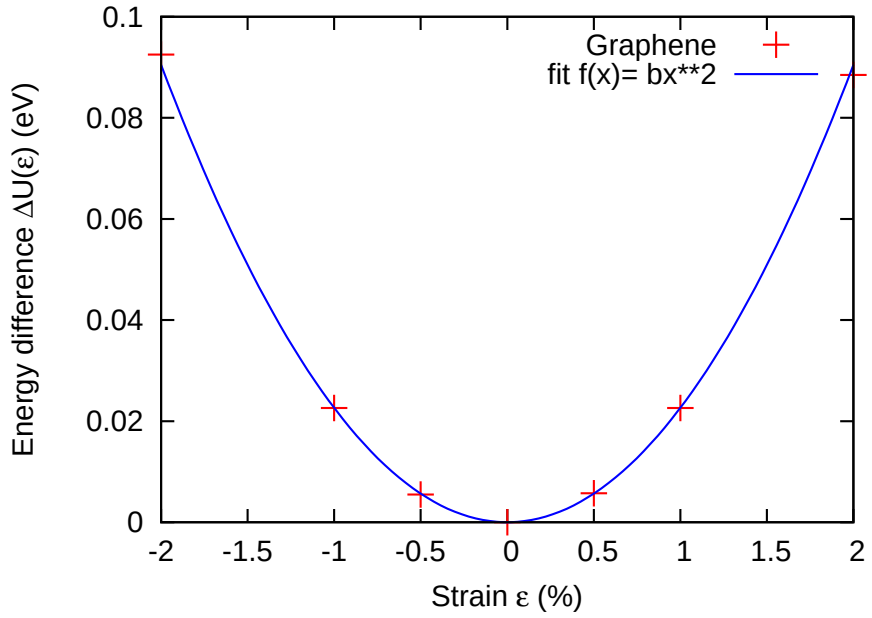

Figure 6.1: Total energy change for graphene (supercell with 8 carbon atoms) as a function of applied strain (calculated with *AIMPRO* (LDA-DFT)), with an associated quadratic fit.

The Young's modulus E can now be written in a more accessible form, considering a harmonic case, using (6.2), (6.4) and (6.5),

$$E = \frac{F}{A_0 \epsilon} = \frac{\partial U(\epsilon)}{\partial \epsilon} \cdot \frac{1}{l_0 \; A_0 \; \epsilon} = \frac{2b\epsilon}{l_0 A_0 \epsilon} = \frac{2b}{V_0} \tag{6.6}$$

where $V_0 = l_0 \cdot A_0$ defines the equilibrium volume. Alternatively, instead of a polynomial expansion, $U(\epsilon)$ can be developed as a Taylor Series [249]

$$U(\epsilon) = \left.\frac{\partial U}{\partial \epsilon}\right|_{\epsilon=0} \epsilon + \frac{1}{2} \left.\frac{\partial^2 U}{\partial \epsilon^2}\right|_{\epsilon=0} \epsilon^2 + \frac{1}{6} \left.\frac{\partial^3 U}{\partial \epsilon^3}\right|_{\epsilon=0} \epsilon^3 + \dots . \tag{6.7}$$

The two approaches are equivalent and the Young's modulus in the regime of small deformations can finally be written in the form of (6.8), including the second derivative of the energy and the volume in equilibrium V_0.

$$E = \frac{1}{V_0} \left.\frac{\partial^2 U}{\partial \epsilon^2}\right|_{\epsilon=0} = \frac{2b}{V_0} \, . \tag{6.8}$$

This approach has been also used successfully by other groups [117, 249, 254] and is the basis for the Young's modulus calculations presented here.

Bulk	This work		Theory	Experiment
Material	E (TPa)	ρ_{bulk} (e^-/a_0^3)	E (TPa)	E (TPa)
Graphite	1.055	0.104	1.041*[255]	1.060 [256]
			1.029*[257]	1.02 [258]
Diamond	1.065	0.158	1.047*[259]	1.051 [91]
			1.061*[87]	1.049*[89]
Si	0.137	0.106	0.138 [260]	0.133*[261]
h-BN	0.880	0.104	0.900*[262]	0.753*[263]
			0.810 [257]	0.700*[264]
WS_2	0.242	0.296	0.238*[265]	0.150 [266]
MoS_2	0.219	0.206	0.202*[265]	0.238 [267]
$MoSe_2$	0.188	0.278	0.178*[265]	-
$MoTe_2$	0.132	0.295	0.124*[265]	-

Table 6.1: Calculated (in-plane) Young's modulus $E_{(100)}$ and average electron density ρ_{bulk} for different layered bulk materials. To allow comparison some literature values have been recalculated (marked with *) based on the given elastic coefficients using $E_{(100)} = \frac{1}{s_{11}} = \frac{(c_{11}+2c_{12})(c_{11}-c_{12})}{c_{11}+c_{12}}$. More informations about the definition of E using the elasticity tensor can be found elsewhere [91, 268, 269]. (with atomic units: e^-: electron charge, a_0: Bohr radius)

Young's modulus of bulk materials

To validate the method and the DFT *AIMPRO* code utilised, pure bulk Young's moduli have been calculated for different materials, including some relevant layered bulk materials, shown in Table 6.1. To obtain the energy curve, the structures were relaxed at $\epsilon = \pm 0.5$, ± 1.0, ± 2.0 % fixed tensile strain (compared to the calculated lattice parameter in equilibrium) along the <100> direction (along the basal planes for layered materials). Other lattice parameters in the orthorhombic supercell were able to relax during optimisation. Here, in all cases, the bulk volume V_0 is clearly defined by the dimension of the unit cell, in my calculations the supercell (SC) respectively ($V_{SC} = V_0$). My results are in reasonably good agreement with

theoretical and experimental values given in the literature. As well defined volumes have been used in these cases, these results show that our potential energy curves are accurately calculated and the error from using a harmonic fit is negligible. The error can be estimated to be less than about ± 3 %.

Young's modulus of nanosheets

Regarding the stated in-plane Young's moduli of nanosheets in the following sections, these have been considered to be isotropic in the sheet plane. It has to be noted that this is only true when applying small strains, and considering staying in the linear elasticity approximation [172, 270, 271]. My calculated values of, for example, graphene along the armchair and zigzag direction are very similar, with a value of 1.059 TPa applying strain along the armchair direction, and 1.061 TPa along the zigzag axis. These differences are a lot smaller than the general error of up to 3 %. Experimentally, these small differences in E will not be observable due to the general error of the measurement (normally in a range up to 20 %) and in most cases in-plane orientation has not been measured [171, 272, 273]. We have additionally to keep in mind that the calculations consider a perfect, infinite and free-standing nanosheet, while in experiments atomic defects, lateral restrictions (edges, grain boundaries) or nanosheet-substrate interaction can occur and influence the measured value. Up to date Raman spectroscopy measurements [272, 273] and SPM setups performing controlled mechanical deformations using sharp cantilevers pushing the nanosheet [171, 274] have lead to reasonably good agreement of experiment and theory. Additionally, the better accessible in-plane Young's modulus bulk values of recent layered materials can be seen as a good first indicator, estimating the stiffness of a single isolated nanosheet of the same material (see also section 6.3 and [29]).

To date, diamond is the stiffest known bulk material with a Young's modulus $E \approx$ 1.22 TPa in the (111) plane [90, 275]. Graphene similarly shows a very high value of E around 1.05 TPa [29, 139, 276], and it is the stiffest 2D nanosheet material known so far.

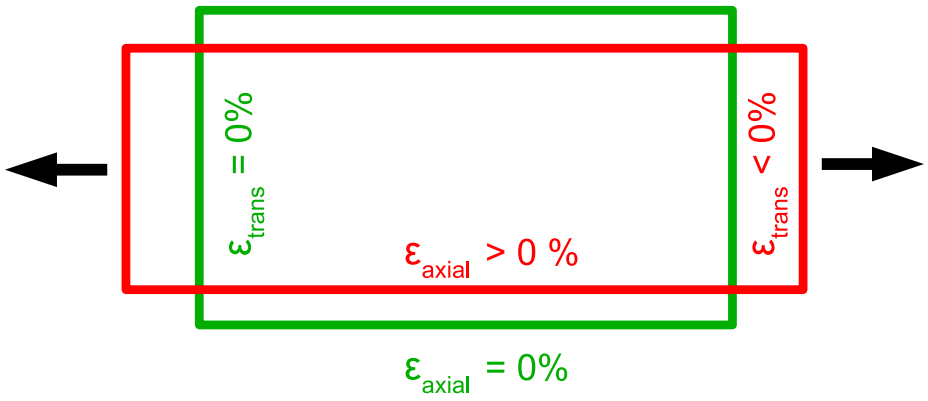

Figure 6.2: Schematic of the axial strain ϵ_{axial} and traversal strain ϵ_{trans} for a isotopic material with Poisson's ratio $\nu = -\epsilon_{trans}/\epsilon_{axial} > 0$, in equilibrum (green) and axial strained (red) indicated by the two arrows.

6.1.2 Poisson's ratio

The Poisson's ratio ν is defined as the negative ratio of transversal strain ϵ_{trans} to axial strain ϵ_{axial} [277]. Assuming a bulk material, when varying the strain along one direction (ϵ_x), there are two Poisson's ratios defined by the strains ϵ_y and ϵ_z in the other two directions orthogonal to x (see Figure 6.2),

$$\nu_{xy} = \nu_{12} = -\frac{\epsilon_{trans}}{\epsilon_{axial}} = -\frac{\epsilon_y}{\epsilon_x} \ , \quad \nu_{xz} = \nu_{13} = -\frac{\epsilon_{trans}}{\epsilon_{axial}} = -\frac{\epsilon_z}{\epsilon_x} \ . \tag{6.9}$$

For all isotropic material, ν must be in the range of -1 to 0.5 [278]. A high value of ν near 0.5 describes weakly compressible materials for example liquids or rubbers. Here, the induced stress in one direction leads primarily to a shape change in the other two directions. Materials like metals, ceramics, polymers or ice show a value around 0.25 - 0.35. Gases have a Poisson ratio of $\nu = 0$; cork behaves very similarly. A negative Poisson's ratio $\nu < 0$ can be measured for re-entrant foams, colloidal crystals or critical fluids [279]. These materials are also called "auxetic". When pulling along an axis, these materials increase in volume. An overview is given in Figure 6.3 where the Poisson's ratio is plotted for different material classes versus B/G, the bulk modulus $B = -V\frac{dP}{dV} = 1/\kappa$ (κ: isothermal compressibility) and the shear modulus $G = \frac{Fl}{A\Delta x}$. The bulk modulus is the resistance of a material

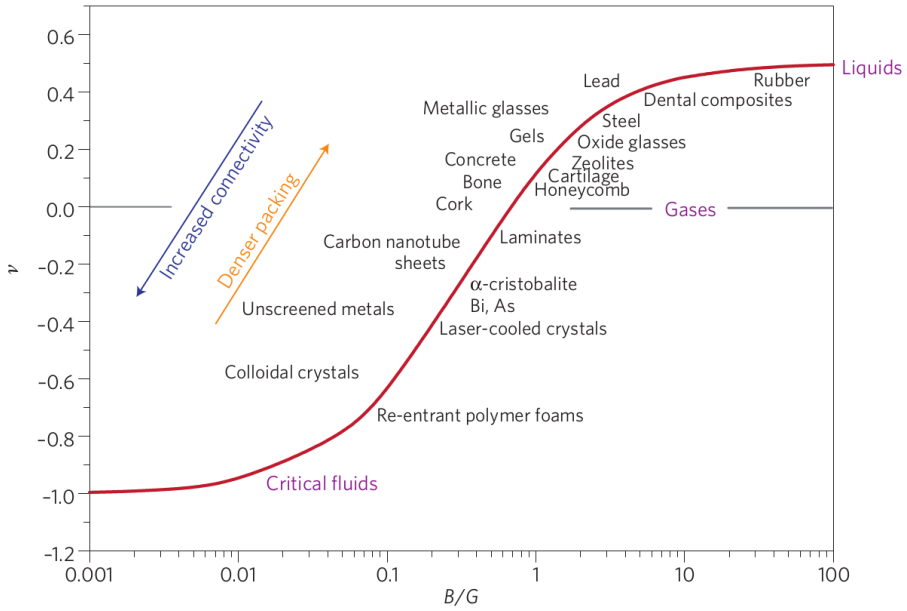

Figure 6.3: Poisson's ratio ν for different isotropic material classes in the range from -1 $\leq \nu \leq$ 0.5, plotted as a function of the ratio of the bulk and shear moduli B/G. (Image from [278])

against uniform pressure, while the shear modulus describes the response to shearing strain. In the non-linear regime, the Poisson's ratio can become lower than -1, considering anisotropic auxetic materials [278].

When calculating the Poisson's ratio of a material, a similar approach as for the Young's modulus can be applied. I have calculated different strained cases, normally using $\epsilon = \pm 0.5, \pm 1.0, \pm 2.0$ % fixed strain along one direction. In the following optimisations, all atoms and the lattice parameters of the non-strained axis are relaxed. I used always orthogonal supercells. By comparing the obtained relaxed lattice parameter orthogonal to the strained axis, the Poisson's ratio can be calculated. To evaluate the out-of-plane Poisson's ratio of graphene, a new volume definition has been applied, introduced in section 6.2.

6.2 Introducing a volume definition based on the average electron density

When making the transition from bulk materials to nanoobjects, this leads to complications, since the object boundaries and hence volume and cross-section have no general and transferable definition. Thus while elastic tensors remain unambiguously defined at these scales, the conversion of both experimental and theoretical strains and forces into mechanical constants such as Young's modulus require a definition of mechanically active volume.

To date, no such generalised and transferable volume definition exists. A common approach for nanoobjects is to use geometric "macroscopic" volume models such as a rectangular slab for flat graphene or an empty cylinder for SWCNTs. However, literature values chosen for the thickness t of the graphene slab or SWCNT cylinder range from t = 0.6 - 3.4 Å [173, 280], leading to wildly different volumes or cross-sections. The result is a wide scatter in reported values of the in-plane Young's modulus for graphene and the axial Young's modulus for SWCNTs, between 0.5 - 5.0 TPa [173, 280].

Currently, the most common approach for graphene is to consider it as a uniform slab with thickness of the interlayer spacing of graphite (3.35 Å). When both theory and experiment adopt this same value, the result is reasonably matching values of the in-plane Young's modulus between theory 0.86 [281] - 1.11 TPa [250] and experiment 1.0 [171] - 1.02 TPa [139]. Simply transferring the graphite inter-layer distance to the cylinder thickness for SWCNTs provokes questions about the influence of curvature on the volume [254, 282], especially for narrow nanotubes.

A common alternative approach is to define volume based on an atomistic approach, creating the resulting volume of a nanoobject by summing each atomic volume. Here, the total volume can be defined based on a sum of spherical overlapping atomic radii, such as the covalent, ionic or Van der Waals radius [283–289]. Today, volumes based on the Van der Waals radius have been established, developed mainly from the chemistry community aiming to calculate the intrinsic volume of molecules, DNA or drug components [290]. Using this atomic "ball" (radii) model

also properties like the solvent accessible surface area (SASA) have been analytically derived [291] (also using the Van der Waals radius). However, by drawing on a library of pre-existing radii, derived from small organic molecules rather than considering the precise system in hand, such definitions suffer from a lack in transferability and of a general conceptual framework. Notably, π-bond systems are very poorly represented via Van der Waals radii as recently pointed out [292].
Thus to date, there exists no really general method to describe mechanically active nanoobject volume, capable of describing different kinds of structures (for example sheets and tubes) without introducing various empirically calculated or experimental parameters, such as atomic radii or bulk inter-layer distances.

My idea is to define a cut-off in the system charge density as a way of defining volume. This is a general concept and transferable. I start with the average electron density ρ of a bulk material. This density can always be defined as $\rho_{bulk} = Q_{total}/V_0$, where Q_{total} gives the total number of electrons in a cell of volume V_0, *e.g.* the conventional unit cell. For any system, the local electron density $n(\vec{r_i})$ $(i = 1..N)$ can be generated in real space at every point i in a fine uniform 3D mesh of N points in a supercell, as implemented in most available DFT codes. The total number of electrons in the supercell (SC) with known volume V_{SC} is fixed, and can be expressed as the sum of the electron density over all points multiplied by the fractional volume associated with every point,

$$Q_{total} = \frac{V_{SC}}{N} \cdot \sum_{i=1}^{N} n(\vec{r_i}) \; . \tag{6.10}$$

This definition is independent of the type of structure or supercell, for example a bulk calculation or a single-layer nanosheet surrounded by vacuum.

In order to define nanoobject volume, an electron density cut-off c is now introduced. Applying c analytically, all grid points $N_{n>c}$ with an electron density $n(\vec{r_i}) > c$ can be found. This leads to the number of electrons $Q(c)$ and volume $V(c)$ within the cut-off, knowing V_{SC} and the number of grid points N,

$$Q(c) = \frac{V_{SC}}{N} \cdot \sum_{i=1}^{N_{n>c}} n(\vec{r_i}) \ , \tag{6.11}$$

$$V(c) = \frac{N_{n>c}}{N} \cdot V_{SC} \ . \tag{6.12}$$

While charge density cut-offs have been proposed previously [250], no suggestion of what cut-off value c to take was clearly made. Thus I propose the following new definition:

The electron density cut-off c can be chosen such that the resultant nanoobject volume encloses the same average electron density as the parent layered bulk material:

$$\boxed{\rho_{bulk} = \left(\frac{Q(c)}{V(c)}\right)_{nanoobject} = \rho(c)_{nanoobject}} \ . \tag{6.13}$$

The new volume definition leads to a new expression for the volume $V(c) = Q(c)/\rho_{bulk}$ where c can be found from the crossing point of the average electron densities for nanosheet or nanotube and parent layered bulk material. This enables a comparison of different volumes of nanoobjects based on a common volume definition, and additionally, for a given cut-off the ratio of enclosed electrons N_Q ($N_Q = Q(c)/Q_{total}$) can be stated for every structure. In Figure 6.4, as example, the cut-off defined by (6.13) is indicated with an arrow for single- (SL), bi- (BL), tri-layer (TL) graphene and the parent bulk graphite.

We can understand this further by examining the variation of $N_Q(c)$ and $V(c)$ (6.12) with electron density cut-off c (c is a local electron density e^-/a_0^3). In Figure 6.5 (a) and (b), single- (SL), bi- (BL), tri-layer (TL) graphene and graphite are shown. In the case of SL graphene, a 48×54×180 point electron density grid in a 7.99×9.23×30.00 a_0^3 orthorhombic cell was used (see also Table 6.3). For the parent bulk graphite, a cut-off of c = 0.0038 e^-/a_0^3 already includes all points in

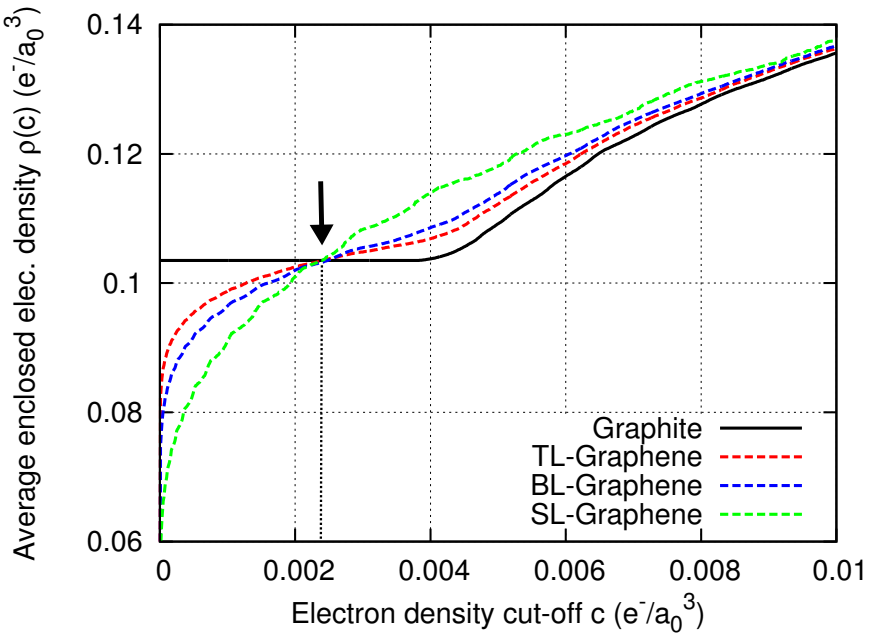

Figure 6.4: Average enclosed electron density $\rho(c) = Q(c)/V(c)$ as a function of the electron density cut-off c for single-layer (SL), bi-layer (BL), tri-layer (TL) graphene and graphite. The arrow indicates the cut-off given by (6.13), exact values of c are listed in Table 6.2. (atomic units: e^-: electron, a_0: Bohr radius)

the cell (see Figure 6.4) and hence for cut-offs less than this there is no change in included volume or electrons. In contrast for graphene, the volume $V(c)$ increases rapidly as the cut-off drops, which can be understood as the surface charge smears out from the graphene into the vacuum around it. Even grid points with $n(\vec{r})$ close to zero can be found. However, this smeared out charge represents only a very small fraction of the total number of electrons (see Figure 6.5 (a)), for example at the minimal graphite cut-off of $c = 0.0038$ e^-/a_0^3, already more than 99 % of the total number of electrons in graphene are included. In the case of graphene, the enclosed volume is relatively insensitive to the precise cut-off value, since the electron density in the region surrounding the volume cut-off drops away rapidly. For example, increasing c from our obtained graphene cut-off value of $c = 0.0024$ e^-/a_0^3 to 0.003 e^-/a_0^3 only decreases the enclosed volume by 4.5% with still $N_Q = 99.52$ %. One still should keep in mind, that this change of volume is influencing directly further calculated properties such as the Young's modulus, and therefore c

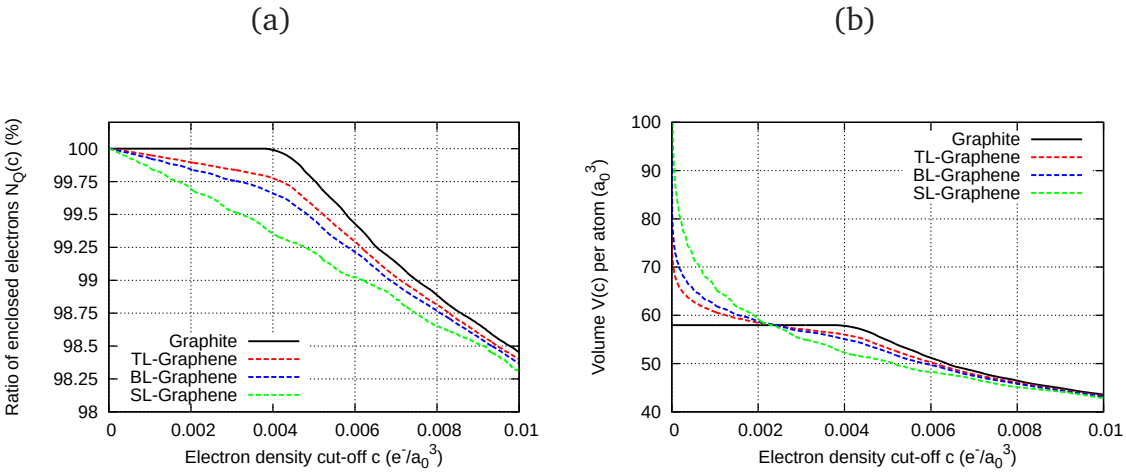

Figure 6.5: (a) Variation of ratio of enclosed electrons N_Q, and (b) volume $V(c)$ divided by the number of atoms in the supercell as a function of electron density cut-off for single-layer (SL), bi-layer (BL), tri-layer (TL) graphene and graphite.

should be calculated individually for every case using (6.13) to minimize the resulting error. Visualized examples of resulting nanosheet volumes of SL graphene and SL MoS_2 are shown in Figure 6.6. Visualising the surface associated with the cut-off defined by (6.13). Clearly, slight undulations of the surfaces are visible, reflecting the lattice structure.

In all systems examined further, these volumes enclose more than 99.35 % of all electrons in the supercell (see Table 6.2 and 6.5). The Young's modulus E can now be expressed using volume $V_0(c)$, which is only dependent on the electron distribution and thus takes directly into account the geometry of the structure,

$$E(c) = \frac{1}{V_0(c)} \left. \frac{\partial^2 U}{\partial \epsilon^2} \right|_{\epsilon=0} . \tag{6.14}$$

This new volume definition provides a robust, transferable and quantitative basis for different kinds of mechanical studies of nanomaterials and equally defect containing nanoobjects [293] or porous materials [294].

(a)

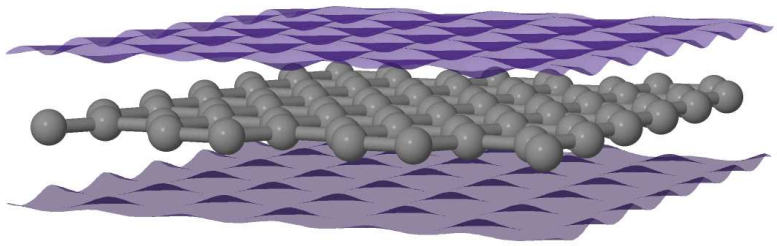

(b)

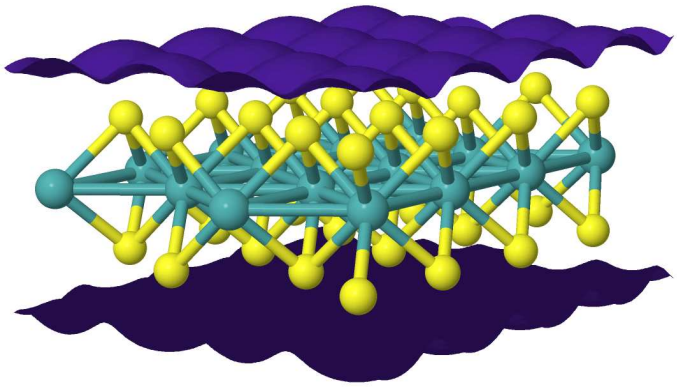

Figure 6.6: Schematic perspective images of nanosheet volumes visualized using the electron density iso-surface associated with the evaluated cut-off c, (a) graphene $c = 0.0024$ e^-/a_0^3 and (b) MoS_2 single-layer nanosheet $c = 0.00293$ e^-/a_0^3. (Atom colors, grey: C, yellow: S, cyan: Mo)

6.3 Young's modulus of graphene and other novel nanosheets

Calculated Young's moduli using the new volume definition (6.14) for single- (SL), bi- (BL), tri- (TL) and 4-layer (4L) graphene are in good agreement with experimental values of about $\approx$ 1 TPa [139] (see Table 6.2). Since these experimental values assume slabs with graphite inter-layer thickness of 3.35 Å, the volumes have been converted additionally into equivalent average slab thicknesses t for comparison. Although I note that the enclosed volumes are in reality not uniform slabs but show surface undulation reflecting the electron distribution in the underlying lattice. The equivalent layer thickness obtained varies with the number of layers, from

3.31 Å for SL-graphene converging towards my LDA-DFT calculated graphite layer spacing of 3.32(3) Å with increasing layer number. This slightly smaller inter-layer distance for graphite results from the chosen pseudo-potentials and the LDA-DFT approach.

Further, the Young's modulus of recently isolated nanosheets (BN, WS_2, MoS_2, $MoSe_2$, $MoTe_2$) [198] was calculated using the new volume definition (Table 6.2). To calculate the nanosheet volumes, every electron density cut-off c has been calculated individually. In general, single-layer average thicknesses are only slightly smaller than the bulk inter-layer distance, due to the absence of extremely weak inter-layer electron delocalization effects [146]. Further good agreement with experiment is obtained for MoS_2 (0.27 $\pm$0.1 TPa [295], 0.33 $\pm$0.07 TPa [274]) and BN (0.6 - 1.5 TPa [296]), the only other two of these novel few-layer nanosheets to be experimentally determined to date, to the best of my knowledge. More details of the calculations can be found in Table 6.3.

It can be stated, that in general, the in-plane Young's moduli for layered nanosheets are close to their parent bulk material: the in-plane force constants are similar, the out-of-plane interactions are weak, and the single-layer volume is close to that of one bulk layer. This observation makes prediction of nanosheet mechanical properties easier when for example the Young's modulus of the parent bulk material is already known.

Since the calculated averaged graphene layer thickness is close to the interlayer spacing of graphite, this suggests that a 3.35 Å thick geometric slab is a reasonable approximation to determine graphene volume. However, there are many situations for which the geometric slab model is no longer applicable: for example defective systems such as vacancy-containing graphene, where the new electron density based volume approach proposed here can still be applied.

Sheets	$E(c)$ (TPa)	c (e^-/a_0^3)	t (Å)	N_Q (%)	$E_{Exp.}$ (TPa)
SL-Graphene	1.059	0.00240	3.31	99.64	
BL-Graphene	1.059	0.00247	3.32	99.81	∼1.05 [139, 171]
TL-Graphene	1.058	0.00237	3.32	99.88	
4L-Graphene	1.055	0.00226	3.32	99.91	
Graphite (bulk)	1.055	-	3.32	100.0	(∗)
SL-BN	0.898	0.00268	3.19	99.60	
BL-BN	0.891	0.00288	3.19	99.78	0.6-1.5 [296]
TL-BN	0.886	0.00277	3.19	99.86	
h-BN (bulk)	0.880	-	3.19	100.0	(∗)
SL-WS_2	0.251	0.00290	6.14	99.89	-
WS_2 (bulk)	0.242	-	6.17	100.0	(∗)
SL-MoS_2	0.222	0.00293	6.12	99.85	0.2-0.4 [274, 295]
MoS_2 (bulk)	0.219	-	6.14	100.0	(∗)
SL-$MoSe_2$	0.188	0.00335	6.35	99.87	-
$MoSe_2$ (bulk)	0.188	-	6.36	100.0	-
SL-$MoTe_2$	0.132	0.00329	6.87	99.87	-
$MoTe_2$ (bulk)	0.132	-	6.91	100.0	-

Table 6.2: Calculated in-plane Young's modulus E for different nanosheets and their parent bulk materials. t indicates the single-layer thickness of a slab with equivalent volume to that defined by the electron density cut-off c. $N_Q = Q(c)/Q_{total}$ gives the ratio of enclosed electrons (charge) compared to the total number of electrons in the supercell. $E_{Exp.}$ gives some measured values of E for nanosheets.
(∗): see Table 6.1. (atomic units: e^-: electron, a_0: Bohr radius)

Sheets	N_{atoms}	c (e^-/a_0^3)	$V_0(c)$ (a_0^3)	a_1 (a_0)	a_2 (a_0)
SL-Graphene	8	0.00240	461.82	7.996	9.232
BL-Graphene	16	0.00247	926.024	7.997	9.234
TL-Graphene	24	0.00237	1390.69	7.997	9.234
4L-Graphene	32	0.00226	1855.15	7.997	9.234
BN	8	0.00268	461.57	8.139	9.397
BL-BN	16	0.00288	921.68	8.143	9.402
TL-BN	24	0.00277	1383.85	8.143	9.407
WS_2	12	0.00290	1426.08	10.316	11.911
MoS_2	12	0.00293	1426.08	10.338	11.938
$MoSe_2$	12	0.00335	1571.81	10.654	12.299
$MoTe_2$	12	0.00329	1962.38	11.451	13.207

Table 6.3: More details to the calculations of the nanosheets. N_{atoms} gives the number of atoms in the used supercell, $V_0(c)$ the volume calculated with the given cutoff c, and a_1, a_2 the relaxed in-plane orthorhombic lattice parameter in equilibrium. In direction a_3 there was always enough distance (> 12 Å) to avoid interactions, always a orthorhombic supercell had been used. (atomic units: e^-: electron, a_0: Bohr radius)

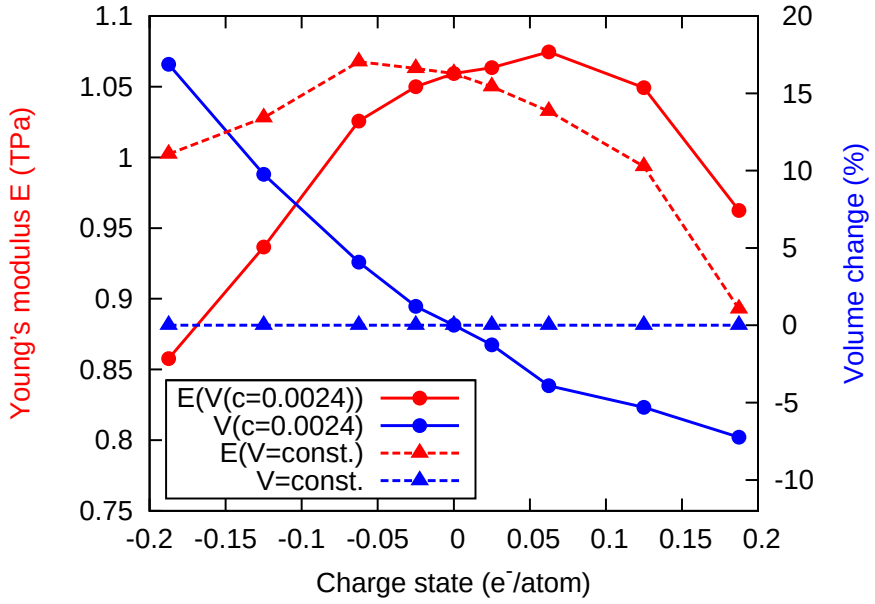

Figure 6.7: Young's modulus E(V(c=0.0024)) and volume V(c=0.0024) for graphene as a function of doping level/charge state, with volume defined using the graphene electron density cut-off of $c = 0.0024$ e$^-$/a$_0^3$. The effective Young's modulus E(V=const.) taking always the fixed volume from the charge neutral case shows the modulus variation due purely to change in bond strength.

6.3.1 Fermi level dependent Young's modulus of graphene

Defining volume via a well-defined cut-off in the system electron density has further conceptual implications. For example, varying the Fermi level can change the Young's modulus by depopulating bonding states or populating anti-bonding states, softening the bond spring constants of the system and hence the $\partial^2 U/\partial\epsilon^2$ term of (6.14). However, since volume is now defined in terms of a cut-off c defined for the system electron density in equilibrium, the enclosed volume will now also be Fermi level dependent. This means that changes in $1/V_0(c)$ in (6.14) can also modify the Young's modulus. The current approach includes both of these effects for the first time in the literature. Figure 6.7 shows the calculated effect of varying the Fermi level on the Young's modulus of graphene. Over moderate doping levels ($\pm$0.0625 e$^-$/atom), a classical fixed volume model would suggest a gradual drop in Young's modulus (dotted red curve with triangles) as the system becomes more

charge state (e^-/atom)	$V(c)$ (a_0^3)	a_1 (a_0)	a_2 (a_0)	N_Q (%)
-0.1875	539.75	8.258	9.535	99.61
-0.1250	506.87	8.143	9.403	99.61
-0.0625	480.66	8.056	9.302	99.62
-0.0250	467.49	8.016	9.255	99.63
0.0	461.82	7.996	9.232	99.64
+0.0250	455.95	7.985	9.219	99.65
+0.0625	443.78	7.979	9.215	99.63
+0.1250	437.30	8.001	9.237	99.66
+0.1875	428.41	8.054	9.297	99.64

Table 6.4: Calculations of charged single-layer graphene. For all volumes $V(c)$ a cut-off $c = 0.0024$ e^-/a_0^3 has been used. $N_Q = Q(c)/Q_{total}$ gives the ratio of enclosed electrons (respectively charge). a_1, a_2 are the relaxed in-plane orthorhombic lattice parameter in equilibrium using a supercell with 8 carbon atoms.

positive (E(V=const.)). However, this modulus trend is actually inverted once the corresponding volume decrease is additionally included (full red curve with circles). Such complex doping-dependence of mechanical properties is not accessible with classical geometrical slab or sphere volume models.

Table 6.4 gives a detailed overview of the results obtained when changing the Fermi level / charge state of a single graphene layer. I note that the enclosed electron ratio N_Q varies very little, demonstrating the use of the constant cut-off $c = 0.0024$ e^-/a_0^3 is reliable.

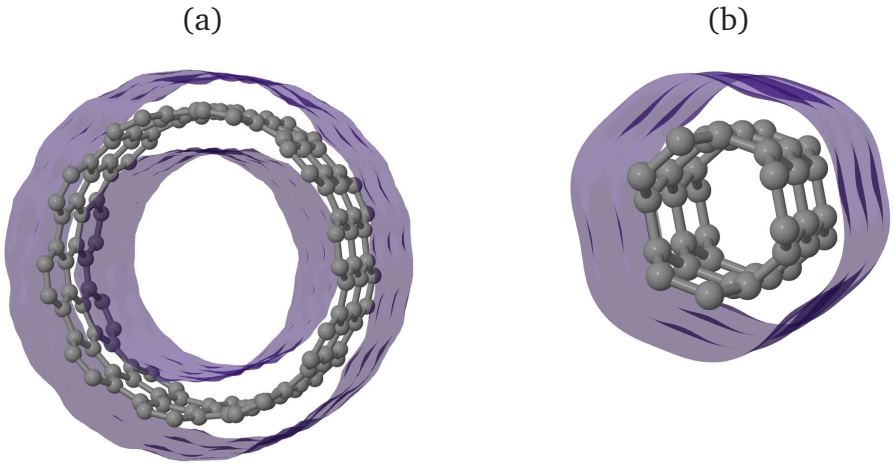

Figure 6.8: Schematic perspective images of volumes visualized using the isosurface of the evaluated cut-off c, (a) segment of (10,10) SWCNT c = 0.00238 e^-/a_0^3 and (b) segment of (3,3) SWCNT c = 0.00255 e^-/a_0^3 (note the lack of interior cavity).

6.4 Young's modulus of carbon nanotubes

As a second example, in order to demonstrate the use of the new volume definition, the Young's moduli (6.14) of different SWCNTs have been calculated. In the literature, different methods have been applied but all have in common an estimated wall thickness. In all previous studies for SWCNTs, an estimated nanotube wall thickness t in the range of 3.07 - 3.4 Å (in principle also the graphite interlayer distance) has been considered to describe the cylinder [116, 117, 254, 282, 298]. Using the new volume definition with equal average electron density ρ to graphite (6.13), I have calculated the axial Young's moduli for a range of armchair, zigzag and chiral SWCNTs all summarized in Table 6.5.

The in-plane Young's moduli converge very well for larger tube diameters, and thus lower curvature, as expected to the value of graphite and graphene. In general, my results are in good agreement with literature, but including additionally the very small diameter SWCNTs (2,2), (3,3), (3,0), (5,0) and (4,1). For detailed comparison with other theoretical studies see Table 6.6. The enclosed electron ratio N_Q similarly converges to the SL graphene value (N_Q = 99.64 %). Therefore, large diameter SWCNTs, with a low curvature of the hexagon carbon network, show an

	SWCNT	$E(c)$ (TPa)	c (e^-/a_0^3)	t (Å)	N_Q (%)
(armchair)	(2,2)	0.642	0.00272	(3.04)	99.45
	(3,3)	1.049	0.00255	(3.21)	99.60
	(4,4)	0.995	0.00246	3.25	99.61
	(5,5)	1.018	0.00243	3.27	99.62
	(8,8)	1.057	0.00240	3.30	99.63
	(10,10)	1.063	0.00238	3.31	99.64
(zigzag)	(3,0)	0.885	0.00295	(3.00)	99.36
	(4,0)	0.969	0.00255	(3.12)	99.53
	(5,0)	0.969	0.00252	(3.20)	99.61
	(6,0)	1.010	0.00247	3.23	99.61
	(9,0)	1.005	0.00240	3.29	99.63
	(12,0)	1.028	0.00240	3.30	99.63
	(17,0)	1.054	0.00236	3.31	99.64
(chiral)	(4,1)	1.001	0.00244	(3.17)	99.60
	(8,2)	1.019	0.00241	3.27	99.63
	(8,4)	1.046	0.00240	3.29	99.63
	(12,6)	1.054	0.00239	3.30	99.63
Graphite	(bulk)	1.055	-	3.32	100.0
Exp. E		$\approx$ 1 TPa [119, 119, 120, 297]			

Table 6.5: Axial Young's modulus E calculated for different SWCNTs. t indicates the hypothetical cylinder thickness (brackets indicate completely filled tubes), centred around the SWCNT atom positions with equivalent volume to that defined by the electron density cut-off c. $N_Q = Q(c)/Q_{total}$ gives the ratio of enclosed electrons and c, the evaluated electron density cut-off.

		This work		Literature
	SWCNT	$E(c)$ (TPa)	d (Å)	E (TPa)
(armchair)	(2,2)	0.642	2.79	-
	(3,3)	1.049	4.17	-
	(4,4)	0.995	5.48	0.960 [282]
	(5,5)	1.018	6.82	1.11 [117]
				0.971 [116]
	(8,8)	1.057	10.83	0.990 [282]
				0.979/1.008 [298]
	(10,10)	1.063	13.46	1.230 [117]
				0.990 [282]
				1.240 [254]
				0.972 [116]
(zigzag)	(3,0)	0.885	2.60	-
	(4,0)	0.969	3.34	0.840 [282]
	(5,0)	0.969	4.04	-
	(6,0)	1.010	4.79	0.960 [282]
	(9,0)	1.005	7.05	1.160 [117]
				0.974/1.017 [298]
	(12,0)	1.028	9.37	-
	(17,0)	1.054	13.20	1.227 [117]
(chiral)	(4,1)	1.001	3.73	-
	(8,2)	1.019	7.21	0.974 [116]
	(8,4)	1.046	8.29	1.176 [117]
	(12,6)	1.054	12.39	1.200 [117]

Table 6.6: Axial Young's modulus calculated in this work compared to theoretical literature values for different SWCNTs. For the potential energy curve the SWCNTs are strained $\pm$0.5, $\pm$1, $\pm$2 % along their axis. Additionally the electron density cut-off c and the tube diameter d (calculated out of 3 carbon atomic positions lying in the same plane perpendicular to the tube axis) are indicated.

equivalent electron density distribution as flat SL graphene. However, the out of the new volume calculated equivalent wall thickness t centred around the carbon atomic positions now varies with the tube diameter (see Table 6.5). In particular for narrow SWCNTs with diameters below around 4.7 Å, the CNTs are completely filled (independent of the chirality). Here the whole concept of a hollow cylinder breaks down. The volumes of a hollow (10,10) and fully filled (3,3) CNT are visualized in Figure 6.8. This finding agrees nicely with the lower diameter limit for the filling of SWCNTs with water [299]. Therefore this approach can help to estimate the penetration of different molecules, fullerenes or (magnetic) clusters into CNTs. It has to be noted, that the exact same *ab initio* approach can be also applied for multi-wall CNTs.

6.5 Poisson's ratio of graphene

The new volume definition also enables access to other mechanical properties such as the out-of-plane Poisson's ratio for surface dominated nanoobjects, since it is possible to calculate the volume and hence an equivalent average thickness change as the sample is strained. The Poisson's ratio is constant for small strains, and I have taken the average for six strained/compressed cases. For the calculations of the out-of-plane Poisson's ratio of graphene, I used the cut-off c = 0.0024 e^-/a_0^3 to calculate the volume for all the different strained/compressed cases (see Table 6.7). The variation in the ratio of enclosed electrons N_Q is negligible, while the volume increases with increasing tension. The stability in the quantity of enclosed electrons demonstrates, similar to changing the Fermi level of graphene, that the cut-off obtained under equilibrium conditions seems to be transferable. Using the same amount of enclosed electrons seems logical, as for bulk material also the average electron density value also remains constant.

For graphene, the in-plane Poisson's ratio has been found to be ν_{12} = 0.20 and for the first time I also calculated the out-of-plane value to be ν_{13} = 0.015. My calculated Poisson's ratios for bulk graphite are ν_{12} = 0.21 and ν_{13} = 0.00. These values and ν_{12} for graphene are in good agreement with literature values [173]. Further, it can be stated that the behaviour of graphene regarding the Young's modulus and the Poisson's ratio are nearly identical to their parent bulk material.

This results rise the question if we can generalise this volume definition to other nanoobjects?
It can be noted that for carbon based "all surface" systems such as single-layer graphene or SWCNTs, an electron density cut-off around 0.0024 e^-/a_0^3 delivers an accurate mechanical volume description with a very stable and very high ratio of enclosed electrons of more than 99.5 %. In the next section 6.6, I apply the same cut-off value of c = 0.0024 e^-/a_0^3 to polymers and H-terminated armchair GNRs. As for these systems no direct parent layer material exists, the c value from graphene

strain ϵ (%)	$V(c)$ (a_0^3)	a (a_0)	b (a_0)	t (Å)	N_Q (%)
-2.0	454.53	7.836	9.269	3.31	99.65
-1.0	458.07	7.916	9.249	3.31	99.64
-0.5	459.96	7.956	9.241	3.31	99.64
0.0	461.86	7.996	9.231	3.31	99.64
+0.5	463.68	8.036	9.225	3.31	99.64
+1.0	465.53	8.076	9.216	3.31	99.64
+2.0	469.23	8.156	9.201	3.31	99.63

Table 6.7: Poisson's ratio calculations of single-layer graphene. For all volumes $V(c)$ a cut-off c = 0.0024 e^-/a_0^3 has been used. $N_Q = Q(c)/Q_{total}$ gives the ratio of enclosed electrons, t the average equivalent slab thickness. a, b are the relaxed in-plane orthorhombic lattice parameter in equilibrium using a supercell with 8 carbon atoms.

is taken for a range of organic polymers and narrow AGNRs. In general, in the case of the AGNRs the middle parts of the ribbons should be well described, similar to SL graphene, while the hydrogenated edges could be described less exactly.

6.6 Young's modulus of AGNRs and related organic polymers chains

Applying the new volume definition based on the electron density to narrow AGNRs can give first insight into the effect of edges, especially for the common modelled singly hydrogenated graphene edges. In the literature there have been so far two different approaches to define the ribbon volume [140, 249]. In both cases, the thickness was considered as the graphite inter-layer distance of 3.35 Å. The difference occur in the width definition of the narrow armchair ribbons. One definition is based on the H-H distance from the opposed edges d_{H-H} using the exact atomic positions [140] (see also chapter 4, section 5.1.4), and the second one uses the opposed edge C-C distance d_{C-C} plus adding twice $r_{VdW,C}$ = 1.78 Å , the carbon Van der Waals radius in graphite [249]. To compare the influence of the chosen approaches, including using my new volume definition, the Young's modulus of AGNRs in the width range of 2 - 20 has been calculated based on the three volume definitions shown in Figure 6.9. In all cases, the infinite ribbons have been strained and compressed axially by $\pm$0.5, $\pm$1, $\pm$2 %. Remembering the expression of the Young's modulus $E = \frac{2b}{V_0}$ (6.8), the difference in E in Figure 6.9 is purely due to the differences in volume V_0, as the parameter b is the same in each approach. Table 6.8 gives the fitting parameter a, b and c for the fitting functions of type $E(x) = \frac{a}{x} + \frac{b}{x^2} + c$ plotted in Figure 6.9. All functions converge close to the Young's modulus of infinite SL graphene of E = 1.059 TPa for large AGNRs. For smaller widths, AGNRs transform into well known polymer chains, such as poly(p-phenylene) for width 3 (PPP, $[C_6H_4]_n$) and cis-polyacetylene for width 2 (PA-cis, $[C_2H_2]_n$), also marked in Figure 6.9. It can be stated that all three approches converge for smaller width to smaller Young's moduli, but with differences up to 25 %. While the H-H distance approach (blue) tends to overestimate the Young's modulus for smaller widths, the approach chosen by Zeinalipour-Yazdi and Christofides [249] (black curve) gives in general smaller values, maximal at width 3 with nearly 28 % difference. Applying the new volume approach (red), based on the cut-off c = 0.0024 e^-/a_0^3, the Young's modulus values are surprisingly good, ranging between the two other volume def-

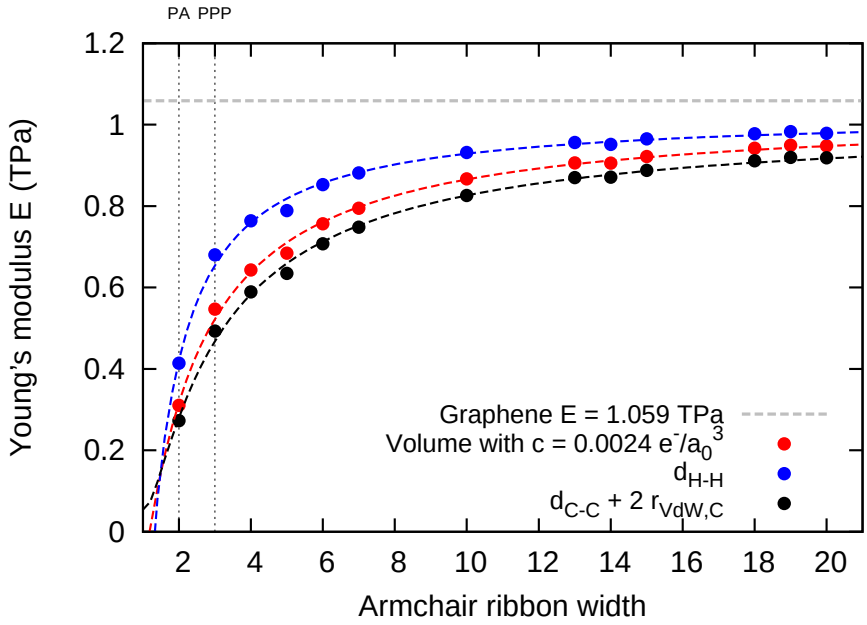

Figure 6.9: Young's moduli of narrow H-terminated armchair GNRs and polymer chains (PPP, PA), applying three different volume definitions. In red the new volume definition with cut-off $c = 0.0024$ e^-/a_0^3 has been used. In blue the exact width of the AGNRs has been defined via the edge hydrogen atomic position [140], in black using the edge carbon atoms plus on each edge $r_{VdW,C} = 1.78$ Å [249]. In both cases (blue/black) a thickness of 3.35 Å has been considered.

initions. It seems that the edges are quite well represented using the new volume definition compared to purely geometrical approaches, even while the atom species are changed to hydrogen. Regarding the simplicity of the new approach and the potential to implement this in other DFT codes, shows the potential of this volume definition based purely on the electron density.

It can be further expected that zigzag GNRs behave similarly as a study by Faccio *et al.* [300] shows. This article also discusses nicely the problem of the width definition for ZGNRs, even stating two different widths (per width based on zigzag dimer rows, see Figure 3.18). Our new approach using an electron density cut-off can also be applied in this case, enabling as well a better comparison between armchair, zigzag and chiral GNRs volumes and therefore mechanical properties.

Figure	Graph	a	b	c	standard deviation
6.9 / 6.10	red	-1.729	0.599	1.032	0.012
6.9	blue	-0.933	-0.557	1.028	0.013
6.9	black	-1.972	1.013	1.013	0.012

Table 6.8: Fit parameters of function $E(x) = \frac{a}{x} + \frac{b}{x^2} + c$ when fitting to the curves of Young's modulus vs ribbon width Figure 6.9 and 6.10. Fit parameter c gives the Young's modulus in TPa for a infinite width ribbon, *i.e.* graphene.

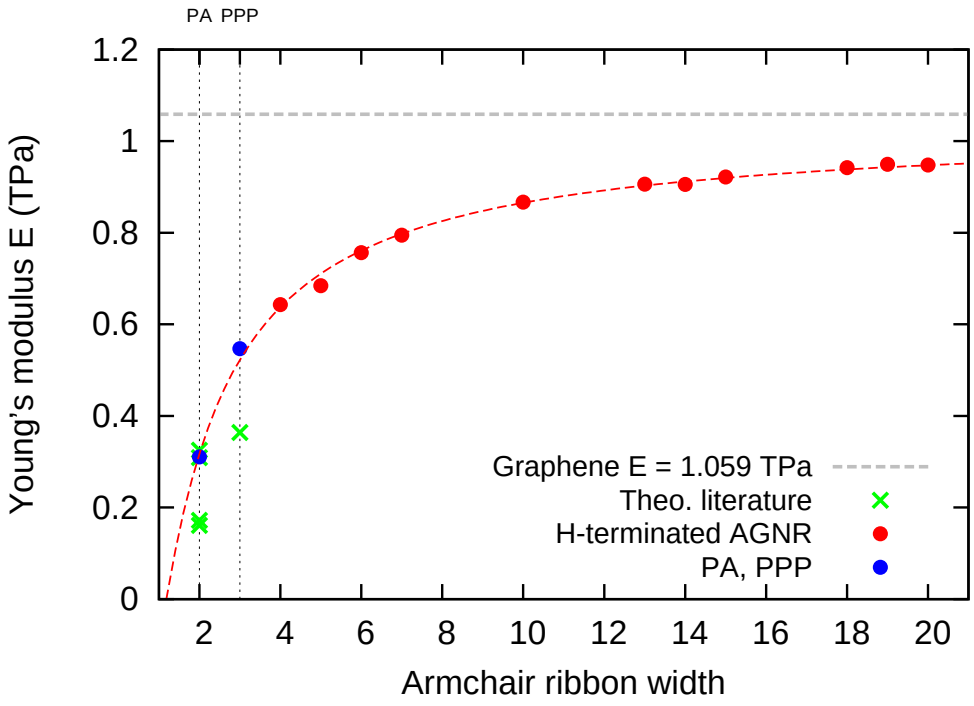

Figure 6.10: Calculated Young's modulus of organic polymers (PA-cis, PPP) and AGNRs, using the electron density cut-off $c = 0.0024$ e^-/a_0^3, compared to theoretical literature values of PA and PPP in green (see also Table 6.9).

		This work		Literature	
Polymers	unit	E (TPa)	A (Å^2)	E (TPa)	A (Å^2)
PA - cis	$[C_2H_2]_n$	0.311	13.83	0.309/0.325 [301]	15.52 [302]
				0.161/0.172 [303]	15.52 [302]
PA - trans	$[C_2H_2]_n$	0.657	12.55	0.591/0.373 [301]	15.52 [302]
				0.389 [303]	15.52 [302]
PE - trans	$[C_2H_4]_n$	0.392	14.99	0.369/0.286 [301]	18.24 [304]
				0.353 [305]	18.24 [304]
PPP	$[C_6H_4]_n$	0.547	17.90	0.364 [306]	21.47 [307]
PPV	$[C_8H_6]_n$	0.455	16.41	0.325 [306]	20.47 [307]

Table 6.9: Calculated Young's moduli of common organic polymer chains compared with theoretical literature values. A is the equivalent cross section estimated for the polymers, dividing the volume by the length along the polymer chains. To calculate the volume the cut-off $c = 0.0024$ e$^-$/a$_0^3$ has been used for all structures.

While, for graphene, the slab thickness plays the crucial role, calculating the Young's moduli for polymers like PA and PPP the edges are getting extremely dominant. To support the flexible use of this new approach using a volume based on the average electron density, I calculated the Young's moduli for a series well known organic polymer chains, such as cis- and trans-polyacetylene (PA), polyethylene (PE), poly(p-phenylene) (PPP) and polyphenylene vinylene (PPV). All this polymers consist of a carbon backbone with hydrogen terminating the remaining dangling bonds. In all cases, the SL graphene cut-off $c = 0.0024$ e$^-$/a$_0^3$ has been used to calculate the volume V_0.

The results are shown in Table 6.9. Additionally to previous Figure 6.9, calculated literature values for PA and PPP are added in Figure 6.10 in green, and some examples of the used volume are visualized in Figure 6.11. The literature values for PPP and PPV from Capaz and Caldas [306] are much lower compared to my value. To calculate E, they use a similar LDA-DFT approach as used by me. One difference is that they used experimental determined cross section A values from

crystalline material [307] to calculate the volume, similar to all other theoretical work so far. As these cross sections are larger than my calculated equivalent cross sections, my higher Young's modulus values are logical. For PA (-cis and -trans) my values are more or less in good agreement with values from Hong and Kertesz [301] using both a direct quantum-chemical method and an analytical method, combined again with cross sections A, estimated based on x-ray-diffraction experiments [302, 304]. The literature values are largely scattered even when considering the same cross section size, as results reported by Tuyarot *et al.* [303] for PA indicate, giving a value nearly half as big applying tight-binding methods. The Young's modulus value for PE-trans is in reasonable good agreement with literature, while the applied cross sections are significantly different. Given the difficulty in precise experimental determination of the cross section notably for one isolated polymer chain, combined with different theoretical level approaches (Tight-Binding, DFT, analytical approaches) the calculated literature values so far show a large scatter. In addition, experimental values extracted from x-ray-diffraction measurements presented by Matsuo and Sawatari [308] for crystalline PE E = 0.213 - 0.229 TPa, also require a definition of cross-section and are influence by additional experimental errors.

In summary, I showed the behaviour of graphene-related polymer chains, PA and PPP, for the first time directly compared with the narrow AGNRs values (see Figure 6.10 (red)), showing values all based on the same transferable and pure *ab initio* volume definition. These new Young's modulus values are reasonable and allow as well a better comparison to other organic polymers like PE or PPV. Regarding Table 6.9 it seems that the new volume tends to give a smaller average cross sectional area than optical experiments on bulk crystalline polymer samples. The Young's moduli of polymer chains are therefore difficult to compare to former theoretical literature. On the other hand, all methods applied to date to calculate these values are rather influenced by empirical or experimental values, and only my approach is purely *ab initio*. Additionally, until now, only for PPP and PPV DFT calculations have been used [306].

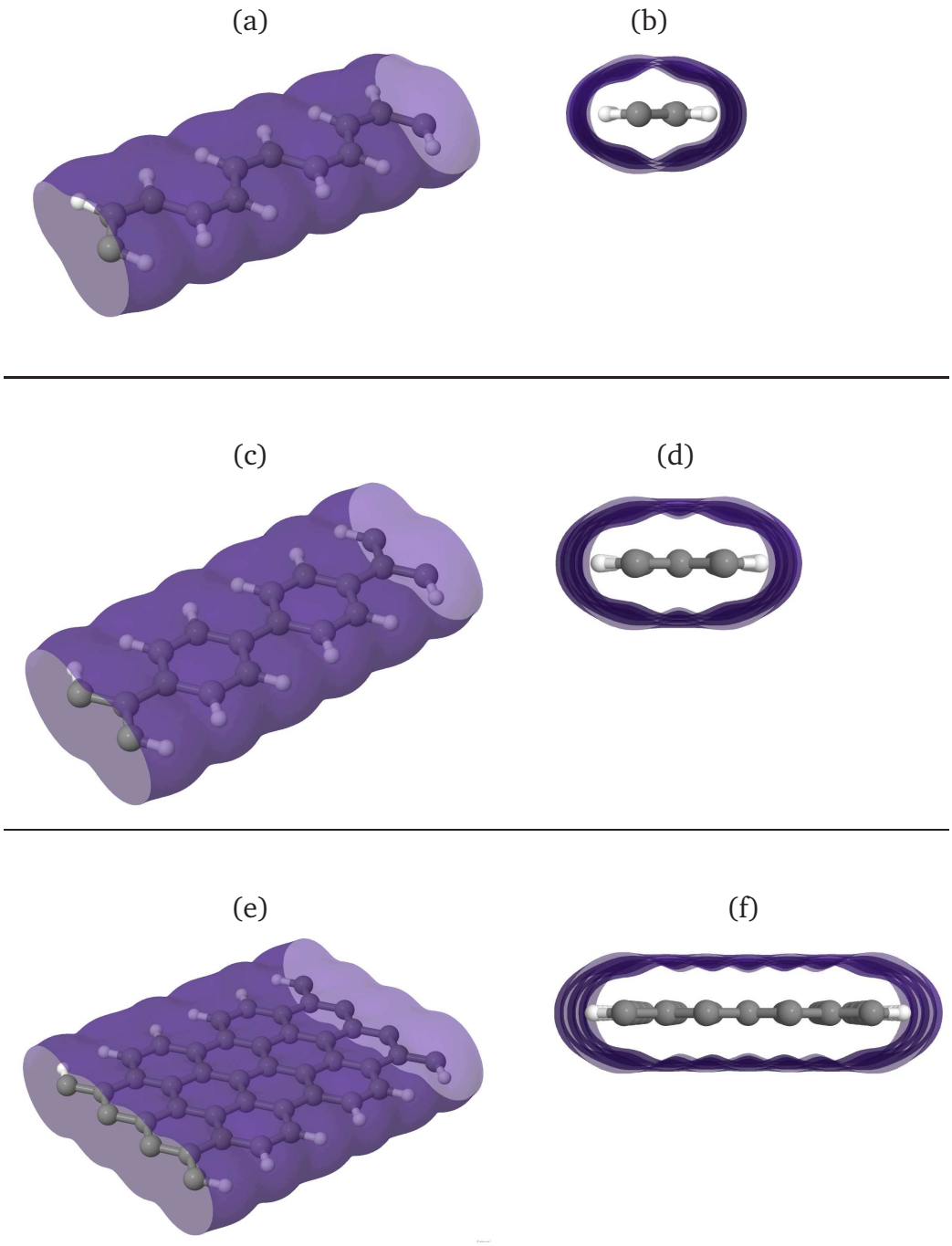

Figure 6.11: Visualization of enclosed volumes showing the $c = 0.0024$ e^-/a_0^3 isosurfaces. (a) Perspective and (b) front view of a cis-PA polymer, (c) perspective and (d) front view of a PPP polymer and (e) perspective and (f) front view of a width 7 AGNR.

All theoretically calculated values have to be verified in experiments using, if possible, single isolated polymer chains. To the best of my knowledge, to date only crystalline polymer sample have been measured to determine the Young's modulus. This has to be interpreted critically, as polymer-polymer interactions take place and additional disordering or defects can occur in the crystalline sample, even when prepared carefully. It further makes sense that the cross section of one isolated polymer chain should be smaller than an estimated value taken from an ordered crystalline system. This is due to the presence of (long range) charge delocalisation effects and interstitial spaces in crystalline systems. It is surprising to me that not more experimental Young's modulus measurements of isolated polymer chains have been performed. As most of the studies have been done already many years ago, I could imagine with modern atomically precise SPM setups this gap could be closed, applying also the new given cross sections for isolated polymer chains based on the new volume definition.

6.7 Computational details

Pseudopotentials are included via the Hartwigsen-Goedecker-Hutter scheme [73]. The basis consists of Gaussian function sets multiplied by polynomial functions including all angular momenta up to maxima p (l=0,1) and d (l=0,1,2) [77]. For carbon a ($pdddp$) basis set was used, resulting in 38 independent functions. The following other basis sets where used: H: (ppp), B: ($pdpp$), N: ($pdpp$), Mo: ($dddd$), W: ($ddddd$), S: ($ppppp$), Se: ($ddpp$) and Te: ($pdppp$). A non-zero electron temperature of kT = 0.04 eV was used, to create electronic level occupation. I confirmed, that all structures were energetically converged. The charge density was fitted to plane waves within an energy cut-off of 175 Ha. All k-point grids were tested to give fully converged energies. The energy tolerance for the DFT calculations were set to $1 \cdot 10^{-7}$ Ha, and for the atomic positions to $1 \cdot 10^{-5}$ Bohr. Additionally an energy tolerance value per SCC of $1 \cdot 10^{-8}$ Ha was used.

Chapter 7

Conclusions and outlook

Many important structural, electronic and chemical properties of pristine infinite flat graphene have already been modelled and described theoretically since the late 1940s, starting with studying one "isolated" layer of the graphite bulk system. After the first well publicised realization of graphene in 2004, this new two-dimensional (2D) material rapidly inspired a large worldwide research community. Shortly thereafter, graphene nanostructures such as nanoribbons (1D) or "flake-like" quantum dots (0D) became hot topics. The smaller and more delimited 2D graphene nanostructures become, the more the edge to surface ratio increases and thus edges and quantum confinement effects are gaining importance. Through changing the graphene edge termination the properties of the graphene nanoobjects can be changed radically. This offers new possibilities to design and manipulate the nanoobject properties, for example the bandgap. Hence, a detailed understanding of the effect of edge structure on graphene properties is very timely. Additionally, new experimental routes to produce graphene nanostructures via "bottom-up" synthetic chemistry have been developed. These techniques also open the door to an atomically precise design of graphene nanoribbons.

The field of graphene research has boomed massively over recent years. This work has therefore focussed on structural, electronic and chemical properties of unterminated and hydrogenated graphene edges, and also complex edge functionalized graphene nanoribbons. Furthermore, mechanical properties of graphene and

related low-dimensional systems (carbon nanotubes, organic polymers, other 2D nanosheets) have been studied, notably the Young's modulus. LDA-DFT techniques as implemented in the *AIMPRO* code were used in the framework of this thesis to model all relevant structures.

To give as compact as possible an overview on the work performed in this thesis, in the following the main conclusions are summarized for the three main thematic priorities studied:

- **Unterminated, tubed and hydrogenated graphene edges**
  Different terminated graphene armchair, zigzag and Klein edges were investigated. To model individual and uncoupled graphene edges wide graphene nanoribbons (around 50 Å width) were used as model system. In addition to the three "standard" edge types, other thermodynamically favourable edge reconstructions, *e.g.* the (5-7) reconstructed zigzag or reconstructed Klein edge, were included in this study. Notably in this work for the first time the Klein and reconstructed Klein edges were rigorously included.

  For unterminated graphene edges, the pristine armchair and the (5-7) reconstructed zigzag edge are found most stable, in good agreement with the literature.
  Unique for 2D materials, a completely new and thermodynamically stable folded back "tubed" edge configuration has been identified, additional to the flat unterminated edge types. In this case, an unreconstructed graphene edge folds back on the graphene plane, bonding the original "free" edge onto the graphene sheet and forming a line of sp^3 bonded atoms. As a consequence, a droplet-like shaped carbon nanotube is formed along the graphene edge. The edge stability is dependent on the tube diameter, and for larger tubes (diameter $\geq$ 11 Å) this edge structure is more stable than all known unterminated flat edge configurations. Studying the electronic properties superposed graphene and nanotube elements were found.

When passivating the graphene edges with hydrogen atoms, the main stable known configurations for armchair and zigzag were calculated, with similar results as reported in earlier studies. An additional new high hydrogen density armchair configuration has been found, arranging the edge groups out-of-plane forming a periodic edge ripple. Surprisingly, new stable hydrogenated edge configurations based on Klein and reconstructed Klein edges could be identified. Unlike hydrogenated zigzag based edges, the hydrogenated Klein based edges have formation energies comparable with hydrogenated armchair edges. In these new cases, a similar behaviour analysing the backbone zigzag line compared to the classic hydrogenated zigzag edges was found. Thus the electronic structures were similar for the most stable hydrogenated zigzag, Klein and reconstructed Klein edge configurations. While for simple hydrogenated zigzag graphene nanoribbons in the literature, possible magnetic edge states have often been discussed, all hydrogenated most stable edge configurations avoid any magnetic states around the Fermi level. These most stable hydrogenated edge configurations show non-magnetic behaviour using spin-polarized LDA-DFT calculations, irrespective of the edge type.

To summarize, for hydrogenated graphene edges the following important general trends have been identified:

- Edge carbon atoms prefer a sp^3-like coordination for pure armchair and Klein edges, forming single bonds with the backbone graphene sheet.
- Hydrogenated edges along the $<2\bar{1}\bar{1}0>$ direction (zigzag and Klein) are most stable with periodic sections containing one sp^3 and two sp^2 coordinated carbon atoms along the last complete zigzag backbone line for both zigzag and (reconstructed) Klein edges.
- Higher hydrogen densities are found most stable for all edge types, forming out-of-plane ripples along the edge.
- Edge-strain induced by high hydrogen densities can be relieved through out-of-plane edge deformations (periodic edge rippling).

- All most stable hydrogenated graphene edge configurations are showing non-magnetic behaviour, thus no fluctuating states at the Fermi level can be found.
- Thin graphene nanoribbons show a bandgap, although for zigzag and reconstr. Klein nanoribbons the gap is much smaller than for armchair nanoribbons.
- During experimental synthesis the hydrogenated edge stability will be strongly dependent on the growth conditions (*e.g.* partial hydrogen pressure, temperature, interactions of the substrate surface with the graphene), and several different hydrogenated edge types are likely to occur.

Derived from this new knowledge about hydrogenated graphene edges, possible new growth models for graphene have been proposed. All models are based on hydrogenated carbon dimers (*e.g.* ethylene groups) attaching to the graphene edges. These models generalize armchair and zigzag edge growth, as in both cases carbon dimer groups are the fundamental building blocks. Furthermore, it has been shown that the edge stabilities of similar edge types can be very close, dependent on experimental growth conditions (temperature, pressure etc.), modelled in this work through shifting the hydrogen chemical potential. This supports the growth model for zigzag edges via intermediate hydrogenated edge configurations and bond rotations.
Additionally, when growing graphene on substrates, surface effects have to be taken into account. Recently, for ethylene-based CVD graphene growth on copper in the literature effects such as surface-catalyzed dehydrogenation of ethylene and graphene lattice construction were proposed as possible activation barriers, in good agreement with this new growth models.

- **Edge-functionalized graphene nanoribbons**
  This fundamental study of edge-functionalized graphene nanoribbons (GNRs) provides a first picture of the underlying physics for adding complex functional groups to graphene edges and in particular armchair edges. In this work, besides simple H-termination, the edge functional groups -F, -Cl, -Br,

and -SH and in particular -OH (hydroxyl) groups were studied, attached to thin GNRs ($<$ 25 Å width).

In general, larger edge functional groups do not induce large strain in GNRs, since the strain is compensated by static ripple formation along the ribbon edge. One can imagine various ways to match a 1D line tension along a ribbon edge against a 2D surface strain in the basal plane. In the case of graphene, with a calculated in-plane Young's Modulus of $\approx$ 1.06 TPa, the in-plane resistance to tension is high and edge distortion is the energetically favoured solution, resulting in static ripple formation at the edge. At the same time, there is an energetic cost associated with ripple induced disruption of the graphene π-network. Hence the ripples remain localised near to the ribbon edge, thus reducing the effective flat basal plane width of the ribbon. Such characteristic ripples form in the majority of ribbon (edge) chiralities and functional groups examined in this thesis. This suggests that flat (ribbon) edges, as observed for simple hydrogenation, may in reality be the exception. It should be noted that this static edge rippling behaviour is a fundamental response of a 2D layered system to 1D edge strain, and as such is also likely to be of importance in the range of new monolayer materials under development such as BN, MoS_2, $MoSe_2$, $MoTe_2$ or WS_2. Furthermore, strain compensation through rippling is likely to be important at other graphene interfaces such as grain boundaries.

These findings rule out edge functional groups as a simple way of inducing large strains in the graphene basal plane. For the first time, I calculated the Young's Modulus for thin armchair GNRs with -H and -OH terminations, and showed that edge ripples can drastically reduce the Young's modulus up to 40 %. I believe this change in mechanical properties depending on edge functionalization could have a direct impact on engineering devices and composites with embedded thin GNRs or related 2D nanostructures.

Additionally, static edge rippling changes locally the chemical reactivity of the ribbon. The ripple periodicity is superimposed on that of the underlying lattice, suggesting another route to superlattices, as shown by the example

of site selective metal atom adsorption near the rippled graphene edge. Regarding electronic properties of armchair GNRs, I found that the bandgap is surprisingly insensitive to static edge rippling, but can change by up to 50 % depending on choice of edge functional group and ribbon width.

- **Mechanical properties of graphene and related nanomaterials**
  Young's modulus was studied for various nanoobjects, including nanostructures such as 2D nanosheets (graphene, BN, MoS_2 ...), carbon nanotubes and conjugated organic polymers.
  To calculate the Young's modulus the volume or cross-section of the object is needed. So far in all studies, the volume of nanoobjects have been based on simple geometric approximations or atomic sphere models, such as the Van der Waals radius. This has led to widely scattered Young's modulus values, and comparison between different nanostructures is difficult. I identified the lack of a transferable, geometry independent and user-friendly volume definition in the literature, in particular needed for low-dimensional nanoobjects with high surface to volume ratios. Therefore, as a first step towards this, a new volume concept adapted for nanoobjects based on the average electron density was developed. The core concept is to keep the average electron density (and therefore the average charge density) for related structures constant (similar composition and bonding configuration), such as for example graphite $\rightarrow$ graphene $\rightarrow$ carbon nanotubes or h-BN bulk $\rightarrow$ BN nanosheets $\rightarrow$ BN nanotubes. For the parent layered bulk-systems (e.g. graphite, h-BN ...), the average electron density is clearly defined by the unit cell, and this value can be used to derive the associated volume for the individual nanosheets or nanotubes.
  This new volume concept for nanoobjects has then been applied successfully to calculate different mechanical properties. I calculated the Young's modulus for graphene, single-wall carbon nanotubes and other recently isolated single-layer nanosheets. For graphene and BN additional nanosheets up to 4 layers were calculated.
  The new volume concept further enables the direct comparison of the Young's

modulus values for different shaped nanoobjects, for example between carbon nanotubes and graphene, and correctly extrapolates to the parent bulk systems (*e.g.* graphite). It should be noted, that all calculated values for infinite nanosheets and nanotubes show good agreement with the parent bulk in-plane Young's modulus. This can be really stated for the first time, as the calculations are based on the same transferable underlying method.

Further, the graphene in-plane Poisson's ratio was calculated, and for the first time a out-of-plane Poisson's ratio has been given, enabled by the new volume concept. Also in the case of the Poisson's ratio, the values are similar compared to the parent bulk graphite.

This new approach using a electron density defined volume allows further to study systems whose volume varies, for example by shifting the Fermi level, as demonstrated the first time for graphene.

Outlook

The results of this thesis will hopefully stimulate both experimental and theoretical future work on graphene and related materials. This work marks a transition from a time where variation in edge structure added complexity, was seen as a problem and was poorly characterised, to the situation now, where edge functionalization is understood and controlled, and thus gives a powerful new tool to define graphene behaviour.

I believe, that in the coming years new experiments will characterise graphene edges in more detail, including hydrogenated and functionalized edges. Notably, non-destructive studies of graphene edges, using for example Raman spectroscopy, could help in the future to confirm and identify the stable edge configurations and terminations found here. This thesis can therefore serve as a guide for these studies on edges. Built on my results, the edge vibrational modes can also now be theoretically calculated.

Additionally the growth of atomically precise nanoribbons is rapidly developing and the controlled attachment of complex functional groups to the ribbon edges

will soon become realistic. My work proposes different edge functional groups and shows their influence, and thus experiments can be designed based on this new important information and understanding. It will be very interesting to characterise the new created nanoribbons and compare their properties with results from this work.
Additionally I believe complex edge functionalized zigzag and reconstructed Klein edges will become important, and should be equally studied in detail in the future, as possible out-of-plane rippling and changes in electronic, chemical and magnetic properties can be expected.

Experimentally, graphene nanostructures are commonly grown and characterised while lying directly on (primarily metal) surfaces. Here, my theoretical work on free-standing edges can be extended taking additional interactions with a surface into account. An important step will also be to compare in more detail the proposed ethylene-based graphene growth models with experiment. Such types of calculations, including a realistic substrate environment, require normally very large systems with several hundred atoms, and thus are costly using standard DFT approaches.
In the framework of this thesis, preliminary calculations of simple hydrogenated and -OH terminated width 7 armchair GNRs on a Cu(111) surface have already been performed. -OH terminated rippled edges seem to be stable on surfaces as preliminary calculations indicate. Interesting behaviour such as an increased graphene to substrate distance has been found. Additionally, the edge rippling leads to alternating surface bound and unbound edge groups. Another interesting impression is that the orientation of the thin GNRs could be strongly influenced by the functionalized rippled edges, and thus the graphene lattice orientation can be decoupled from the substrate lattice orientation. I believe it could be very interesting to study the alignment of edge-dominated graphene nanostructures with functionalized edges on surfaces or steps, as the orientation could be strongly influenced by the choice of the edge termination. This suggests that it may be possible to use edge functionalization to determine graphene/substrate orientation, rather than

the graphene/substrate lattice matching. Notably, the arrangement and connectivity between graphene nanostructures could be handled in the future with well designed functionalized graphene edges.

For future theoretical work, larger system sizes will become more easily accessible due to the recent development of a new filtration method for DFT calculations. This important extension is already implemented in the *AIMPRO* code, and will be fully usable after a present intensive testing phase. This offers also great new opportunities to model other topological distortions (*e.g.* twisting) and possibly even complete small graphene transistor systems, with the accuracy of DFT.

Also new composite materials will be influenced by the graphene research and I think my work on mechanical properties can perhaps support and guide these efforts. The route to a universal transferable definition of nanoobject volume has been demonstrated and seems promising. Furthermore, the convergence and overlap from graphene with polymer science is rich and offers new challenges, while here both physics and chemistry become interwoven into nanoscience.

Regarding proposed new integrated circuits based on graphene nanoribbons and new advanced graphene composite materials, I am strongly convinced that the control and design of edge and surface functionalization will play a key role. If the efforts in graphene research and engineering continue at the same rate as in recent years, much can be expected from this fantastic material in the 21st century.

Bibliography

[1] J. S. Kilby, “Turning Potential into Reality: The Invention of the Integrated Circuit”, Nobel Lecture (2000).

[2] P. O. Hahn, “The 300 mm silicon wafer — a cost and technology challenge”, Microelectronic Engineering, **56**, 3 (2001).

[3] M. Watanabe and S. Kramer, “450 mm Silicon: An Opportunity and Wafer Scaling”, ECS - Interface, **15**, 28 (2006).

[4] H. Iwai and S. Ohmi, “Silicon integrated circuit technology from past to future”, Microelectronics Reliability, **42**, 465 (2002).

[5] K. Jeong and A. Kahng, “A power-constrained MPU roadmap for the International Technology Roadmap for Semiconductors (ITRS)”, SoC Design Conference (ISOCC) 2009, 49 (2009).

[6] H. Iwai, “Roadmap for 22 nm and beyond”, Microelectron. Eng., **86**, 1520 (2009).

[7] R. Van Noorden, “Chemistry: The trials of new carbon”, Nature News, **469**, 14 (2011).

[8] K. S. Novoselov, V. I. Fal’ko, L. Colombo, P. R. Gellert, M. G. Schwab, and K. Kim, “A roadmap for graphene”, Nature, **490**, 192 (2012).

[9] M. S. P. Shaffer and A. H. Windle, “Fabrication and Characterization of Carbon Nanotube/Poly(vinyl alcohol) Composites”, Adv. Mater., **11**, 937 (1999).

[10] O. Breuer and U. Sundararaj, "Big returns from small fibers: A review of polymer/carbon nanotube composites", Polym. Compos., **25**, 630 (2004).

[11] S. Stankovich, D. A. Dikin, G. H. B. Dommett, K. M. Kohlhaas, E. J. Zimney, E. A. Stach, R. D. Piner, S. T. Nguyen, and R. S. Ruoff, "Graphene-based composite materials", Nature, **442**, 282 (2006).

[12] R. J. Young, I. A. Kinloch, L. Gong, and K. S. Novoselov, "The mechanics of graphene nanocomposites: A review", Composites Sci. Tech., **72**, 1459 (2012).

[13] S. Iijima, "Helical microtubules of graphitic carbon", Nature, **354**, 56 (1991).

[14] K. Novoselov, A. Geim, S. Morozov, D. Jiang, Y. Zhang, S. Dubonos, I. Grigorieva, and A. Firsov, "Electric field effect in atomically thin carbon films", Science, **306**, 666 (2004).

[15] A. K. Geim, "Random walk to graphene", Nobel Lecture (2010).

[16] A. K. Geim and K. S. Novoselov, "The rise of graphene", Nature Mater., **6**, 183 (2007).

[17] B. Partoens and F. M. Peeters, "From graphene to graphite: Electronic structure around the K point", Phys. Rev. B, **74**, 075404 (2006).

[18] M. Klintenberg, S. Lebègue, C. Ortiz, B. Sanyal, J. Fransson, and O. Eriksson, "Evolving properties of two-dimensional materials: from graphene to graphite", J. Phys.: Condens. Matter, **21**, 335502 (2009).

[19] M. Ohring, *Engineering Materials Science* (Academic Press, San Diego, 1995).

[20] C. Kittel, *Introduction to Solid State Physics*, 7th ed. (Wiley, New York, 1996).

[21] D. Chung, "Review Graphite", J. Mater. Sci., **37**, 1475 (2002).

[22] P. J. F. Harris, *Carbon Nanotubes and Related Structures: New Materials for the Twenty-first Century* (Cambridge University Press, 2004).

[23] M. Grundmann, *The Physics of Semiconductors: An Introduction Including Devices and Nanophysics* (Springer, Berlin, 2006).

[24] S. M. Sze and K. K. Ng, *Physics of Semiconductor Devices*, 3rd ed. (Wiley-Interscience, Hoboken, New Jersey, 2007).

[25] A. H. Castro Neto, F. Guinea, N. M. R. Peres, K. S. Novoselov, and A. K. Geim, "The electronic properties of graphene", Rev. Mod. Phys., **81**, 109 (2009).

[26] M. J. Allen, V. C. Tung, and R. B. Kaner, "Honeycomb Carbon: A Review of Graphene", Chem. Rev., **110**, 132 (2010).

[27] Y. Zhu, S. Murali, W. Cai, X. Li, J. W. Suk, J. R. Potts, and R. S. Ruoff, "Graphene and Graphene Oxide: Synthesis, Properties, and Applications", Adv. Mater., **22**, 3906 (2010).

[28] C. Stampfer, S. Fringes, J. Güttinger, F. Molitor, C. Volk, B. Terrés, J. Dauber, S. Engels, S. Schnez, A. Jacobsen, S. Dröscher, T. Ihn, and K. Ensslin, "Transport in graphene nanostructures", Front. Phys., **6**, 271 (2011).

[29] Ph. Wagner, V. V. Ivanovskaya, M. J. Rayson, P. R. Briddon, and C. P. Ewels, "Mechanical properties of nanosheets and nanotubes investigated using a new geometry independent volume definition", J. Phys.: Condens. Matter, **25**, 155302 (2013).

[30] P. R. Wallace, "The Band Theory of Graphite", Phys. Rev., **71**, 622 (1947).

[31] J.-C. Charlier, J.-P. Michenaud, and X. Gonze, "First-principles study of the electronic properties of simple hexagonal graphite", Phys. Rev. B, **46**, 4531 (1992).

[32] M. S. Dresselhaus and G. Dresselhaus, "Intercalation compounds of graphite", Adv. Phys., **51**, 1 (2002).

[33] S. V. Morozov, K. S. Novoselov, M. I. Katsnelson, F. Schedin, D. C. Elias, J. A. Jaszczak, and A. K. Geim, "Giant Intrinsic Carrier Mobilities in Graphene and its Bilayer", Phys. Rev. Lett., **100**, 016602 (2008).

[34] X. Du, I. Skachko, A. Barker, and E. Y. Andrei, "Approaching ballistic transport in suspended graphene", Nature Nanotech., **3**, 491 (2008).

[35] Z. Jiang, Y. Zhang, Y.-W. Tan, H. Stormer, and P. Kim, "Quantum Hall effect in graphene", Solid State Commun., **143**, 14 (2007).

[36] M. I. Katsnelson, K. S. Novoselov, and A. K. Geim, "Chiral tunnelling and the Klein paradox in graphene", Nature Phys., **2**, 620 (2006).

[37] V. Barone, O. Hod, and G. E. Scuseria, "Electronic Structure and Stability of Semiconducting Graphene Nanoribbons", Nano Lett., **6**, 2748 (2006).

[38] Y.-W. Son, M. L. Cohen, and S. G. Louie, "Energy Gaps in Graphene Nanoribbons", Phys. Rev. Lett., **97**, 216803 (2006).

[39] L. Jiao, L. Zhang, X. Wang, G. Diankov, and H. Dai, "Narrow graphene nanoribbons from carbon nanotubes", Nature, **458**, 877 (2009).

[40] L. Tapaszto, G. Dobrik, P. Lambin, and L. P. Biro, "Tailoring the atomic structure of graphene nanoribbons by scanning tunnelling microscope lithography", Nature Nanotech., **3**, 397 (2008).

[41] J. Cai, P. Ruffieux, R. Jaafar, M. Bieri, T. Braun, S. Blankenburg, M. Muoth, A. P. Seitsonen, M. Saleh, X. Feng, K. Mullen, and R. Fasel, "Atomically precise bottom-up fabrication of graphene nanoribbons", Nature, **466**, 470 (2010).

[42] P. Ruffieux, J. Cai, N. C. Plumb, L. Patthey, D. Prezzi, A. Ferretti, E. Molinari, X. Feng, K. Müllen, C. A. Pignedoli, and R. Fasel, "Electronic Structure of Atomically Precise Graphene Nanoribbons", ACS Nano, **6**, 6930 (2012).

[43] R. O. Jones and O. Gunnarsson, "The density functional formalism, its applications and prospects", Rev. Mod. Phys., **61**, 689 (1989).

[44] R. G. Parr and W. Yang, "Density-Functional Theory of the Electronic Structure of Molecules", Annu. Rev. Phys. Chem., **46**, 701 (1995).

[45] C. P. Ewels, *Density Functional Modelling of point defects in semiconductors*, Phd thesis, University of Exeter, UK (1997).

[46] K. Capelle, "A bird's-eye view of density-functional theory", Arxiv.org, **cond-mat**, 0211443 (2002).

[47] F. Jensen, *Introduction to Computational Chemistry*, 2nd ed. (Wiley, 2006).

[48] A. J. Cohen, P. Mori-Sánchez, and W. Yang, "Challenges for Density Functional Theory", Chem. Rev., **112**, 289 (2011).

[49] E. Schrödinger, "Die gegenwärtige Situation in der Quantenmechanik", Naturwissenschaften, **23**, 807 (1935).

[50] E. Schrödinger, "Quantisierung als Eigenwertproblem", Annalen der Physik, **384**, 361 (1926).

[51] E. Schrödinger, "Der stetige Übergang von der Mikro- zur Makromechanik", Naturwissenschaften, **14**, 664 (1926).

[52] M. Born and R. Oppenheimer, "Zur Quantentheorie der Molekeln", Annalen der Physik, **389**, 457 (1927).

[53] D. R. Hartree, "The Wave Mechanics of an Atom with a Non-Coulomb Central Field. Part I. Theory and Methods", Math. Proc. of the Cambridge Phil. Soc., **24**, 89 (1928).

[54] J. C. Slater, "Note on Hartree's Method", Phys. Rev., **35**, 210 (1930).

[55] J. C. Slater, "A Simplification of the Hartree-Fock Method", Phys. Rev., **81**, 385 (1951).

[56] P. Hohenberg and W. Kohn, "Inhomogeneous Electron Gas", Phys. Rev., **136**, B864 (1964).

[57] W. Kohn and L. J. Sham, "Self-Consistent Equations Including Exchange and Correlation Effects", Phys. Rev., **140**, A1133 (1965).

[58] D. M. Ceperley and B. J. Alder, "Ground State of the Electron Gas by a Stochastic Method", Phys. Rev. Lett., **45**, 566 (1980).

[59] J. P. Perdew and A. Zunger, "Self-interaction correction to density-functional approximations for many-electron systems", Phys. Rev. B, **23**, 5048 (1981).

[60] L. A. Cole and J. P. Perdew, "Calculated electron affinities of the elements", Phys. Rev. A, **25**, 1265 (1982).

[61] J. P. Perdew and Y. Wang, "Accurate and simple analytic representation of the electron-gas correlation energy", Phys. Rev. B, **45**, 13244 (1992).

[62] C. Lee, W. Yang, and R. G. Parr, "Development of the Colle-Salvetti correlation-energy formula into a functional of the electron density", Phys. Rev. B, **37**, 785 (1988).

[63] A. D. Becke, "Density–functional thermochemistry. III. The role of exact exchange", J. Chem. Phys., **98**, 5648 (1993).

[64] P. J. Stephens, F. J. Devlin, C. F. Chabalowski, and M. J. Frisch, "Ab Initio Calculation of Vibrational Absorption and Circular Dichroism Spectra Using Density Functional Force Fields", J. Phys. Chem., **98**, 11623 (1994).

[65] R. Jones and P. Briddon, *The ab initio cluster method and the dynamics of defects in semiconductors*, Chapter 6, Semiconductors and Semimetals, Vol. 51 (Academic Press, Boston, 1998).

[66] M. J. Rayson and P. R. Briddon, "Highly efficient method for Kohn-Sham density functional calculations of $500 - 10\,000$ atom systems", Phys. Rev. B, **80**, 205104 (2009).

[67] M. J. Rayson, "Rapid filtration algorithm to construct a minimal basis on the fly from a primitive Gaussian basis", Comput. Phys. Commun., **181**, 1051 (2010).

[68] P. R. Briddon and M. J. Rayson, "Accurate Kohn-Sham DFT with the speed of tight binding: Current techniques and future directions in materials modelling", Phys. Status Solidi B, **248**, 1309 (2011).

[69] H. Hellmann, "A New Approximation Method in the Problem of Many Electrons", J. Chem. Phys., **3**, 61 (1935).

[70] J. Harris and R. O. Jones, "Pseudopotentials in Density-Functional Theory", Phys. Rev. Lett., **41**, 191 (1978).

[71] U. von Barth and C. D. Gelatt, "Validity of the frozen-core approximation and pseudopotential theory for cohesive energy calculations", Phys. Rev. B, **21**, 2222 (1980).

[72] http://en.wikipedia.org/wiki/Pseudopotential (2012).

[73] C. Hartwigsen, S. Goedecker, and J. Hutter, "Relativistic separable dual-space Gaussian pseudopotentials from H to Rn", Phys. Rev. B, **58**, 3641 (1998).

[74] G. B. Bachelet, D. R. Hamann, and M. Schlüter, "Pseudopotentials that work: From H to Pu", Phys. Rev. B, **26**, 4199 (1982).

[75] N. Troullier and J. L. Martins, "Efficient pseudopotentials for plane-wave calculations", Phys. Rev. B, **43**, 1993 (1991).

[76] P. R. Briddon and R. Jones, "LDA Calculations Using a Basis of Gaussian Orbitals", Phys. Status Solidi B, **217**, 131 (2000).

[77] J. Goss, M. Shaw, and P. Briddon, "Marker-Method Calculations for Electrical Levels Using Gaussian-Orbital Basis Sets", Topics Appl. Physics, **104**, 69 (2007).

[78] F. Bloch, "Über die Quantenmechanik der Elektronen in Kristallgittern", Zeitschrift für Physik A Hadrons and Nuclei, **52**, 555 (1929).

[79] L. Brillouin, *Wave Propagation in Periodic Structures*, 2nd ed. (Dover Publications, New York, 1953).

[80] H. J. Monkhorst and J. D. Pack, "Special points for Brillouin-zone integrations", Phys. Rev. B, **13**, 5188 (1976).

[81] R. P. Feynman, "Forces in Molecules", Phys. Rev., **56**, 340 (1939).

[82] H. Hellmann, "Einführung in die Quantenchemie", Angew. Chem., **54**, 156 (1941).

[83] M. Hestenes and E. Stiefel, "Methods of conjugate gradients for solving linear systems", J. Res. Nat. Bur. Stand., **49**, 406 (1952).

[84] M. C. Payne, M. P. Teter, D. C. Allan, T. A. Arias, and J. D. Joannopoulos, "Iterative minimization techniques for ab initio total-energy calculations: molecular dynamics and conjugate gradients", Rev. Mod. Phys., **64**, 1045 (1992).

[85] J. W. Patrick, ed., *Porosity in Carbons: Characterization and Applications*, 1st ed. (Halsted Press, 1994).

[86] E. Frieden, "Chemical Elements of Life", Scientific American, **227**, 52 (1972).

[87] A. Fukumoto, "First-principles pseudopotential calculations of the elastic properties of diamond, Si, and Ge", Phys. Rev. B, **42**, 7462 (1990).

[88] S. J. Sque, *Bulk and transfer doping of diamond*, Phd thesis, University of Exeter, UK (2005).

[89] H. J. McSkimin and W. L. Bond, "Elastic Moduli of Diamond", Phys. Rev., **105**, 116 (1957).

[90] C. A. Klein and G. F. Cardinale, "Young's modulus and Poisson's ratio of CVD diamond", Diamond Relat. Mater., **2**, 918 (1993).

[91] F. Szuecs, M. Werner, R. S. Sussmann, C. S. J. Pickles, and H. J. Fecht, "Temperature dependence of Young's modulus and degradation of chemical vapor deposited diamond", J. Appl. Phys., **86**, 6010 (1999).

[92] S. V. Kidalov and F. M. Shakhov, "Thermal Conductivity of Diamond Composites", Materials, **2**, 2467 (2009).

[93] T. Evans and P. F. James, "A Study of the Transformation of Diamond to Graphite", Proc. Royal Soc. London, Series A, **277**, 260 (1964).

[94] A. Mainwood, "Theoretical modelling of dopants in diamond", J. Mater. Sci.: Mater. Electron., **17**, 453 (2006).

[95] V. N. Mochalin, O. Shenderova, D. Ho, and Y. Gogotsi, "The properties and applications of nanodiamonds", Nature Nanotech., **7**, 11 (2012).

[96] J. D. Bernal, "The Structure of Graphite", Proc. Royal Soc. London, Series A, **106**, 749 (1924).

[97] R. E. Franklin, "The structure of graphitic carbons", Acta Cryst., **4**, 253 (1951).

[98] J. C. Slonczewski and P. R. Weiss, "Band Structure of Graphite", Phys. Rev., **109**, 272 (1958).

[99] J.-C. Charlier, X. Gonze, and J.-P. Michenaud, "First-principles study of the electronic properties of graphite", Phys. Rev. B, **43**, 4579 (1991).

[100] N. B. Hannay, T. H. Geballe, B. T. Matthias, K. Andres, P. Schmidt, and D. MacNair, "Superconductivity in Graphitic Compounds", Phys. Rev. Lett., **14**, 225 (1965).

[101] S. M. Heald and E. A. Stern, "Extended-x-ray-absorption-fine-structure study of the Br_2-graphite system", Phys. Rev. B, **17**, 4069 (1978).

[102] A. Yaya, C. P. Ewels, I. Suarez-Martinez, Ph. Wagner, S. Lefrant, A. Okotrub, L. Bulusheva, and P. R. Briddon, "Bromination of graphene and graphite", Phys. Rev. B, **83**, 045411 (2011).

[103] H. W. Kroto, J. R. Heath, S. C. O'Brien, R. F. Curl, and R. E. Smalley, "C60: Buckminsterfullerene", Nature, **318**, 162 (1985).

[104] H. W. Kroto, A. W. Allaf, and S. P. Balm, "C60: Buckminsterfullerene", Chem. Rev., **91**, 1213 (1991).

[105] www.ewels.info (2012).

[106] www.de.wikipedia.org/wiki/Fullerene (2012).

[107] W. Krätschmer, L. D. Lamb, K. Fostiropoulos, and D. R. Huffman, "Solid C60: a new form of carbon", Nature, **347**, 354 (1990).

[108] P. W. Dunk, N. K. Kaiser, C. L. Hendrickson, J. P. Quinn, C. P. Ewels, Y. Nakanishi, Y. Sasaki, H. Shinohara, A. G. Marshall, and H. W. Kroto, "Closed network growth of fullerenes", Nature Comm., **3**, 855 (2012).

[109] N. Gonzalez Szwacki, A. Sadrzadeh, and B. I. Yakobson, "B_{80} Fullerene: An Ab Initio Prediction of Geometry, Stability, and Electronic Structure", Phys. Rev. Lett., **98**, 166804 (2007).

[110] S. Iijima and T. Ichihashi, "Single-shell carbon nanotubes of 1-nm diameter", Nature, **363**, 603 (1993).

[111] X. Zhao, Y. Liu, S. Inoue, T. Suzuki, R. O. Jones, and Y. Ando, "Smallest Carbon Nanotube Is 3 Å in Diameter", Phys. Rev. Lett., **92**, 125502 (2004).

[112] P. M. Ajayan, "Nanotubes from Carbon", Chem. Rev., **99**, 1787 (1999).

[113] www-ibmc.u-strasbg.fr/ict/article83.html?lang=fr (2012).

[114] P. J. F. Harris, *Carbon Nanotube Science* (Cambridge University Press, UK, 2009).

[115] M. Dresselhaus, G. Dresselhaus, and R. Saito, "Physics of carbon nanotubes", Carbon, **33**, 883 (1995).

[116] J. P. Lu, "Elastic Properties of Carbon Nanotubes and Nanoropes", Phys. Rev. Lett., **79**, 1297 (1997).

[117] S. Gupta, K. Dharamvir, and V. K. Jindal, "Elastic moduli of single-walled carbon nanotubes and their ropes", Phys. Rev. B, **72**, 165428 (2005).

[118] E. W. Wong, P. E. Sheehan, and C. M. Lieber, "Nanobeam Mechanics: Elasticity, Strength, and Toughness of Nanorods and Nanotubes", Science, **277**, 1971 (1997).

[119] M. Yu, B. S. Files, S. Arepalli, and R. S. Ruoff, "Tensile Loading of Ropes of Single Wall Carbon Nanotubes and their Mechanical Properties", Phys. Rev. Lett., **84**, 5552 (2000).

[120] J. N. Coleman, U. Khan, W. J. Blau, and Y. K. Gun'ko, "Small but strong: A review of the mechanical properties of carbon nanotube-polymer composites", Carbon, **44**, 1624 (2006).

[121] M. Terrones, "SCIENCE AND TECHNOLOGY OF THE TWENTY-FIRST CENTURY: Synthesis, Properties, and Applications of Carbon Nanotubes", Annu. Rev. Mater. Res., **33**, 419 (2003).

[122] B. J. Landi, M. J. Ganter, C. D. Cress, R. A. DiLeo, and R. P. Raffaelle, "Carbon nanotubes for lithium ion batteries", Energy & Environmental Science, **2**, 638 (2009).

[123] K. Kostarelos, A. Bianco, and M. Prato, "Promises, facts and challenges for carbon nanotubes in imaging and therapeutics", Nature Nanotech., **4**, 627 (2009).

[124] J.-C. Charlier, L. Arnaud, I. V. Avilov, M. Delgado, F. Demoisson, E. H. Espinosa, C. P. Ewels, A. Felten, J. Guillot, R. Ionescu, R. Leghrib, E. Llobet, A. Mansour, H.-N. Migeon, J.-J. Pireaux, F. Reniers, I. Suarez-Martinez, G. E. Watson, and Z. Zanolli, "Carbon nanotubes randomly decorated with gold clusters: from nano 2 hybrid atomic structures to gas sensing prototypes", Nanotechnology, **20**, 375501 (2009).

[125] N. D. Mermin and H. Wagner, "Absence of Ferromagnetism or Antiferromagnetism in One- or Two-Dimensional Isotropic Heisenberg Models", Phys. Rev. Lett., **17**, 1133 (1966).

[126] H. P. Boehm, A. Clauss, G. O. Fischer, and U. Hofmann, "Dünnste Kohlenstoff-Folien", Zeitschrift für Naturforschung B, **17**, 150 (1962).

[127] K. S. Novoselov, A. K. Geim, S. V. Morozov, D. Jiang, M. I. Katsnelson, I. V. Grigorieva, S. V. Dubonos, and A. A. Firsov, "Two-dimensional gas of massless Dirac fermions in graphene", Nature, **438**, 197 (2005).

[128] Y. Zhang, Y.-W. Tan, H. L. Stormer, and P. Kim, "Experimental observation of the quantum Hall effect and Berry's phase in graphene", Nature, **438**, 201 (2005).

[129] J. C. Meyer, A. K. Geim, M. I. Katsnelson, K. S. Novoselov, T. J. Booth, and S. Roth, "The structure of suspended graphene sheets", Nature, **446**, 60 (2007).

[130] A. Fasolino, J. H. Los, and M. I. Katsnelson, "Intrinsic ripples in graphene", Nature Mater., **6**, 858 (2007).

[131] K. S. Novoselov and A. H. Castro Neto, "Two-dimensional crystals-based heterostructures: materials with tailored properties", Phys. Scripta, **T146**, 014006 (2012).

[132] Y. Hernandez, V. Nicolosi, M. Lotya, F. M. Blighe, Z. Sun, S. De, I. T. McGovern, B. Holland, M. Byrne, Y. K. Gun'Ko, J. J. Boland, P. Niraj, G. Duesberg, S. Krishnamurthy, R. Goodhue, J. Hutchison, V. Scardaci, A. C. Ferrari, and J. N. Coleman, "High-yield production of graphene by liquid-phase exfoliation of graphite", Nature Nanotech., **3**, 563 (2008).

[133] W. A. de Heer, C. Berger, X. Wu, P. N. First, E. H. Conrad, X. Li, T. Li, M. Sprinkle, J. Hass, M. L. Sadowski, M. Potemski, and G. Martinez, "Epitaxial graphene", Solid State Commun., **143**, 92 (2007).

[134] L. Gao, J. R. Guest, and N. P. Guisinger, "Epitaxial Graphene on Cu(111)", Nano Lett., **10**, 3512 (2010).

[135] D. R. Dreyer, R. S. Ruoff, and C. W. Bielawski, "From Conception to Realization: An Historial Account of Graphene and Some Perspectives for Its Future", Ang. Chem. Intern. Edition, **49**, 9336 (2010).

[136] O. C. Compton and S. T. Nguyen, "Graphene Oxide, Highly Reduced Graphene Oxide, and Graphene: Versatile Building Blocks for Carbon-Based Materials", Small, **6**, 711 (2010).

[137] C. Vallés, J. David Núñez, A. M. Benito, and W. K. Maser, "Flexible conductive graphene paper obtained by direct and gentle annealing of graphene oxide paper", Carbon, **50**, 835 (2012).

[138] I. Suarez-Martinez, N. Grobert, and C. P. Ewels, "Nomenclature of sp^2 carbon nanoforms", Carbon, **50**, 741 (2012).

[139] C. Lee, X. Wei, Q. Li, R. Carpick, J. W. Kysar, and J. Hone, "Elastic and frictional properties of graphene", Phys. Status Solidi B, **246**, 2562 (2009).

[140] Ph. Wagner, C. P. Ewels, V. V. Ivanovskaya, P. R. Briddon, A. Pateau, and B. Humbert, "Ripple edge engineering of graphene nanoribbons", Phys. Rev. B, **84**, 134110 (2011).

[141] A. A. Balandin, S. Ghosh, W. Bao, I. Calizo, D. Teweldebrhan, F. Miao, and C. N. Lau, "Superior Thermal Conductivity of Single-Layer Graphene", Nano Lett., **8**, 902 (2008).

[142] M. D. Stoller, S. Park, Y. Zhu, J. An, and R. S. Ruoff, "Graphene-Based Ultracapacitors", Nano Lett., **8**, 3498 (2008).

[143] C. Berger, Z. Song, T. Li, X. Li, A. Y. Ogbazghi, R. Feng, Z. Dai, A. N. Marchenkov, E. H. Conrad, P. N. First, and W. A. de Heer, "Ultrathin Epitaxial Graphite: 2D Electron Gas Properties and a Route toward Graphene-based Nanoelectronics", J. Phys. Chem. B, **108**, 19912 (2004).

[144] Y.-M. Lin, C. Dimitrakopoulos, K. A. Jenkins, D. B. Farmer, H.-Y. Chiu, A. Grill, and P. Avouris, "100-GHz Transistors from Wafer-Scale Epitaxial Graphene", Science, **327**, 662 (2010).

[145] F. Bonaccorso, Z. Sun, T. Hasan, and A. C. Ferrari, "Graphene photonics and optoelectronics", Nature Photonics, **4**, 611 (2010).

[146] J.-C. Charlier, X. Gonze, and J.-P. Michenaud, "Graphite Interplanar Bonding: Electronic Delocalization and van der Waals Interaction", Europhys. Lett., **28**, 403 (1994).

[147] D. Klein, "Graphitic polymer strips with edge states", Chem. Phys. Lett., **217**, 261 (1994).

[148] K. Nakada, M. Fujita, G. Dresselhaus, and M. S. Dresselhaus, "Edge state in graphene ribbons: Nanometer size effect and edge shape dependence", Phys. Rev. B, **54**, 17954 (1996).

[149] C. Girit, J. Meyer, R. Erni, M. Rossell, C. Kisielowski, L. Yang, C. Park, M. Crommie, M. Cohen, S. Louie, and A. Zettl, "Graphene at the edge: stability and dynamics", Science, **323**, 1705 (2009).

[150] K. Suenaga and M. Koshino, "Atom-by-atom spectroscopy at graphene edge", Nature, **468**, 1088 (2010).

[151] Y. Kobayashi, K. Fukui, T. Enoki, K. Kusakabe, and Y. Kaburagi, "Observation of zigzag and armchair edges of graphite using scanning tunneling microscopy and spectroscopy", Phys. Rev. B, **71**, 193406 (2005).

[152] Y. Kobayashi, K.-i. Fukui, T. Enoki, and K. Kusakabe, "Edge state on hydrogen-terminated graphite edges investigated by scanning tunneling microscopy", Phys. Rev. B, **73**, 125415 (2006).

[153] X. Jia, M. Hofmann, V. Meunier, B. G. Sumpter, J. Campos-Delgado, J. M. Romo-Herrera, H. Son, Y.-P. Hsieh, A. Reina, J. Kong, M. Terrones, and M. S. Dresselhaus, "Controlled Formation of Sharp Zigzag and Armchair Edges in Graphitic Nanoribbons", Science, **323**, 1701 (2009).

[154] J. Tian, H. Cao, W. Wu, Q. Yu, and Y. P. Chen, "Direct Imaging of Graphene Edges: Atomic Structure and Electronic Scattering", Nano Lett., **11**, 3663 (2011).

[155] T. Enoki, S. Fujii, and K. Takai, "Zigzag and armchair edges in graphene", Carbon, **50**, 3141 (2012).

[156] T. Wassmann, A. P. Seitsonen, A. M. Saitta, M. Lazzeri, and F. Mauri, "Structure, Stability, Edge States, and Aromaticity of Graphene Ribbons", Phys. Rev. Lett., **101**, 096402 (2008).

[157] C. K. Gan and D. J. Srolovitz, "First-principles study of graphene edge properties and flake shapes", Phys. Rev. B, **81**, 125445 (2010).

[158] P. S. Branicio, M. H. Jhon, C. K. Gan, and D. J. Srolovitz, "Properties on the edge: graphene edge energies, edge stresses, edge warping, and the Wulff shape of graphene flakes", Modell. Simul. Mater. Science Engineering, **19**, 054002 (2011).

[159] L. Sun, P. Wei, J. Wei, S. Sanvito, and S. Hou, "From zigzag to armchair: the energetic stability, electronic and magnetic properties of chiral graphene nanoribbons with hydrogen-terminated edges", J. Phys.: Condens. Matter, **23**, 425301 (2011).

[160] V. V. Ivanovskaya, A. Zobelli, Ph. Wagner, M. I. Heggie, P. R. Briddon, M. J. Rayson, and C. P. Ewels, "Low-Energy Termination of Graphene Edges via the Formation of Narrow Nanotubes", Phys. Rev. Lett., **107**, 065502 (2011).

[161] P. Koskinen, S. Malola, and H. Häkkinen, "Self-Passivating Edge Reconstructions of Graphene", Phys. Rev. Lett., **101**, 115502 (2008).

[162] P. Koskinen, S. Malola, and H. Häkkinen, "Evidence for graphene edges beyond zigzag and armchair", Phys. Rev. B, **80**, 73401 (2009).

[163] M. Acik and Y. J. Chabal, "Nature of Graphene Edges: A Review", Jap. J. Appl. Phys., **50**, 070101 (2011).

[164] X. Jia, J. Campos-Delgado, M. Terrones, V. Meunier, and M. S. Dresselhaus, "Graphene edges: a review of their fabrication and characterization", Nanoscale, **3**, 86 (2011).

[165] M. Katsnelson and K. Novoselov, "Graphene: New bridge between condensed matter physics and quantum electrodynamics", Solid State Commun., **143**, 3 (2007).

[166] J. Berashevich and T. Chakraborty, "On the Nature of Interlayer Interactions in a System of Two Graphene Fragments", J. Phys. Chem. C, **115**, 24666 (2011).

[167] G. Li, A. Luican, and E. Y. Andrei, "Scanning Tunneling Spectroscopy of Graphene on Graphite", Phys. Rev. Lett., **102**, 176804 (2009).

[168] J. Hass, F. Varchon, J. E. Millán-Otoya, M. Sprinkle, N. Sharma, W. A. de Heer, C. Berger, P. N. First, L. Magaud, and E. H. Conrad, "Why Multilayer Graphene on 4H-SiC(0001$^-$) Behaves Like a Single Sheet of Graphene", Phys. Rev. Lett., **100**, 125504 (2008).

[169] J. M. B. Lopes dos Santos, N. M. R. Peres, and A. H. Castro Neto, "Graphene Bilayer with a Twist: Electronic Structure", Phys. Rev. Lett., **99**, 256802 (2007).

[170] F. Liu, P. Ming, and J. Li, "Ab initio calculation of ideal strength and phonon instability of graphene under tension", Phys. Rev. B, **76**, 064120 (2007).

[171] C. Lee, X. Wei, J. W. Kysar, and J. Hone, "Measurement of the Elastic Properties and Intrinsic Strength of Monolayer Graphene", Science, **321**, 385 (2008).

[172] I. G. Masters and K. E. Evans, "Models for the elastic deformation of honeycombs", Composite Struc., **35**, 403 (1996).

[173] F. Scarpa, S. Adhikari, and A. Srikantha Phani, "Effective elastic mechanical properties of single layer graphene sheets", Nanotechnology, **20**, 065709 (2009).

[174] H. Zhao, K. Min, and N. R. Aluru, "Size and Chirality Dependent Elastic Properties of Graphene Nanoribbons under Uniaxial Tension", Nano Lett., **9**, 3012 (2009).

[175] L. Gong, R. J. Young, I. A. Kinloch, I. Riaz, R. Jalil, and K. S. Novoselov, "Optimizing the Reinforcement of Polymer-Based Nanocomposites by Graphene", ACS Nano, **6**, 2086 (2012).

[176] C. Tao, L. Jiao, O. V. Yazyev, Y.-C. Chen, J. Feng, X. Zhang, R. B. Capaz, J. M. Tour, A. Zettl, S. G. Louie, H. Dai, and M. F. Crommie, "Spatially resolving edge states of chiral graphene nanoribbons", Nature Phys., **7**, 616 (2011).

[177] F. Cervantes-Sodi, G. Csányi, S. Piscanec, and A. C. Ferrari, "Edge-functionalized and substitutionally doped graphene nanoribbons: Electronic and spin properties", Phys. Rev. B, **77**, 165427 (2008).

[178] M. Ezawa, "Peculiar width dependence of the electronic properties of carbon nanoribbons", Phys. Rev. B, **73**, 045432 (2006).

[179] M. Baldoni, A. Sgamellotti, and F. Mercuri, "Electronic properties and stability of graphene nanoribbons: An interpretation based on Clar sextet theory", Chem. Phys. Lett., **464**, 202 (2008).

[180] T. Wassmann, A. P. Seitsonen, A. M. Saitta, M. Lazzeri, and F. Mauri, "Clar's Theory, π-Electron Distribution, and Geometry of Graphene Nanoribbons", J. Am. Chem. Soc., **132**, 3440 (2010).

[181] D. Prezzi, D. Varsano, A. Ruini, A. Marini, and E. Molinari, "Optical properties of graphene nanoribbons: The role of many-body effects", Phys. Rev. B, **77**, 041404 (2008).

[182] D. V. Kosynkin, A. L. Higginbotham, A. Sinitskii, J. R. Lomeda, A. Dimiev, B. K. Price, and J. M. Tour, "Longitudinal unzipping of carbon nanotubes to form graphene nanoribbons", Nature, **458**, 872 (2009).

[183] L. Jiao, X. Wang, G. Diankov, H. Wang, and H. Dai, "Facile synthesis of high-quality graphene nanoribbons", Nature Nanotech., **5**, 321 (2010).

[184] A. L. Elías, A. R. Botello-Méndez, D. Meneses-Rodríguez, V. Jehová González, D. Ramírez-González, L. Ci, E. Munoz-Sandoval, P. M. Ajayan, H. Ter-

rones, and M. Terrones, "Longitudinal Cutting of Pure and Doped Carbon Nanotubes to Form Graphitic Nanoribbons Using Metal Clusters as Nanoscalpels", Nano Lett., **10**, 366 (2010).

[185] K. Kim, A. Sussman, and A. Zettl, "Graphene Nanoribbons Obtained by Electrically Unwrapping Carbon Nanotubes", ACS Nano, **4**, 1362 (2010).

[186] L. Xie, H. Wang, C. Jin, X. Wang, L. Jiao, K. Suenaga, and H. Dai, "Graphene Nanoribbons from Unzipped Carbon Nanotubes: Atomic Structures, Raman Spectroscopy, and Electrical Properties", J. Am. Chem. Soc., **133**, 10394 (2011).

[187] A. Fasoli, A. Colli, A. Lombardo, and A. C. Ferrari, "Fabrication of graphene nanoribbons via nanowire lithography", Phys. Status Solidi B, **246**, 2514 (2009).

[188] J. Bai, X. Duan, and Y. Huang, "Rational Fabrication of Graphene Nanoribbons Using a Nanowire Etch Mask", Nano Lett., **9**, 2083 (2009).

[189] H. Terrones, R. Lv, M. Terrones, and M. S. Dresselhaus, "The role of defects and doping in 2D graphene sheets and 1D nanoribbons", Rep. Prog. Phys., **75**, 062501 (2012).

[190] M. Terrones, A. R. Botello-Méndez, J. Campos-Delgado, F. López-Urías, Y. I. Vega-Cantú, F. J. Rodríguez-Macías, A. L. Elías, E. Munoz-Sandoval, A. G. Cano-Márquez, J.-C. Charlier, and H. Terrones, "Graphene and graphite nanoribbons: Morphology, properties, synthesis, defects and applications", Nano Today, **5**, 351 (2010).

[191] Z. Chen, Y. Lin, M. J. Rooks, and P. Avouris, "Graphene nano-ribbon electronics", Physica E, **40**, 228 (2007).

[192] L. Yang, M. L. Cohen, and S. G. Louie, "Excitonic Effects in the Optical Spectra of Graphene Nanoribbons", Nano Lett., **7**, 3112 (2007).

[193] V. Ryzhii, V. Mitin, M. Ryzhii, N. Ryabova, and T. Otsuji, "Device Model for Graphene Nanoribbon Phototransistor", Appl. Phys. Express, **1**, 063002 (2008).

[194] Q. Su, S. Pang, V. Alijani, C. Li, X. Feng, and K. Mullen, "Composites of Graphene with Large Aromatic Molecules", Adv. Mater., **21**, 3191 (2009).

[195] Y. Yoon and J. Guo, "Effect of edge roughness in graphene nanoribbon transistors", Appl. Phys. Lett., **91**, 073103 (2007).

[196] D. Cochin, M. Passmann, G. Wilbert, R. Zentel, E. Wischerhoff, and A. Laschewsky, "Layered Nanostructures with LC-Polymers, Polyelectrolytes, and Inorganics", Macromolecules, **30**, 4775 (1997).

[197] D. W. Kim, J. Kumar, and A. Blumstein, "Ordered assembly of conjugated ionic polyacetylenes within clay nanoplatelets: layer-by-layer assembly and intercalative polymerization", Appl. Clay Sci., **30**, 134 (2005).

[198] J. N. Coleman, M. Lotya, A. O'Neill, S. D. Bergin, P. J. King, U. Khan, K. Young, A. Gaucher, S. De, R. J. Smith, I. V. Shvets, S. K. Arora, G. Stanton, H. Kim, K. Lee, G. T. Kim, G. S. Duesberg, T. Hallam, J. J. Boland, J. J. Wang, J. F. Donegan, J. C. Grunlan, G. Moriarty, A. Shmeliov, R. J. Nicholls, J. M. Perkins, E. M. Grieveson, K. Theuwissen, D. W. McComb, P. D. Nellist, and V. Nicolosi, "Two-Dimensional Nanosheets Produced by Liquid Exfoliation of Layered Materials", Science, **331**, 568 (2011).

[199] H. Manzano, A. N. Enyashin, J. S. Dolado, A. Ayuela, J. Frenzel, and G. Seifert, "Do Cement Nanotubes exist?", Adv. Mater., **24**, 3239 (2012).

[200] A. H. C. Neto and K. Novoselov, "New directions in science and technology: two-dimensional crystals", Rep. Prog. Phys., **74**, 082501 (2011).

[201] C. R. Dean, A. F. Young, I. Meric, C. Lee, L. Wang, S. Sorgenfrei, K. Watanabe, T. Taniguchi, P. Kim, K. L. Shepard, and J. Hone, "Boron nitride substrates for high-quality graphene electronics", Nature Nanotech., **5**, 722 (2010).

[202] J. Li and V. B. Shenoy, "Graphene quantum dots embedded in hexagonal boron nitride sheets", Appl. Phys. Lett., **98**, 013105 (2011).

[203] A. Gómez-Rodríguez, L. Beltrán-del Río, and R. Herrera-Becerra, "SimulaTEM: Multislice simulations for general objects", Ultramicroscopy, **110**, 95 (2010).

[204] Z. Liu, K. Suenaga, P. J. F. Harris, and S. Iijima, "Open and Closed Edges of Graphene Layers", Phys. Rev. Lett., **102**, 015501 (2009).

[205] V. V. Ivanovskaya, Ph. Wagner, A. Zobelli, I. Suarez-Martinez, A. Yaya, and C. P. Ewels, "Graphene edge structures: Folding, scrolling, tubing, rippling and twisting", Springer Series Carbon Nanostructures, GraphITA 2011, 75 (2012).

[206] I. Suarez-Martinez, G. Savini, A. Zobelli, and M. Heggie, "Dislocations in Carbon Nanotube Walls", J. Nanosci. Nanotechnol., **7**, 3417 (2007).

[207] Z. Xu and M. J. Buehler, "Geometry Controls Conformation of Graphene Sheets: Membranes, Ribbons, and Scrolls", ACS Nano, **4**, 3869 (2010).

[208] M. Gass, U. Bangert, A. Bleloch, P. Wang, R. Nair, and A. Geim, "Free-standing graphene at atomic resolution", Nature Nanotechnol., **3**, 676 (2008).

[209] I. Suarez-Martinez, G. Savini, G. Haffenden, J. Campanera, and M. Heggie, "Dislocations of Burgers vector c/2 in graphite", Phys. Status Solidi C, **4**, 2958 (2007).

[210] S. Sawada and N. Hamada, "Energetics of carbon nano-tubes", Solid State Commun., **83**, 917 (1992).

[211] L. Qin, X. Zhao, K. Hirahara, Y. Miyamoto, Y. Ando, and S. Iijima, "Materials science: The smallest carbon nanotube", Nature, **408**, 50 (2000).

[212] L. Guan, K. Suenaga, and S. Iijima, "Smallest carbon nanotube assigned with atomic resolution accuracy", Nano Lett., **8**, 459 (2008).

[213] N. Chopra, L. Benedict, V. Crespi, M. Cohen, S. Louie, and A. Zettl, "Fully collapsed carbon nanotubes", Nature, **377**, 135 (1995).

[214] L. Chernozatonskii, E. Sheka, and A. Artyukh, "Graphene-nanotube structures: Constitution and formation energy", JETP Lett., 352 (2009).

[215] G. Lee and K. Cho, "Electronic structures of zigzag graphene nanoribbons with edge hydrogenation and oxidation", Phys. Rev. B, **79**, 165440 (2009).

[216] J. Kunstmann, C. Ozdoğan, A. Quandt, and H. Fehske, "Stability of edge states and edge magnetism in graphene nanoribbons", Phys. Rev. B, **83**, 045414 (2011).

[217] T. Enoki, Y. Kobayashi, and K. Fukui, "Electronic structures of graphene edges and nanographene", Int. Rev. Phys. Chem., **26**, 609 (2007).

[218] X. Zheng, L. Huang, X. Wang, J. Lan, and Z. Zeng, "Band gap engineering in armchair-edged graphene nanoribbons by edge dihydrogenation", Comput. Mater. Science, **62**, 93 (2012).

[219] E. Clar, *The Aromatic Sextet* (Wiley, London, 1972).

[220] M. D. Watson, A. Fechtenkötter, and K. Müllen, "Big Is Beautiful–"Aromaticity" Revisited from the Viewpoint of Macromolecular and Supramolecular Benzene Chemistry", Chem. Rev., **101**, 1267 (2001).

[221] J. Wu, W. Pisula, and K. Müllen, "Graphenes as Potential Material for Electronics", Chem. Rev., **107**, 718 (2007).

[222] H. Lee, Y.-W. Son, N. Park, S. Han, and J. Yu, "Magnetic ordering at the edges of graphitic fragments: Magnetic tail interactions between the edge-localized states", Phys. Rev. B, **72**, 174431 (2005).

[223] Y.-W. Son, M. L. Cohen, and S. G. Louie, "Half-metallic graphene nanoribbons", Nature, **444**, 347 (2006).

[224] D.-e. Jiang, B. G. Sumpter, and S. Dai, "Unique chemical reactivity of a graphene nanoribbon's zigzag edge", J. Chem. Phys., **126**, 134701 (2007).

[225] J. Jung, T. Pereg-Barnea, and A. H. MacDonald, "Theory of Interedge Superexchange in Zigzag Edge Magnetism", Phys. Rev. Lett., **102**, 227205 (2009).

[226] Y. Niimi, T. Matsui, H. Kambara, K. Tagami, M. Tsukada, and H. Fukuyama, "Scanning tunneling microscopy and spectroscopy of the electronic local density of states of graphite surfaces near monoatomic step edges", Phys. Rev. B, **73**, 085421 (2006).

[227] X. Li, W. Cai, J. An, S. Kim, J. Nah, D. Yang, R. Piner, A. Velamakanni, I. Jung, E. Tutuc, S. K. Banerjee, L. Colombo, and R. S. Ruoff, "Large-Area Synthesis of High-Quality and Uniform Graphene Films on Copper Foils", Science, **324**, 1312 (2009).

[228] L. Gao, W. Ren, J. Zhao, L.-P. Ma, Z. Chen, and H.-M. Cheng, "Efficient growth of high-quality graphene films on Cu foils by ambient pressure chemical vapor deposition", Appl. Phys. Lett., **97**, 183109 (2010).

[229] K. Celebi, M. T. Cole, K. B. K. Teo, and H. G. Park, "Observations of Early Stage Graphene Growth on Copper", Electrochem. Solid-State Lett., **15**, K1 (2011).

[230] M. W. Chase, "NIST - JANAF Themochemical Tables", J. Phys. Chem. Ref. Data, **9**, 1 (1998).

[231] G.-D. Lee, C. Z. Wang, E. Yoon, N.-M. Hwang, and K. M. Ho, "Reconstruction and evaporation at graphene nanoribbon edges", Phys. Rev. B, **81**, 195419 (2010).

[232] J. N. B. Rodrigues, P. A. D. Gonçalves, N. F. G. Rodrigues, R. M. Ribeiro, J. M. B. Lopes dos Santos, and N. M. R. Peres, "Zigzag graphene nanoribbon edge reconstruction with Stone-Wales defects", Phys. Rev. B, **84**, 155435 (2011).

[233] A. Stone and D. Wales, "Theoretical studies of icosahedral C60 and some related species", Chem. Phys. Lett., **128**, 501 (1986).

[234] C. Ewels, M. Heggie, and P. Briddon, "Adatoms and nanoengineering of carbon", Chem. Phys. Lett., **351**, 178 (2002).

[235] D. Gunlycke, J. Li, J. W. Mintmire, and C. T. White, "Edges Bring New Dimension to Graphene Nanoribbons", Nano Lett., **10**, 3638 (2010).

[236] X. Peng and S. Velasquez, "Strain modulated band gap of edge passivated armchair graphene nanoribbons", Appl. Phys. Lett., **98**, 023112 (2011).

[237] G. Gui, J. Li, and J. Zhong, "Band structure engineering of graphene by strain: First-principles calculations", Phys. Rev. B, **78**, 075435 (2008).

[238] F. Guinea, M. I. Katsnelson, and A. K. Geim, "Energy gaps and a zero-field quantum Hall effect in graphene by strain engineering", Nature Phys., **6**, 30 (2010).

[239] C. Cocchi, A. Ruini, D. Prezzi, M. J. Caldas, and E. Molinari, "Designing All-Graphene Nanojunctions by Covalent Functionalization", J. Phys. Chem. C, **115**, 2969 (2011).

[240] V. B. Shenoy, C. D. Reddy, A. Ramasubramaniam, and Y. W. Zhang, "Edge-Stress-Induced Warping of Graphene Sheets and Nanoribbons", Phys. Rev. Lett., **101**, 245501 (2008).

[241] R. C. Thompson-Flagg, M. J. B. Moura, and M. Marder, "Rippling of graphene", Europhys. Lett., **85**, 46002 (2009).

[242] O. Hod, V. Barone, J. E. Peralta, and G. E. Scuseria, "Enhanced Half-Metallicity in Edge-Oxidized Zigzag Graphene Nanoribbons", Nano Lett., **7**, 2295 (2007).

[243] G. Henkelman, B. Uberuaga, and H. Jonsson, "A climbing image nudged elastic band method for finding saddle points and minimum energy paths", J. Chem. Phys., **113**, 9901 (2000).

[244] N. Rosenkranz, C. Till, C. Thomsen, and J. Maultzsch, "Ab initio calculations of edge-functionalized armchair graphene nanoribbons: Structural, electronic, and vibrational effects", Phys. Rev. B, **84**, 195438 (2011).

[245] L. Brey and H. A. Fertig, "Electronic states of graphene nanoribbons studied with the Dirac equation", Phys. Rev. B, **73**, 235411 (2006).

[246] F. J. Martín-Martínez, S. Fias, G. Van Lier, F. De Proft, and P. Geerlings, "Electronic Structure and Aromaticity of Graphene Nanoribbons", Chemistry - A European Journal, **18**, 6183 (2012).

[247] M. Jain, J. R. Chelikowsky, and S. G. Louie, "Reliability of Hybrid Functionals in Predicting Band Gaps", Phys. Rev. Lett., **107**, 216806 (2011).

[248] V. Barone, O. Hod, J. E. Peralta, and G. E. Scuseria, "Accurate Prediction of the Electronic Properties of Low-Dimensional Graphene Derivatives Using a Screened Hybrid Density Functional", Acc. Chem. Res., **44**, 269 (2011).

[249] C. D. Zeinalipour-Yazdi and C. Christofides, "Linear correlation between binding energy and Young's modulus in graphene nanoribbons", J. Appl. Phys., **106**, 054318 (2009).

[250] G. Van Lier, C. Van Alsenoy, V. Van Doren, and P. Geerlings, "Ab initio study of the elastic properties of single-walled carbon nanotubes and graphene", Chem. Phys. Lett., **326**, 181 (2000).

[251] I. Suarez-Martinez, A. Felten, J. J. Pireaux, C. Bittencourt, and C. P. Ewels, "Transition Metal Deposition on Graphene and Carbon Nanotubes", J. Nanosci. Nanotechnol., **9**, 6171 (2009).

[252] I. López-Corral, E. Germán, M. Volpe, G. Brizuela, and A. Juan, "Tight-binding study of hydrogen adsorption on palladium decorated graphene and carbon nanotubes", Int. J. Hydrogen Energy, **35**, 2377 (2010).

[253] X. Wang, X. Zheng, M. Ni, L. Zou, and Z. Zeng, "Theoretical investigation of Möbius strips formed from graphene", Appl. Phys. Lett., **97**, 123103 (2010).

[254] E. Hernádez, C. Goze, P. Bernier, and A. Rubio, "Elastic Properties of C and $B_xC_yN_z$ Composite Nanotubes", Phys. Rev. Lett., **80**, 4502 (1998).

[255] Y. Qi, H. Guo, J. Hector, and A. Timmons, "Threefold Increase in the Young's Modulus of Graphite Negative Electrode during Lithium Intercalation", J. Electrochem. Soc., **157**, A558 (2010).

[256] A. Kis, D. Mihailovic, M. Remskar, A. Mrzel, A. Jesih, I. Piwonski, A. J. Kulik, W. Benoît, and L. Forró, "Shear and Young's Moduli of MoS_2 Nanotube Ropes", Adv. Mat., **15**, 733 (2003).

[257] K. N. Kudin, G. E. Scuseria, and B. I. Yakobson, "C_2F, BN, and c nanoshell elasticity from ab initio computations", Phys. Rev. B, **64**, 235406 (2001).

[258] O. L. Blakslee, D. G. Proctor, E. J. Seldin, G. B. Spence, and T. Weng, "Elastic Constants of Compression–Annealed Pyrolytic Graphite", J. Appl. Phys., **41**, 3373 (1970).

[259] R. Maranganti and P. Sharma, "A novel atomistic approach to determine strain-gradient elasticity constants: Tabulation and comparison for various metals, semiconductors, silica, polymers and the (Ir) relevance for nanotechnologies", J. Mech. Phys. of Solids, **55**, 1823 (2007).

[260] W. Zhang, H. Yu, S. Lei, and Q. Huang, "Modelling of the elastic properties of crystalline silicon using lattice dynamics", J. Phys. D: Appl. Phys., **44**, 335401 (2011).

[261] K. Jakata and A. G. Every, "Determination of the dispersive elastic constants of the cubic crystals Ge, Si, GaAs, and InSb", Phys. Rev. B, **77**, 174301 (2008).

[262] N. Ohba, K. Miwa, N. Nagasako, and A. Fukumoto, "First-principles study on structural, dielectric, and dynamical properties for three BN polytypes", Phys. Rev. B, **63**, 115207 (2001).

[263] A. Bosak, "Elasticity of hexagonal boron nitride: Inelastic x-ray scattering measurements", Phys. Rev. B, **73** (2006).

[264] L. Duclaux, B. Nysten, J. Issi, and A. W. Moore, "Structure and low-temperature thermal conductivity of pyrolytic boron nitride", Phys. Rev. B, **46**, 3362 (1992).

[265] S. V. Khare, *Ab-initio Modeling of Slippery Hexagonal Solids*, COLLABORATIVE RESEARCH AND DEVELOPMENT (CR&D) (2008).

[266] C. Sourisseau, F. Cruege, M. Fouassier, and M. Alba, "Second-order Raman effects, inelastic neutron scattering and lattice dynamics in 2H-WS2", Chem. Phys., **150**, 281 (1991).

[267] J. Feldman, "Elastic constants of 2H-MoS2 and 2H-NbSe2 extracted from measured dispersion curves and linear compressibilities", J. Phys. Chem. Solids, **37**, 1141 (1976), ISSN 0022-3697.

[268] K. H. Michel and B. Verberck, "Theory of the elastic constants of graphite and graphene", Phys. Status Solidi B, **245**, 2177 (2008).

[269] M. Poot and H. S. J. van der Zant, "Mechanical systems in the quantum regime", Phys. Reports, **511**, 273 (2012).

[270] E. Cadelano, P. L. Palla, S. Giordano, and L. Colombo, "Nonlinear Elasticity of Monolayer Graphene", Phys. Rev. Lett., **102**, 235502 (2009).

[271] L. Colombo and S. Giordano, "Nonlinear elasticity in nanostructured materials", Rep. Prog. Phys., **74**, 116501 (2011).

[272] G. Tsoukleri, J. Parthenios, K. Papagelis, R. Jalil, A. C. Ferrari, A. K. Geim, K. S. Novoselov, and C. Galiotis, "Subjecting a Graphene Monolayer to Tension and Compression", Small, **5**, 2397 (2009).

[273] O. Frank, M. Bousa, I. Riaz, R. Jalil, K. S. Novoselov, G. Tsoukleri, J. Parthenios, L. Kavan, K. Papagelis, and C. Galiotis, "Phonon and Structural Changes in Deformed Bernal Stacked Bilayer Graphene", Nano Lett., **12**, 687 (2012).

[274] A. Castellanos-Gomez, M. Poot, G. A. Steele, H. S. J. van der Zant, N. Agraït, and G. Rubio-Bollinger, "Elastic Properties of Freely Suspended MoS2 Nanosheets", Adv. Mat., **24**, 772 (2012).

[275] R. Kuschnereit, P. Hess, D. Albert, and W. Kulisch, "Density and elastic constants of hot-filament-deposited polycrystalline diamond films: methane concentration dependence", Thin Solid Films, **312**, 66 (1998).

[276] B. Hajgató, S. Güryel, Y. Dauphin, J.-M. Blairon, H. E. Miltner, G. Van Lier, F. De Proft, and P. Geerlings, "Theoretical Investigation of the Intrinsic Mechanical Properties of Single- and Double-Layer Graphene", J. Phys. Chem. C, **116**, 22608 (2012).

[277] S. D. Poisson, Traité Méchanique, **2**, 476 (1811).

[278] G. N. Greaves, A. L. Greer, R. S. Lakes, and T. Rouxel, "Poisson's ratio and modern materials", Nature Mater., **10**, 823 (2011).

[279] R. Lakes, "Foam Structures with a Negative Poisson's Ratio", Science, **235**, 1038 (1987).

[280] Y. Huang, J. Wu, and K. C. Hwang, "Thickness of graphene and single-wall carbon nanotubes", Phys. Rev. B, **74**, 245413 (2006).

[281] Q. Pei, Y. Zhang, and V. Shenoy, "A molecular dynamics study of the mechanical properties of hydrogen functionalized graphene", Carbon, **48**, 898 (2010).

[282] B. Akdim, R. Pachter, X. Duan, and W. W. Adams, "Comparative theoretical study of single-wall carbon and boron-nitride nanotubes", Phys. Rev. B, **67**, 245404 (2003).

[283] L. Pauling, "Atomic Radii and Interatomic Distances in Metals", J. Am. Chem. Soc., **69**, 542 (1947).

[284] A. Bondi, "Van der Waals Volumes and Radii", J. Phys. Chem., **68**, 441 (1964).

[285] J. C. Slater, "Atomic Radii in Crystals", J. Chem. Phys., **41**, 3199 (1964).

[286] E. Clementi, D. L. Raimondi, and W. P. Reinhardt, "Atomic Screening Constants from SCF Functions. II. Atoms with 37 to 86 Electrons", J. Chem. Phys., **47**, 1300 (1967).

[287] B. Deb, R. Singh, and N. Sukumar, "A universal density criterion for correlating the radii and other properties of atoms and ions", J. Mol. Structure: THEOCHEM, **259**, 121 (1992).

[288] P. Pyykkö and M. Atsumi, "Molecular Single-Bond Covalent Radii for Elements 1-118", Chem. Eur. J., **15**, 186 (2009).

[289] M. Mantina, A. C. Chamberlin, R. Valero, C. J. Cramer, and D. G. Truhlar, "Consistent van der Waals Radii for the Whole Main Group", J. Phys. Chem. A, **113**, 5806 (2009).

[290] Y. H. Zhao, M. H. Abraham, and A. M. Zissimos, "Fast Calculation of van der Waals Volume as a Sum of Atomic and Bond Contributions and Its Application to Drug Compounds", J. Org. Chem., **68**, 7368 (2003).

[291] K. V. Klenin, F. Tristram, T. Strunk, W. Wenzel, K. V. Klenin, F. Tristram, T. Strunk, and W. Wenzel, "Derivatives of molecular surface area and volume: Simple and exact analytical formulas, Derivatives of molecular surface area and volume: Simple and exact analytical formulas", J. Comp. Chem., **32**, 2647 (2011).

[292] P. L. Warburton, J. L. Wang, and P. G. Mezey, "On the Balance of Simplification and Reality in Molecular Modeling of the Electron Density", J. Chem. Theory Comput., **4**, 1627 (2008).

[293] A. Zobelli, V. Ivanovskaya, Ph. Wagner, I. Suarez-Martinez, A. Yaya, and C. P. Ewels, "A comparative study of density functional and density functional tight binding calculations of defects in graphene", Phys. Status Solidi B, **249**, 276 (2012).

[294] D. Jiang, V. R. Cooper, and S. Dai, "Porous Graphene as the Ultimate Membrane for Gas Separation", Nano Lett., **9**, 4019 (2009).

[295] S. Bertolazzi, J. Brivio, and A. Kis, "Stretching and Breaking of Ultrathin MoS2", ACS Nano, **5**, 9703 (2011).

[296] L. Song, L. Ci, H. Lu, P. B. Sorokin, C. Jin, J. Ni, A. G. Kvashnin, D. G. Kvashnin, J. Lou, B. I. Yakobson, and P. M. Ajayan, "Large Scale Growth and Characterization of Atomic Hexagonal Boron Nitride Layers", Nano Lett., **10**, 3209 (2010).

[297] J. Salvetat, G. A. D. Briggs, J. Bonard, R. R. Bacsa, A. J. Kulik, T. Stöckli, N. A. Burnham, and L. Forró, "Elastic and Shear Moduli of Single-Walled Carbon Nanotube Ropes", Phys. Rev. Lett., **82**, 944 (1999).

[298] S. Ogata and Y. Shibutani, "Ideal tensile strength and band gap of single-walled carbon nanotubes", Phys. Rev. B, **68**, 165409 (2003).

[299] S. Cambré, B. Schoeters, S. Luyckx, E. Goovaerts, and W. Wenseleers, "Experimental Observation of Single-File Water Filling of Thin Single-Wall Carbon Nanotubes Down to Chiral Index (5,3)", Phys. Rev. Lett., **104**, 207401 (2010).

[300] R. Faccio, P. A. Denis, H. Pardo, C. Goyenola, and A. W. Mombrú, "Mechanical properties of graphene nanoribbons", J. Phys.: Condens. Matter, **21**, 285304 (2009).

[301] S. Y. Hong and M. Kertesz, "Theoretical evaluation of Young's moduli of polymers", Phys. Rev. B, **41**, 11368 (1990).

[302] C. R. Fincher, C. E. Chen, A. J. Heeger, A. G. MacDiarmid, and J. B. Hastings, "Structural Determination of the Symmetry-Breaking Parameter in trans-$(CH)_x$", Phys. Rev. Lett., **48**, 100 (1982).

[303] D. E. Tuyarot, B. Koiller, and R. B. Capaz, "Tight-binding total-energy method applied to polyacetylene", Phys. Rev. B, **61**, 7187 (2000).

[304] C. W. Bunn, "The crystal structure of long-chain normal paraffin hydrocarbons. The "shape" of the <CH2 group", Transactions of the Faraday Society, **35**, 482 (1939).

[305] R. J. Meier, "Regarding the ultimate Young's modulus of a single polyethylene chain", Macromolecules, **26**, 4376 (1993).

[306] R. B. Capaz and M. J. Caldas, "Ab initio calculations of structural and dynamical properties of poly(p-phenylene) and poly(p-phenylene vinylene)", Phys. Rev. B, **67**, 205205 (2003).

[307] S. J. Martin, D. D. C. Bradley, P. A. Lane, H. Mellor, and P. L. Burn, "Linear and nonlinear optical properties of the conjugated polymers PPV and MEH-PPV", Phys. Rev. B, **59**, 15133 (1999).

[308] M. Matsuo and C. Sawatari, "Elastic modulus of polyethylene in the crystal chain direction as measured by x-ray diffraction", Macromolecules, **19**, 2036 (1986).

RÉSUMÉ et MOTS-CLÉS

MODÉLISATION DU GRAPHÈNE AVEC LES TECHNIQUES *AB INITIO*

Le travail de cette thèse porte sur l'étude du matériau graphène et de nanostructures dérivées, par modélisation *ab initio*. L'influence des terminaisons chimiques des bords du feuillet graphène (armchair, zigzag et Klein, en considérant aussi des reconstructions possible) a été étudiée. En l'absence de terminaisons, une nouvelle configuration stable «repliée» a été identifiée; qui correspond à la création de structure nanotube le long des bords du feuillet. Une étude des bords hydrogénés a été effectuée, qui montrait des nouvelles configurations de bords Klein reconstruites énergétiquement favorable. En outre, les bords hydrogénés joueront un rôle clef dans les processus de croissance du graphène, et d'éventuels modèles de croissance adaptés via l'addition des dimères de carbone sont proposés. Des terminaisons plus complexes sur des nanorubans de graphène de type armchair de 4 à 25 Å de largeur ont été modélisées également, par exemple impliquant -OH (hydroxyle). L'influence sur la structure et les propriétés électronique, chimique et mécaniques des nanorubans a été étudiée. Cette partie a conduit à rediscuter la notion de module de Young de nanofeuillets (graphène, BN, MoS_2, $MoTe_2$ etc.). Notamment ce travail propose une définition de «volume à prendre en compte» sur la base d'une densité électronique moyenne. Cette nouvelle approche offre un cadre transférable sous-jacent pour calculer le module de Young, et donc de pouvoir extrapoler correctement les valeurs entre le graphène, des nanotubes de carbone et du graphite. Le concept a aussi été étendu à des polymères organiques.

Mots-clés : Graphène, DFT, Modélisation, Nanofeuillets, Nanorubans, Nanotubes, Bords, Module de Young

AB INITIO MODELLING OF GRAPHENE

In this thesis graphene and related nanostructures were studied, using density functional *ab initio* modelling techniques. The influence of different edge terminations has been investigated for typical pristine graphene edges (armchair, zigzag and Klein) and several reconstructed edge configurations. For unterminated graphene edges a new stable folded back edge has been identified, creating a nanotube along the graphene edge. A systematic study of hydrogenated edges was performed, and new favourable reconstructed Klein edge configurations were found. Furthermore hydrogenated edges are expected to play an important role for graphene growth processes, and thus possible adapted growth models via carbon dimer addition are proposed. Next more complex edge functionalisations such as hydroxylated (-OH) edges were studied, in particular modelling thin 4 - 25 Å wide armchair graphene nanoribbons. Notably the influence on structural, electronic, chemical and mechanical properties has been investigated. This promises new routes towards controlled design of specific nanoribbon properties. Finally the in-plane Young's modulus of various nanosheets (including graphene, BN, MoS_2, $MoTe_2$ etc.) were calculated. In this context a new geometry independent volume definition for nanoobjects has been developed, based on the average electron density. This new approach offers a transferable underlying framework to calculate the Young's modulus, and thus values correctly extrapolate for example between graphene, carbon nanotubes and bulk graphite. The concept was further extended to organic polymers.

Keywords: Graphene, DFT, Modelling, Nanosheets, Nanoribbons, Nanotubes, Edges, Young's modulus